Alfred-Wegener-Institut Helmholtz Zentrum für Polar- und Meeresforschung
Forschungsstelle Potsdam, Sektion Periglazialforschung

Organic carbon in ice-rich permafrost: Characteristics, quantity, and availability

Dissertation
zur Erlangung des akademischen Grades
"doctor rerum naturalium"
(Dr. rer. nat.)
in der Wissenschaftsdisziplin "Geologie"

als publikationsbasierte Arbeit eingereicht an der
Mathematisch-Naturwissenschaftlichen Fakultät
der Universität Potsdam

von
Jens Strauß

Potsdam, den 30.09.2014

für Judith, Ida und Emma

Paper Chapter 2	© John Wiley & Sons 2012, license number 3460420538537
Paper Chapter 3	© Authors 2013, Creative Commons Attribution-Non-Commercial License
Paper Chapter 4	© Authors 2014, Creative Commons Attribution 3.0 License
Paper Appendix I	© Authors 2014, Creative Commons Attribution 3.0 License
Paper Appendix II	© Authors 2014, Creative Commons Attribution 3.0 License

Table of contents

Abstract VII
Zusammenfassung IX
Abbreviations and nomenclature XII

1 Introduction 1
1.1 Scientific background 1
1.1.1 Permafrost and its degradation features: A climate-sensitive phenomenon 1
1.1.2 Permafrost carbon: A dormant organic carbon pool under climate pressure 2
1.1.3 Study region: Regional focus, global significance 4
1.2 Aims and objectives 8
1.3 Basic method overview 8
1.3.1 Field studies 8
1.3.2 Sedimentology and biogeochemistry 9
1.3.3 Remote sensing methods 10
1.3.4 Lipid biomarkers 10
1.3.5 Statistical analyses 10
1.4 Thesis organization 11
1.5 Overview of publications 13
1.5.1 Publication "Grain-size properties and organic-carbon stock of Yedoma Ice Complex permafrost from the Kolyma lowland, northeastern Siberia" 13
1.5.2 Publication "The deep permafrost carbon pool of the Yedoma region in Siberia and Alaska" 14
1.5.3 Publication "Organic matter quality of deep permafrost carbon - a study from Arctic Siberia" 15
1.5.4 Appendix publication "Estimated stocks of circumpolar permafrost carbon with quantified uncertainty ranges and identified data gaps" 16
1.5.5 Appendix publication "Observation-based modeling of permafrost carbon fluxes with accounting for deep carbon deposits and thermokarst activity" 17

2 Grain-size properties and organic-carbon stock of Yedoma Ice Complex permafrost from the Kolyma lowland, northeastern Siberia 19
2.1 Abstract 19
2.2 Introduction 20
2.3 Material and methods 20
2.3.1 Study site 20
2.3.2 Field work 23
2.3.3 Grain-size distribution 23
2.3.4 End-member modeling 23
2.3.5 Interactive peak fitting 24
2.3.6 Biogeochemistry 25
2.4 Results 26
2.4.1 Lithological features of the Yedoma Ice Complex 26
2.4.2 Granulometric characteristics and calculations 27
2.4.3 End-member modeling 28

2.4.4 Interactive peak fitting grain size pattern 30
2.4.5 Organic matter characteristics and calculations 31
2.5 Discussion 32
2.5.1 Origin of the Yedoma Ice Complex at Duvanny Yar 32
2.5.2 Changes in organic matter parameters 35
2.6 Conclusions 36
3 The deep permafrost carbon pool of the Yedoma region in Siberia and Alaska 37
3.1 Abstract 37
3.2 Introduction 37
3.3 Methods 39
3.3.1 Sampling and organic carbon measurement 40
3.3.2 Bulk density calculation 39
3.3.3 Wedge-ice volume calculation 41
3.3.4 Statistical methods 41
3.4 Results 41
3.4.1 Data and statistical methods 41
3.4.2 Biogeochemical and physical parameters 42
3.4.3 Yedoma region coverage 43
3.4.4 Inventory estimations 44
3.5 Discussion 44
3.6 Conclusion 46
4 Organic matter quality of deep permafrost carbon - a study from Arctic Siberia 47
4.1 Abstract 47
4.2 Introduction 48
4.3 Material and methods 50
4.3.1 Study area 50
4.3.2 Field work 51
4.3.3 Indicators of organic matter quality 51
4.3.4 Biomarker proxies/indices 55
4.3.5 Principal component analysis 57
4.4 Results 58
4.4.1 Organic matter quality of Yedoma deposits 58
4.4.2 Organic matter quality of thermokarst deposits 62
4.5 Discussion 66
4.5.1 Sediment facies 66
4.5.2 Organic matter degradation 66
4.5.3 Fate of organic matter 71
4.6 Conclusions 73
5 Synthesis 74
5.1 Yedoma origin: How did Yedoma deposits accumulate? 74
5.2 Storage of organic carbon: How much is stored in the Yedoma and permafrost region? 76
5.2.1 Yedoma region 76
5.2.2 Northern circumpolar permafrost region 80

5.3 Quality of organic carbon Quality: What is the susceptibility of the permafrost region's carbon for future decomposition? 81
5.3.1 Quality of Yedoma region's carbon 81
5.3.2 Potential response of the permafrost region's organic carbon to warming 82
5.4 Outlook: opportunities for future research 84
References 86

Financial and technical support 107

Appendix I Estimated stocks of circumpolar permafrost carbon with quantified uncertainty ranges and identified data gaps A-1
I-1 Abstract A-2
I-2 Introduction A-2
I-3 Methods A-5
I-3.1 Calculating 0 to 3 m SOC stocks A-5
I-3.2 Calculating deltaic SOC stocks A-8
I-3.3 Calculating Yedoma region permafrost SOC stocks A-9
I-3.4 Estimating SOC stock uncertainties A-9
I-3.5 Statistical tests of significance A-10
I-4 Results A-11
I-4.1 Mean 0 to 3 m SOC storage and depth distribution in soil classes across regions A-11
I-4.2 Upscaled soil area and SOC stocks across regions A-13
I-4.3 Storage of SOC below 3 m depth in deltaic deposits A-17
I-4.4 Storage of permafrost SOC in the Yedoma region A-19
I-5 Discussion A-19
I-5.1 Differences to previous estimates A-20
I-5.2 Distribution patterns of SOC stored in 0 to 3 m soil A-22
I-5.3 Estimate uncertainties and data gaps A-24
I-5.4 Deposits with significant SOC stocks below 3 m depth A-31
I-5.5 Potential vulnerability and remobilization of permafrost region SOC stocks A-31
I-6 Conclusions A-32
I-7 Supplemental material A-35
I-7.1 Supplemental methods A-35
I-7.2 Supplemental figures and tables A-44

Appendix II Observation-based modeling of permafrost carbon fluxes with accounting for deep carbon deposits and thermokarst activity A-51
II-1 Abstract A-51
II-2 Introduction A-52
II-3 Multi-pool permafrost model A-55
II-3.1 Model structure A-56
II-3.2 Model initialization A-59
II-3.3 Permafrost thaw and carbon release A-61
II-3.4 Model limitations A-61
II-4 Model results A-62
II-4.1 Permafrost degradation A-62
II-4.2 Permafrost carbon release A-65

II-4.3 Contribution of deep deposits A-68
II-4.4 Permafrost-affected warming A-69
II-5 Discussion and conclusions A-69
II-6 Outlook A-74
II-7 Supplementary material A-76
II-7.1 Model initialization A-76
II-7.2 Thaw rate parameterization A-77
II-7.3 Anaerobic soil fractions A-79
II-7.4 Carbon release A-82
II-7.5 Carbon-cycle and climate model A-84
Appendix III Supplementary material for Chapter 3: The deep permafrost carbon pool of the Yedoma region in Siberia and Alaska A-85
III-1 Terminology and methods A-85
III-1.1 Terminology and abbreviations A-85
III-1.2 Total organic carbon (TOC) measurement A-86
III-1.3 Calculation of the bulk density, segregated ice, and organic carbon density A-86
III-1.4 Calculation of the wedge-ice volume (WIV) A-87
III-1.5 Calculation of Yedoma region coverage A-89
III-1.6 Calculation of the Yedoma region atmospheric CO_2 contribution A-90
III-1.7 Mean-bootstrapping technique to calculate organic carbon budgets A-90
III-1.8 Inventory calculation based on simple-mean values A-91
III-2 Supplementary figures A-91
III-3 Supplementary tables A-96
Appendix IV Supplementary material for Chapter 4: Organic matter quality of deep permafrost carbon - a study from Arctic Siberia A-100
Acknowledgements - Danksagung A-103
Eidesstattliche Erklärung A-105

Abstract

Permafrost, defined as ground that is frozen for at least two consecutive years, is a distinct feature of the terrestrial unglaciated Arctic. It covers approximately one quarter of the land area of the Northern Hemisphere (23,000,000 km²). Arctic landscapes, especially those underlain by permafrost, are threatened by climate warming and may degrade in different ways, including active layer deepening, thermal erosion, and development of rapid thaw features. In Siberian and Alaskan late Pleistocene ice-rich Yedoma permafrost, rapid and deep thaw processes (called thermokarst) can mobilize deep organic carbon (below 3 m depth) by surface subsidence due to loss of ground ice. Increased permafrost thaw could cause a feedback loop of global significance if its stored frozen organic carbon is re-introduced into the active carbon cycle as greenhouse gases, which accelerate warming and inducing more permafrost thaw and carbon release. To assess this concern, the major objective of the thesis was to enhance the understanding of the origin of Yedoma as well as to assess the associated organic carbon pool size and carbon quality (concerning degradability). The key research questions were:

- How did Yedoma deposits accumulate?
- How much organic carbon is stored in the Yedoma region?
- What is the susceptibility of the Yedoma region's carbon for future decomposition?

To address these three research questions, an interdisciplinary approach, including detailed field studies and sampling in Siberia and Alaska as well as methods of sedimentology, organic biogeochemistry, remote sensing, statistical analyses, and computational modeling were applied. To provide a panarctic context, this thesis additionally includes results both from a newly compiled northern circumpolar carbon database and from a model assessment of carbon fluxes in a warming Arctic.

The Yedoma samples show a homogeneous grain-size composition. All samples were poorly sorted with a multi-modal grain-size distribution, indicating various (re-) transport processes. This contradicts the popular pure loess deposition hypothesis for the origin of Yedoma permafrost. The absence of large-scale grinding processes via glaciers and ice sheets in northeast Siberian lowlands, processes which are necessary to create loess as material source, suggests the polygenetic origin of Yedoma deposits.

Based on the largest available data set of the key parameters, including organic carbon content, bulk density, ground ice content, and deposit volume (thickness and coverage) from Siberian and Alaskan study sites, this thesis further shows that deep frozen organic carbon in the Yedoma region consists of two distinct major reservoirs,

Yedoma deposits and thermokarst deposits (formed in thaw-lake basins). Yedoma deposits contain ~80 Gt and thermokarst deposits ~130 Gt organic carbon, or a total of ~210 Gt. Depending on the approach used for calculating uncertainty, the range for the total Yedoma region carbon store is ±75 % and ±20 % for conservative single and multiple bootstrapping calculations, respectively. Despite the fact that these findings reduce the Yedoma region carbon pool by nearly a factor of two compared to previous estimates, this frozen organic carbon is still capable of inducing a permafrost carbon feedback to climate warming. The complete northern circumpolar permafrost region contains between 1100 and 1500 Gt organic carbon, of which ~60 % is perennially frozen and decoupled from the short-term carbon cycle.

When thawed and re-introduced into the active carbon cycle, the organic matter qualities become relevant. Furthermore, results from investigations into Yedoma and thermokarst organic matter quality studies showed that Yedoma and thermokarst organic matter exhibit no depth-dependent quality trend. This is evidence that after freezing, the ancient organic matter is preserved in a state of constant quality. The applied alkane and fatty-acid-based biomarker proxies including the carbon-preference and the higher-land-plant-fatty-acid indices show a broad range of organic matter quality and thus no significantly different qualities of the organic matter stored in thermokarst deposits compared to Yedoma deposits. This lack of quality differences shows that the organic matter biodegradability depends on different decomposition trajectories and the previous decomposition/incorporation history. Finally, the fate of the organic matter has been assessed by implementing deep carbon pools and thermokarst processes in a permafrost carbon model. Under various warming scenarios for the northern circumpolar permafrost region, model results show a carbon release from permafrost regions of up to ~140 Gt and ~310 Gt by the years 2100 and 2300, respectively. The additional warming caused by the carbon release from newly-thawed permafrost contributes 0.03 to 0.14°C by the year 2100. The model simulations predict that a further increase by the 23rd century will add 0.4°C to global mean surface air temperatures.

In conclusion, Yedoma deposit formation during the late Pleistocene was dominated by water-related (alluvial/fluvial/lacustrine) as well as aeolian processes under periglacial conditions. The circum-arctic permafrost region, including the Yedoma region, contains a substantial amount of currently frozen organic carbon. The carbon of the Yedoma region is well-preserved and therefore available for decomposition after thaw. A missing quality-depth trend shows that permafrost preserves the quality of ancient organic matter. When the organic matter is mobilized by deep degradation processes, the northern permafrost region may add up to 0.4°C to the global warming by the year 2300.

Zusammenfassung

Permafrost, definiert als mehr als zwei aufeinander folgende Jahre gefrorenes Bodenmaterial, ist eines der prägenden Merkmale der unvergletscherten arktischen Landgebiete. Verursacht durch extrem kalte Wintertemperaturen und geringe Schneebedeckung nimmt das Permafrost-Verbreitungsgebiet mit ~23.000.000 km² rund ein Viertel der Landfläche der Nordhemisphäre ein. Von Permafrost unterlagerte arktische Landschaften sind besonders anfällig hinsichtlich einer Erwärmung des Klimas. Verglichen mit der globalen Mitteltemperatur prognostizieren Klimamodelle für die Arktis einen doppelt so starken Anstieg der Temperatur. In einer sich erwärmenden Arktis bewirken Störungen des thermisch-hydrologischen Gleichgewichts eine Degradation von Permafrost und Veränderungen des Oberflächenreliefs. Diese Störungen können zum Beispiel zu einer Vertiefung der saisonalen Auftauschicht, zu thermisch bedingter Erosion sowie zu schneller Oberflächenabsenkung und Thermokarst führen. Im Verbreitungsgebiet der spätpleistozänen eisreichen Permafrost-Ablagerungen Sibiriens und Alaskas, bezeichnet als Yedoma, können Thermokarstprozesse auch mehr als 3 m tiefe organischen Kohlenstoffspeicher verfügbar machen, wenn durch schmelzendes Grundeis und Schmelzwasserdrainage die Oberfläche abgesenkt wird. So kann das Tauen von Permafrost eine globale Bedeutung entwickeln, indem vorher eingefrorener Kohlenstoff wieder dem aktiven Kohlenstoffkreislauf zugeführt wird. Dies kann durch Treibhausgasfreisetzung aus Permafrost zu einer sich selbst verstärkenden weiteren Erwärmung und somit zu fortschreitendem Tauen mit weiterer Kohlenstofffreisetzung führen. Diesen Prozess nennt man Permafrost-Kohlenstoff Rückkopplung.

Um das Verständnis der Permafrostkohlenstoffdynamik grundlegend zu verbessern, wurde in dieser Doktorarbeit die Entstehung der Yedoma-Ablagerungen eingeschlossen des darin gespeicherten organischen Kohlenstoffs untersucht. Die konkreten Forschungsfragen der Arbeit sind:

- Wie wurden die Yedoma-Sedimente abgelagert?
- Wie viel Kohlenstoff ist in der Yedoma Region gespeichert?
- Wie ist die Anfälligkeit dieses Kohlenstoffs für eine Degradation in der Zukunft?

Um die oben genannten drei Forschungsfragen zu beantworten, wurde ein interdisziplinärer Forschungsansatz gewählt. In Sibirien und Alaska wurden detaillierte Felduntersuchungen durchgeführt und Methoden der Sedimentologie, der organischen Biogeochemie, der Fernerkundung sowie der statistischen Analyse und computergestützten Modellierung angewendet. Um diese Ergebnisse in den panarktische Kontext zu setzen, enthält diese Doktorarbeit ebenfalls Ergebnisse einer Studie, wel-

che auf Grundlage einer neu zusammengestellten Datenbank den gesamten Kohlenstoff des arktischen Permafrosts abschätzt. Eine Modellierungsstudie ergänzt die Arbeit bezüglich einer Abschätzung der Kohlenstoffflüsse der Permafrostregion und deren Einfluss auf die globale Erwärmung.

Die Ergebnisse zur Yedoma-Entstehung zeigen, dass die Korngrößenverteilungen dieser Ablagerungen, tiefenabhängig betrachtet, sehr homogen sind. Alle gemessenen Korngrößenverteilungen sind schlecht sortiert. Dies deutet auf eine Vielzahl von Transportprozessen hin und widerspricht der populären Hypothese einer reinen Löß-Ablagerung. Interpretiert im Kontext mit der Abwesenheit von Gletschern sowie Eisschilden, als Ausgangsgebiete von Löß-Ablagerungen, in den sibirischen Tiefländern des Spätpleistozäns, zeigt diese Arbeit, dass Yedoma-Ablagerungen polygenetischen Ursprungs sind.

Basierend auf dem größten verfügbaren Datensatz der Schlüsselparameter Kohlenstoffgehalt, Lagerungsdichte, Grundeis und Volumen der Ablagerungen von über 20 Untersuchungsgebieten in Sibirien und Alaska zeigt diese Arbeit mit Yedoma- und Thermokarstablagerungen zwei wesentliche Kohlenstoffspeicher der Yedoma Region auf. Yedoma-Ablagerungen enthalten ~80 Gt und Thermokarstablagerungen ~130 Gt organischen Kohlenstoffs, was einer Gesamtmenge von ~210 Gt organischen Kohlenstoffs entspricht. Abhängig vom gewählten Ansatz der Fehlerberechnung liegt der Unsicherheitsbereich dieser Quantitätsabschätzung bei ±75 % (einfaches Bootstrapping) oder ±20 % (wiederholtes Bootstrapping). Obwohl diese Zahlen die bisherigen Berechnungen des Yedoma-Region-Kohlenstoffspeichers vorhergehender Studien halbieren, stellen 210 Gt organischen Kohlenstoffs noch immer einen großen Kohlenstoffspeicher dar, der eine positive Rückkopplung zur globalen Klimaerwärmung bewirken könnte. Die gesamte Permafrostregion beinhaltet zwischen 1100 und 1500 Gt Kohlenstoff, wovon ~60 % dauerhaft gefroren und somit dem derzeitigen Kohlenstoffkreislauf entzogen sind.

Wenn dieser Kohlenstoff freigesetzt wird, ist ein weiterer Faktor, die Kohlenstoffqualität, relevant. Die Untersuchungen zur Kohlenstoffqualität zeigen keinen tiefenabhängigen Trend in Yedoma- und Thermokarstablagerungen. Dies belegt, dass nach dem Einfrieren die fossile organische Substanz konserviert wurde. Die genutzten Biomarkerdaten, z.B. der 'carbon preference' Index und der 'higher land plant fatty acid' Index zeigen sowohl für Yedoma- als auch für Thermokarstablagerungen keine signifikanten Unterschiede der Kohlenstoffqualität. Das bedeutet, dass der Kohlenstoffabbau nach dem Auftauen von unterschiedlichen Faktoren abhängig ist. Dazu gehören verschiedene Abbauwege oder schon vor dem Einfrieren geschehener Abbau. Um die Bedeutung des aufgetauten Kohlenstoffs abzuschätzen, wurden Ther-

mokarstprozesse in ein Permafrost-Kohlenstoff-Modell einbezogen. Unter Berücksichtigung verschiedener Erwärmungsszenarien könnte die zirkumarktische Permafrostregion bis zum Jahr 2100 ~140 Gt Kohlenstoff und bis 2300 ~310 Gt in die Atmosphäre freisetzen. Dies entspricht einer Erwärmung der mittleren globalen Oberflächentemperatur von ~0,03 bis ~0,14°C bis 2100 und bis zu ~0,4°C bis 2300.

Zusammenfassend stellt diese Dissertation heraus, dass die Yedoma-Ablagerungen während des Spätpleistozäns durch eine Kombination verschiedener aquatischer (alluviale, fluviale, lakustrine) sowie äolische Prozesse entstanden sind. Die zirkumarktische Region, inklusive der Yedoma Region, beinhaltet eine erhebliche Menge an derzeit eingefrorenem organischen Kohlenstoffs. Dieser Kohlenstoff ist gut erhalten und damit nach dem Auftauen für den mikrobiellen Abbau verfügbar. Eine fehlende Tiefenabhängigkeit der Kohlenstoffqualität zeigt, dass Permafrost die Qualität zum Einfrierzeitpunkt bewahrt. Wenn auch der tiefliegende organische Kohlenstoff durch Thermokarstprozesse verfügbar gemacht wird, kann die Permafrostregion bis zum Jahr 2300 bis zu 0,4°C zur mittleren globalen Oberflächentemperatur beitragen.

Abbreviations and nomenclature

Notation	Meaning	**Unit** (if applicable related to SI units)
~	approximately	
°C	degree Celsius	273.15 °K
°E	longitudinal position in degrees east of the prime median	
°N	latitudinal position in degrees north of the equator	
°W	longitudinal position in degrees west of the prime median	
µg	micro gram	1×10^{-9}kg
µm	micro meter	1×10^{-6} m
%	percent; a number or ratio as a fraction of 100	
‰	per mille; a number or ratio as a fraction of 1000	
©	copyright	
a	Latin: annus; year	3.1536×10^{7} s
A	aerobic/anaerobic environment	
ā	soil-specific thermal diffusivities	
ACL	average chain length	
AER	aerobic	
ALD	active layer depth	
AMS	accelerator mass spectrometry	
BD	bulk density	10^3kg/m³ = g/cm³
BP	before present (1950)	a
Buo	Buor Khaya	
$C^{\uparrow}(t)$	carbon release	
C	carbon	
C/N	total organic carbon/total nitrogen ratio	
ca.	Latin: circa; approximately	
CH_4	methane	
CI	confidence interval	
Cl	clay	
cm	centimeter	1×10^{-2} m
CO_2	carbon dioxide	
CPI	carbon preference index	
$d\overline{T}'(t)$	high-latitude surface air temperature anomaly	
dT(t)	surface air temperature anomaly	
DY	Duvanny Yar	
e.g.	Latin: exempli gratia; for example	
EM	end-member	
eq.	equation	
ESM	Earth system model	
et al.	Latin:et alii; and others	
etc.	Latin: et cetera; and so on	
F(t)	area fraction	
g	gram	1×10^{-3} kg
GC	gas chromatography	
GIS	geographic information system	
GSD	grain-size distribution	
Gt	gigatonne	1×10^{12} kg
h	hour	3600 s
HPA	higher plant alcohol index	
HPFA	higher plant fatty acid index	
i.e.	Latin: id est; that is	
IC	ice complex	
IPF	interactive peak fitter	
ka	Latin: kilo annus; thousand years	3.1536×10^{10} s
kg	kilogram	1 kg
km^2	square kilometer	1×10^{6} m^2
lat	latitude band	
log	logarithm	
m	meter	1 m
m a.r.l.	meter above river level	
m a.s.l.	meter above surface level	
m b.s.l.	meter below surface level	
m²	square meter	1 m²

m^3	cubic meter	1 m^3
MAGT	mean annual ground temperature	
max	maximum	
min	minute *or* minimum	
ml	milliliter	$10^{-6}m^3$
mm	millimeter	10^{-3} m
MPa	megapascal	1×10^6Pa
MPLC	medium-pressure liquid chromatography	
MS	mass spectrometer *or* mineral soil	
Mt	megaton	1×10^9kg
n	sample number *or* porosity	
NCSCD	northern circumpolar soil carbon database	
NSO	nitrogen, sulfur and oxygen containing fraction	
Ø	diameter	
OC	organic carbon	
OM	organic matter	
ORG	organic soils	
OX	fraction of oxidized carbon	
PCA	principal component analysis	
Pg	petagram	1×10^{12}kg
ppm	parts per million	1 ppm = 10^{-6}
Q	organic matter quality	
Q^{10}	temperature coefficient of the rate of change by increasing the temperature by 10°C	
R(t)	release rates	
R^2	root mean square error	
RCP	representative concentration pathway	
RMS	root mean square error	
RTK	refrozen thermokarst deposits	
s	second	1 s
S(t)	soil carbon pool	
Sa	sand	
SEI	segregated ice	wt%
SEIV	segregated ice volume	vol%
Si	silt	
SOC	soil organic carbon	
sp.	species	
StD	standard deviation	
TC	total carbon	
TIC	total inorganic carbon	
TKL	thermokarst lake	
TN	total nitrogen	wt%
TOC	total organic carbon	wt%
TOC_{kg/m^3}	total organic carbon	kg/m^3
$TOC_{wt\%}$	total organic carbon	wt%
TR	thaw rates	
TS(t)	monthly soil temperatures	
VC(t)	pool-specific amount of vulnerable carbon	
vol%	per cent by volume	
VPDB	Vienna PeeDee belemnite	‰
WET	wetland	
WGS84	world geodetic system 1984	
WI	wedge ice	
WIV	wedge-ice volume	vol%
wt%	per cent by weight	
Y	Yedoma	
yr	year	3.1536×10^7 s
z	depth level	
$\delta^{13}C$	stable TOC isotope ratio	‰ vs. VPDB
Σ	summation sign	

1 Introduction

1.1 Scientific background

1.1.1 Permafrost and its degradation features: A climate-sensitive phenomenon

Permafrost is a characteristic feature of the majority of the northern circumpolar terrestrial region that is not covered by ice sheets and glaciers (Figure 1-1). Defined as ground material that remains at or below 0 °C for at least two consecutive years (van Everdingen, 2005), permafrost is caused by extremely cold winter temperatures and low snow depth, resulting in a long-term negative annual heat energy balance of the land surface. The permafrost region covers approximately 23 million km², which is ~24 % of the terrestrial area of the Northern Hemisphere (Zhang et al., 2008). During the Pleistocene up to ~50 % of the unglaciated Northern Hemisphere was affected by permafrost (French, 2007). Thus, 25 % of its coverage has been lost due to postglacial warming. Based on modeling experiments, another 15 to 30 % of the recent permafrost coverage could be lost along southern permafrost margins (Figure 1-2) by the end of the 21st century (Anisimov and Reneva, 2006; Euskirchen et al., 2006). Observations indicate warming and thawing permafrost in many regions (Romanovsky et al., 2010a), an irreversible process on human timescales (Schaefer et al., 2011; MacDougall et al., 2012). Thus, permafrost is a climate-sensitive phenomenon and its fate depends on the complex interaction of climatic and ecological processes (Shur and Jorgenson, 2007).

Figure 1-1. Permafrost extent in the Northern Hemisphere; after Ahlenius (2007) in Romanovsky et al. (2007). The transect shown in Figure 1-2 is illustrated by a dashed black line.

Permafrost degrades in different ways. The major processes are (1) top-down thaw by long-term thickening of the active layer, a layer of ground that is subject to seasonal thawing and freezing (Hinkel and Nelson, 2003; Schuur et al., 2008; Schaefer et al., 2011), (2) thermo-erosion along coasts, rivers, and lake shores (Rachold et al.,

2000; Jones et al., 2009; Jones et al., 2011; Günther et al., 2013) and (3) rapid thaw induced by thermokarst and thermoerosion processes (Lantz and Kokelj, 2008; Grosse et al., 2011a; 2011b; Biskaborn et al., 2013; Morgenstern et al., 2013). Especially thermokarst and talik (zone of unfrozen ground inside permafrost, Figure 1-6) formation, caused by lake development with melting of excess ground ice (ice exceeding the pore volume) and draining of melt water, can result in deep thaw and surface subsidence of up to 30 m (Ulrich et al., 2014).

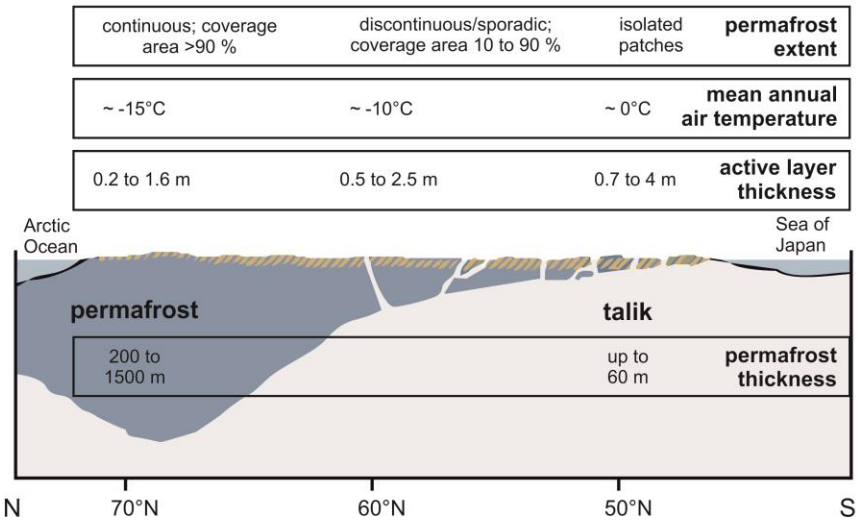

Figure 1-2. North to south transect of the permafrost of East Siberia; modified after French (2007).

1.1.2 Permafrost carbon: A dormant organic carbon pool under climate pressure

The northern circumpolar ecosystems, including the permafrost region, provide immense services to the Earth's climate system: by cooling the Earth through e.g. reflecting sunlight directly and sequestering carbon, circumpolar regions function like a global air conditioner (Euskirchen et al., 2013). But polar regions respond more quickly (~twice the global mean temperature warming) to climate change than do the other regions on Earth (AMAP, 2011; UNEP, 2012). This phenomenon is called polar amplification (Serreze and Barry, 2011), an presages potentially increasing disturbances in a warming permafrost region (Grosse et al., 2011a). Moreover, the abovementioned thermokarst degradation processes have the ability to also mobilize deeper permafrost carbon. After Hugelius et al. (2014), "deep" means deeper than 3 m. Permafrost thaw could re-introduce the frozen organic carbon (OC) pools into the carbon cycle and start a potential feedback loop of carbon release from thawed permafrost, causing warming again (Figure 1-3). Thus, although permafrost and its carbon stocks are located in one of the world most remote regions, it is of great importance to consider permafrost in context of the global carbon cycle and climate change.

The deep OC is often several thousands of years older than the surface OC because deep permafrost carbon has been disconnected from the surface carbon turnover by freezing during the late Quaternary. This condition is quite unique to permafrost environments. Some permafrost areas are of particular interest: the ice-rich (>20 % excess ice content) permafrost areas (8.8 % of the total northern circumpolar permafrost region (Zhang et al., 2008)). Here, the large amount of excess ground ice affects the vulnerability of permafrost deposits to disturbances (Grosse et al., 2011a). In particular, here deep surface subsidence may occur if the excess ice thaws and the resulting melt water drains. Thus, ground ice is a key feature for permafrost carbon stabilization. Though all permafrost can be affected by thawing, degradation of ice-rich permafrost potentially causes particularly strong feedbacks to permafrost ecosystems and the carbon cycle (Rowland et al., 2010).

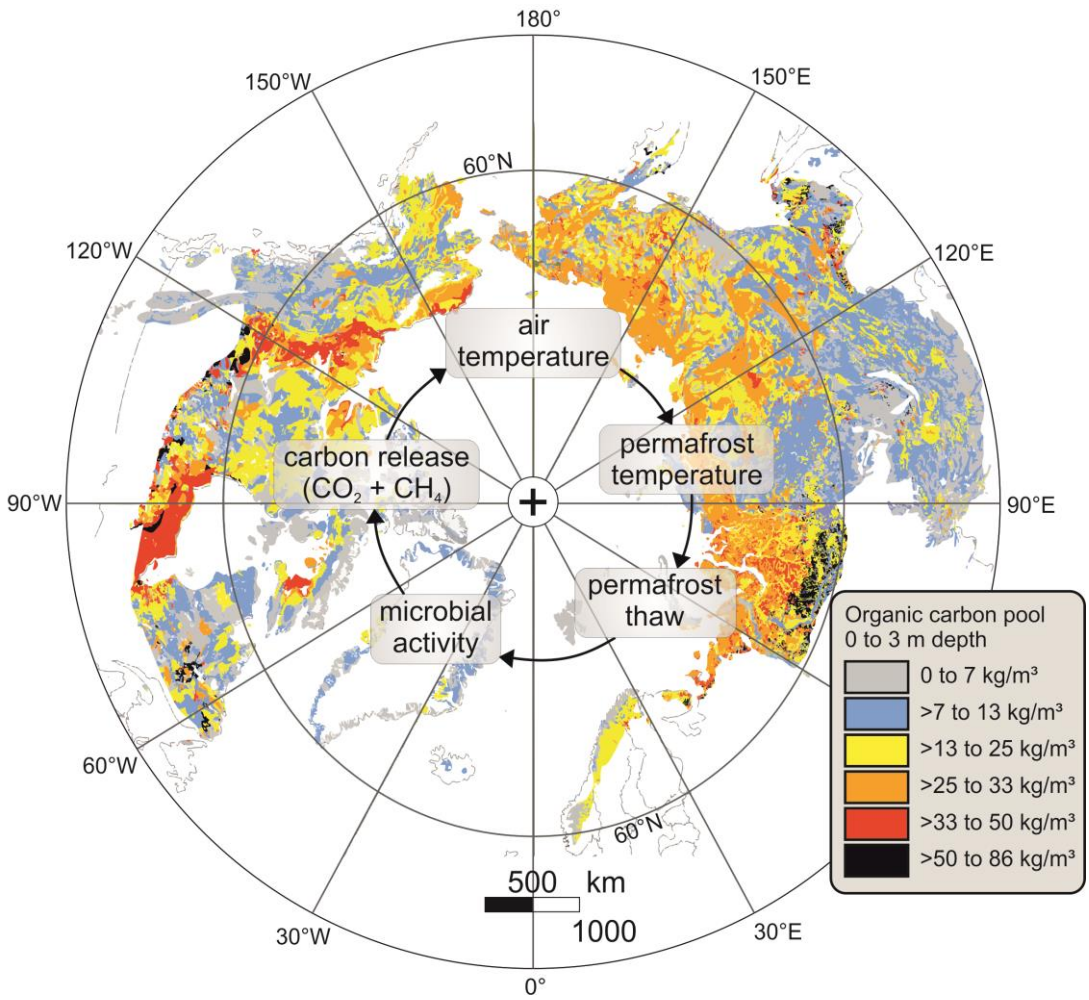

Figure 1-3. Map of estimated 0 to 3 m carbon inventory stored in the circumpolar permafrost region (modified after Hugelius et al., 2014). The potential arctic carbon climate feedback is illustrated in the middle.

The size of the permafrost carbon pool has been discussed in the scientific literature (e.g. van Huissteden and Dolman, 2012). The recent numbers range from 270 Gt

(Tarnocai et al., 2003) for the first 1 m up to 1850 Gt (McGuire et al., 2009) for 0 to 3 m including some deeper deposits at 25 to 50 m depth. Nevertheless, it is agreed that a large pool of OC has been accumulating in the terrestrial Arctic for thousands of years (Figure 1-3). Cold and waterlogged conditions substantially slow down organic matter (OM) degradation, and once soils become perennially frozen OM degradation ceases entirely (Davidson and Janssens, 2006).

Another important question is the fate of the OC held in permafrost. There are studies regarding the permafrost deposits as a (temporary) carbon sink (Kutzbach et al., 2007; van der Molen et al., 2007; van Huissteden and Dolman, 2012; Walter Anthony et al., 2014). Other studies of permafrost ecosystems regard the permafrost region as an active or upcoming carbon source (McGuire et al., 2009; Hayes et al., 2011; Natali et al., 2014). Once unlocked by thaw, permafrost OM may decompose and release CO_2 or CH_4 (Walter et al., 2006; Schuur et al., 2009; Mackelprang et al., 2011); processes like carbon sequestration by vegetation act in the opposite direction. Nevertheless, model projections suggest that greenhouse gas emissions from permafrost by 2300 (IPCC representative concentration pathways 8.5 scenario) (Schneider von Deimling et al., 2012) will be comparable in amount to all pre-2000 anthropogenic emissions, thus affecting the global carbon cycle significantly and amplifying surface warming (McGuire et al., 2009; Koven et al., 2011; Schaefer et al., 2011; Burke et al., 2012a; Ciais et al., 2012; DeConto et al., 2012; Schuur et al., 2013). Because of the high uncertainties in the amount and fate of permafrost OC, this thesis investigates the source of one of the less understood but potentially very significant carbon-climate feedbacks: The permafrost carbon feedback.

1.1.3 Study region: Regional focus, global significance

Major parts of the northern permafrost area remained unglaciated during the last ice age. Because of a lower sea level, the shelf of the Arctic Ocean, including the Bering Strait, was not flooded and thus an interconnected landmass stretched from the Taymyr Peninsula to Alaska between the Scandinavian and Laurentian ice sheets. This region is called Beringia (Hopkins, 1982). The eastern part of Siberia is also called western Beringia and Alaska is the eastern part of Beringia. A vast part of this region (Figure 1-4) is composed of ice-rich silts penetrated by large ice wedges (Figure 1-5), resulting from sedimentation and syngenetic freezing accompanied by wedge-ice growth driven by certain climatic and environmental conditions during the late Pleistocene. These unique materials are called Yedoma deposits and their origin is discussed in the scientific literature (Table 1-1). In Yedoma deposits, due to fast incorporation into permafrost from the seasonally-thawed active layer, OC-bearing

sediments up to 50 m thick have accumulated (Kanevskiy et al., 2011; Schirrmeister et al., 2013). As mentioned above, the ice-rich permafrost, like Yedoma, is especially prone to degradation. Thus, while the deposits of the Yedoma region are indeed a regional phenomenon, they have the potential for global significance if they degrade and release large amounts of OC.

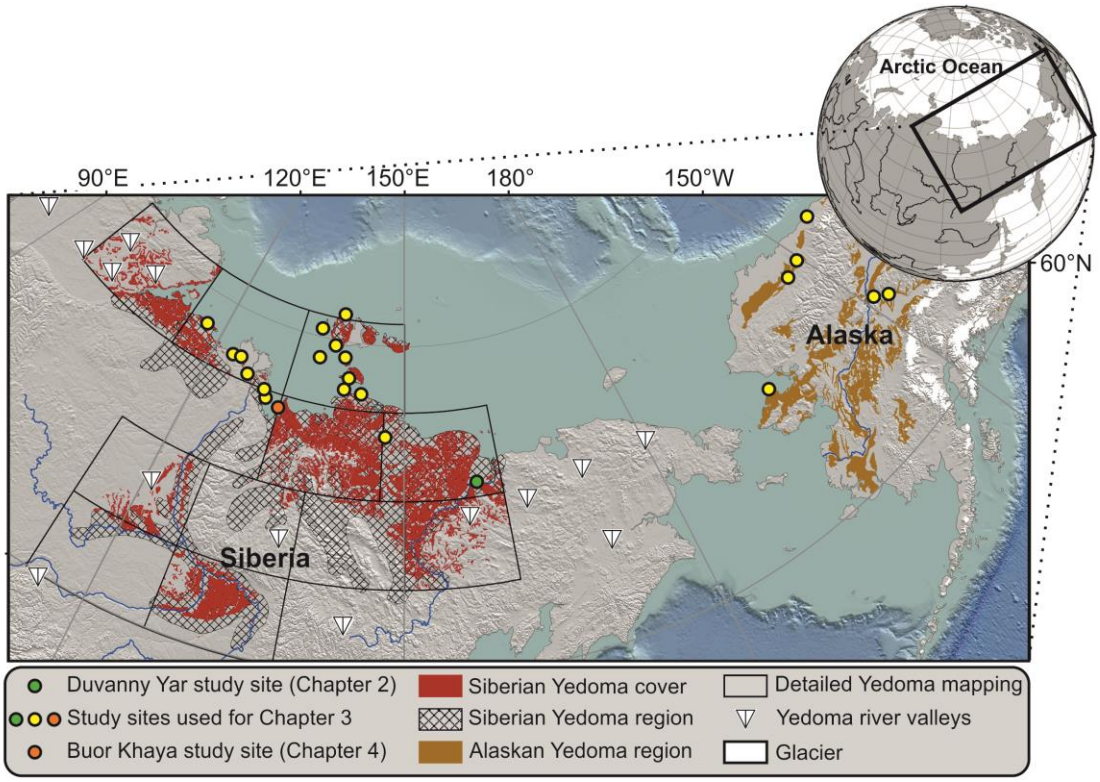

Figure 1-4. The Yedoma region, including the potential (Romanovskii, 1993) and fragmented (Jorgenson et al., 2008; Grosse et al., 2013b) area of Yedoma deposits in Arctic and sub-Arctic lowlands. The study sites of the included chapters (Table 1-2) are visualized in different colors (green: Chapter 2; green-yellow-orange: Chapter 3; orange Chapter 4). The box inside the inset globe illustrates the extent of the map below.

Table 1-1. Different hypotheses on Yedoma origin in Siberia, modified after Siegert et al. (1999) and Schirrmeister et al. (2013)

Origin	Citation
Fluvial and fluvial-related	
e.g. Fluvial and alluvial sediments of meandering rivers	*Vtyurin et al. (1957)*
Aeolian	
Cryogenic-aeolian ("loess ice") formation	*Tomirdiaro et al. (1984)*
Loess and retransported loess	*Péwé and Journaux (1983)*
Floodplains and slopes	
e.g. Floodplain sediments, proluvial slope sediments	*Slagoda (1993)*
Lacustrine and swamp	
e.g. Sediments of river deltas and swamps dammed by a shelf ice sheet	*Nagaoka (1994)*
Glacial and glacial-related	
Proglacial deposits in basins dammed by a shelf glacier	*Grosswald (1998)*
Polygenetic	
Polygenetic (fluvial, slope, aeolian, etc.); Nival-polygenetic (aeolian, fluvial, solifluction) sediments delivered from melting snow patches)	*Sher et al. (1987), Kunitsky (2002), Galabala (1997)*

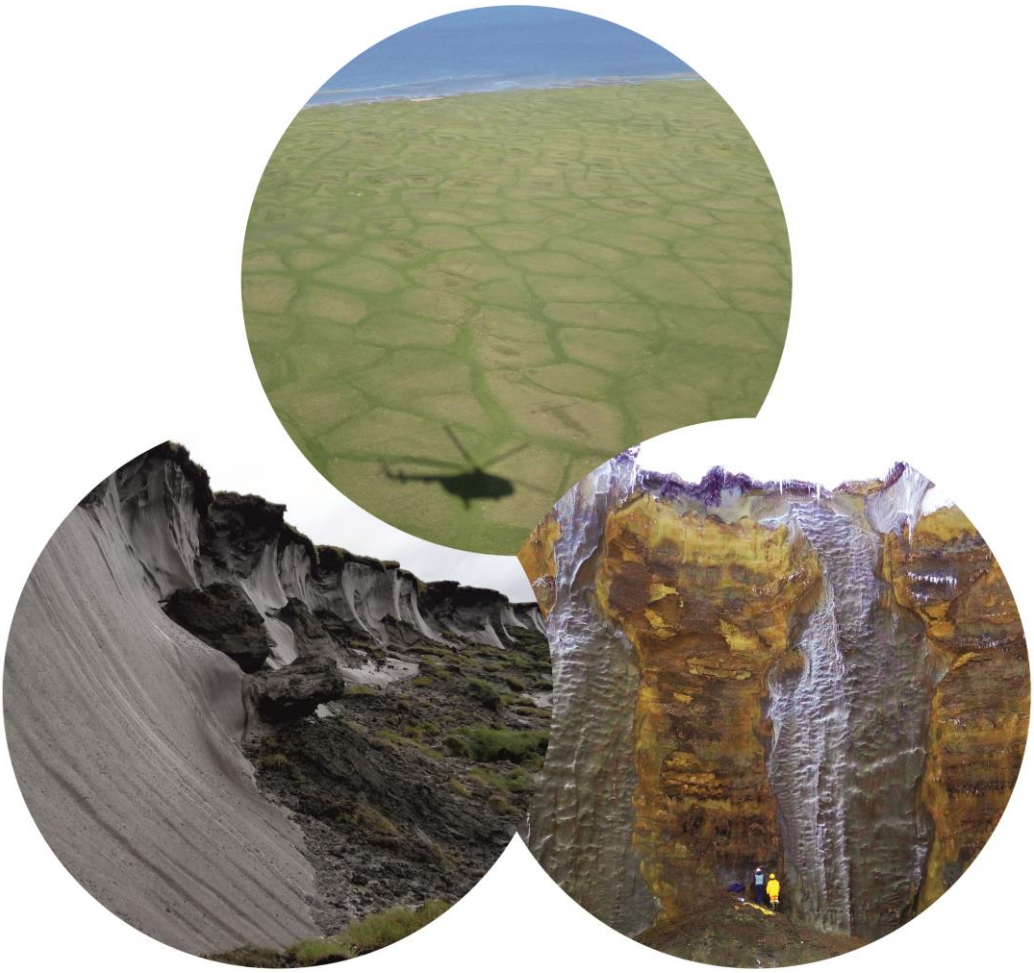

Figure 1-5. Top: surface polygonal network caused by winter frost cracking (Buor Khaya Peninsula, picture by P. Overduin); left: ice wedges occurring at the Laptev Sea coast, picture taken parallel to the shoreline (Buor Khaya Peninsula, Siberia, picture by F. Günther); right: Yedoma deposits consisting of sediment column (brownish colors) framed by late Pleistocene ice wedges (grey colors, Itkillik River, Alaska, picture by J. Strauss)

Yedoma degradation has been occurring due to postglacial warming since the end of the Pleistocene (Kaplina et al., 1986; Romanovskii et al., 2000; Morgenstern et al., 2013). Therefore, the Yedoma region comprises another major stratigraphic type of deposits that are associated with thermokarst landforms. Such sediments in thermokarst depressions are composed of reworked Yedoma deposits and Holocene accumulation during sub aquatic and sub aerial phases. Yedoma and thermokarst deposits are ubiquitous in the Yedoma region. However, due to remoteness and harsh climates, access to these study regions and deposits is logistically difficult and usually connected to expensive field expeditions.

Samples used for this thesis (Table 1-2) were collected from exposures eroded by the shelf seas of the Arctic Ocean or rivers. A substantial advantage of naturally-exposed bluffs is that the sampling locations can be studied in a wider cryostratigraphic context. All study sites, including their geographic position, are given in Table 1-2.

Table 1-2. Study sites used in this thesis sorted from Siberia (top) to Alaska (bottom).

Site	Region	Coordinates			
Cape Mamontov Klyk	Western Laptev Sea	N	73.6075°	E	117.1824°
Nagym (Ebe Sise Island)	Lena Delta	N	72.8814°	E	123.2164°
Khardang Island	Lena Delta	N	72.9510°	E	124.2220°
Kurungnakh Island	Lena Delta	N	72.3344°	E	126.3092°
Bykovsky Peninsula	Central Laptev Sea	N	71.8900°	E	129.6252°
Muostakh Island	Central Laptev Sea	N	71.6129°	E	129.9436°
Buor Khaya Peninsula	Central Laptev Sea	N	71.3836°	E	132.0840°
Bel'kovsky Island	New Siberian Archipelago	N	75.3658°	E	135.5890°
Stolbovoy Island	New Siberian Archipelago	N	74.0600°	E	136.0800°
Kotel'ny Island (Cap Anisii)	New Siberian Archipelago	N	76.1703°	E	139.0136°
Kotel'ny Island (Khomurgunnakh River)	New Siberian Archipelago	N	76.1727°	°E	139.2266°
Maly Lyakhovsky Island	New Siberian Archipelago	N	74.2461°	E	140.3509°
Cape Svyatoy Nos	Dmitry Laptev Strait	N	72.8400°	E	140.8500°
Bol'shoy Lyakhovsky Island	Dmitry Laptev Strait	N	73.3304°	E	141.3454°
Oyogos Yar Coast	Dmitry Laptev Strait	N	72.6835°	E	143.4753°
Chokurdakh (Berelekh River)	Indigirka Lowland	N	70.8413°	E	147.4384°
Duvanny Yar (Kolyma River)	Kolyma Lowland	N	68.6328°	E	159.0876°
Kitluk River	Seward Peninsula	N	66.5781°	W	164.4307°
Colville River	Alaskan North Slope	N	69.2469°	W	152.8528°
Itkillik River	Alaskan North Slope	N	69.3404°	W	150.5157°
Dalton Highway	Interior Alaska	N	65.5492°	W	148.8909°
Vault Creek	Interior Alaska	N	65.0687°	W	147.7558°
Camden Bay	Beaufort Sea Coast	N	69.9794°	W	144.8137°

1.2 Aims and objectives

The overarching aim of the thesis is to answer the question of the origin of Yedoma deposits (Chapter 2) including Yedoma region OC pool size (Chapter 3) and OM quality/availability (Chapter 4). The research questions and objectives (Figure 1-6) to characterize the Yedoma region and the OC are:

(1) How did Yedoma deposits accumulate?
(2) How much OC is stored in the Yedoma region?
(3) What is the susceptibility of the Yedoma region's carbon for future decomposition?

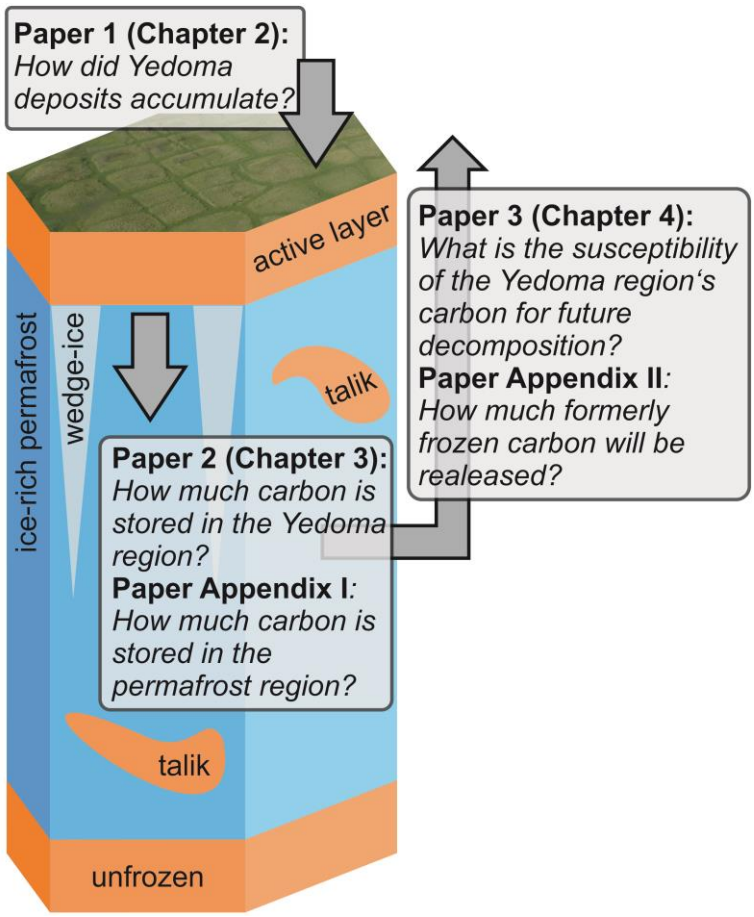

Figure 1-6. Diagram of the vertical structure of ice-rich permafrost consisting of the active layer, permafrost including ground ice such as ice wedges, and unfrozen parts called taliks. The topics of the papers are informed by the research questions.

1.3 Basic method overview

To address the research questions, an interdisciplinary approach was applied including detailed field studies and sampling in Siberia and Alaska, sediment and carbon laboratory analytics and statistical data analysis and interpretation (Figure 1-7). In the following, a general overview of the applied methods is provided. Detailed method descriptions are included in the thesis sections.

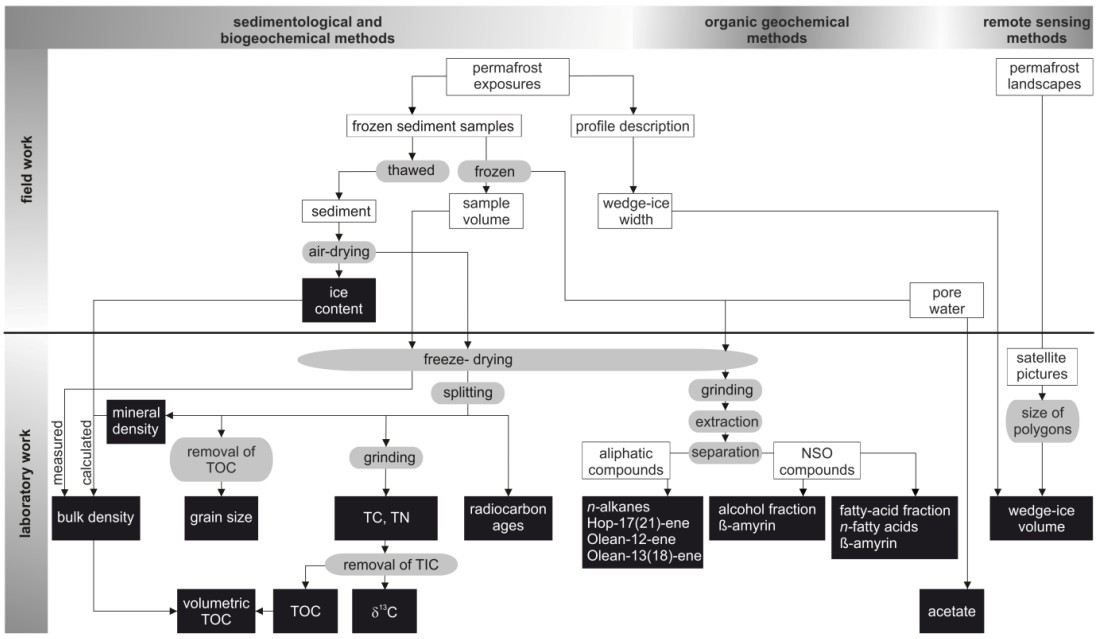

Figure 1-7. Chart of the applied interdisciplinary method approach. The parameters are highlighted with black shaded boxes and white text, the methodical steps with light-grey shaded ovals. Statistical analyses of individual parameters are not included in this figure.

1.3.1 Field studies

For all publications in this thesis, the Yedoma and thermokarst exposures were studied and sampled in (sub-)profiles exposed on separate thermokarst mounds or at a cliff wall. After the profiles were cleaned, photographed, and sketched, the exposed deposits were described according to sediment characteristics, visible OM, and cryostructures. In the field, the ice content and the volume of the frozen samples were determined.

1.3.2 Sedimentology and biogeochemistry

The following sedimentological and biogeochemical methods were applied in this thesis. To infer the bulk density (BD) indirectly from the ice content (called "calculated" in Figure 1-7), the density of the solid fraction was measured using a helium gas displacement pycnometer (AccuPyc-1330, Micromeritics). To determine the grain-size distributions (GSDs), a laser particle sizer (LS 200, Beckmann-Coulter) was used. The weight percentages of elemental total carbon (TC) and total nitrogen (TN) contents were measured with a carbon-nitrogen-sulphur analyzer (Vario EL III, Elementar). The total organic carbon ($TOC_{wt\%}$) content was measured with a TOC analyzer (Vario Max C, Elementar). Stable carbon isotopes of TOC ($\delta^{13}C$) were determined with a Finnigan MAT Delta-S mass spectrometer combined with a FLASH elemental analyzer and a CONFLO III gas mixing system. Ages were determined by radiocarbon dating. The present measurements were performed at the Poznań Radio-

carbon Laboratory, Poland, by using compact carbon accelerator mass spectrometry (Goslar et al., 2004).

1.3.3 Remote sensing methods

For quantifying the wedge-ice volume (WIV) in Chapter 3, besides field ice-wedge size data, ice-wedge polygon size data were required. These sizes were determined by mapping high-resolution (<1 m/pixel spatial resolution; GeoEye and Kompsat-2) satellite imagery of selected study sites.

1.3.4 Lipid biomarkers

Organic geochemistry methods were used to estimate the OM quality (concerning biodegradability) in Chapter 4. Therefore, the ground-up sediment was placed in an extraction cell of an accelerated solvent extractor (ASE 200, Dionex). Using a medium-pressure liquid chromatography (MPLC) system, the extract was separated into fractions of different polarity (aliphatic and polar hetero (nitrogen, sulfur, and oxygen-containing fraction (NSO) components). Afterwards, the NSO fraction was split into a fatty acids and an alcohol fraction. The aliphatic fraction (containing e.g. *n*-alkanes and triterpenoid compounds) and the NSO fraction (containing e.g. *n*-fatty acids and β-amyrin) were measured by a gas chromatography–mass spectrometry (GC–MS) device (GC: Trace GC Ultra; MS: DSQ; both Thermo Fisher Scientific). To determine the acetate content, pore water extracts were analyzed twice using ion chromatography with conductivity detection (ICS 3000, Dionex).

1.3.5 Statistical analyses

1.3.5.1 End-member modeling

For reconstructing the origin of Yedoma deposits (Chapter 2) end-member (EM) modeling of the GSD curves was performed using a Matlab algorithm by Dietze et al. (2012). Important criteria for obtaining feasible models include insuring that EMs are non-negative, and that they fulfill the constant-sum constraints. EMs are defined by two characteristics: first the loadings, which are the GSDs of the EMs, and second the scores, which typify their quantitative variation throughout the profile. In this study, grain-size data were transformed using a W-transformation.

1.3.5.2 Bootstrapping

To quantify the OC inventory of the Yedoma region (Chapter 3), calculations of the carbon budget and the OC density are based on bootstrapping techniques. Observed values (TOC, BD, WIV, thickness) were resampled 10,000 times. The mean value was calculated afterwards from the 10,000 values. Because TOC and BD are genu-

inely correlated, paired values are used in the resampling process. Computations were performed using R software (boot package).

1.3.5.3 Principal component analysis

To investigate the relations between the multiple degradation proxies and their host material (Chapter 4), we applied principal component analysis (PCA). Prior to the PCA, concentration data were transformed using a log (x+1) transformation; TOC ($_{wt\%}$ and $_{kg/m^3}$) data were square-root transformed to reduce the range. Computations were performed using R software and the "vegan" package (Oksanen, 2013).

1.4 Thesis organization

The introductory part (Chapter 1) of this cumulative dissertation provides scientific background and relevance concerning organic carbon in ice-rich permafrost deposits. Chapter 1 defines the objectives of the thesis and gives a short methodical overview as well as an overview of the research articles, including a contribution statement.

Following Chapter 1, three main parts (Chapters 2 to 4) are included. These chapters and the appendix contain original research articles, which have been published or are under review in international peer-reviewed journals (Table 1-3). In detail, Chapter 2 deals with the topic of how Yedoma deposits, including the OM, have been deposited (Strauss et al., 2012). Chapter 3 quantifies the amount of OC sequestered in the deep permafrost deposits (Strauss et al., 2013). Chapter 4 addresses the topic of OM quality to answer the question of how the OM potentially responds to thaw (Strauss et al., 2014). In Chapter 5, results and implications of the individual thesis papers are synthesized and generally discussed.

The appendix contains two co-authored publications. These publications are included in this thesis because they integrate Chapters 2 to 4 into the context of the circum-arctic permafrost region; in addition they broaden the scale of Chapters 2 to 4 concerning their importance and implications in a warming Arctic. The first appendix paper (Appendix I) is an Arctic-wide permafrost carbon quantification (Hugelius et al., 2014). This publication discusses the amount of carbon and the uncertainty and data gaps in the Arctic region. The second co-authored paper included (Appendix II) deals with climatic consequences of thawing permafrost deposits using a modeling approach (Schneider von Deimling et al., 2014). The supplementary material of Chapter 3 (Appendix III) and Chapter 4 (Appendix IV) are attached here as well.

Table 1-3: Overview of publications within this thesis.

	Publication
Chapter 2	*Grain-size properties and organic-carbon stock of Yedoma Ice Complex permafrost from the Kolyma lowland, northeastern Siberia* Strauss, J., Schirrmeister, L., Wetterich, S., Borchers, A., and Davydov, S.P. (2012), Global Biogeochemical Cycles, 26, GB3003, doi:10.1029/2011GB004104
Chapter 3	*The deep permafrost carbon pool of the Yedoma region in Siberia and Alaska* Strauss, J., Schirrmeister, L., Grosse, G., Wetterich, S., Ulrich, M., Herzschuh, U., and Hubberten, H.-W. (2013), Geophys. Res. Lett., 40, 6165-6170, doi:10.1002/2013GL058088
Chapter 4	*Organic matter quality of deep permafrost carbon - a study from Arctic Siberia* Strauss, J., Schirrmeister, L., Mangelsdorf, K., Eichhorn, L., Wetterich, S., and Herzschuh, U. (2014), Biogeosciences Discussions, 11, 15945–15989, doi:10.5194/bgd-11-15945-2014
Appendix I	*Estimated stocks of circumpolar permafrost carbon with quantified uncertainty ranges and identified data gaps* Hugelius, G., Strauss, J., Zubrzycki, S., Harden, J., Schuur, E. A. G., Ping, C.-L., Schirrmeister, L., Grosse, G., Michaelson, G., Koven, C., O'Donnel, J., Elberling, B., Mishra, U., Camill, P., Yu, Z., Palmtag, J., and Kuhry, P. (2014), Biogeosciences, 11, 6573-6593, doi:10.5194/bg-11-6573-2014
Appendix II	*Observation-based modeling of permafrost carbon fluxes with accounting for deep carbon deposits and thermokarst activity* Schneider von Deimling, T., Grosse, G., Strauss, J., Schirrmeister, L., Morgenstern, A., Schaphoff, S., Meinshausen, M., and Boike, J. (2014) Biogeosciences Discuss., 11, 16599-16643, doi:10.5194/bgd-11-16599-2014
Appendix III	Supplementary material for *The deep permafrost carbon pool of the Yedoma region in Siberia and Alaska* (Chapter 3)
Appendix IV	Supplementary material for *Organic matter quality of deep permafrost carbon - a study from Arctic Siberia* (Chapter 4)

1.5 Overview of publications

1.5.1 Publication "Grain-size properties and organic-carbon stock of Yedoma Ice Complex permafrost from the Kolyma lowland, northeastern Siberia"

by Strauss, J., Schirrmeister, L., Wetterich, S., Borchers, A., and Davydov, S.P.

in Global Biogeochemical Cycles, 26, GB3003, doi:10.1029/2011GB004104, 2012

1.5.1.1 Contribution statement

The sampling in 2008 at Duvanny Yar was planned and conducted by L. Schirrmeister and S. Wetterich. J. Strauss carried out all laboratory analyses and interpreted all the data including reviewing the relevant literature. J. Strauss planned and wrote the entire publication with input of all the co-authors.

1.5.1.2 Summary

This paper aims to clarify the Yedoma deposit origin in order to get closer to an understanding of how the OM accumulated. Because of its potential to degrade and release OC, the OC inventory of Yedoma deposits is relevant to current concerns about the effects of global warming. Within this paper a new approach for BD calculation in ice-saturated deposits was developed, because this BDs are required for volumetric carbon estimations. Therefore, we analyzed the grain size and the OM characteristics of the deposits exposed at the Duvanny Yar stratigraphic key site (lower Kolyma River, northeast Siberia). A distinct bi-modal GSD reveals a polygenetic origin of the frozen sediments from a floodplain environment (Figure 1-8). The $TOC_{wt\%}$ content averages 1.5±1.4 wt% while the mean TOC_{kg/m^3} is 14±8 kg/m³. In conclusion, it was found that Yedoma deposit formation at Duvanny Yar was dominated by

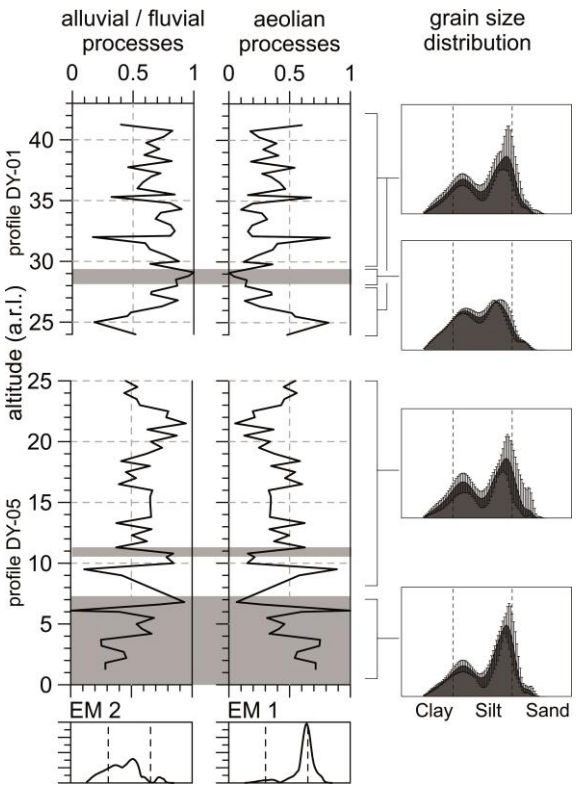

Figure 1-8. Variation of the end-member (EM) modeling scores (left) and laser-derived grain-size distributions (GSDs, right). The GSDs are stacked into sections of similar shape, and variability of each grain-size class within these sections is indicated by error bars. The grain-size fractions are labeled as clay, silt, and sand. Background boxes indicate paleocryosols horizons.

water-related (alluvial/fluvial/lacustrine) as well as aeolian processes. The TOC content of the studied deposits is lower than that of other Yedoma profiles described in the literature, but it is still a significant pool.

1.5.2 Publication "The deep permafrost carbon pool of the Yedoma region in Siberia and Alaska"

by Strauss, J., Schirrmeister, L., Grosse, G., Wetterich, S., Ulrich, M., Herzschuh, U., and Hubberten, H.-W.

in Geophysical Research Letters, 40, 6165–6170, doi:10.1002/2013GL058088, 2013

1.5.2.1 Contribution statement

J. Strauss collected samples and provided data on site-specific permafrost and geological conditions for the Buor Khaya Peninsula and Itkillik River study sites. Samples for laboratory analyses of the Buor Khaya, Itkillik River, and Duvanny Yar sites were prepared by J. Strauss. The other sampling campaigns (Table 1-2) and laboratory work were conducted by L. Schirrmeister, S. Wetterich, and G. Grosse. M. Ulrich digitized and calculated ice-wedge polygon sizes using satellite imagery. G. Grosse and L. Schirrmeister conducted remote-sensing and/or field studies used for determining the WIV. G. Grosse provided updated data on the distribution of Yedoma and thermokarst deposits. J. Strauss compiled the field sampling datasets from 1998 to 2013 and conducted the OC budget calculation including all prerequisite calculations. U. Herzschuh carried out the bootstrapping statistics. J. Strauss planned and wrote the entire paper, with input from all co-authors.

1.5.2.2 Summary

In this study the amount of OC stored in the Yedoma region was quantified. Because rapid inclusion of labile OM into permafrost ceases its decomposition, this region has been considered as a long-term carbon sink. In the paper it is shown that the deep frozen OC in the Yedoma region consists of two distinct major sub-reservoirs: Yedoma deposits (late Pleistocene ice- and organic-rich silty deposits) and deposits formed in thaw-lake basins (generalized as thermokarst deposits). Using a data set of 956 frozen samples from 23 Siberian and Alaskan study sites, we measured and modeled the primary parameters (Figure 1-9) necessary to quantify the overall frozen OC pool (including thickness, spatial coverage, BD, WIV, and $TOC_{wt\%}$).

We used the following equation for the carbon inventory calculation:

$$\text{OC budget (Gt)} = \frac{\text{thickness (m)} \times \text{coverage}(\text{m}^2) \times \text{BD}\left(10^3\,\text{kg/m}^3\right) \times \frac{100\text{-WIV}}{100} \times \frac{\text{TOC}_{\text{wt\%}}}{100}}{1{,}000{,}000{,}000} \qquad \text{eq. 1-1}$$

A substantial frozen OC pool of ~211+160/-153 Gt, stored in Yedoma (83+61/-57 Gt) and frozen thermokarst deposits (128+99/-96 Gt), was confirmed. It was also suggested that this pool size may have been previously overestimated (Zimov et al., 2006a), caused mainly by an overestimation of the BD (Figure 1-9). Furthermore, we propose that the thermokarst deposits contain the quantitatively more important pool (Yedoma to thermokarst deposits ratio ~2:3) and that the substantial amount of thaw-vulnerable OC in the Yedoma region must be accounted for in global models.

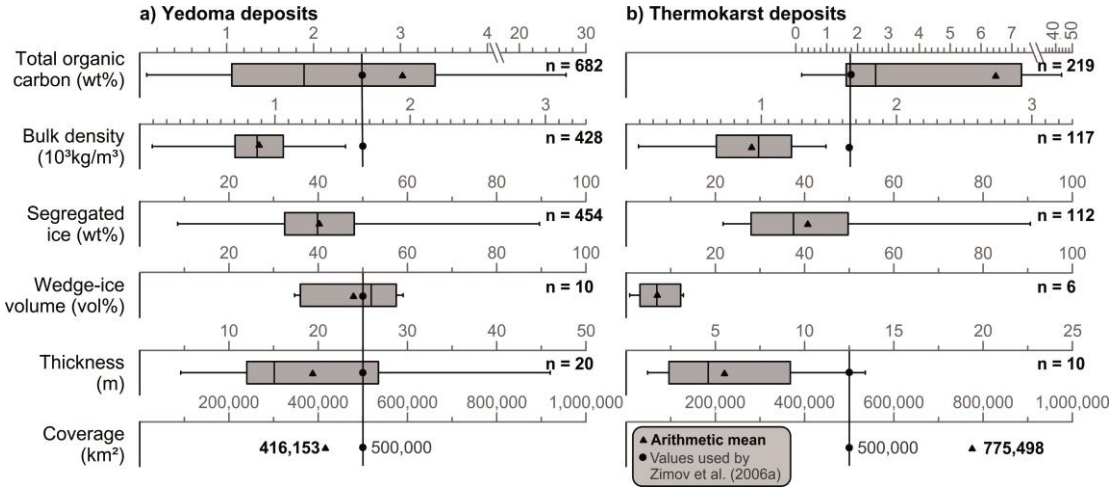

Figure 1-9. Box plots of the key parameters for (a) Yedoma and (b) thermokarst deposit organic carbon estimation. The literature estimate (Zimov et al., 2006a) is given by the vertical black line for comparison. Note the different axis scale in a) and b) for total organic carbon and thickness.

1.5.3 Publication "Organic matter quality of deep permafrost carbon - a study from Arctic Siberia"

by Strauss, J., Schirrmeister, L., Mangelsdorf, K., Eichhorn, L., Wetterich, S., and Herzschuh, U.

in Biogeosciences Discussions, 11, 15945–15989,doi:10.5194/bgd-11-15945-2014, 2014

1.5.3.1 Contribution statement

J. Strauss, L. Schirrmeister, and S. Wetterich carried out and coordinated all sediment sampling during the Buor Khaya field campaign in 2010. K. Mangelsdorf supported the biomarker analysis and interpretation. J. Strauss carried out the laboratory analyses, except for one profile, which was analyzed by L. Eichhorn. U. Herzschuh designed the statistical analyses. J. Strauss planned and wrote the publication with input from all co-authors.

1.5.3.2 Summary

In this paper the research question of how the OM stored in permafrost of the Yedoma region could respond under future climatic warming was addressed. The objective of this case study was the development of a stratigraphically differentiated OM quality characterization of Yedoma and thermokarst deposits on the Buor Khaya

Peninsula. For this purpose the degree of OM decomposition was estimated by using a multiproxy approach. It was found that the Yedoma and thermokarst OM qualities exhibit no obvious degradation-depth trend. Moreover, both sediment types show partially similar OM qualities (Figure 1-10). Thus, the thermokarst OM pool seems to be quantitatively more important, as shown in Chapter 3 (Strauss et al., 2013), and this pool shows a similar quality as Yedoma deposits. These similarities revealed that the OM decomposition vulnerability is heterogeneous and depends on different decomposition trajectories and former decomposition/incorporation history. By adding biomarker data, it was possible to show that the permafrost OM degradation processes occur likely via a combination of (uncompleted) degradation cycles. We conclude that the amount of OM in the studied sediments is high for mineral soils and susceptible for future decomposition. The missing depth-dependent quality trends reveal that permafrost acts like a giant freezer, preserving the ancient OM. During mobilization of undecomposed Yedoma deposits via thermokarst processes, the fate of this carbon depends largely on the environmental conditions, which also could conserve the undecomposed state until refreezing occurs.

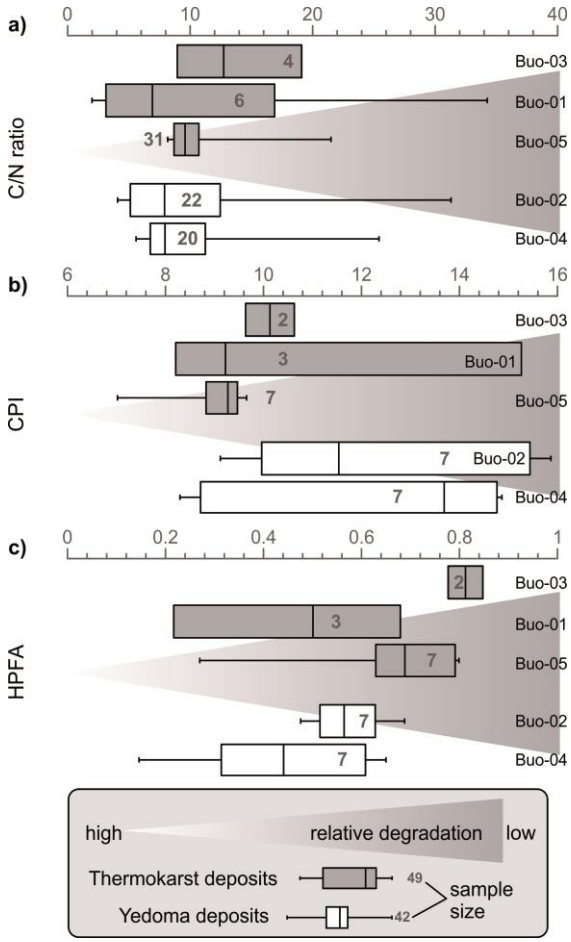

Figure 1-10. Diagram of the degradation state of the organic matter in Yedoma and thermokarst deposits, estimated by different applied proxies; a) TOC/CN (C/N) ratio, b) carbon preference index (CPI), and c) Higher Plant Fatty Acid (HPFA) index. The boxplots show the studied profiles separately with Yedoma deposits, white boxes, below the thermokarst deposits, gray boxes.

1.5.4 Appendix publication "Estimated stocks of circumpolar permafrost carbon with quantified uncertainty ranges and identified data gaps"

by Hugelius, G., Strauss, J., Zubrzycki, S., Harden, J., Schuur, E. A. G., Ping, C.-L., Schirrmeister, L., Grosse, G., Michaelson, G., Koven, C., O'Donnel, J., Elberling, B., Mishra, U., Camill, P., Yu, Z., Palmtag, J., and Kuhry, P.

in Biogeosciences, 11, 6573–6593, 2014, doi:10.5194/bg-11-6573-2014

1.5.4.1 Contribution statement

G. Hugelius planned and coordinated this manuscript and wrote the major parts of this paper. As the second author, J. Strauss wrote the Yedoma-region-specific parts. Therefore, J. Strauss partly sampled and did the laboratory work to produce the data used to calculate the Yedoma region carbon quantity. J. Strauss conducted the Yedoma region deep OC budget calculation, including its uncertainty, by using bootstrapping statistics including all prerequisite calculations.

1.5.4.2 Summary

This study reports OC quantity in deposits of the northern circumpolar permafrost region. Estimates of the permafrost OC pool, including quantitative uncertainty estimates, are given in different depth intervals; 0 to 0.3 m, 0 to 1 m, 1 to 3 m, and the whole range from 0 to 3 m (Figure 1-3). Moreover, deeper sediments (>3 m) in deltaic deposits of major rivers and in the Yedoma region of Siberia and Alaska are included. The estimates are based on the largest database available for the permafrost region, and the upscaling of the point measurements is based on regional soil maps.

It is shown that the permafrost region OC stocks are 217±12 and 472±27 Gt for the 0 to 0.3 m and 0 to 1 m soil depths, respectively (±95 % confidence intervals). The whole range of soils from 0 to 3 m contains 1034±150 Gt OC. Based on generalized calculations, storage of OC in deep deltaic alluvium (>3 m) of major Arctic rivers is estimated to be 91±52 Gt. In the Yedoma region, estimated >3 m OC stocks are 181±54 Gt. A total estimated mean storage for the permafrost region of ca. 1300 Gt with an uncertainty range of 1100 to 1500 Gt encompasses the combined revised estimates. Of this total ~800 Gt is perennially frozen, highlighting the relevance of this enormous carbon reservoir in a warming Arctic.

1.5.5 Appendix publication "Observation-based modeling of permafrost carbon fluxes with accounting for deep carbon deposits and thermokarst activity"

by Schneider von Deimling, T., Grosse, G., Strauss, J., Schirrmeister, L., Morgenstern, A., Schaphoff, S., Meinshausen, M., and Boike, J.

in Biogeosciences Discussions (doi:10.5194/bgd-11-16599-2014)

1.5.5.1 Contribution statement

The model developed here was planned and programmed by T. Schneider von Deimling. J. Strauss initiated the collaboration between T. Schneider von Deimling (Potsdam Institute for Climate Impact Research) and co-authors from the Alfred Wegener Institute (L. Schirrmeister, G. Grosse, J. Boike, and A. Morgenstern). J. Strauss calculated the Yedoma and thermokarst carbon inventory and provided input for

model parameterization, in particular carbon pool qualities of Yedoma and thermokarst deposits as well as the vulnerability related to ground ice contents. T. Schneider von Deimling wrote the paper with input from all co-authors.

1.5.5.2 Summary

This study aimed to develop a simplified multi-pool model for estimating the strength and timing of future greenhouse gas fluxes from recently-frozen permafrost. For the first time, by implementing abrupt thaw under thermokarst lakes, the carbon release from deep deposits in Yedoma regions was simulated. It was found that under the moderate warming conditions of the representative concentration pathway (RCP) 2.6 scenario, cumulative CO_2 fluxes from newly-thawed permafrost carbon will amount to 20 to 58 Gt OC (68 % range) by the year 2100. In 2300 40 to 98 Gt OC will be reached. A much larger permafrost degradation under strong warming (RCP8.5) results in cumulative CO_2 release of 42 to 141 Gt OC and 157 to 313 Gt OC by the years 2100 and 2300, respectively. CH_4 release from newly-thawed carbon in wetland-affected deposits was found to be discernible in the 22nd and 23rd centuries. This delay is due to the absence of abrupt thaw processes. Moreover, the Yedoma regions were found to crucially affect the simulated circum-arctic CH_4 fluxes. An additional warming through the release from newly-thawed permafrost carbon proved to be only slightly dependent on the pathway of anthropogenic emission and will amount to about 0.03 to 0.14°C by end of the century. The warming was projected to increase further in the 22nd and 23rd centuries and was most pronounced under the RCP6.0 scenario, adding 0.16 to 0.39°C to simulated global mean surface air temperatures.

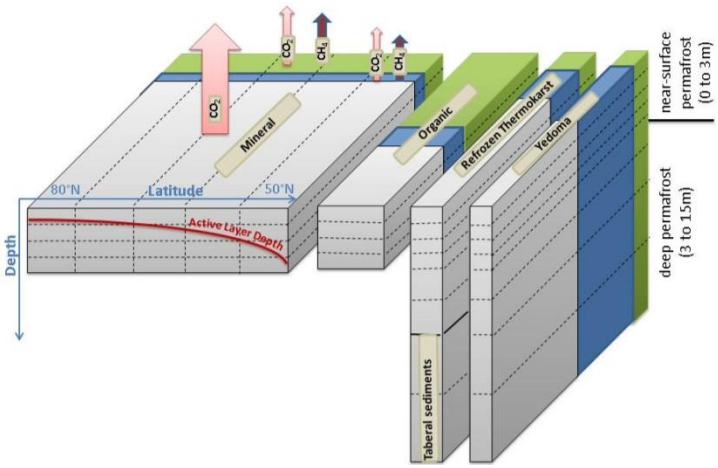

Figure 1-11. Subdivision of permafrost deposit carbon stocks into the four main pools (mineral, organic, Yedoma, and thermokarst deposits) and into aerobic (grey) and anaerobic (blue: thermokarst lake, green: wetland) fractions. For the mineral deposit carbon pool the N-S gradient of active layer depth (red line) and organic carbon release as CO_2 and CH_4 are also roughly visualized (arrows).

2 Grain-size properties and organic-carbon stock of Yedoma Ice Complex permafrost from the Kolyma lowland, northeastern Siberia

Strauss, J.[1], Schirrmeister, L.[1], Wetterich, S.[1], Borchers, A.[1], and Davydov, S. P.[2]

[1]Alfred Wegener Institute Helmholtz Centre for Polar and Marine Research, Periglacial Research Unit Potsdam, Potsdam, Germany.

[2]Northeast Scientific Station, Pacific Institute for Geography, Far-East Branch, Russian Academy of Sciences, Cherskii, Russia.

Published in: Global Biogeochemical Cycles, Vol. 26, 2012

Citation: Strauss, J., Schirrmeister, L., Wetterich, S., Borchers, A., and Davydov, S. P., Grain-size properties and organic-carbon stock of Yedoma Ice Complex permafrost from the Kolyma lowland, northeastern Siberia, Global Biogeochemical Cycles, 26, GB3003, doi:10.1029/2011GB004104, 2012.

2.1 Abstract

The organic carbon stock in permafrost is of increasing interest in environmental research, because during the late Quaternary a large pool of organic carbon accumulated in the sedimentary deposits of arctic permafrost. Because of its potential to degrade and release organic carbon, the organic-matter inventory of Yedoma Ice Complex deposits is relevant to current concerns about the effects of global warming. In this context, it is essential to improve the understanding of preserved carbon quantities and characteristics. The paper aims to clarify the Yedoma Ice Complex origin, and to develop an approach for volumetric organic-matter quantification. Therefore, we analyzed the grain size and the organic-matter characteristics of the deposits exposed at the stratigraphic key site Duvanny Yar (lower Kolyma River, northeast Siberia). A distinct bimodal grain-size distribution confirms a polygenetic origin of the frozen sediments from a floodplain environment. The total organic-carbon content averages 1.5±1.4 wt% while the volumetric organic-carbon content averages 14±8 kg/m³. However, large-scale extrapolations for Yedoma Ice Complex deposits in general are not reasonable yet because of their rather unclear spatial distribution. We conclude that Yedoma Ice Complex formation at Duvanny Yar was dominated by water-related (alluvial/fluvial/lacustrine) as well as aeolian processes. The total organic-carbon content of the studied deposits is low if compared to other profiles, but it is still a significant pool.

2.2 Introduction

A large pool of organic carbon accumulated in arctic permafrost during the late Quaternary, representing a significant long-term carbon sink. According to recent estimations, about half of the global below-ground organic carbon is stored in permafrost soils (1024 Gt in the first three meters depth below surface) (Tarnocai et al., 2009). In addition to the upper permafrost soil layers and peatlands (Hugelius and Kuhry, 2009), the fine-grained late Pleistocene Yedoma Ice Complex (IC) deposits are believed to contain a huge organic-carbon inventory (Zimov et al., 2006a). Yedoma IC deposits are well-exposed along the coasts and riverbanks in the northern East Siberian lowlands. Kanevskiy et al. (2011) and Schirrmeister et al. (2013) give a detailed definition of a Yedoma IC deposits; they describe it as remnant hills of a former surface plain, which rises by several dozens of meters above the surrounding terrain.

Polar regions respond more quickly and more strongly to climate change than do other regions on Earth (Rigor et al., 2000; Johannessen et al., 2004; Graversen et al., 2008). With regard to climate change, it is predicted that Yedoma ICs will be transformed from carbon reservoirs to carbon sources if these organic-rich sediments thaw and greenhouse gases are subsequently released (Walter et al., 2006; Zimov et al., 2006a; Schuur et al., 2008; Kuhry et al., 2009). Recent attention has focused on the fossil organic matter in such deposits (Schirrmeister et al., 2011b), although detailed studies of the size of the carbon pool, the level of release risk, and the release timescales are still rare. This study focuses on the Yedoma IC deposition environment to achieve a better understanding of sediment properties and organic-carbon stock, and employs the sedimentary archive of two Yedoma IC profiles at the Duvanny Yar permafrost section, located at the right lower Kolyma riverbank.

The samples were taken during the joint Russian-German Beringia/Kolyma 2008 expedition (Wetterich et al., 2011). The objectives of this paper are (1) to deduce the origin of the Duvanny Yar Yedoma IC deposits from its grain-size properties, and (2) to develop a new volume-based approach for quantifying organic carbon in permafrost.

2.3 Material and methods

2.3.1 Study site

Duvanny Yar is considered to be a stratigraphic key site for the late Quaternary (Kaplina et al., 1978; Sher et al., 1979) and an important reference site for the late Pleistocene history of Beringia (Hopkins, 1982). Beringia is the former interconnected landmass stretching from the Taymyr Peninsula to Alaska which was not glaciated

during the late Quaternary. Duvanny Yar (68° 37′N, 159° 06′E, Figure 2-1) is situated on the right bank of the lower Kolyma River in the northeastern part of Yakutia. Lopatina and Zanina (2006) and Zanina et al. (2011) describe the study site location and its research history in detail.

The Duvanny Yar section was first described by Barandova (1957) and Biske (1957). Sher (1971) studied horse bones paleozoologically and differentiated the permafrost sequence in a lower mid Pleistocene and an upper late Pleistocene part. Cryolithological and sedimentological structures of Duvanny Yar were described in detail by Kaplina et al. (1978), Arkhangelov et al. (1979), Sher et al. (1979), and Konishchev (1983). Vasil'chuk et al. (1988) worked on stable isotope data and pollen records from ice wedges. Paleopedological studies were carried out by Gubin (1995). Vasil'chuk et al. (2001) suggested that the Duvanny Yar Yedoma IC deposits accumulated between ~40 and 13 ka BP. More recent studies are about soil respiration and methane production (Dutta et al., 2006; Zimov et al., 2006a).

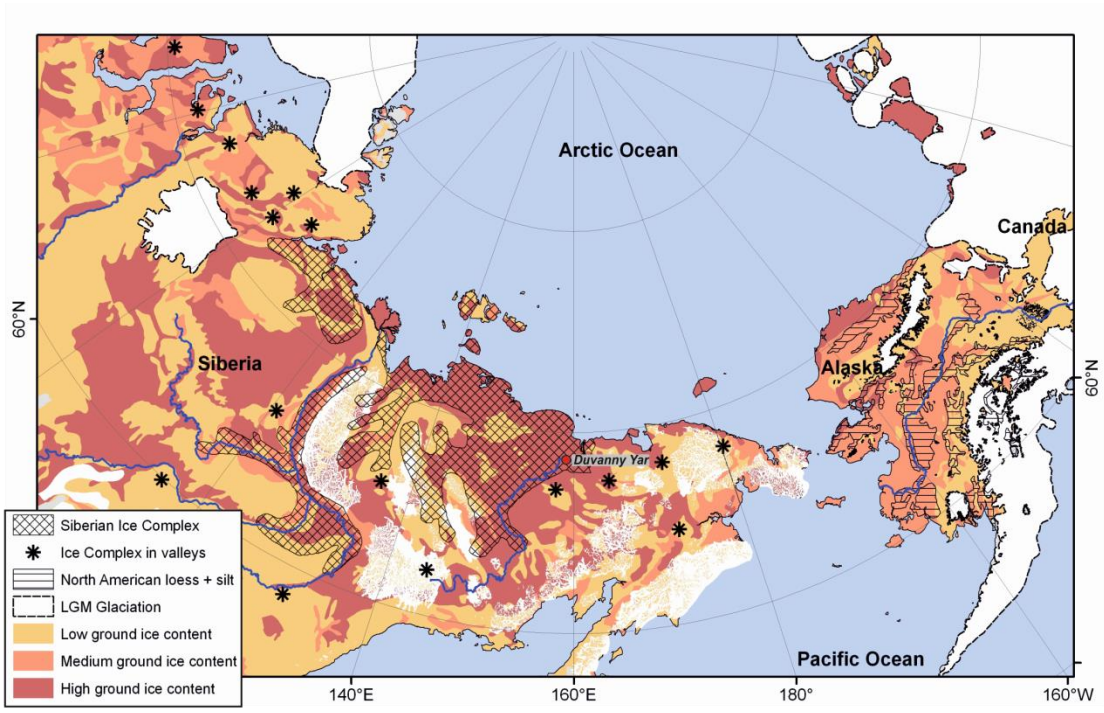

Figure 2-1. Location of the Duvanny Yar study site and the area of ice-rich permafrost deposit distribution in arctic and subarctic lowlands in the region of late Pleistocene Beringia. From Schirrmeister et al. (2013), based on Romanovskii (1993) for Siberian Yedoma Ice Complex deposits, Péwé (1975) and Wolfe et al. (2009) for North American loess, Ehlers and Gibbard (2003) for last glacial maximum glaciation, and Brown et al. (1997) for ground-ice content. Map compiled by G. Grosse (University of Alaska Fairbanks).

The Yedoma IC deposits are exposed in an approximately 12-km-long outcrop, which consists of Yedoma hills as high as 50 m above river level (a.r.l.) dissected by deep thermo-erosional valleys and thermokarst depressions. Giterman et al. (1982)

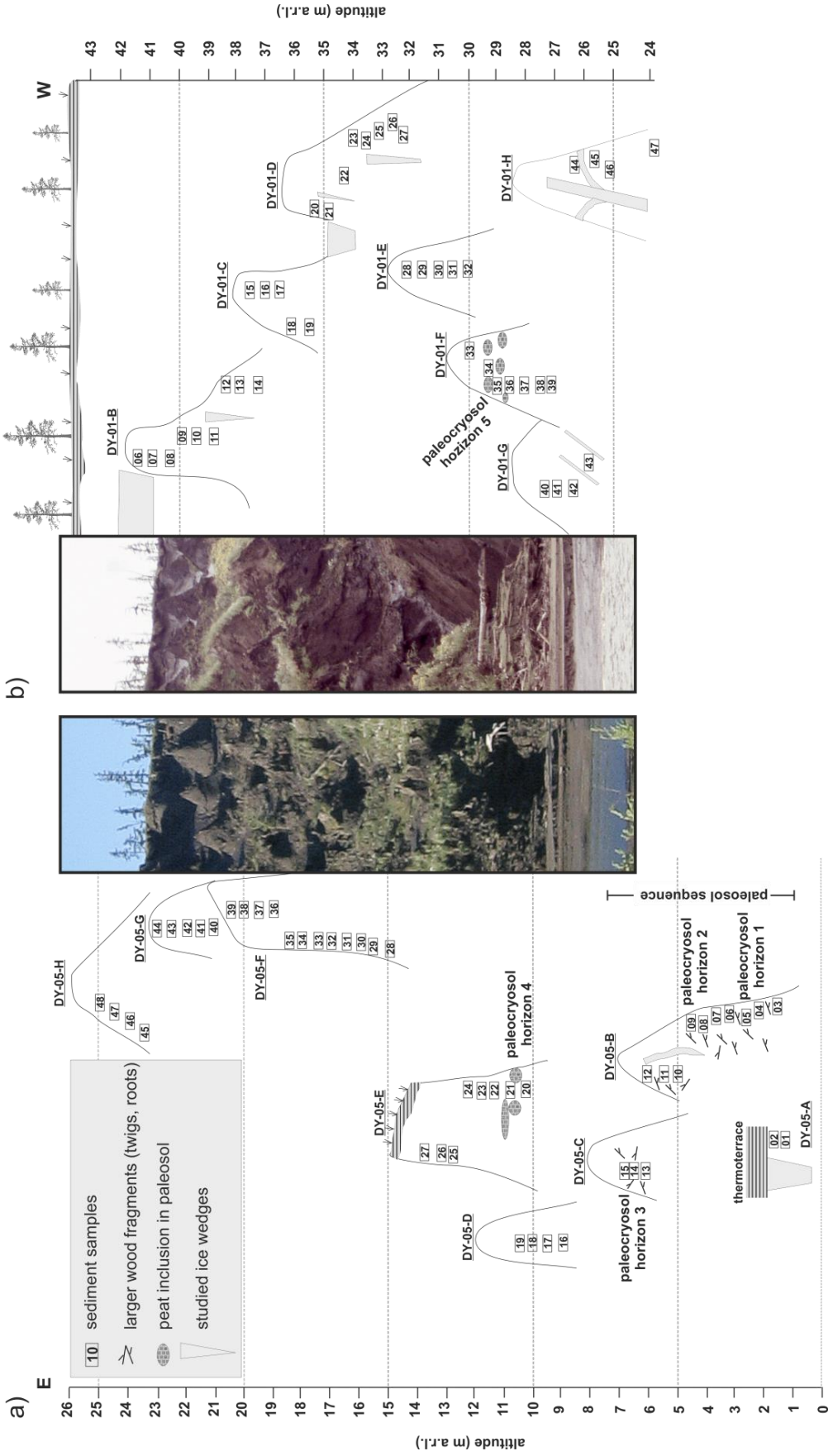

Figure 2-2. Scheme and photo of the composite Yedoma Ice Complex profiles (a) DY-05 and (b) DY-01. The paleocryosol sequence (1.3 to 6.8 m a.r.l.) including the paleocryosols 1 to 3 and paleocryosols 4 and 5 are labeled accordingly. Modified after Wetterich et al. (2011).

differentiate the Duvanny Yar section stratigraphically into four units. At river level, unit I is described as last interglacial lacustrine silts in ice-wedge pseudomorphs. Unit II is composed of woody and peaty sediments from the mid Pleistocene. Unit III is described as the late Pleistocene Yedoma IC which is investigated in this study (Figure 2-2). The uppermost unit IV is the Holocene cover on top of the Yedoma IC.

Based on field observations, a general description of the matrix and color, cryostructures, and organic compounds of the various paleocryosol and homogeneously composed deposits of the geological sections is given in the results section.

2.3.2 Field work

The Yedoma IC profiles were studied and sampled in sub-profiles exposed on separate thermokarst mounds (baydzherakhs) in river cliff thaw slumps. After cleaning the sample profiles, the exposed deposits were described according to sediment characteristics and cryostructures, photographed, and sketched. To consider a maximized sediment sequence, various sub-profiles from different thermokarst mounds were stacked together into a composite profile. To determine the absolute ice content (ice content in relation to wet sample weight), frozen samples were placed in aluminum boxes and weighed. Boxed samples were dried on an oven and then weighed again to calculate the absolute ice content using the weight difference.

2.3.3 Grain-size distribution

The grain-size distribution (GSD) between 0.375 and 1000 µm was analyzed using a laser particle sizer (Beckmann-Coulter LS 200). In order to measure only clastic grains and to disaggregate the sample, organic components were removed by adding 35 % hydrogen peroxide three times a week to the samples which were shaken for 6 weeks. The organic-free samples were diluted and 'washed' to neutral pH values by centrifugation. After that, the samples were dispersed in 1 % ammonia solution and 1 g dispersing agent ($Na_4P_2O_7 \cdot 10\ H_2O$) and shaken for 5 h. Finally, the samples were repeatedly split and two sub-samples were analyzed and averaged. The resulting GSD comprises 92 grain-size classes. GSD results were used in the calculation of grain-size parameters (mean diameter, sorting and skewness) used for the lithostratigraphical classification. Grain-size parameters were calculated after Folk and Ward (1957) using the Gradistat software (Blott and Pye, 2001).

2.3.4 End-member modeling

Statistical analysis of the GSD curves was performed using an end-member (EM) modeling algorithm written with Matlab software by Dietze et al. (2012). Compared to other statistical procedures, EM modeling provides a statistically and genetically

meaningful solution by unmixing compositional data sets (Weltje, 1997; Weltje and Prins, 2007). Important criteria for obtaining feasible models include insuring that EMs are nonnegative, and that they fulfill the constant-sum constraints. EMs are defined by two characteristics: first the loadings, which are the GSDs of the EMs, and second the scores, which typify their quantitative variation throughout the profile. In this study, grain-size data were transformed using a W-transformation after Manson and Imbrie (1964) and Klovan and Imbrie (1971) as described in Miesch (1976) and Weltje (1997). To minimize effects of scale, this transformation of the data is necessary (Dietze et al., 2012).

2.3.5 Interactive peak fitting

Interactive peak fitting (IPF, Version 4.1) (O'Haver, 2010) was the second method used to segregate the components of compositional data sets and to separate changes in the processes of sediment transportation and accumulation. Unlike EM modeling, IPF needs minor mathematical presumptions for GSD peak decomposition. Like EM modeling, IPF partitioning reveals information about the transport and deposition processes affecting each component. The IPF software is a Matlab extension for time series signals and uses an unconstrained nonlinear optimization algorithm to separate an overlapping peak signal.

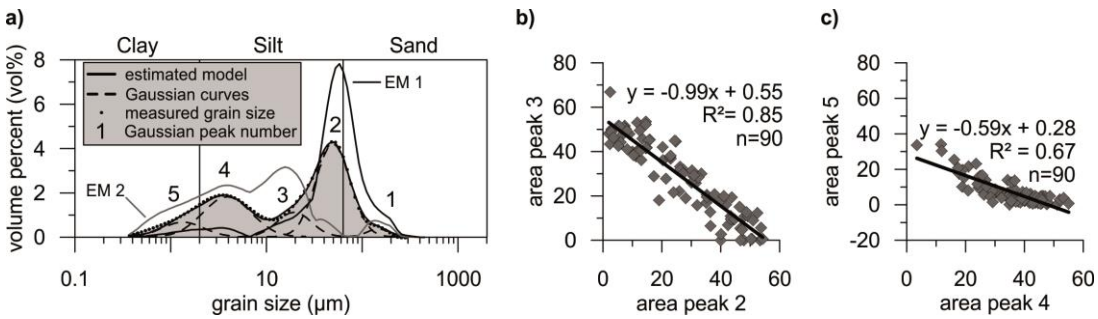

Figure 2-3. a) Example of peak fitting for one sample and an explanation of the interactive peak fitter outputs. For comparison the end-member distributions are added. Correlation of b) peak pairs 3 and 2, and c) pairs 5 and 4.

The peak type was set to Gaussian distribution. The Gaussian normal function is often used to describe the statistical law of polymodal GSDs (Ashley, 1978). Fitting experiments by Sun et al. (2002) indicate that the normal function also works on samples with asymmetrical components. Every GSD was fitted graphically by applying it to several Gaussian curves (Figure 2-3) until the root mean square (RMS) error was acceptable (<2). Finally, the percentage of each mode area compared to the total curve area was calculated. The area of the Gaussian curves is taken because it provides a more robust estimate than other measured parameters like position, height, and width.

2.3.6 Biogeochemistry

Total organic carbon (TOC) and total nitrogen (TN) contents and TOC/TN (C/N) ratios reflect variations in bioproductivity, organic matter accumulation, composition, and degradation (Meyers, 1994). Before measurement, the samples were homogenized and milled using a planetary mill. Therefore, coarser organic fragments are also included in the TOC content. For very organic-rich samples, sintercorundum instead of agate grinding jars were used. Carbonate was removed by hydrochloric acid (4 % HCl). Samples were then wrapped in tin foil. The sediment samples were measured twice with a carbon-nitrogen-sulfur (CNS) analyzer (Elementar Vario EL III). In each series of measurements a blank capsule was used for background detection and standards were measured after every 20 samples to ensure correct analytical values with a device-specific accuracy of ±0.1 wt%. For the TN measurements the procedure was the same, except different calibration standards and no carbonate removal procedures were used.

The carbon isotope content ($\delta^{13}C$) of TOC was measured with a Thermo Finnigan MAT Delta-S mass spectrometer. Measuring control standards at the beginning of each run and repeating control measurements after every seventh experimental measurement ensured correct analytical values of better than ±0.15 ‰ compared against the Vienna Pee Dee Belemnite (VPDB) standard.

Bulk density is a pedological standard parameter describing the mass of a volume unit of soil. The total volume includes both solid and pore volume. In this study, the bulk density of the sediment was determined to be the basic parameter for volumetric carbon quantification to account for ice-rich permafrost deposits. The density of the solid fraction (ρ_s, $10^3 kg/m^3$) was measured using a helium gas displacement pycnometer (AccuPyc-1330, Micromeritics). For bulk density (ρ_b, $10^3 kg/m^3$) calculation the volume of the solids (V_s, $10^{-6} m^3$) was derived first. Moreover, the mass of solid particles (m_s) is used in eq. 2-1.

$$V_s = \frac{m_s}{\rho_s} \qquad \text{eq. 2-1}$$

After that, the porosity (n)

$$n = \frac{V_p}{V_p + V_s} \qquad \text{eq. 2-2}$$

was calculated using the volume of the pores (V_p, $10^{-6} m^3$). Finally, determining the negative linear correlation

$$\rho_b = (n-1) \times (-\rho_s) \qquad \text{eq. 2-3}$$

(Horn, 2002) with the sediment porosity allows bulk density to be calculated.

For most parts of Yedoma IC it is convenient to assume that all pores are ice-saturated. We defined ice content >20 wt% as threshold for ice saturation. With this assumption, the absolute ice content gives an estimation of the pore volume. For the determination of ice volume ($V_{ice} = m_{ice}/\rho_{ice}$) an ice density of 0.91 10^3kg/m³ (Lide et al., 2008) was assumed.

For calculating the organic-carbon inventory, the density measurements were combined with TOC values. The reference volume (V_{ref}) was chosen to be 1 m³. The volumetric organic carbon (C_{org}) calculation (kg TOC /m³) was performed according to:

$$\text{volumetric } C_{org} \text{ content} = V_{ref} \times \rho_b \times \frac{TOC_{wt\%}}{100} \qquad \text{eq. 2-4}$$

2.4 Results

2.4.1 Lithological features of the Yedoma Ice Complex

The results refer to a lower profile, DY-05, and an upper profile, DY-01 (Figure 2-2). The two profiles were not stacked together because there was a distance of approximately two kilometers between them (Wetterich et al., 2011). The Yedoma IC sequence was subdivided into 2 groups, consisting of paleocryosols 1 to 5 (Figure 2-2 and Figure 2-4) and more homogeneously composed sediments.

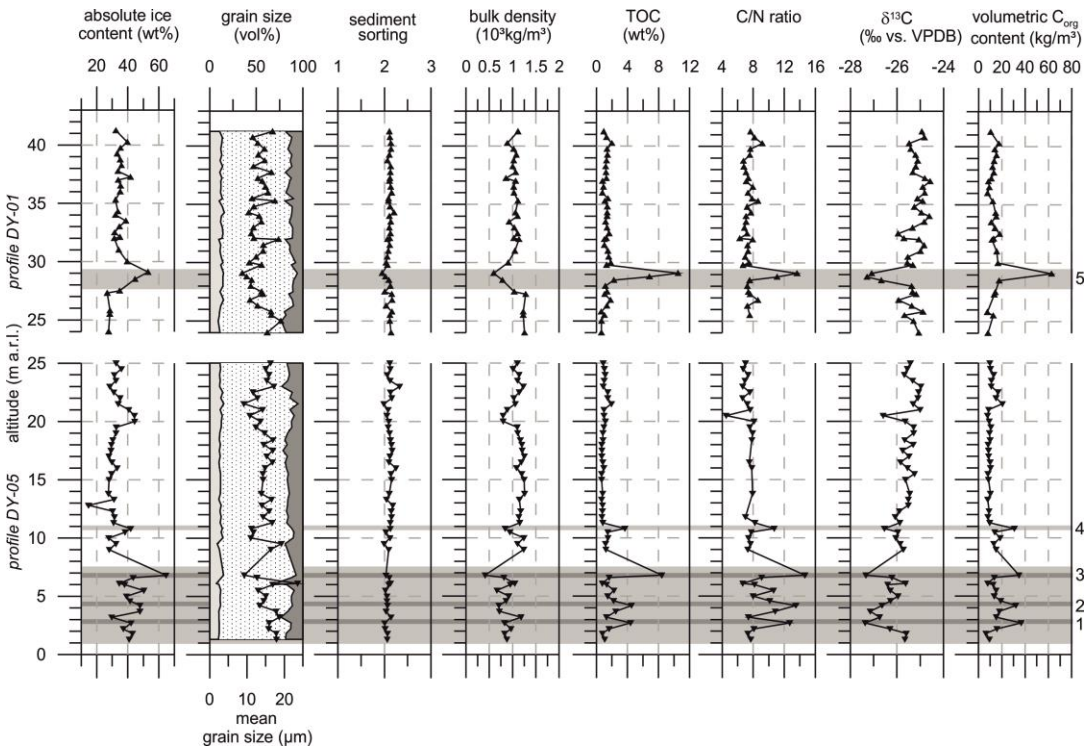

Figure 2-4. Summary of sedimentological and organic-carbon parameters for the Yedoma Ice Complex profiles DY-05 and DY-01. The grain-size fractions are illustrated as follows: clay: light gray, silt: white with black dots, sand: dark gray. The paleocryosols are highlighted with horizontal gray bars labeled from 1 to 5. At the paleocryosol sequence (1.3 to 6.8 m a.r.l) the whole sequence is highlighted. The labeled paleocryosols 1 to 3 are marked with dark gray boxes.

We use the term paleocryosol to designate buried or fossil frozen soils horizon, which were found at various heights within the Yedoma IC deposits. These horizons differ from the surrounding sediment by the presence of brownish and dark-brown patches, indicating enrichment by plant and wood fragments, and higher TOC contents as well as cryoturbation features.

In the lower paleocryosol sequence (Figure 2-4, 1.3 to 6.8 m a.r.l., including paleocryosols 1 to 3) of profile DY-05, the deposits contain plant detritus, dark-brown patches, and wood fragments such as shrub twigs or roots. The matrix of light-brown fine sand contains numerous filamentous roots and black spots. The cryostructures are banded, laminated-lenticular, or micro-lenticular. In some places, horizontal ice bands 2 to 3 cm thick as well as separate ca. 3-cm-long vertical ice veins occur. Here, the absolute ice content reaches 65 wt%. A distinct 5-cm-thick peaty horizon, paleocryosol 4, occurs at 10.8 m a.r.l. This former soil horizon is distinguished by dark-brown peat inclusions up to 2 to 3 cm in diameter, cryoturbation, filamentous roots, single plant remains, and horizontal micro to fine lens-like cryostructures and a high ice content (42 wt%). The dark-brown paleocryosol 5 with organic bands, cryoturbation, and peaty organic and larger wood fragments (Figure 2-4) occurs between 28.8 and 29.1 m a.r.l. in profile DY-01. Here, the cryostructures are irregular lenticular with diagonal ice veins and ice segregation around wood fragments. Like in the paleocryosols 1 to 4 below, high ice content (53 wt%) of this paleocryosol covaries with high TOC content (10.5 wt%).

The homogeneous part of the Yedoma IC also contains roots, plant fragments, and peat materials, and hence supported vegetation during exposed conditions. Unlike paleocryosols 1 to 5, no clear evidence for pedogenesis is visible. The homogeneous parts of the Yedoma IC at DY-05 consist of light gray-brown sandy silt with filamentous roots. The cryostructure is structureless (no visible ice) to micro-lenticular and the absolute ice content varies up to 41 wt%. Some separate parts contain larger, more distributed plant fragments and peat inclusions.

2.4.2 Granulometric characteristics and calculations

Grain-size analysis of the DY-05 and DY-01 profiles reveals a homogeneous composition (Figure 2-5a,b). All samples are poorly to very-poorly sorted (mean sorting degree after *Folk and Ward* (1957), 2.1±0.1) clayish to sandy silts (mean grain-size diameter 9 to 24 µm, mean skewness 0.3). The GSD curves show a distinct bimodal distribution with a smaller peak in the fine-silt fraction (between 3 and 4 µm) and a larger peak between 40 and 60 µm. A less-distinct third peak in the fine-sand fraction is found in some samples, which is most pronounced at 16, 22, and 23 m a.r.l. The

mentioned differentiation of the paleocryosol at 28.8 to 29.1 m a.r.l. (paleocryosol 5) is shown in the sand fraction as well. Here, the lowest sand content occurs and the GSD curve stands out from the general pattern, because of a relative enrichment in the medium-silt fraction.

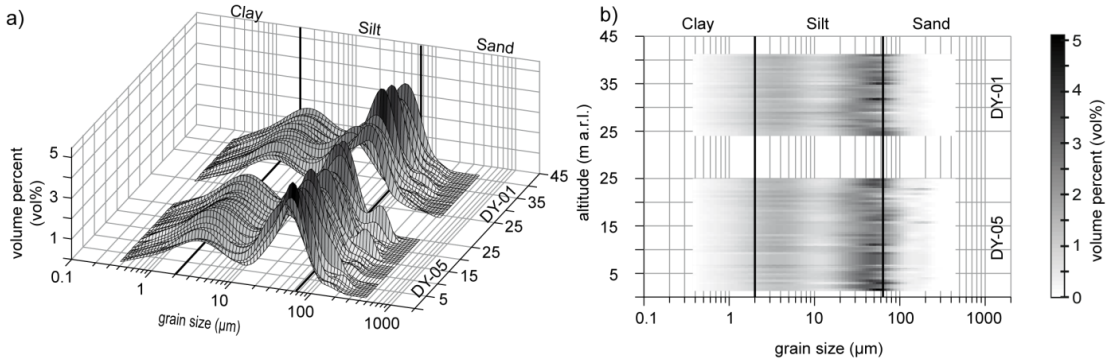

Figure 2-5. Grain-size distributions of the Yedoma Ice Complex samples as individual representations against profile depth with a view from a) the side and b) above. No trend of shifting peak location is obvious in either view.

2.4.3 End-member modeling

The mean coefficient of determination (R^2 mean) displays the explained variance of each modeled grain-size class. It was calculated to estimate the minimum number of EMs required to adequately representing the original data. Weltje (1997) and Prins and Weltje (1999) showed that the minimum adequate number of EMs corresponds to the position of the inflection point of the 'number of end-members - explained cumulative variance' curve (0.88 for 2 EMs). For the Yedoma IC sediments of Duvanny Yar, the R^2 indicates that two EMs (Figure 2-6a) are adequate to describe the original grain-size data set. The model with two EMs explains 55 % of the total variance (R^2 mean 0.55, Figure 2-6a and d). Figure 2-6c shows that the modeling error is independent of the profile height. The R^2 statistics of the single grain-size classes (Figure 2-6d) reveal that the highest uncertainties are found in the coarse (>100 µm) size classes and at the point of intersection of the two EMs. The uncertainty of the coarse fraction is caused by low absolute content of material within this size class, and thus relatively high modeling errors compared to classes with greater amounts of material. The low R^2 at the point of intersection (Figure 2-6d) is the result of a modeling error induced by the simplification to two EMs. To improve the R^2, especially at the intersection point, it is possible to increase the number of EMs (Figure 2-6a). However, following the law of parsimony we decided to use only 2 EMs. For the studied deposits more EMs are difficult to interpret in a sedimentological context and the risk of over-interpreting our data would rise precipitously.

EM 2 is characterized by an approximately unimodal GSD with a maximum in the fine-to-medium-silt fraction (Figure 2-6b). In the paleocryosol sequence, including paleocryosols 1 to 3, EM 2 scatters across a wide range, from 6 to 100 % (Figure 2-7).

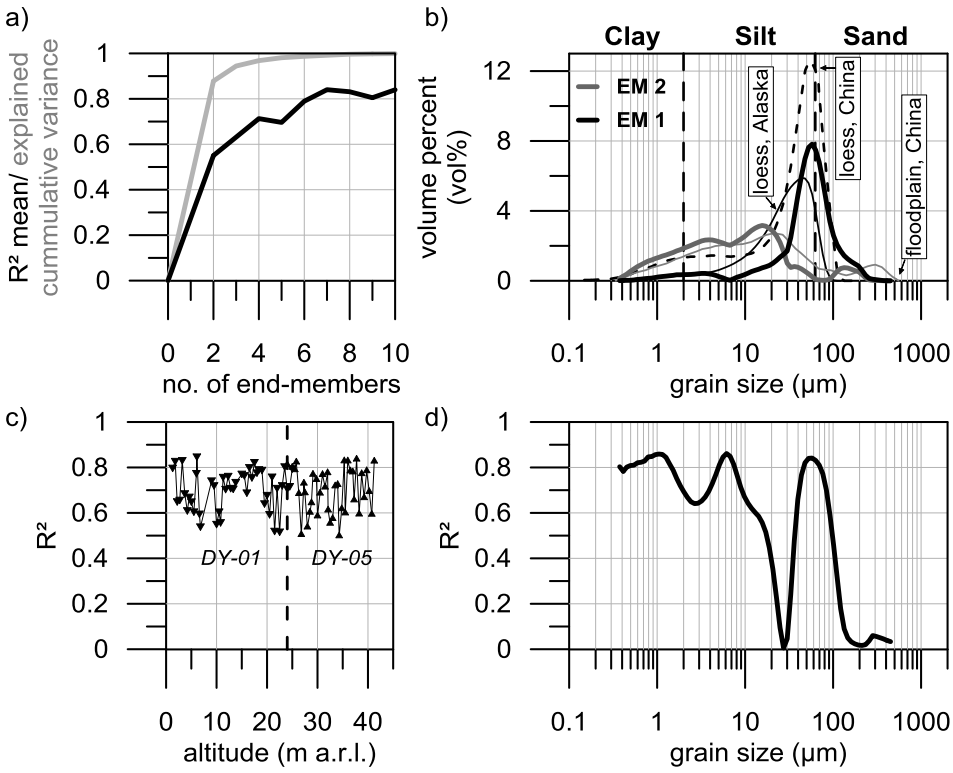

Figure 2-6. End-member modeling results. a) Mean coefficient of determination of all size classes for each end-member model. b) Grain-size distributions of the two end-members with natural end-member from Alaskan (Vault Creek Tunnel near Fairbanks, Alaska, USA (Meyer et al., 2009); data from L. Schirrmeister (unpublished data, 2008)) and Chinese (Yulin, northern part of the Loess Plateau, China; data from Sun et al., 2002) loess as well as Chinese floodplain deposits (Bahe formation, Shaanxi Province, northern China; data from Kenkkilä (2005)). c) Coefficients of determination for each sample of the model with two end-members. d) Coefficients of determination for each size class of the model with two end-members.

The range in the homogeneously composed deposits of DY-05 is smaller, with a mean value of 60 %. Paleocryosol 5 shows scores of up to 100 % for EM 2. Here, the GSDs are characterized by two peaks of nearly the same size and height. Above, the mean value of EM 2 stabilizes, as it did in the homogeneously composed deposits of DY-05, at around 67 %. EM 1 is characterized by a unimodal GSD with a maximum at the coarse silt - fine sand border (~62 mm). Because of the constant-sum constraint the development of EM 1 is opposite to that of EM 2.

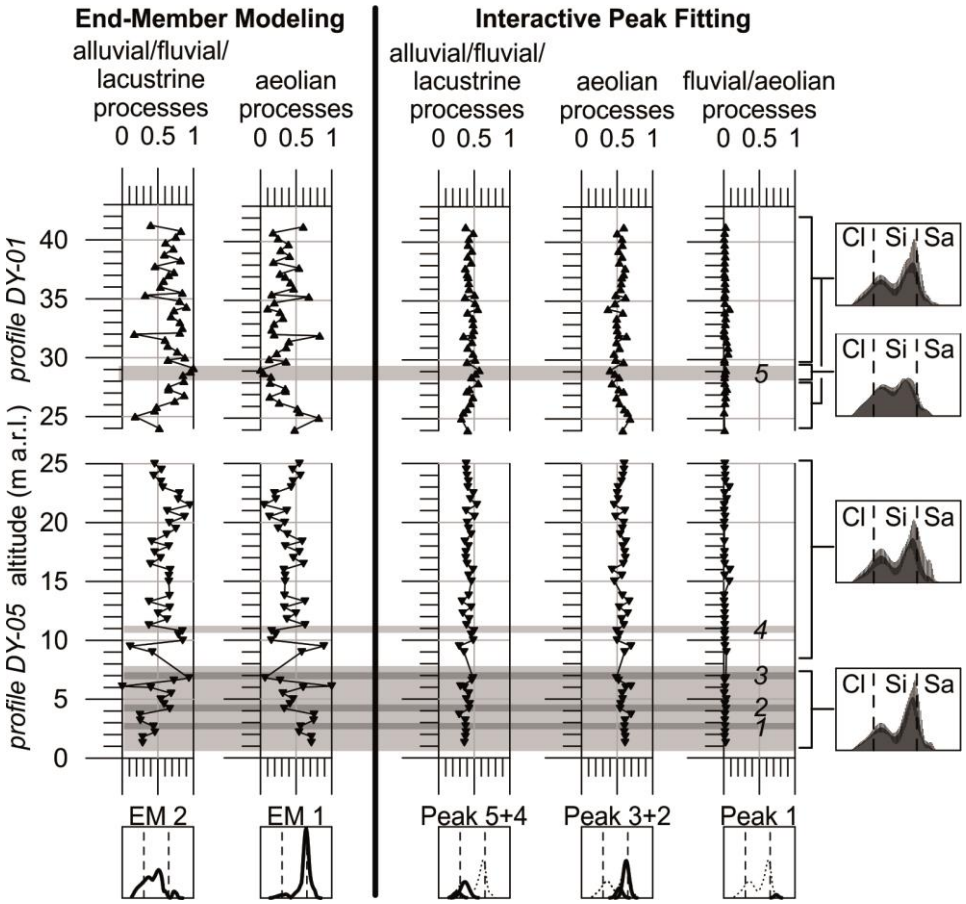

Figure 2-7. Variation of the end-member and interactive peak fitter scores. Laser-derived grain-size distributions (right) are stacked for sections with similar shape, and variability of each grain-size class within these sections is indicated by error bars. The grain-size fractions are labeled as clay (Cl), silt (Si), and sand (Sa). Background boxes indicate paleocryosols according to Figure 2-4.

2.4.4 Interactive peak fitting grain size pattern

Like the EMs, the IPF-separated peaks were attributed to the supposed main mechanisms of transportation and sedimentation.

In the application of IPF the areas of Gaussian curves 5 and 4 as well as 3 and 2 (Figure 2-3a) were merged due to the assumption that each Gaussian pair, 5+4 and 3+2, are related to the same processes. This assumption is evident by the linear relationship of the pairs (Figure 2-3b and c). In profile DY-05, the area of peak 5+4 ranges between 29 and 54 % (median 41 %) and in profile DY-01 between 32 and 57 % (median 44 %). In profile DY-05, peak 3+2 ranges between 43 and 69 % (median 58 %). With some exceptions, this grain-size peak is the major one and therefore represents the main sedimentation process. Like in the lower Yedoma IC profile, peak 3+2 at DY-01 is the largest with an area between 37 and 68 % (median 53 %), but a smaller gap between the median of peak 5+4 and peak 3+2 reveals a diminish-

ing influence of peak 3+2. The value of the minor peak 1 in the fine-sand fraction is between <1 and 6 %. In some samples this peak is not clearly obvious.

2.4.4.1 Assumptions for end-member modeling and interactive peak fitting interpretation

For grain-size modeling with EMs and 'graphical' fitting with IPF, the different GSDs are attributed to the supposed main mechanisms of transportation and sedimentation. Both methods (EM and IPF) have been applied in sedimentology (Sun et al., 2002; Dietze et al., 2012) and possibly support each other. The main mechanisms are chosen on the basis of natural EMs, like loess deposits from Alaska (L. Schirrmeister, unpublished data, 2008) and from China (Sun et al., 2002) as well as floodplain deposits from China (Kaakinen and Lunkka, 2003; Kenkkilä, 2005) (Figure 2-6). The supposed main mechanisms causing the GSDs are water related (alluvial/fluvial/lacustrine) processes (including loess reworked by water). Floodplain overbank deposition is assumed for EM 2 and peak 5+4, and aeolian for EM 1 and peak 3+2. The small peak 1 is termed fluvial/aeolian because its GSD allows no clear distinction to be made. After Sun et al. (2002) this small peak as well as the small peak of EM 2 and the shoulder of EM 1 can be interpreted as a signal of the saltation component of alluvial/ fluvial/lacustrine and aeolian processes.

2.4.5 Organic matter characteristics and calculations

The C/N ratio indicates the degree of organic-matter decomposition due to microbial activities and pedogenic processes (low ratios: more strongly decomposed; high ratios: less decomposed (Kumada, 1987; Ping et al., 1998). Furthermore, paleoclimatic information is stored in organic carbon data. Variations in $\delta^{13}C$ values indicate different origins of organic matter (e.g., marine, terrestrial, sub-aerial/aquatic), and the degree of decomposition of plant material by different processes of isotopic fractionation during carbon turnover. Lower $\delta^{13}C$ values indicate less-decomposed organic matter, while higher $\delta^{13}C$ indicate that stronger decomposition has occurred (Meyers, 1994). The TOC values and C/N ratio in paleocryosols 1 to 5 (Figure 2-4) are variable. High TOC values of >4 wt% and C/N ratios of >12 occur. C/N ratios of up to 15 reveal a small degree of organic-matter decomposition compared to the homogeneous Yedoma IC (C/N ~8). The TOC content in the homogenously composed Yedoma IC remains constant, between 1 and 2 wt%, in the majority of the samples. A deviation from the homogenous pattern is observed for the low C/N ratio (4.5) at 20.5 m a.r.l., where the ice content is higher.

The $\delta^{13}C$ in the paleocryosols ranges from -27.4 to -25.6 ‰. This is lighter than the homogeneous parts, which range from -25.9 to -24.6 ‰. The $\delta^{13}C$ value of the per-

mafrost deposits can be interpreted as an integrative signal of e.g., seasonal effects, water conditions (Welker et al., 1993; Gundelwein et al., 2007), and decomposition rates (Pfeiffer and Janssen, 1993).

The estimated bulk density was combined with the TOC contents to calculate the volumetric organic-carbon content (eq. 2-4). Bulk density of the homogeneous sequences primarily varied due to ice content rather than to TOC content because the latter was relatively low (<2 wt%). The lower paleocryosol sequence (1.3 to 6.8 m a.r.l.) is characterized by a bulk density that alternates between 0.4 and 1.2 10^3 kg/m³. The organic-carbon content spans a wide range, between 6 and 37 kg/m³. The mean value of 19 kg/m³ at the paleocryosol sequence is significantly higher than in the homogenous Yedoma IC units. Paleocryosol 4 contains 31 kg/m³. Paleocryosol 5 with its peat inclusions and high ice content exhibits a minimum bulk density and maximum volumetric organic-carbon content (63 kg/m³). Over the entire range of the homogeneously composed deposits, the volumetric organic-carbon content was below 20 kg/m³ (mean 12 kg/m³). The total mean volumetric organic-carbon content of the Yedoma IC deposits at Duvanny Yar is 14±8 kg/m³. For the active layer of Kolyma Lowland soils, Mergelov and Targulian (2011) report an average volumetric organic-carbon stock of 15.1 kg C/m², with the greater part of organic carbon (60 to 90 %) in the mineral part of the soils. In our calculation we exclude the active layer and the Holocene cover on top of the Yedoma IC. Our calculated organic carbon stock provides evidence that the deeper mineral horizons contain nearly as much carbon as the active layer, emphasizing the great significance of the deep fossil organic carbon pool.

2.5 Discussion

2.5.1 Origin of the Yedoma Ice Complex at Duvanny Yar

The studied Kolyma River cliff cut in vertically or diagonally polygonal ice-wedge systems. It is suggested that the Yedoma hills are remnants of former accumulation plains (Schirrmeister et al., 2013). There is still no widely accepted concept of Yedoma ICs genesis, but it seems clear that neither glacial-related sedimentation, such as hypothesized by Nagaoka et al. (1995) and Grosswald (1998), nor shallow-marine sedimentation, such as postulated by Bol’shiyanov et al. (2009), was involved. An overview of the different Yedoma ICs origin concepts is given by Vasil’chuk (1992).

It is agreed that Yedoma IC material was sub-aerially exposed most of the time and froze syngenetically during permafrost accumulation (Kanevskiy et al., 2011). Based on more than 50 radiocarbon dates for adjacent sediments (Vasil'chuk et al., 2001),

we know that the ice wedges at Duvanny Yar were formed between ~37 and 13 ka BP by syngenetic freezing of permafrost deposits. Our studies confirm the syngenetic freezing process because lenticular and layered cryostructures occur. The average absolute ice content of all studied deposits is 35 wt%. Assuming that ice wedges can account for about 50 vol% in Yedoma IC sequences (Schirrmeister et al., 2002; Zimov et al., 2006a), the total absolute ground-ice content can constitute up to three quarters of the total outcrop volume. This clearly shows the vulnerability of Yedoma IC deposits to warming temperatures and surface subsidence during thawing.

Three granulometric characteristics can be seen in the GSDs (Figure 2-5). First, a sand maximum, as shown by the sand maximum sample at 6.1 m a.r.l., could be caused by a higher energetic transport level such as increased streaming velocity during a flooding period, as has been suggested by our EM modeling. In some samples a distinct third small peak in the fine-sand fraction is obvious. This can be explained by an increased fraction of seasonal or temporal inundation of a floodplain due to stronger streaming conditions or increased aeolian activity resulting in enrichment of the fine-sand fraction by a larger fraction of saltating and rolling sediments (Reineck and Singh, 1980). Second, an enrichment of the finer fractions, especially the medium-silt fraction, like in paleocryosol 5, can indicate ponding water, in which the settling velocity of the suspended medium-silt fraction allows for its deposition (Hjulström, 1939). At this paleocryosol our EM 2 for alluvial, fluvial, and lacustrine processes rises to 100 %. Additionally, the increased TOC could be caused by ponding water and boggy conditions in low-center polygons, under which the accumulation of organic matter is higher and the decomposition rate is lowered. Third, paleocryosols are characterized by more alternating mean grain sizes. This could be a consequence of faster environmental changes, increased plant growth, or thaw and cryoturbation processes during warmer periods. Despite these specific characteristics, the grain-size analysis and magnetic susceptibility data indicate stable sediment sources as well as persistent transport conditions.

Loess material, formed as a result of cryogenic weathering and glacial grinding processes, is rather common in (peri)glacial environments and drifts from outwash plains via aeolian transport. Therefore, Pye (1995) defined a subcategory of loess named ‘periglacial loess’. Moreover, Pye (1987) states that the GSD of a ‘typical’ loess shows a pronounced mode in the 28 to 48 µm range and is positively skewed (toward the finer sizes). Smalley and Smalley (1983) define loess-sized material as between 20 to 60 µm, which corresponds perfectly with the observed large peak of the studied deposits.

Sub-aquatic fluvial and lacustrine silts can also be loess-like, as can some alluvial and colluvial deposits (Konishchev, 1987). Especially the first peak, described by EM 2 and peak 5+4, cannot be explained by pure aeolian processes. Walger (1962) states that products of each of the three basic transport and deposition mechanisms, namely suspension, saltation, and rolling, are represented in every single GSD. However, because of sediment variations and sampling uncertainties, polymodal GSDs are recorded. Due to the absence of visible layered structures, and considering Walger's hypothesis, IPF and EM modeling were conducted. The results of these modeling efforts clearly indicate that the GSD of each single sample is characterized by at least bimodal curves and consists of numerous single populations of mono-modal GSDs, indicating the participation of various processes of transport and (re-) sedimentation during Yedoma IC formation in agreement with a polygenetic formation concept (Sher, 1995; Sher et al., 2005). In this context, EM 2 is believed to be an alluvial, fluvial, and lacustrine signal, and EM 1 is interpreted as an aeolian component. IPF peak 4+5 is interpreted as the water-dependent analogue to EM 2, peak 3+2 as aeolian, and peak 1 as the fluvial/aeolian component (Figure 2-6b and Figure 2-7).

This interpretation of the GSDs is based on natural EMs like Chinese (Sun et al., 2002) and Alaskan loess (L. Schirrmeister, unpublished data, 2008), as well as on alluvial/fluvial/lacustrine deposits from northern China (Kaakinen and Lunkka, 2003; Kenkkilä, 2005). Another EM for periglacial loess(-like) sediment was described by Zech et al. (2008) at the Tumara palaeosol sequence in northeast Siberia.

Both EM modeling and IPF reveal a relatively balanced proportion of the peaks/distributions interpreted as the alluvial/fluvial/lacustrine component (EM: 61±21 %; IPF: 43±6 %) and the aeolian component (EM: 39±21 %; IPF: 55±7 %).

The consistency of the EM modeling and the IPF scores indicates stable accumulation conditions. Another process for producing fine-grained sediments could be in situ frost weathering of the material. After deposition, repeated freezing and thawing of ice/water-bearing sediments results in production of silt-sized particles (Konishchev and Rogov, 1993; Wright et al., 1998; Schwamborn et al., 2008). When this process is significant, the post-depositional transformation conceals the primary transport and accumulation signal, distorting and complicating the interpretation. In addition, winnowing/eroding of the fine fraction by shallow overland flow caused by rain or thawing events could have altered the depositional GSDs (Farenhorst and Bryan, 1995).

Due to the (very) poorly sorted polymodal sediments lacking in carbonates, and the absence of glaciers and ice sheets with their grinding processes (Seppälä, 2004) in northeast Siberian lowlands (Velichko et al., 1997; Hubberten et al., 2004; Svendsen et al., 2004), the Yedoma IC at Duvanny Yar is interpreted to be of polygenetic origin. Water-related (like floodplain overbank deposition) and aeolian deposition were the controlling processes. It is also likely that seasonally differentiated deposition occurs here. A possible scenario of seasonal deposition is flooding of alluvial areas after snowmelt and during periods of high river discharge (today around June, Kolymskoye Stream Discharge Station, ArcticRIMS). Aeolian deposition likely occurs in dryer seasons. During fall and winter, river discharge volume is extremely reduced. As a consequence, parts of the formerly submerged floodplain areas become susceptible to wind activity (Muhs and Bettis, 2003).

2.5.2 Changes in organic matter parameters

The TOC content of the homogenous parts of the studied Yedoma IC deposits is between 0.5 and 2.0 wt%, which is rather low compared to other Yedoma IC studies (~4 wt% (Schirrmeister et al., 2011b)). The paleocryosols are characterized by TOC values of up to 10.5 wt%. The mean organic-carbon value for the whole profile is 1.5±1.4 wt%, and the $\delta^{13}C$ values range between -27.4 and -24.6 ‰. These parameters, in combination with high C/N ratios, suggest that fresh water and sub-aerial terrestrial environments were the dominant sources of organic matter during Yedoma IC formation. In the paleocryosol samples a higher input of terrestrial plant associations is revealed. The local environmental conditions under which the paleocryosol sequences were formed are likely to have been more humid and favorable for plant growth. Hence, the formation period of the lowermost paleocryosol sequence fits well into the Middle Weichselian (50 to 30 ka BP) interstadial period (Schirrmeister et al., 2002). This hypothesis is based on the stratigraphical position, and on parameters such as high TOC contents, high C/N ratios, and low $\delta^{13}C$ values (Figure 2-4). These are typical indications of interstadial periods with increased bioproductivity and moderate organic-matter decomposition under wet/moist conditions (Wetterich et al., 2009; Schirrmeister et al., 2011c). Moreover, the alternating behavior observed in the paleocryosols can be explained, according to Gundelwein et al. (2007), as the result of a patchy environment such as a distinctive mosaic-like polygonal tundra with moist anaerobic (lower $\delta^{13}C$) and dryer aerobic conditions (higher $\delta^{13}C$). On the contrary, in the homogeneously composed sediments of the Yedoma IC stadial periods were characterized by less variable, generally lower TOC contents and low C/N ratios (higher decomposition). Despite the low TOC values compared to other Yedoma IC studies, the Yedoma IC at Duvanny Yar contains a considerable organic-

carbon inventory with a mean of 14±8 kg/m³ . Given that the Yedoma IC deposits accumulated at relatively fast rates and low temperatures, the organic matter had only a short time to decompose before it was incorporated into a permanently frozen state. Therefore, Yedoma IC deposits are believed to contain a labile and vulnerable carbon-matter stock. Applying broad upscaling, Zimov et al. (2006b) estimated the organic-carbon reservoir in Siberian ICs to be ~500 Gt.

Our data from Duvanny Yar show lower TOC content and lower bulk densities; therefore, we hypothesize that the Yedoma IC carbon inventory is lower than estimated by Zimov et al. (2006b). Large-scale extrapolations should be considered as preliminary because of great uncertainties about the controlling factors, e.g., Yedoma IC distribution/area, thickness, and local heterogeneity. When considering the different studies of spatial variation of carbon-bearing Yedoma IC deposits (Walter et al., 2006; Zimov et al., 2006b; Tarnocai et al., 2009), it becomes obvious that our knowledge about the quantities and qualities of this organic-matter pool is insufficient for extrapolating possible effects of a warming climate on the Yedoma IC organic-carbon stock. Nevertheless, as a large carbon inventory that is vulnerable to release, the Yedoma IC deposits contain an important carbon pool, which is relevant to current discussions about the effect of global climate warming.

2.6 Conclusions

The very poor sorting of sediments, bi- to polymodal grain-size distributions, a lack of carbonate, and the absence of historic ice sheets in the region show the Yedoma Ice Complex at Duvanny Yar to be of polygenetic origin, formed in the polygonally patterned floodplain of the Kolyma River. Alluvial and fluvial processes on a former floodplain and aeolian deposition were the controlling processes. Seasonally differentiated deposition probably occurred.

The carbon inventory of Duvanny Yar amounts to 14±8 kg/m³ (organic-carbon concentration 1.5±1.4 wt%). Thus, the Yedoma Ice Complex deposits contain a significant carbon inventory. Large-scale extrapolations of the organic-carbon inventory should be considered preliminary because of great uncertainties about the controlling factors such as Yedoma Ice Complex area, thickness, and local heterogeneity.

Acknowledgments

We thank the German Science Foundation (DFG) for financial support of the joint Russian-German Beringia/Kolyma 2008 expedition which occurred within the framework of the DFG SCHI 530/8-1 cooperative project. In addition, the expedition was supported by the International Polar Year projects "Thermal State of Permafrost" (TSP) and "Past Permafrost." We thank all Russian and German colleagues who helped us during field work and laboratory studies, especially U. Bastian, A. Eulenburg, D. G. Fyodorov-Davydov, A. L. Kholodov, G. N. Kraev, V. A. Mironov, and S. A. Zimov.

3 The deep permafrost carbon pool of the Yedoma region in Siberia and Alaska

Strauss, J.[1], Schirrmeister, L.[1], Grosse, G.[1,2], Wetterich, S.[1], Ulrich, M.[3], Herzschuh, U.[1], and Hubberten, H.-W.[1]

[1]Alfred Wegener Institute Helmholtz Centre for Polar and Marine Research, Periglacial Research Unit, Potsdam, Germany.
[2]Geophysical Institute, University of Alaska Fairbanks, Fairbanks, USA.
[3]Institute for Geography, Leipzig University, Leipzig, Germany.

Published in: Geophysical Research Letters, Vol 40, 2013

Citation: Strauss, J., Schirrmeister, L., Grosse, G., Wetterich, S., Ulrich, M., Herzschuh, U., and Hubberten, H.-W., The deep permafrost carbon pool of the Yedoma region in Siberia and Alaska, Geophysical Research Letters, 40, 6165–6170, doi:10.1002/2013GL058088, 2013.

3.1 Abstract

Estimates for circumpolar permafrost organic carbon (OC) storage suggest that this pool contains twice the amount of current atmospheric carbon. The Yedoma region sequestered substantial quantities of OC and is unique because its deep OC, which was incorporated into permafrost during ice age conditions. Rapid inclusion of labile organic matter into permafrost halted decomposition and resulted in a deep long-term sink. We show that the deep frozen OC in the Yedoma region consists of two distinct major sub-reservoirs: Yedoma deposits (late Pleistocene ice- and organic-rich silty sediments) and deposits formed in thaw-lake basins (generalized as thermokarst deposits). We quantified the OC pool based on field data and extrapolation using geospatial data sets to 83+61/-57 Gt for Yedoma deposits and to 128+99/-96 Gt for thermokarst deposits. The total Yedoma region 211+160/-153 Gt is a substantial amount of thaw-vulnerable OC that must be accounted for in global models.

3.2 Introduction

Organic carbon (OC) reservoirs of global importance include the ocean, atmosphere, living terrestrial biomass, and terrestrial sediments. Recent studies suggest that 1400 to 1850 Gt of frozen OC are stored in northern high-latitude permafrost soils (McGuire et al., 2009; Tarnocai et al., 2009). In the vast northern permafrost Yedoma region that remained unglaciated during the last ice age, alluvial floodplains, hill slopes, and polygonal lowlands (Strauss et al., 2012) accumulated OC in Yedoma deposits ≤50 m thick (Kanevskiy et al., 2011), while segregated ice (SEI) and massive wedge ice (WI) concurrently formed within the sediments (Figure 3-1, Figure 3-2, and Figure appendix III-1). Yedoma region (Figure 3-1) permafrost-preserved OC, including ice-rich peat in thaw-lake basins and refrozen lacustrine deposits, is

weakly decomposed (Schirrmeister et al., 2011b) due to fast incorporation into permafrost from the seasonally thawed active layer. Once frozen, organic matter degradation ceases. Observations and models indicate warming and thawing permafrost in many regions (Romanovsky et al., 2010a), an irreversible process on human timescales (Schaefer et al., 2011; MacDougall et al., 2012). Once unlocked by thaw, permafrost organic matter decomposes and CO_2 or CH_4 are produced and released (Walter et al., 2006; Schuur et al., 2009; Mackelprang et al., 2011). Projections suggest that greenhouse gas emissions from permafrost until 2300 (Representative Concentration Pathways 8.5 scenario) (Schneider von Deimling et al., 2012) are comparable in amount to all pre-2000 anthropogenic emissions, thus affecting the global carbon cycle and amplifying surface warming (McGuire et al., 2009; Koven et al., 2011; Schaefer et al., 2011; Burke et al., 2012a; Ciais et al., 2012; DeConto et al., 2012; Schneider von Deimling et al., 2012; Schuur et al., 2013)

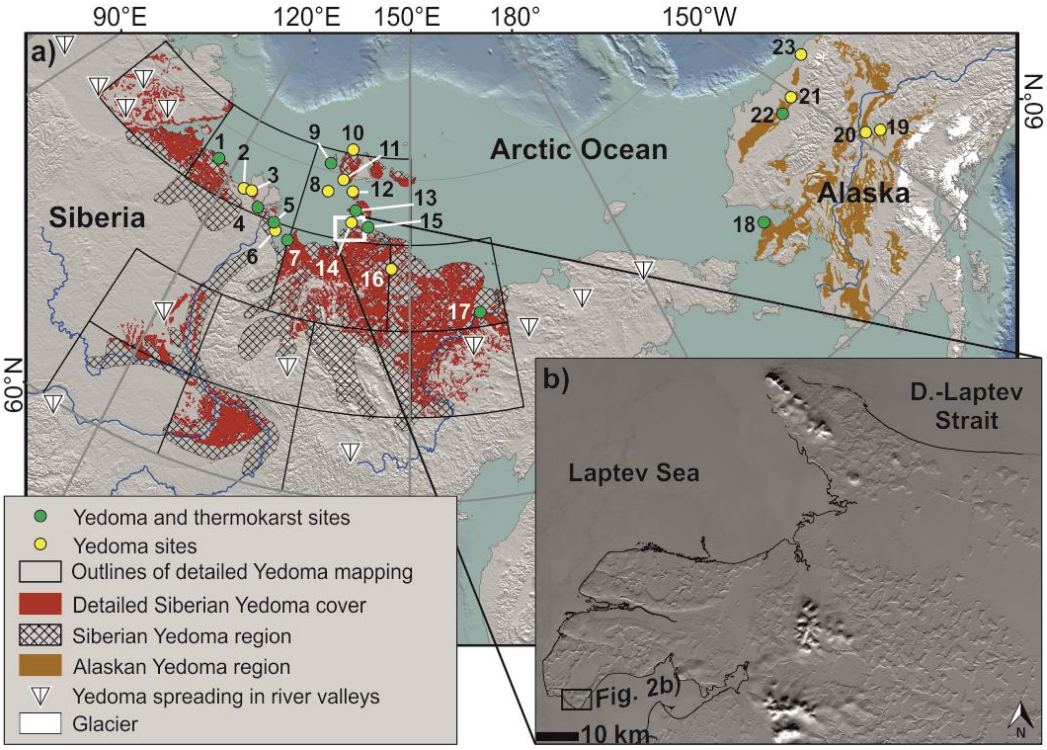

Figure 3-1. Location of the study sites. (a) Potential (Romanovskii, 1993) and fragmented (Jorgenson et al., 2008; Grosse et al., 2013b) area of Yedoma deposits in Arctic and sub-Arctic lowlands, including the studied thermokarst deposit areas. Sites are numbered; 1, Cape Mamontov Klyk; 2, Nagym Island; 3, Khardang Island; 4, Kurungnakh Island; 5, Bykovsky Peninsula; 6, Muostakh Island; 7, Buor Khaya Peninsula; 8, Stolbovoy Island; 9, Bel'kovsky Island; 10 and 11, Kotel'ny Island; 12, Maly Lyakhovsky Island; 13, Bol'shoy Lyakhovsky Island; 14, Cape Svyatoy Nos; 15, Oyogos Yar; 16, Kytalyk; 17, Duvanny Yar; 18, Kitluk River; 19, Vault Creek tunnel; 20, Dalton Highway; 21, Itkillik River; 22, Colville River; and 23, Camden Bay. For site 18, only thermokarst deposit samples are available, resulting in 22 Yedoma and 10 thermokarst deposit sites. (b) A panchromatic Landsat-7 image of the wintery Svyatoy Nos and Shirokostan peninsulas (12 March 2012, extent of the white box shown in a), illustrating several granite domes mantled by Yedoma deposits and strong dissection by thermokarst depressions (Landsat data source: USGS EROS Data Center). The black box marks the location of the area shown in Figure 3-2b.

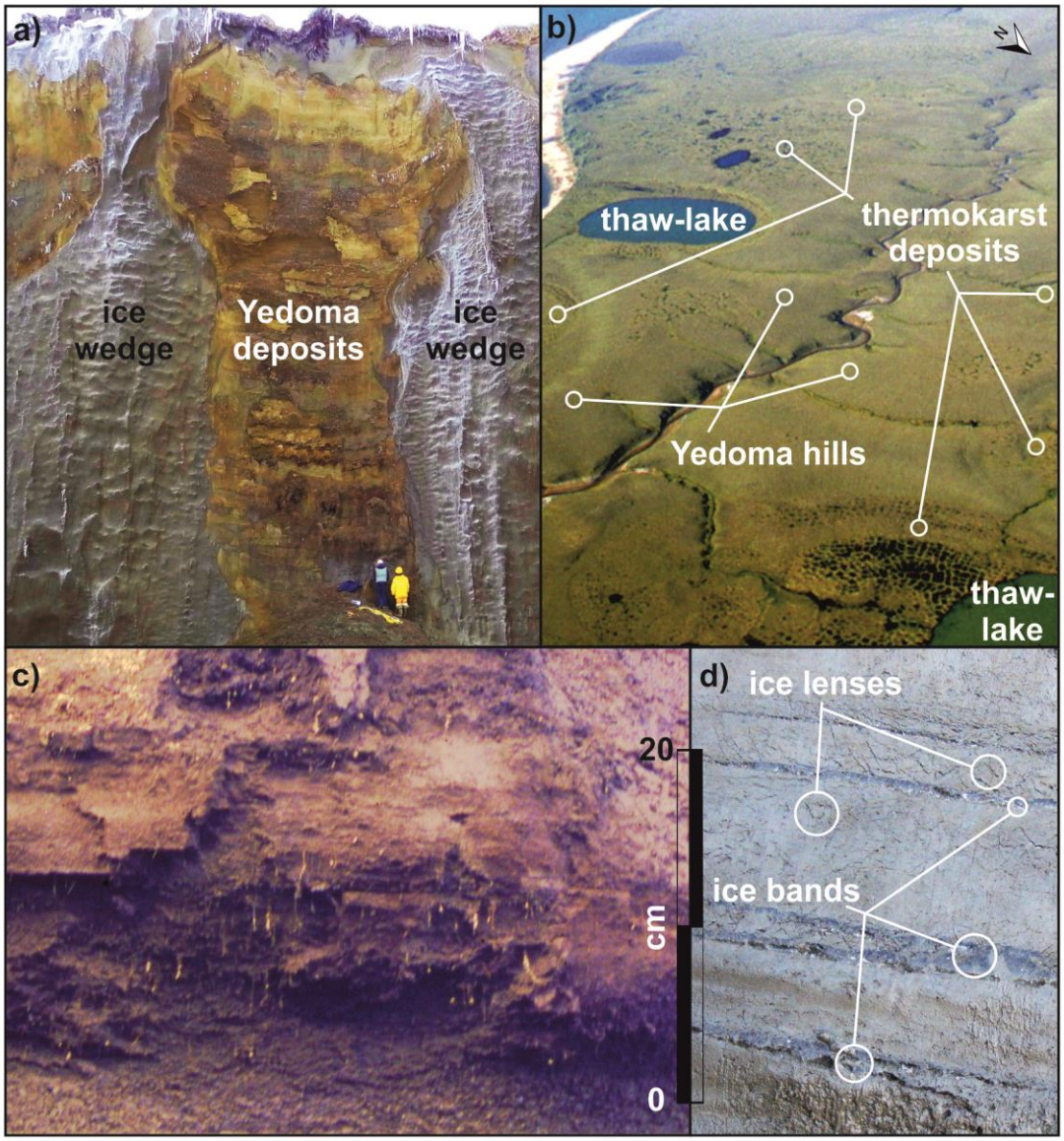

Figure 3-2. Pictures of studied deposits. (a) Yedoma deposits with wedge ice (WI) exposed at the Itkillik River, Alaska (Figure 3-1, site 21, photo from J. Strauss 2012); (b) photo of a Yedoma-thermokarst landscape on Shirokostan Peninsula, Laptev Sea (black box in Figure 3-1b, photo from L. Schirrmeister 1999); (c) example of fossil root-bearing Yedoma deposits from Bykovsky Peninsula, Laptev Sea (Figure 3-1, site 5, photo from L. Schirrmeister, 1998); and (d) example of segregated ice (SEI) (ice lenses and ice bands) at Buor Khaya Peninsula (Figure 3-1, site 7, photo from J. Strauss, 2010).

Various factors could lead to quick Yedoma region OC mobilization, including active layer thickening (Schaefer et al., 2011), widespread thermokarst formation in icy substrates, or accelerated coastal erosion by a sea ice-free Arctic Ocean (Lantuit et al., 2012). However, large uncertainties for the Yedoma region OC pool remain due to scarce data on OC spatial variability, ground ice content, bulk density (BD), and limited knowledge of Yedoma deposit thickness and spatial extent as well as scarce data on presence of other deposits in this region. Because >50 % of the modeling-scenario spread in permafrost OC climate response is caused by uncertainties in the

permafrost OC pool size (Burke et al., 2012a), better size estimates of deep frozen OC pools are essential. The objective of this study is to assess the deep OC pool of the Yedoma region (Appendix III; potential area of Yedoma-deposit distribution, including thermokarst deposit areas) to reduce quantitative uncertainty concerning thaw-vulnerable permafrost OC.

The Yedoma region OC pool was previously estimated at 450 Gt based on mean 2.56 wt% OC content, mean 25 m deposit thickness, and an estimated 1,000,000 km² coverage (Zimov et al., 2006a). However, recent studies (Grosse et al., 2013b) (Figure 3-1) have shown that Yedoma deposits are fragmented by thermokarst processes and cover only part of the Yedoma region.

3.3 Methods

3.3.1 Sampling and organic carbon measurement

Twenty-two Yedoma and 10 thermokarst deposit profiles were studied and sampled from river or coastal bluffs exposed by rapid thaw and erosion. In total, 956 individual samples with at least one measured parameter (total organic carbon (TOC), BD, or thickness) were used. The profiles were described and sampled in the frozen state. Samples were extracted manually with hatchet and hammer or hand drills. Samples were kept cooled or frozen and were transported to laboratories for further analysis. TOC samples were measured with a carbon-nitrogen-sulphur analyzer (Elementar Vario EL III) or a TOC analyzer (Elementar Vario Max).

3.3.2 Bulk density calculation

For BD and SEI calculation, samples were weighed in wet and oven-dry state during field expeditions. BD (10^3kg/m³) was then calculated using its inverse relationship with porosity (n, eq. 3-1)

$$BD = (n-1) \times (-\rho_s) \qquad \text{eq. 3-1}$$

whereas ρ_s is the solid fraction density. Because pore volume is assumed to be ice saturated, the pore volume can be directly inferred from SEI. In addition, 133 direct BD measurements were conducted in the field lab by determining the volume of frozen samples extracted from exposures with the Archimedes Principle, i.e., quantifying the water volume displaced by the frozen sample in a glass beaker filled with water. After freeze-drying in the laboratory (Sublimator 3-4-5, ZIRBUS Technology), the SEI and BD were calculated.

3.3.3 Wedge-ice volume calculation

Wedge-Ice Volume (WIV) was calculated using eq. appendix III-4 and eq. appendix III-5 (Appendix III). For epigenetic ice wedges, it is assumed that a frontal cut of an ice wedge has a shape of an isosceles triangle (Figure appendix III-1, right side). For syngenetic Yedoma deposit ice wedges, we deduced an eq. appendix III-5, assuming that a frontal cut of this ice wedge type is rectangular in shape (Figure appendix III-1, left side). WI width is based on field measurements extracted from the literature. The Yedoma and thermokarst deposit ice-wedge polygon sizes were determined by mapping very high resolution satellite imagery for four study sites (Appendix III).

3.3.4 Statistical methods

Calculations of carbon budget and OC density are based on bootstrapping techniques, i.e., using resampled (10,000 times) observed values (TOC, BD, WIV, thickness) and deriving the mean afterward. Because TOC and BD are genuinely correlated, we used paired values in the resampling process. For that purpose, the missing BD values were calculated using an exponential function ($BD= 1.126^{-0.0601 \times TOC}$) that was fitted to those data for which both values were available. After bootstrapping the population of observation (called "observation-based"), the mean was derived. In addition, we tested an alternate approach using bootstrapping of single variable means before budget calculation (Appendix III) to ease the comparison of results to those derived by previous upscaling studies. Because using single value estimates reduces the variability (Appendix III) of the obtained distribution, we choose this observation-based method to have a conservative uncertainty range of OC carbon budget from the Yedoma region. The error estimates in this study represent the 16th and 84th percentiles to reflect the standard deviation which is typically presented in comparable studies (with the assumption of normal distribution). Computations were performed using R software (boot package).

3.4 Results

The Yedoma region permafrost OC pool largely consists of OC in remaining Yedoma deposits (Figure 3-2a) and refrozen thermokarst deposits (Figure 3-2b), including mineral sediments, peat, WI, and SEI (Figure 3-2a, c, and d). Other non-perennially frozen OC pools, such as active layer or lake and river sediments, are not included in our study.

3.4.1 Data and statistical methods

Using a data set of 956 frozen samples from 23 Siberian and Alaskan study sites (Figure 3-1), we measured and modeled the primary parameters (Figure 3-3) neces-

sary to quantify the overall frozen OC pool, including thickness, spatial coverage, BD (including SEI volume (SEIV)), WI volume (WIV), and total OC (TOC) content of Yedoma and thermokarst deposits of the Yedoma region (Table appendix III-1 to III-5). For calculation, we used eq. 3-2 as follows:

$$\text{OC budget (Gt)} = \frac{\text{thickness (m)} \times \text{coverage}(\text{m}^2) \times \text{BD}(10^3\text{kg/m}^3) \times \frac{100\text{-WIV}}{100} \times \frac{\text{TOC}_{\text{wt\%}}}{100}}{1{,}000{,}000{,}000} \qquad \text{eq. 3-2}$$

Because of high inherent (spatial) heterogeneity and non-normal input parameter distributions (Figure 3-3 and Figure appendix III-5), we used and report observation-based bootstrapping mean values (rather than simple means) for OC budget calculation and error estimation. For comparison with previous studies, we use our parameter data set and also calculate a pool based on the simple arithmetic mean (Appendix III and Table appendix III-1).

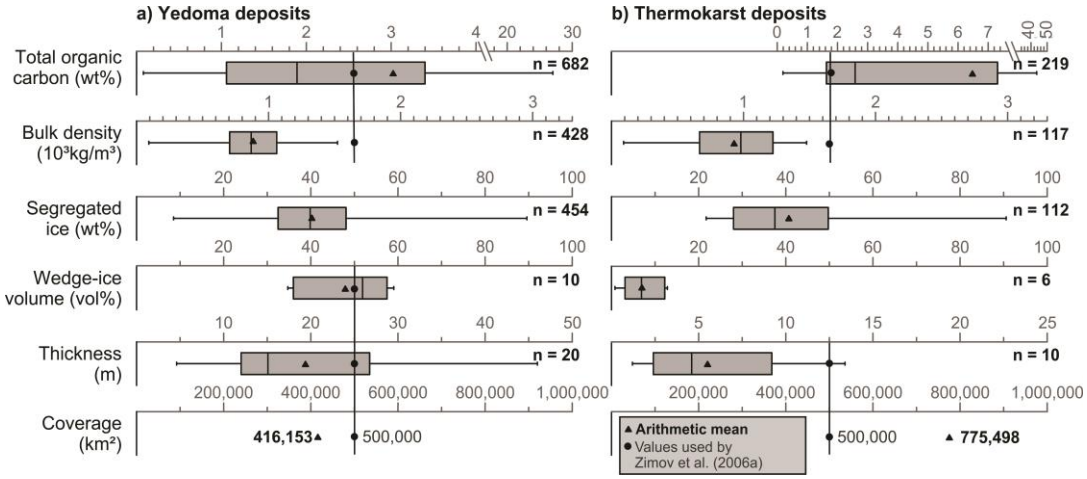

Figure 3-3. Box plots of the key parameters for (a) Yedoma and (b) thermokarst deposit organic carbon estimation. The literature estimate (Zimov et al., 2006a) is given by the vertical black line for comparison. Note the different axis scale in Figure 3-3a and b for total organic carbon (TOC) and thickness. Table appendix III-2 to III-5 contain these parameters with uncertainty estimates.

3.4.2 Biogeochemical and physical parameters

Mean TOC for Yedoma deposits in Siberia and Alaska is 3.0+1.6/-2.2 wt% and 6.5+3.9/-5.0 wt% of the thermokarst deposits, respectively. The BD calculation includes SEI (Strauss et al., 2012) (Appendix III). Direct measurements on 92 Yedoma and 41 thermokarst deposit samples and calculated values for an additional 334 Yedoma and 76 thermokarst deposit samples (Figure appendix III-2) yielded a BD mean of 0.88+0.26/-0.25 10^3kg/m³ and 0.93+0.33/-0.38 10^3kg/m³ for Yedoma and thermokarst deposits, respectively, comparable to earlier estimates of 0.98 10^3kg/m³ for Yedoma deposits (Dutta et al., 2006).

To accurately estimate WIV, a three-dimensional assessment of ice-wedge polygons and WI structures would be necessary. Neither geophysical nor any other technique is available to directly derive such data for deep syngenetic WI. Indirect approaches include WIV estimation from coastal or riverine bluffs (Kanevskiy et al., 2011), or remote-sensing and field survey estimations of polygon sizes combined with WI width data. Using this latter approach (Figure appendix III-2, Figure appendix III-3, and Table appendix III-6), we assume a mean 4.0+0.5/-1.4 m Yedoma deposit WI width and 1.7+1.1/-0.9 m thermokarst deposit WI width and a mean 13.0+0.4/-1.4 m Yedoma deposit polygon diameter and 22.1+1.1/-1.8 m thermokarst deposit polygon diameter (Table appendix III-6). Accordingly, the mean Yedoma deposit WIV is 48 vol%, while younger Holocene thermokarst deposits contain 7 vol% WIV due to smaller ice wedges. The sum of SEIV plus WIV equals a mean total volumetric ground ice content of ~82 vol% for Yedoma and ~67 vol% for frozen thermokarst deposits. When this ground ice thaws in a warmer climate, substantial surface subsidence will ensue.

To best approximate deposit thickness, we used the mean profile depths of the sampled Yedoma and thermokarst deposits. The Yedoma base was reached at 12 out of 20 of our study sites. Hence, Yedoma thickness is potentially underestimated. The mean 19.4 m Yedoma deposit thickness is about 4 times larger than the mean 5.5 m thermokarst deposit thickness. Due to lack of sufficient samples and spatial variability, we do not include any OC pools below Yedoma and below frozen thermokarst deposits in our calculation, which potentially contain relevant amounts of carbon (Schirrmeister et al., 2011b).

3.4.3 Yedoma region coverage

Using a digital Siberian Yedoma region map (Romanovskii, 1993) and the distribution of Alaskan ice-rich silt deposits equivalent to Yedoma (Jorgenson et al., 2008), we calculated the core Yedoma region extent as ~1,387,000 km² (Figure 3-1a, appendix section IV-1.5). Yedoma deposit distribution is discontinuous due to thermoerosion and thermokarst processes (Figure 3-1b). Data from local- and regional-scale analyses of Yedoma deposit versus thermokarst-affected areas (Appendix III and Table appendix III-7) indicate that ~70 % of the Yedoma region area is affected by degradation. The remaining Yedoma deposit extent is ~416,000 km². We further estimate that ~10 % of the Yedoma region is covered with lakes and rivers and thus underlain by unfrozen deposits (150,000 km²) and ~4 % is covered with other deposits including deltaic and fluvial sediments (50,000 km²), leaving ~56 % (775,000 km²) of the Yedoma region covered by frozen thermokarst deposits (Figure 3-2b and appendix section IV-1.5) in drained thermokarst lakes.

3.4.4 Inventory estimations

Combining all available spatial, physical, and biogeochemical parameters (eq. 3-2, Figure 3-3), we calculated the Yedoma deposit frozen OC pool as 10+7/-6 kg/m³ and thermokarst deposits as 31+23/-18 kg/m³. WIV is included in this calculation. To show OC density separate from wedge ice for comparability with previous studies, the Yedoma deposit frozen OC pool contain 19+13/-11 kg/m³ and thermokarst deposits 33+25/-19 kg/m³ when excluding the WIV. Adding the total stored Yedoma deposit OC, 83+61/-57 Gt, and the frozen thermokarst deposit OC, 128+99/-96 Gt, the total frozen Yedoma region contains 211+160/-153 Gt OC (not including active layer nor deeper organic matter deposits below Yedoma or frozen thermokarst deposits). Inferred 16th and 84th percentiles (Yedoma: 22 Gt, 140 Gt; thermokarst: 29 Gt, 224 Gt) are markedly large because of our conservative (observation-based) approach using all measurements for bootstrapping and deriving the mean afterward. The use of single-value estimates such as mean reduces the variability of the obtained distribution.

3.5 Discussion

Our results suggest that we must reconsider whether Yedoma or thermokarst deposits constitute the dominant current Yedoma region OC pool. Moreover, it is essential to make appropriate statistical assumptions previous to the inventory calculations, because a calculation based on observation-based bootstrapping mean values results in a ~40 % smaller inventory compared to simple mean approach (Table appendix III-1.

The previous estimate (Zimov et al., 2006a) suggests that 60 % of the Yedoma region OC is stored in Yedoma deposits and 40 % in thermokarst deposits. Our study reveals the reverse ratio, 40 % is stored in Yedoma deposits and 60 % in frozen thermokarst deposits. The total Yedoma region frozen OC represents a substantial pool of ancient thaw-vulnerable ice-rich OC deposits. For comparison, global plant biomass contains 350 to 540 Gt OC (McGuire et al., 2009). Thaw-related Yedoma region OC release will potentially affect large-scale carbon cycling. Paleoclimate models (Ciais et al., 2012; DeConto et al., 2012) reveal the influence of permafrost OC thaw on Earth's past climate. Ciais et al. (2012) found that 10,000,000 km² of thawing Eurasian tundra could at least partly constitute the missing cause of an ice-core-inferred 100 ppm atmospheric CO_2 increase during the Pleistocene-Holocene transition. Our calculated 211 Gt Yedoma region OC pool is entirely vulnerable to thaw. When OC will be released, it is presently unclear due to complex positive and negative climate feedback. Nevertheless, if even 20 % of this frozen OC pool is emitted as CO_2, in the long term, ~10±7 ppm atmospheric CO_2 increase could result (Appendix III, calculation according to Battle et al., 2000 and Schneider von

Deimling et al., 2012). In this calculation OC emission as CH_4 could not be included because of various uncertainties and unknowns, e.g., a landscape-level carbon dioxide to methane emission ratio.

For further evaluation of OC pool relevance, two questions are important regarding subsequent soil OC mobilization: How was OC incorporated originally (OC source/quality) and what are the OC release trajectories and timescales (OC vulnerability)? Before OC refreezes, it accumulates in the active layer and transition zone above permafrost, either directly by cryoturbation and root growth or indirectly via sediment burying. Cold soils near the permafrost table thaw for only a short time in summer, and organic matter decomposition is severely limited, contributing to the generally high OC content of permafrost-affected soils (Tarnocai et al., 2009; Grosse et al., 2011a). Evidence of rapid OC preservation in Yedoma deposits includes in situ ancient grass roots (Figure 3-2c) and well-preserved mammal carcasses. Frozen thermokarst deposits are generally more heterogeneous than Yedoma deposits, as revealed by considerable scattering in TOC data (Figure 3-3 and Figure appendix III-5). Some thermokarst deposits formed in lakes that drained; sediments subsequently refroze and terrestrial peat accumulated over time. Hence, reworked late Pleistocene and Holocene OC and in situ growing organic matter are important contributors to thermokarst deposit OC, resulting in a mean TOC content (6.5 wt%) twice as high compared to Yedoma deposits (3.0 wt%). Since not all Yedoma region organic matter is equally vulnerable to post-thaw decomposition, microbial turnover rates must be known to quantify future OC fluxes. Labile organic matter easily undergoes microbial turnover, but more complex compounds are more inert (Dutta et al., 2006; Burke et al., 2012a; Lee et al., 2012). Organic matter decomposition vulnerability measured by mineralization rates is slightly higher for Yedoma deposits than for thermokarst deposits (Knoblauch et al., 2013), because portions of refrozen thermokarst organic matter decomposed under originally unfrozen conditions. Frozen thermokarst deposits 2 to 3°C warmer than adjacent Yedoma deposits (Romanovsky et al., 2010a) have been found, suggesting that frozen thermokarst deposits may thaw before Yedoma deposits and the thermokarst OC pool may be affected earlier by Arctic warming. Thaw processes will cause WI melting, subsidence, and rapid erosion. Based on total volumetric SEI and WI content, surface subsidence of ~50 to 70 % is possible, exposing deep OC pools on short timescales. Exposure to sunlight and thaw stimulates bacterial decomposition (Cory et al., 2013). In addition, the development of new and expansion of existing thermokarst lakes in ice-rich deposits may lead to increased release of CH_4 formed in lake sediments and expanding thaw bulbs under lakes (Walter et al., 2006).

Most climate model projections either ignore or underestimate the potential atmospheric impact of permafrost OC release (MacDougall et al., 2012). Driven by large uncertainties in size, distribution, and vulnerability, models have been slow to embrace the Yedoma region OC pool. Koven et al. (2011) suggest that the Yedoma region, located in Siberia's coldest parts, may not thaw substantially in the near future. However, field data and maps (Figure 3-1) suggest that both Yedoma and thermokarst deposits occur across a wide mean annual ground temperature range, from -15°C (Figure 3-1, site 10) to -3°C (Figure 3-1, site 19). Current global-scale models are limited because they only implement one-dimensional vertical thaw; rapid sub grid-cell processes such as thermokarst and erosion with strong lateral dynamics are disregarded. However, these processes are essential for understanding and projecting the response of ice- and organic-rich permafrost to warming. Implementation of a wide range of permafrost thaw processes is needed for realistic permafrost and global carbon cycle modeling.

3.6 Conclusion

In conclusion, based on a bootstrapping-mean approach of a large number of field samples, we confirm a substantial frozen OC pool of ~211+160/-153 Gt in the Yedoma region, stored in Yedoma and frozen thermokarst deposits. We also suggest that this pool size may have been previously overestimated (Zimov et al., 2006a). Furthermore, we propose a ~2:3 ratio between the Yedoma deposit and thermokarst deposit OC pools. Thawing portions of these significant OC pools will amplify climate change in a warmer Arctic. To further improve OC calculation, sensitivity analysis revealed that especially more data on deposit thickness will reduce Yedoma region OC pool uncertainty.

Acknowledgments

We acknowledge support of this research by the German Ministry of Science and Education (project "System Laptev Sea" and grant 01DM12011). T. Opel, M. Z. Kanevskiy, Y. L. Shur, E.A.G. Schuur, and K. M. Walter Anthony are acknowledged for comments on the manuscript. We also thank the many Russian, U.S., and German partners who were involved in field research in the Siberian and Alaskan Arctic, and F. Günther for providing high-resolution satellite images. J. Strauss thanks the German National Academic Foundation for financial support. G. Grosse was supported by NSF OPP 0732735 and NASA NNX08AJ37G.

4 Organic matter quality of deep permafrost carbon - a study from Arctic Siberia

Strauss, J.[1], Schirrmeister, L.[1], Mangelsdorf, K.[2], Eichhorn, L.[3], Wetterich, S.[1] and Herzschuh, U.[1]

[1]Alfred Wegener Institute Helmholtz Centre for Polar and Marine Research, Periglacial Research Unit, Potsdam, Germany.
[2]Helmholtz Centre Potsdam GFZ German Research Centre for Geosciences, Potsdam, Germany
[3]International Max Planck Research School for Global Biogeochemical Cycles (Max-Planck-Institute for Biogeochemistry and Friedrich Schiller University), Jena, Germany

Submitted to: Biogeosciences

Citation: Strauss, J., Schirrmeister, L., Mangelsdorf, K., Eichhorn, L., Wetterich, S., and Herzschuh, U., Organic Matter Quality of Deep Permafrost Carbon - a Study from Arctic Siberia, Biogeosciences Discussions, 11, 15945–15989, doi:10.5194/bgd-11-15945-2014, 2014.

4.1 Abstract

The organic carbon (OC) pool accumulated in Arctic permafrost (perennially frozen ground) equals the carbon stored in the recent atmosphere. To give an idea of how Yedoma region permafrost could respond under future climatic warming, we conducted a case study to quantify the organic matter quality for future decomposition of late Pleistocene (Yedoma) and Holocene (thermokarst) deposits on the Buor Khaya Peninsula, northeast Siberia. The objective of this study was to develop a stratigraphic classified organic matter quality characterization. For this purpose the degree of organic matter decomposition was estimated by using a multiproxy approach. We applied sedimentological (grain-size analyses, bulk density, ice content) and geochemical parameters (total OC, stable carbon isotopes ($\delta^{13}C$), carbon : nitrogen (C/N) ratios) as well as lipid biomarkers (*n*-alkanes, *n*-fatty acids, hopanes, triterpenoids, and biomarker proxies/indices: average chain length, carbon preference index (CPI), and higher plant fatty acid index (HPFA)). Our results show that the Yedoma and thermokarst organic matter qualities exhibit no obvious degradation - depth trend. The C/N, $\delta^{13}C$, and hop-17(21)-ene values and the HPFA index show a better quality of the organic matter stored in thermokarst deposits compared to Yedoma deposits, but the CPI points in the other direction. As the ranges of the proxies mostly overlap, we interpret this as to indicate similar quality for both kind of deposits with perhaps slightly better thermokarst organic matter quality. Supported by principal component analyses, the sediment parameters and quality proxies of Yedoma and thermokarst deposits could not be clearly separated from each other. This lack of clear quality differences revealed that the organic matter vulnerability is heterogeneous and depends on different decomposition trajectories and the previous decomposi-

tion/incorporation history. Elucidating this was one of the benefits of our multiproxy approach. With the addition of biomarker data, it was possible to show that permafrost organic matter degradation likely occurs via a combination of (uncompleted) degradation cycles or a cascade of degradation steps rather than as a linear function of age or sediment facies. We conclude that the amount of organic matter in the studied sediments is high for mineral soils and of good quality and therefore susceptible to future decomposition. The missing depth trends reveal that permafrost acts like a giant freezer, preserving the constant quality of ancient organic matter. When undecomposed Yedoma organic matter is mobilized via thermokarst processes, the fate of this carbon depends largely on the environmental conditions; the carbon could be preserved in an undecomposed state till refreezing occurs. If recent input has occurred, thermokarst organic matter could be of a better quality than that found in Yedoma deposits.

4.2 Introduction

During the late Quaternary, the rate of organic matter decomposition in the Arctic has been slower than plant growth, sedimentation, and freezing rates. Thus, a large pool of organic carbon (OC) accumulated in the Arctic and was deeply sequestered in the permafrost. Hugelius et al. (2014) estimates an OC storage of 1300 Gt for the circum-Arctic permafrost region with ~850 Gt OC sequestered in permafrost. This is approximately the carbon stored in the recent atmosphere (Dlugokencky and Tans, 2014). During warming and permafrost thawing, this formerly cryo-sequestered OC gradually entered the recent biogeochemical cycle by microbial turnover. By thawing and microbial activity, the permafrost deposits can turn from a carbon sink to a source (Schuur et al., 2009), releasing greenhouse gases such as carbon dioxide and methane to the atmosphere. Besides the near-surface carbon pool, and because of rapid permafrost thawing processes like thermokarst and thermoerosion, deep OC pools, especially those held in ice-rich permafrost deposits in the Yedoma region, are also relevant to current concerns about the effects of global warming. According to Strauss et al. (2013) the Yedoma region is defined as the area of potential late Pleistocene silty ice and organic rich (Yedoma) deposits distributed in Siberia and Alaska. Estimates of OC stored in the Yedoma region amount to 83+61/-57 Gt for late Pleistocene Yedoma deposits and to 128+99/-96 Gt for Holocene thermokarst deposits in an area of about 1,387,000 km^2 of which about 70 % is already affected by permafrost degradation (thermokarst) (Strauss et al., 2013). Kuhry et al. (2009) and Schirrmeister et al. (2011b) showed that Yedoma deposits accumulated at fast rates, implying a short time for the organic matter to decay before it became locked into a perennially-frozen state. Therefore, the organic matter availability for microorgan-

isms is expected to be excellent, resulting in great vulnerability to warming ground conditions (Mu et al., 2014). To elucidate how Yedoma region permafrost could respond under conditions of future climatic warming, we studied the organic matter quality of Yedoma and its Holocene degradation features (called thermokarst deposits) on Buor Khaya Peninsula, Eastern Laptev Sea. In both kinds of deposits the OC was deeply (deeper than 3 m) incorporated into permafrost (Schirrmeister et al., 2013; Strauss et al., 2013). As shown by models and extrapolation from recent observations, the more southern portions of Yedoma deposits thawed during the last deglaciation, resulting in large emissions of greenhouse gases to the atmosphere (Walter et al., 2007a; Ciais et al., 2012; Walter Anthony et al., 2014). Recent ground warming has been observed in the permafrost zone (Romanovsky et al., 2010b), and incubation experiments reveal that permafrost warming is accompanied by a substantial outgassing of greenhouse gases (Lee et al., 2012; Knoblauch et al., 2013; Schädel et al., 2014). As an illustration of the important influence of ground temperature on organic matter quality, a higher respiration rate at greater depth close to the permafrost table (Mangelsdorf et al., 2009; Waldrop et al., 2010) was found inside the seasonally-thawed active layer and interpreted as a greater lability of the organic matter close to the perennially frozen ground. Focusing on permafrost deposits in the Laptev Sea region, which includes our Buor Khaya study site, Schirrmeister et al. (2011b) characterize the Yedoma region permafrost organic matter as weakly decomposed.

Biomarkers are used for paleoenvironmental reconstruction of terrestrial permafrost (Andersson et al., 2011) or characterization of permafrost organic matter degradation (Andersson and Meyers, 2012; Vonk et al., 2013a; Routh et al., 2014). In our study we estimate molecular markers (*n*-alkanes, *n*-fatty acids, hopanes, and triterpenoids) and use biomarker proxies/indices (absolute lipid concentration, average chain length (ACL), carbon preference index (CPI), hop-17(21)-ene, higher plant fatty acid (HPFA) index, and an Oleanen ratio) to test whether they are useful mirrors of organic matter decomposition, i.e. organic matter quality in permafrost deposits. Rather established methods, both cryolithological (grain size analyses, bulk density, ice content) and biogeochemical (total organic carbon ($TOC_{wt\%}$), stable carbon isotope ratios ($\delta^{13}C$ in TOC), total nitrogen (TN), and $TOC_{wt\%}$/TN (C/N) ratios), are applied to our sample set. Finally, principal components analysis (PCA) highlights the relationships between different organic matter degradation proxies. Because the future feedback from the Yedoma region permafrost OC to climate forcing is driven by both (1) the pool size, estimated to be ~211 Gt (Strauss et al., 2013), and (2) the quality of OC stored in the studied deposits, the objective of this study is the development of a

stratigraphically differentiated organic matter quality characterization using sample material representative of widespread Yedoma and thermokarst permafrost.

4.3 Material and methods

4.3.1 Study area

The Buor Khaya Peninsula study site (71°34'N, 132°12'E) is located in the north-eastern part of Siberia (Figure 4-1).

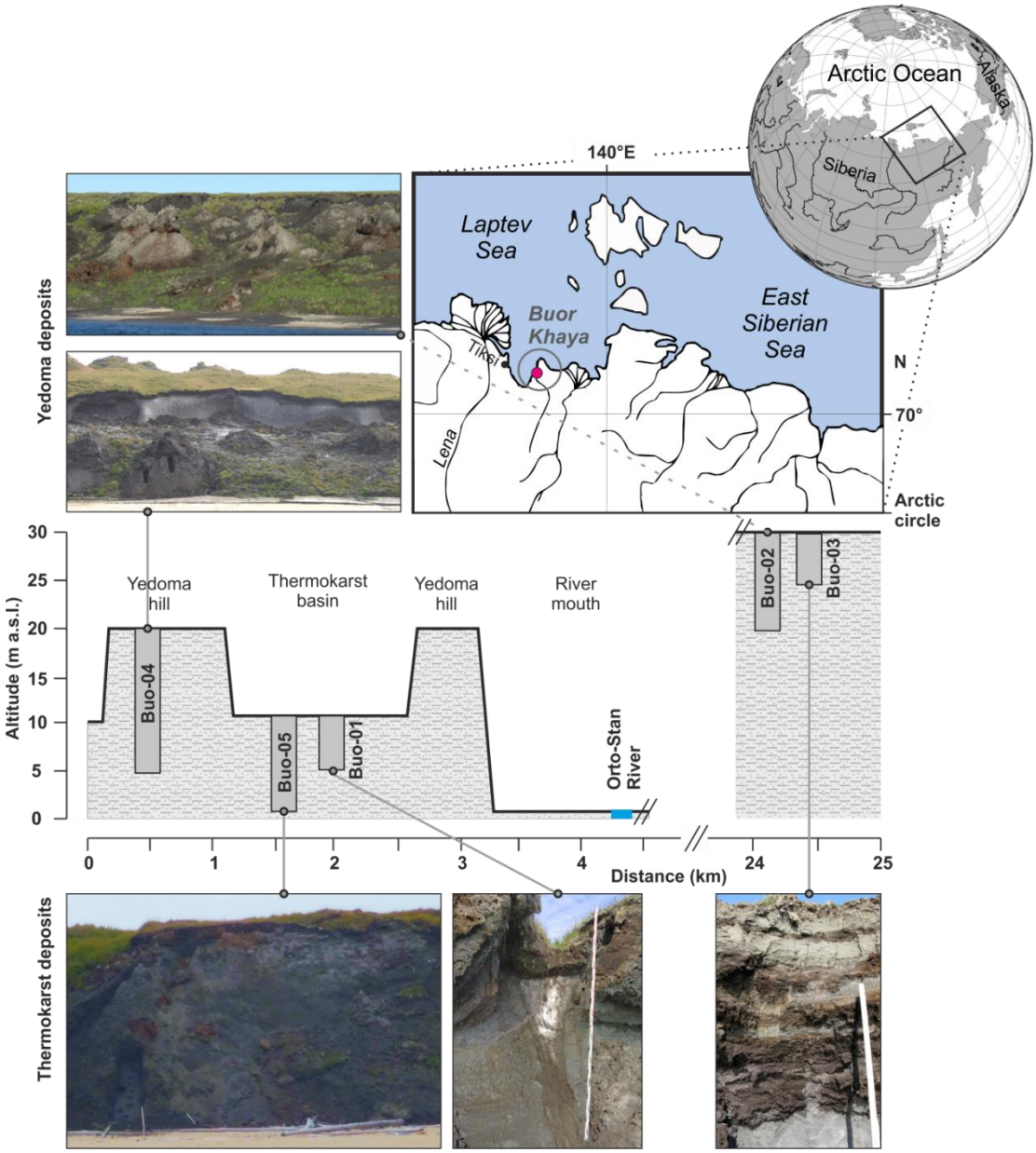

Figure 4-1. Location of the Buor Khaya Peninsula and the study area. The square black box in the globe inset indicates the area shown in the map below. The profile diagram and the photographs below it show the profiles and their positions relative to each other. Modified after Strauss and Schirrmeister (2011), pictures taken by J. Strauss.

Buor Khaya Peninsula is framed by the Laptev Sea, a shallow epicontinental part of the Arctic Ocean, and geologically by two rift structures (Drachev et al., 1998). Buor Khaya is underlain by continuous permafrost with ground temperatures of less than -11°C (Drozdov et al., 2005). The permafrost thicknesses is estimated to be between 450 and 650 m (Romanovskii et al., 2004). Stratigraphically, outcrops from two sediment units are distinguished and studied; (1) ice-rich permafrost, called Yedoma deposits, and (2) deposits in permafrost rapid thaw features, generalized as thermokarst deposits. Three profiles of thermokarst deposits (in a thermokarst basin: Buo-01 and Buo-05; initial thermokarst on top of a Yedoma hill: Buo-03) and two profiles of Yedoma deposits (Buo-02, Buo-04) were studied and sampled. Figure 4-1 shows an overview of the sampled profiles and their position relative to each other.

4.3.2 Field work

Field studies were undertaken in summer 2010 at outcrops situated at the western coast of the Buor Khaya Peninsula. The sediment of the profiles and sub-profiles, exposed at the cliff wall or partly in thermokarst mounds in thaw slumps, were dug by spades and cleaned with hacks. The cryolithology, sediment characteristics, and visible organic matter in the sediments of the chosen sequences were surveyed and described. Moreover, the profiles were photographed and sketched. Sub-profiles were stacked together to create composite profiles. Sampling positions in neighboring sub-profiles were correlated by height estimation using measuring tape. The upper edge of each profile was calibrated with tacheometer measurements (Günther et al., 2012). In the field laboratory all sample volumes were measured with a balance and Archimedes principle, and the absolute ice content was determined by drying the sample. In total, 91 samples were taken and kept cool for transport to laboratories for further analysis. Detailed sampling positions for each profile are shown in Strauss and Schirrmeister (2011).

4.3.3 Indicators of organic matter quality

To validate and to extend the sedimentological approach used, and to estimate the organic matter quality, lipid biomarkers were measured to estimate the degree of organic matter degradation. For biomarker studies we used a “fingerprint” approach by focusing on identifiable markers related to organic matter quality. Below, the utilized geochemical indicators and biomarkers are described.

4.3.3.1 Grain-size analyses

To disaggregate the sample and to measure only clastic grains, organic components were removed by adding 35 % hydrogen peroxide three times a week to the samples. The samples were continuously shaken (Innova 2300, New Brunswick) for 6 weeks.

The organic-free samples were 'washed' to neutral pH values by repeated decantation after centrifugation (Heraeus Cryofuge 8500i, Thermo Scientific). Samples were dispersed in 1 % ammonia solution and 1 g dispersing agent ($Na_4P_2O_7 \times 10\ H_2O$) and shaken (RS12 Rotoshake, Gerhardt) for at least 5 hours. Finally, each sample was split by a rotary cone sample divider (Laborette 27, Fritsch) and two sub-samples of each main sample were analyzed using a laser particle sizer (LS 200, Beckmann-Coulter). Grain sizes between 0.375 and 1000 µm were determined (Figure 4-2, Figure appendix IV-1). Because no grain fractions >1000 µm occurred, there was no need for fraction reintegration. Grain-size calculations were done after Folk and Ward (1957) using Gradistat v8 (Blott and Pye, 2001).

4.3.3.2 Elemental composition

To determine the total elemental carbon and total nitrogen (TN) content, the samples were freeze-dried (sublimator 3-4-5, Zirbus Technology) and homogenized by grinding (Pulverisette 5 planetary mill, Fritsch) before being measured by a carbon-nitrogen-sulphur analyzer (Vario EL III, Elementar). Two 5 mg sub-samples per sample were taken and encapsulated in two zinc capsules. For ensuring complete oxidation of the sample during measurements ~10 mg of tungsten-(VI)-oxide was added. Background signals were detected by measuring a blank capsule at the beginning and calibration standards after each 20 samples. The quantified measurement accuracy is <±0.1 wt%. $TOC_{wt\%}$ was measured with a TOC analyzer (Vario Max C, Elementar). Therefore, depending on the previously measured TC content, up to 100 mg were weighed in a crucible and analyzed. The C/N ratio was calculated as the quotient of $TOC_{wt\%}$ and TN values. The volumetric TOC content (TOC_{kg/m^3}) was calculated according to Strauss et al. (2013).

The C/N ratio has been used as a general indicator of the degree of organic matter decomposition (Stevenson, 1994). Based on the assumption that organic matter components are degraded selectively, degradation modifies elemental compositions and hence C/N in deposits. Because a decrease in the C/N ratio has been observed in aerated deposits with microbial immobilization of TN (nitrogen stays in the system) accompanied by the re-mineralization of TOC (Sollins et al., 1984) and CO_2 emission, this ratio is used in the following way: The higher the C/N ratio, the lower the degree of decomposition. This assumption implies a similar source signal.

4.3.3.3 Bulk density and volumetric carbon content

Bulk density (BD) measurements were performed in two steps; (1) in the field lab by determining the volume of frozen samples with the Archimedes Principle (quantifying the water displaced in a water-filled glass beaker using a balance (FCB 8K0.1,

Kern; accuracy ±0.1 g), and (2) in the freeze-dried laboratory samples; BD was calculated using eq. 4-1.

$$\text{BD}\left(\frac{10^3\text{kg}}{\text{m}^3}\right)=\frac{\text{sample dry weight }(10^3\text{kg})}{\text{sample volume }(\text{m}^3)} \qquad \text{eq. 4-1}$$

Estimating the BD is required to convert the measured-weight-based $TOC_{wt\%}$ content per sample to a volume-based value. Thus, the TOC_{kg/m^3} was calculated according to eq. 4-2:

$$TOC_{kg/m^3}=\text{BD }(10^3\text{kg/m}^3)\times\frac{TOC_{wt\%}}{100} \qquad \text{eq. 4-2}$$

4.3.3.4 Carbon isotope studies

Stable TOC carbon isotopes were determined with a Finnigan MAT Delta-S mass spectrometer combined with a FLASH elemental analyzer and a CONFLO III gas mixing system. Before analysis, samples were treated with hydrochloric acid (1.3 molar) and heated at 97°C for three hours to remove the carbonate. After that, the samples were washed to a neutral pH value, dried, and weighed in silver capsules. The sub-sample mass was dependent upon $TOC_{wt\%}$ content of each sample. The $\delta^{13}C$ value was determined by the ratio of ^{13}C to ^{12}C atoms expressed in per mille (‰). In order to quantify the deviations of the $^{13}C/^{12}C$ ratios, the international standard Vienna Pee Dee Belemnite (VPDB) is used. The stable carbon isotopes of OC reflect (1) initial contribution from different plant species and plant components, and (2) subsequent degradation processes (Gundelwein et al., 2007). Assuming constant photosynthetic isotope fractionation in source plants in the region (C_3 plants are ubiquitous in the Arctic, Tieszen, 1973), we use $\delta^{13}C$ ratios as a degradation proxy. After Heyer et al. (1976), decomposition discriminates against the lighter isotope (^{12}C), resulting in more negative $\delta^{13}C$ ratios. Thus, this proxy is used in the following way: Lower (more negative) $\delta^{13}C$ values are connected to less degraded material, while higher (less negative) $\delta^{13}C$ values reflect greater decomposition.

Ages were determined by radiocarbon dating of selected macroscopic plant remains. The present measurements were performed at the Poznań Radiocarbon Laboratory, Poland, using compact carbon accelerator mass spectrometry (AMS) (Goslar et al., 2004). The presented radiocarbon ages are uncalibrated ages; Table 4-1 includes calibrated ages as well. Radiocarbon ages are given in year before present (a BP).

4.3.3.5 Lipid biomarkers

To look more closely at the molecular composition, we used specific lipid biomarkers. Molecular fossils or biomarkers were studied by chromatography methods coupled with mass spectrometers. Characteristic fractions like *n*-alkanes, *n*-fatty ac-

ids, sterols, and hopanes were isolated. Because the $TOC_{wt\%}$ in the profiles is not equally distributed, we calculated and visualized the biomarker concentration as µg/g$TOC_{wt\%}$ and µg/gSediment (µg/gSed). For the results, we focus on µg/g$TOC_{wt\%}$.

Extraction and fraction separation

For lipid biomarker analyses 2 to 12 g of ground sediment was weighed in an extraction cell with an accelerated solvent extractor (ASE 200, Dionex). Samples were extracted with dichloromethane/methanol (99:1). Each sample was held in a static phase for 20 min at 75 °C (after 5 min heating, no preheating) at a pressure of 5 MPa. Afterwards, the dissolved compounds were concentrated with a Turbo Vap (Zymark) closed cell concentrator and further dried by evaporating the solvent in a stream of nitrogen gas. After that, internal standards (5α-androstane for the aliphatic fraction, ethylpyrene for the aromatic fraction, 5α-androstan-17-on for nitrogen-, sulfur-, and oxygen- (NSO-) containing compounds, and erucic acid for the NSO fatty acid fraction) were added. The amount of internal standards depended on the $TOC_{wt\%}$ content (<10 wt%: 8 µg; >10 to ≤25 wt%: 20 µg; >25 wt%: 50 µg). After the removal of the *n*-hexane-insoluble fraction (by the addition of a large excess of *n*-hexane, called 'asphaltene' precipitation), the hexane-soluble portion of the extract was separated by medium-pressure liquid chromatography (MPLC; (Radke et al., 1980) into fractions of different polarity (aliphatic and aromatic hydrocarbons as well as polar hetero (NSO) components). Afterwards, the NSO fraction was split into a fatty acids and an alcohol fraction using a KOH-impregnated silica gel column (Schulte et al., 2000).

For this study, the focus was placed on the aliphatic fraction (containing *n*-alkanes and triterpenoid compounds) and the NSO fraction (containing *n*-fatty acids). The fractions were measured by gas chromatography–mass spectrometry (GC–MS). All compounds of interest were identified using the Xcalibur software (Thermo Fisher Scientific).

GC-MS measurement and compound quantification

The *n*-alkanes, *n*-alcohols, hopenes (hop-17(21)-ene), and other triterpenoids (β-amyrin (olean-12-en-3β-ol), Olean-12-ene, and Olean-13(18)-ene) were measured with a GC-MS system (GC: Trace GC Ultra; MS: DSQ, both Thermo Fisher Scientific). Prior to the measurements, the *n*-fatty acids were methylated with diazomethane and the alcohols were silylated with *N*-methyl-*N*-trimethylsilyltrifluoroacetamide (MSTFA). The GC was equipped with a programmable temperature vaporization (PTV) injector system (starting temperature of 50 °C; heating rate of 10°C/sec to 300°C; isothermal holding time of 10 minutes; operated in splitless

mode) and a fused silica capillary column (SGE BPX5, 50 m length, 0.22 mm inner diameter, 0.25 µm film thickness). For the measurements the GC oven was programmed with a starting temperature of 50°C, a heating rate of 3°C/min to 310°C, and an isothermal holding time of 30 minutes. Helium with a constant flow rate of 1 ml/min was used as a carrier gas. For the *n*-fatty acid fraction a different temperature program (starting temperature of 50°C, 1 min isotherm, heating rate of 3°C/min to 350°C, isothermal holding time 25 minutes) was used. For compound identification, the gas chromatograph was linked to a mass spectrometer, which was operated in electron impact ionization mode at 70 eV. The temperature of the ion source was set to 230°C. Full scan mass spectra were recorded from m/z 50 to 600 Da at a scan rate of 2.5 scans/sec. For the *n*-fatty acids fraction the scan rate was m/z 50 to 650 Da.

Quantification of *n*-alkanes, *n*-fatty acids, and β-amyrin was done in the GC-MS total ion current chromatogram by relating the peak area of the target compound to the peak area of an internal standard of known concentration. Other triterpenoids like Olean-12-ene, Olean-13(18)-ene, and hopene were quantified using the m/z 191 mass trace relative to the peak area of the β,β-diploptene (in the m/z 191 mass trace), the concentration of which was calculated in the total ion current chromatogram relative to the internal standard.

4.3.4 Biomarker proxies/indices

4.3.4.1 Absolute lipid concentration

The absolute lipid concentration is used as rough estimator of organic matter quality in the following sense: The higher the concentration, the better the conservation of the lipid, and the better the quality of the organic matter.

4.3.4.2 Carbon preference index

The CPI was introduced by Bray and Evans (1961) as the ratio of odd- to neighboring even-numbered alkanes, which is a measure of the alteration of organic matter. Here we use the improved formula after Marzi et al. (1993). In addition, we also applied the CPI for fatty acids in which even-numbered fatty acids predominate over adjacent odd *n*-fatty acids (Glombitza et al., 2009).

$$\mathrm{CPI}=\frac{\left(\sum_{i=n}^{m} C_{2i+1}\right)+\left(\sum_{i=n+1}^{m+1} C_{2i+1}\right)}{2\times\left(\sum_{i=n+1}^{m+1} C_{2i}\right)} \qquad \text{eq. 4-3}$$

n: starting dominating chain length/2; m: ending dominating chain length/2; i: index (carbon number); C: concentration

The CPI is used as a degradation/alteration proxy by quantifying the odd/even (*n*-alkanes, Figure appendix IV-2) or even/odd (*n*-fatty acids, Figure appendix IV-3) of

the carbon chains (Bray and Evans, 1961; Glombitza et al., 2009). A low CPI means mature/degraded organic matter (e.g. CPI of crude oil ~1).

4.3.4.3 Average chain length

As introduced by Poynter (1989), the *n*-alkane ACL value is the concentration-weighted mean of different carbon chain lengths in a geological sample. For *n*-alkanes we use the C_{23}-C_{33} interval, for *n*-fatty acids the C_{20}-C_{34}:

$$ACL = \frac{\sum i \times C_i}{\sum C_i} \qquad \textit{i: index (carbon number); C: concentration} \qquad \text{eq. 4-4}$$

The ACL is a rough OC source parameter. A schematic showing different chain lengths in different organisms is given in Figure appendix IV-4. The higher C_3 land plants are expected to have an ACL of ~28-29.

4.3.4.4 Hop-17(21)-ene

We use hop-17(21)-ene as another marker for low-maturity organic material. The hop-17(21)-ene is produced by bacteria. The assumption here is that during degradation and diagenesis the hop-17(21)-ene will be transformed into saturated hopane (Luo et al., 2012).

4.3.4.5 Higher Plant Fatty Acid index

The ratio of the major even wax alcohols over the sum of major odd wax alkanes plus even alcohols was introduced by Poynter (1989) as the Higher Plant Alcohol (HPA) index. It is applied as an indicator for chemical degradation of the wax components. Based on this index, but using fatty acids instead of alcohols, we developed the HPFA index. The general assumption for this index is that it reflects the preservation degree of the organic matter due to the higher lability of *n*-fatty acids in relation to *n*-alkanes.

$$HPFA = \frac{\sum n\text{-fatty acids}C_{24},C_{26},C_{28}}{\sum n\text{-fatty acids}C_{24},C_{26},C_{28} + \sum n\text{-alkanes}C_{27},C_{29},C_{31}} \qquad \text{eq. 4-5}$$

The HPFA ratio cannot be considered an absolute index of degradation, but is an indicator of the relative amounts of the more labile fatty acids that remain in a sample. Since *n*-alkanes are preserved preferentially compared to *n*-fatty acids, a decrease in this index indicates increased decomposition (the more degraded, the lower the HPFA index).

4.3.4.6 Oleanen ratio

β-amyrin (olean-12-en-3β-ol) is a triterpenoid produced by higher land plants. As a first degradation step, β-amyrin is expected to lose its hydroxy-group and will be transformed to Olean-12-ene. A second step would be a shift of the double bond forming Olean-13(18)-ene. Thus, fresh organic material is associated with a lower

oleanen ratio, while more degraded organic matter is reflected in a higher ratio. This index is calculated:

$$\text{oleanen ratio (\%)} = \frac{\text{Olean-12-ene + Olean-13(18)-ene}}{\beta\text{-amyrin}} \times 100 \qquad \text{eq. 4-6}$$

4.3.4.7 Acetate

Pore water was obtained from each sample by centrifugation in specific pore water tubes. Water extracts were analyzed twice using ion chromatography with conductivity detection (ICS 3000, Dionex). An analytical column (AS 11 HC, 2 × 250 mm, Dionex) was used at constant 35°C. The sample was eluted with KOH solution of varying concentration over time. The initial concentration was 1.4 mM. Between 0 and 6 minutes, the KOH solution was increased at a constant rate to 1.6 mM. Between 6 and 12 minutes the solution was increased to 10.0 mM KOH and a concentration of 15.0 mM KOH was reached at 22 minutes. After 32 minutes, 60.0 mM KOH concentration was achieved, and maintained for 1 minute, followed by a rapid decrease to 1.4 mM after 33 minutes where samples were fixed for 45 minutes to equilibrate the system. For quantification of acetate, standards containing the investigated compound were measured. The standard deviation of the sample and of standard quantification was <5 %. Because acetate can act as excellent feedstock for microbes (Smith and Mah, 1980; Vieth et al., 2008) and it has been shown that acetate was rapidly consumed in the presence of oxygen and nitrate (Kuesel and Drake, 1995), we use this parameter in the following way. If there is an acetate concentration of >1 mg/l, the deposit, including its acetate, was less available for degradation, resulting in good organic matter quality.

4.3.5 Principal component analysis

Multivariate statistical techniques, like the PCA used here, allow the analysis of multiple variables in order to investigate connections between the different degradation proxies. Prior to the PCA, concentration data were transformed using a log (x+1) transformation, and TOC ($_{wt\%}$ and $_{kg/m^3}$) data were transformed using a square root transformation. We performed three PCA runs. First, a PCA of the sediment parameters was implemented to infer differences between Yedoma and thermokarst deposits. Second, a PCA of biomarker proxies was performed. For this purpose, other characteristics were added as supplementary variables ($TOC_{wt\%}$, TOC_{kg/m^3}, C/N, $\delta^{13}C$, grain size, BD, ice content, and depth) without inclusion in the PCA calculation. These supplementary variables have no influence on the PCA and were plotted afterwards in the PCA biplot. Third, a PCA was conducted on samples of the major odd *n*-alkanes to infer possible changes of the source organisms with the same supplementary variables as described above to relate the different biomarker proxies to each

other. Computations were performed using the "vegan" package of R software (Oksanen, 2013).

4.4 Results

Stratigraphically, there are two types of deposition units at the study site. The first unit is composed of Yedoma deposits. The second unit represents thermokarst deposits resulting from thermal degradation of Yedoma. Grain-size distributions (Figure 4-2, Figure appendix IV-1) and PCA of sediments illustrate that thermokarst deposits are made up of degraded Yedoma sediments. After Gubin and Veremeeva (2010) and Zanina et al. (2011) the Yedoma deposits soil types are mainly less-developed cryopedoliths containing more-developed paleocryosol parts (Figure 4-3 and Figure 4-4, labeled and grey-shaded areas).

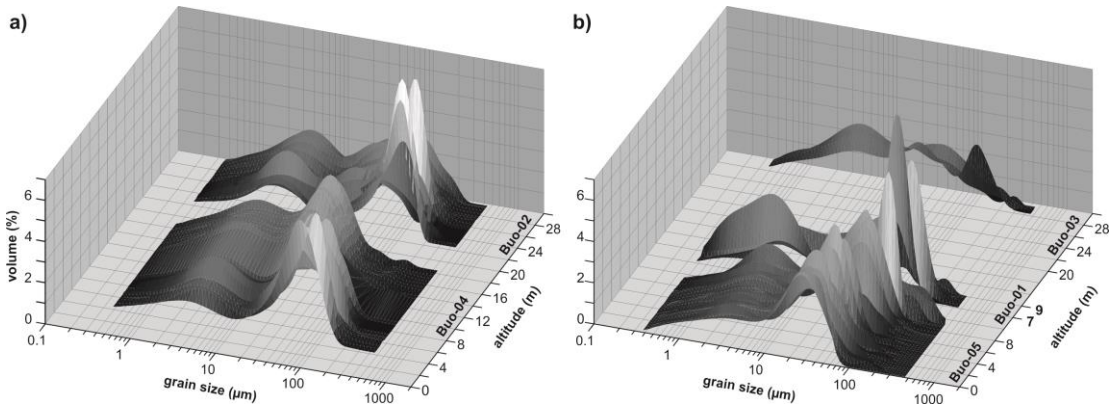

Figure 4-2. Three-dimensional grain-size distributions of a) Yedoma and b) thermokarst profiles. To avoid an overlap of Buo-05 and Buo-01 in b), the altitude axis was adapted and does not ascend consistently. A two-dimensional grain-size plot is shown in Figure appendix IV-1.

4.4.1 Organic matter quality of Yedoma deposits

4.4.1.1 Sedimentological and biogeochemical proxies

The radiocarbon ages (Table 4-1) of the Yedoma deposits range from infinite ages (>55,000 a BP) at the very bottom to 30,100 a BP at the uppermost sampled Yedoma unit. This is comparable to other Yedoma sequences in the region (Schirrmeister et al., 2011c). The mean grain sizes show a decreasing trend in the Buo-04 lower Yedoma profile, from 28 µm at the bottom to 11 µm in the upper part of Buo-04-A. The Buo-02 Yedoma profile shows no trend, but exhibits a more heterogeneous mean-grain size including three maxima at 22.5 m above sea level (a.s.l.) (32 µm), 23.7 m a.s.l. (34 µm), and 25.5 m a.s.l. (33 µm). Nevertheless, all Yedoma deposit samples are classified as poorly-sorted medium-to-coarse silts with a stable low clay fraction (<15 %).

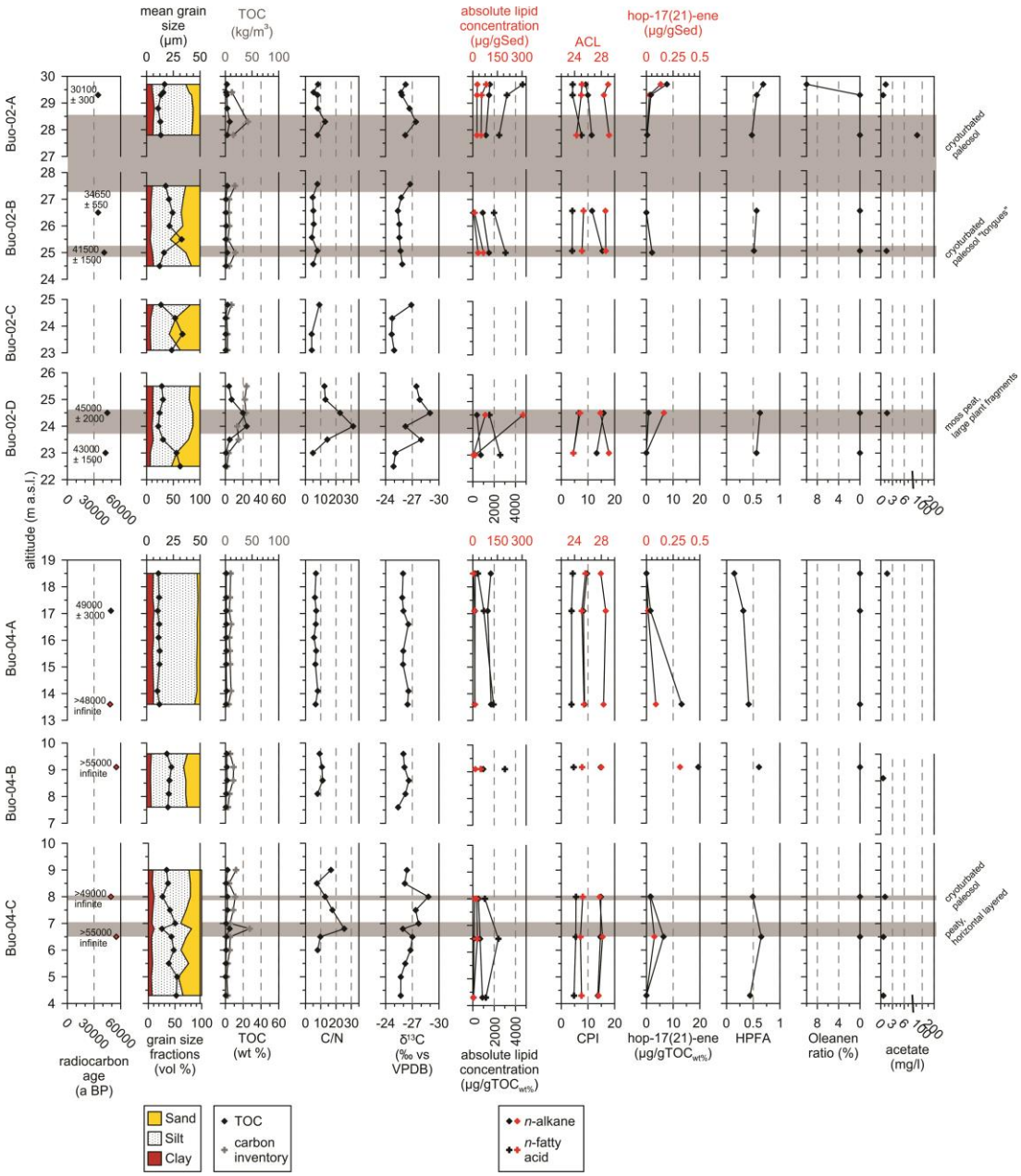

Figure 4-3. Summary of sedimentological, biogeochemical, and biomarker parameters for the Buo-04 and Buo-02 Yedoma profiles. All diagrams are drawn in such a way as to show more degraded samples on the left and less degraded samples on the right side. Thus, the axis of $\delta^{13}C$ values and the Oleanen ratio are descending. In the text, the paleocryosol parts are reported with altitude measurements from the lowest to the highest sample of each paleocryosol. The grey shaded areas are for visualization, not for exact height estimations of the paleocryosols.

The $TOC_{wt\%}$ contents vary from 0.2 wt% at 5 m a.s.l to 24.0 wt% in a peaty paleocryosol horizon at 24 m a.s.l. (Figure 4-3). The mean $TOC_{wt\%}$ content is 2.4 wt% (median 0.97 wt%). Calculating the TOC_{kg/m^3} according to Strauss et al. (2013) by utilizing the BD (between 0.1 and 1.5 10^3kg/m³ (*10^3kg/m³=g/cm³*)) and ice content (without ice wedges; 21 to 90 vol%), the Yedoma sediments contain from 3 to 46 kg C/m³ with a mean of 14 kg C/m³ (median 9 kg C/m³). The maxima corre-

spond to the peaty horizons with large $TOC_{wt\%}$ contents and a low BD. Within the paleocryosol horizons, located at 6.8, 24.0 to 24.5, 24.8, and 27.8 to 28.9 m a.s.l., maxima in the C/N ratio are observable. The C/N range in these horizons is 8 to 31. In the cryopedolith profile parts the C/N maximum is reached at the lowermost Buo-04-C sub-profile (17.7 and 16.7).

The C/N of the rest of the Yedoma profile falls between 4.1 (at Buo-02-C, 23.7 m a.s.l.) and 14.3 (below the paleocryosol at 23.5 m a.s.l.) The $\delta^{13}C$ of the Yedoma deposits ranges between -29.0 and -24.7 ‰. The minima fit well to the maxima of the C/N ratio in the paleocryosol horizons at 6.8, 24.0 to 24.5, 24.8, and 27.8 to 28.9 m a.s.l. The minimum C/N of the Buo-02-C sub-profile corresponds approximately to the $\delta^{13}C$ maximum (-25.0 to -24.7 ‰).

Table 4-1. Radiocarbon AMS dating on plant macro remains. Calibrations were done by using Calib 6.0 software and the IntCal09 calibration curve (Stuiver et al., 2010). Depth is given in meter below surface level (m b.s.l.) and height in meter above sea level (m a.s.l.). Age is given as year before present (a BP). Poz: Poznań Radiocarbon Laboratory, Poland.

Lab. no.	Sample name	Depth (m b.s.l.)	Height (m a.s.l.)	Age (a BP)	±	Calibrated ages 2σ (a BP)	±	
Poz-42080	Buo-03-A-03	1.3	28.7	4760	40	5519	70	thermokarst deposits
Poz-42072	Buo-01-A-02	0.7	8.7	3665	35	3990	100	
Poz-42073	Buo-01-A-04	1.8	7.6	8140	50	9075	78	
Poz-42086	Buo-05-A-04	0.8	8.7	5990	40	6837	103	
Poz-42087	Buo-05-B-10	3.4	6.1	8000	80	8817	215	
Poz-42088	Buo-05-B-19	6.1	3.4	7940	50	8811	122	
Poz-42090	Buo-05-C-23	7.3	2.2	5280	35	6059	74	
Poz-42091	Buo-05-C-29	9.2	0.3	6710	90	7566	138	
Poz-42074	Buo-02-A-03	0.7	29.3	30,100	300	34613	596	Yedoma deposits
Poz-42075	Buo-02-B-09	3.5	26.5	34,650	550	39813	1242	
Poz-42076	Buo-02-B-12	5	25	41,500	1500	45312	2649	
Poz-42077	Buo-02-D-20	5.5	24.5	45,000	2000	47614	2386	
Poz-42078	Buo-02-D-23	7	23	43,000	1500	46,830	2678	
Poz-42081	Buo-04-A-02	1.5	17.1	49,000	3000			
Poz-42082	Buo-04-A-08	5	13.6	>48,000				
Poz-42083	Buo-04-B-10	8.5	9.1	>55,000				
Poz-42084	Buo-04-C-16	10.5	8	>49,000				
Poz-42085	Buo-04-C-20	11.7	6.8	>55,000				

4.4.1.2 Biomarker proxies/indices

Every radiocarbon-dated sample and additional samples were used for biomarker analysis. In total 25 biomarker samples were analyzed. A series of long-chain *n*-alkanes that exhibit a strong odd-carbon preference ranging from *n*-C_{21} to *n*-C_{33} are recognized in all Yedoma samples (Figure appendix IV-2). Moreover, the *n*-alkanes show a unimodal distribution maximizing at the C_{27}, C_{29}, or C_{31} *n*-alkane (Figure appendix IV-2). The *n*-fatty acids show strong even-over-odd carbon number predominance and a bimodal distribution ranging from C_{14} to C_{30} (Figure appendix IV-3). The maxima are generally located at *n*-C_{16} in the lower carbon number range and at *n*-C_{24} in the higher carbon number range. Total *n*-alkanes and *n*-fatty acids concentrations related to $TOC_{wt\%}$ and sediment weight show a homogeneous pattern similar to that of the $TOC_{wt\%}$ and C/N values. The *n*-alkane concentration ranges from 3 to 75 µg/gSed (mean 20 µg/gSed) and from 387 to 1715 µg/$TOC_{wt\%}$ (mean 1132 µg/$TOC_{wt\%}$). The *n*-fatty acids range from 4 to 306 µg/gSed (mean 51 µg/gSed) and from 475 to 4669 µg/TOC (mean 2196 µg/$TOC_{wt\%}$).

This Yedoma series shows distinct preference between even and odd carbon. The mean CPI values of the *n*-alkanes (12.2, ranging between 8.3 and 15.9) are higher than the CPI values of the *n*-fatty acids (4.9, ranging between 3.8 and 7.6). Because *n*-fatty acids are functional compounds (including a functional group, e.g. a carboxyl group), their degradation rates are much higher compared to those of *n*-alkanes (Poynter and Eglinton, 1990). This statement is also based on the assumption of similar sources. The ACL of the *n*-alkanes and *n*-fatty acids is very stable at around 28.4 (range 27.6 to 29.2) and 25.0 (range 23.8 to 25.6), respectively.

Higher hop-17(21)-ene concentrations are used as an indicator for lower organic matter degradation state. In the lower Yedoma profile the hop-17(21)-ene ranges from 0.0 µg/gTOC at the lowermost and uppermost samples (4.3 and 18.5 m a.s.l.) to the overall maximum at the Buor Khaya site (19.4 µg/gTOC) at 9.1 m a.s.l. At Buo-02, the hop-17(21)-ene concentration is lower compared to the other Yedoma profile with a mean of 1.9 µg/$gTOC_{wt\%}$ and a maximum of 7.7 µg/$gTOC_{wt\%}$ in the potentially Holocene-contaminated uppermost sample. The HPFA ratio for the Yedoma samples is very stable around the mean value of 0.50 (median 0.54) with a minimum at 18.5 m a.s.l. (0.15) and a maximum at the uppermost sample (0.69) at 29.7 m a.s.l. For Yedoma, the Oleanen ratio is 0.0 (except a ratio of 10.0 at the uppermost sample). The acetate content of the Yedoma sample is between 0.6 and 57.5 mg/l with a mean of 6.7 mg/l (median 1.2 mg/l).

4.4.2 Organic matter quality of thermokarst deposits

4.4.2.1 Sedimentological and biogeochemical proxies

The radiocarbon dating shows Holocene ages between 8140 and 3665 a BP (Figure 4-4). The lowermost Buo-05-C profile shows an age inversion for the two samples, Buo-05-C-29 at 0.3 and Buo-05-C23 at 2.2 m a.s.l. The mean grain size at Buo-05 from the bottom to 6.7 m a.s.l. is 13 µm. Above, the mean grain size increases to 19 µm. The Buo-05 clay fraction is stable at a low level (<15 %). The Buo-01 profile shows a very scattered grain size ranging from 4 to 44 µm mean grain size. For the whole dataset, there is a maximum in the clay fraction (35 %) in the peat horizon at 8.7 m a.s.l. Buo-03 shows a slight decrease from 18 to 11 µm. All thermokarst deposits are classified as (very) poorly-sorted silts. Similar to the Yedoma deposits, the BD of the thermokarst deposits is between 0.1 and 1.5 10^3kg/m³ and the ice content (without the ice wedges) is 23 to 87 wt%.

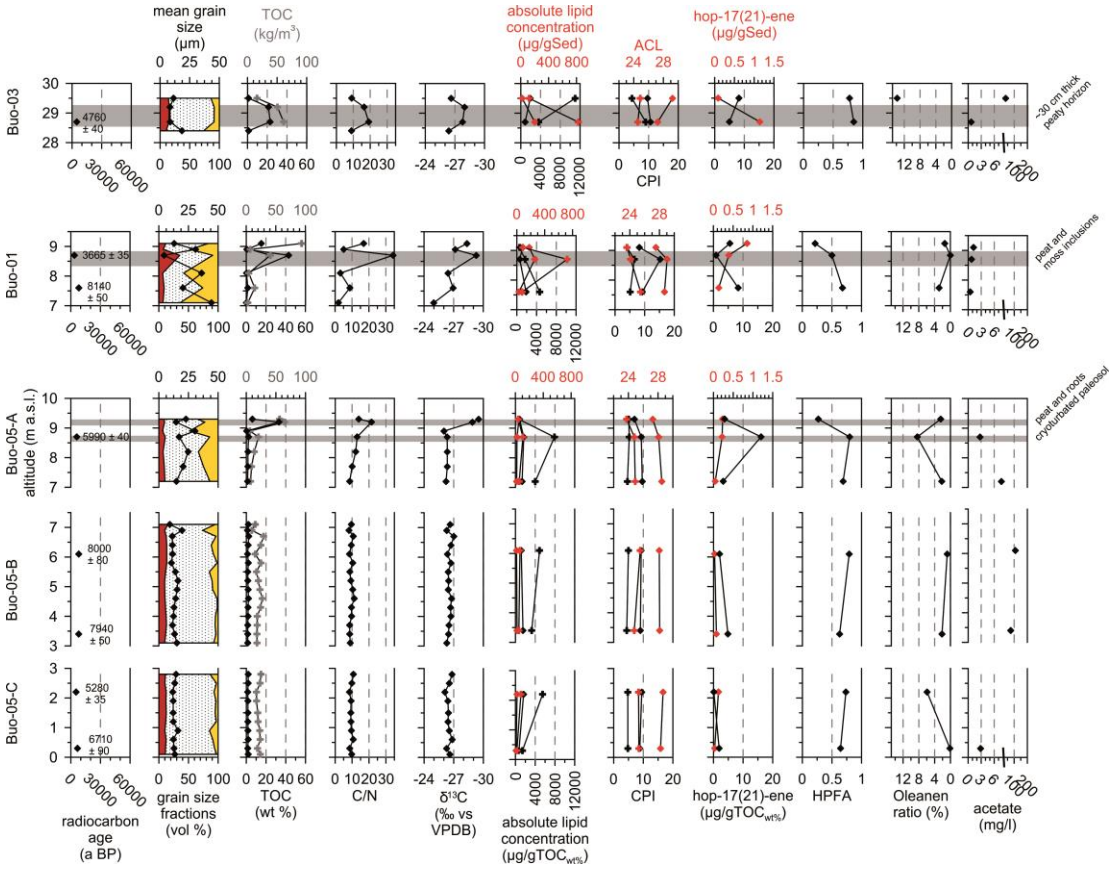

Figure 4-4. Summary of sedimentological, biogeochemical, and biomarker parameters for the Buo-05, Buo-01, and Buo-03 thermokarst profiles. The grain-size colors and the *n*-alkane and *n*-fatty acid symbols are explained in Figure 4-3. All diagrams are drawn in such a way as to show more degraded samples on the left and less degraded samples on the right side (descending axis of $\delta^{13}C$ values and Oleanen ratio). In the text, the paleocryosol parts are reported with altitude measurements from the lowest to the highest sample of each paleocryosol. The grey shaded areas are for visualization, not for exact height estimations of the paleocryosols.

The mean $TOC_{wt\%}$ contents of the thermokarst deposits, 4.7 wt% (median 1.7 wt%), are higher compared to Yedoma deposits, varying between 0.2 wt% (Buo-01-A-05) and 43.0 wt% (Buo-01-A-02). Minimum and maximum $TOC_{wt\%}$ both occur at Buo-01 and exhibit the same scatter as in the grain sizes. TOC_{kg/m^3} ranges between 2.8 and 93.5 kg C/m³ (mean 24 kg C/m³, median 19 kg C/m³).

At Buo-05 the C/N ratio is stable around 9 to 10, except for a paleocryosol horizon at 9.2 m a.s.l. that shows a value of 22. At Buo-01, the C/N ratio below the paleocryosol horizon is remarkably low, between 2 and 9, followed by the overall maximum in the peaty horizon with a ratio of 34 (Buo-01-A-02). The Buo-03 cryopedolith samples show C/N ratios around 10, while the paleocryosol samples exhibit C/N ratios from 16 to 19. The $\delta^{13}C$ values range between -29.5 and -25.0 ‰, with minima corresponding to the C/N maxima at the paleocryosol horizons (anti-correlated to the C/N, Figure 4-5a).

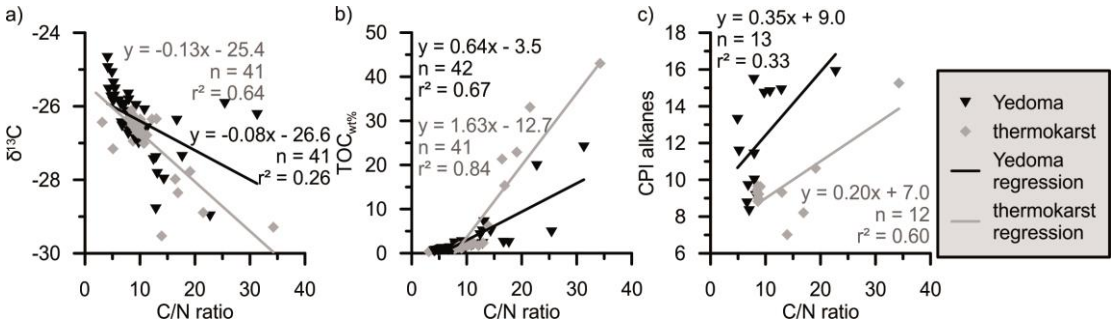

Figure 4-5. Scatter plots of selected degradation markers. Yedoma deposits are shown as black triangles, thermokarst deposits as grey diamonds. Regression equations, the r², and the sample number (n) are inserted as texts.

4.4.2.2 Biomarker proxies/indices

The absolute lipid concentration of *n*-alkanes are in the same range but slightly higher compared to the Yedoma profiles. The *n*-alkane average is 1275.7 µg/$gTOC_{wt\%}$ (median 1260.1 µg/$gTOC_{wt\%}$), ranging from 599.7 (Buo-01-A-02, 8.7 m a.s.l.) to 1907.2 µg/$gTOC_{wt\%}$ (Buo-03-A-01, 29.5 m a.s.l.). The *n*-fatty acids average is nearly double that found in the Yedoma samples. On average, 4096.1 µg/$gTOC_{wt\%}$ (median 3805.7 µg/$gTOC_{wt\%}$) are stored in the thermokarst deposits of Buor Khaya, ranging from 554.5 (uppermost Buo-01 sample) to 11013.3 (uppermost Buo-03 sample) µg/$gTOC_{wt\%}$.

A series of long-chain *n*-alkanes were recognized in all thermokarst samples with a strong odd carbon number preference ranging from *n*-C_{21} to *n*-C_{33}. Nearly all samples show a unimodal distribution of *n*-alkanes maximized at C_{27}, C_{29}, or C_{31} (Figure appendix IV-2). Sample Buo-03-A-03 alone does not fit into this scheme because it maximizes at *n*-C_{25}. Compared to Yedoma samples, the short-chain fraction < *n*-C_{27}

is more pronounced (Figure appendix IV-2). The *n*-fatty acids show strong even-carbon-number preference and a bimodal distribution between *n*-C_{14} and *n*-C_{30} (Figure appendix IV-3), but the *n*-C_{16} is less pronounced than in the Yedoma deposits. An exception to this is found in sample Buo-01-A-02, where the C_{16} monomer reaches the overall maximum of the distribution. Apart from that, the maxima are generally located at the C_{24} *n*-fatty acid.

The *n*-alkane CPI of thermokarst averages 9.6 (median 9.3) and is lower compared to the Yedoma deposits, although the CPI values are in the same range (between 7.0 and 15.3). The CPI of the fatty acids ranges from 4.0 to 9.0 (mean 5.3, median 4.9). The ACL of *n*-alkanes and fatty acids reveal a homogeneous signal between 27.2 and 29.2 (mean 28.3) for *n*-alkanes and 23.6 to 25.6 (mean 24.8) for *n*-fatty acids.

Except for the maximum value of 16.1 µg/gTOC$_{wt\%}$ at 8.7 m a.s.l., the hop-17(21)-ene concentration at Buo-05 is quite stable, between 0.1 and 4.9 µg/gTOC$_{wt\%}$. Buo-01 paleocryosol values are 0.9 (8.7 m a.s.l.) and 8.4 at the lowermost sample (7.8 m a.s.l.). For Buo-03 the hop-17(21)-ene concentration ranges from 5 µg/gTOC$_{wt\%}$ up to 8 µg/gTOC$_{wt\%}$.

The HPFA ratio for the Buo-05 thermokarst samples is high, between 0.6 and 0.8; only the uppermost sample (9.3 m a.s.l.) shows a significantly lower value of 0.2. The Buo-01 profile decreases from 0.7 at the lowest sample to 0.2 at the top. Buo-03 shows high parameter values of 0.8 and 0.9. The Oleanen ratio for the thermokarst deposits ranges between 0 (Buo-01) and 13.8 (Buo-03). The overall mean Oleanen ratio in thermokarst is 3.7 (median 2.2), which is remarkably higher compared to the Yedoma deposits.

The acetate content of the thermokarst samples is between 0.4 and 109.4 mg/l with a mean of 23.5 mg/l (median 2.8 mg/l). Large acetate contents are found especially in the middle part of Buo-05, from 3.4 m a.s.l. (74.1 mg/l) to 6.1 m a.s.l. (109.4 mg/l), and in the uppermost Buo-03 sample (35.3 mg/l).

4.4.2.3 Principal component analyses

The first PCA diagram (Figure 4-6a) shows that thermokarst sediments, especially at Buo-05, could not be separated from Yedoma deposits. This diagram, including the first two principal components, explains 79 % (pc1 57 %, pc2 22 %) of the total data set variance. The second PCA diagram (Figure 4-6b) illustrates that biomarker quality estimators in Yedoma samples have slightly lower variability because they cluster in an area at pc1 and pc2>0, while the thermokarst samples do not cluster. In this diagram 53 % of the data set variance is explained. Moreover, this PCA shows that there is good consistency between the CPI_{alkane} quality estimator and the C/N ratio

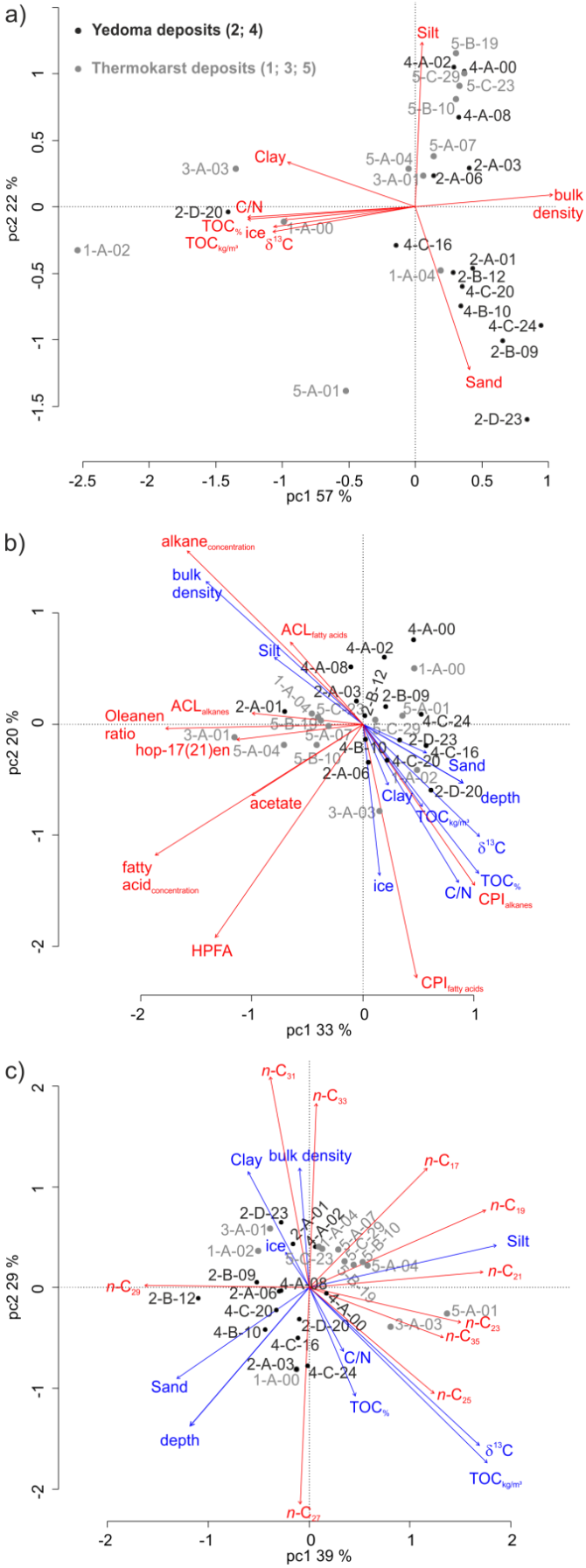

Figure 4-6. Ordination plots of the principal component analyses. In diagram a) the sedimentological parameters are plotted. In b) a PCA of biomarker proxies is shown. Supplementary variables (in blue: $TOC_{wt\%}$, C/N, $\delta^{13}C$, grain size, BD, ice content) were added without including them in the PCA calculation. In diagram c) the PCA of the major odd *n*-alkanes is visualized using the same supplementary variables as in b).

(Figure 4-6b). The PCA of the *n*-alkane chain length (Figure 4-6c) shows that the best separating variables for thermokarst are the shorter-chain *n*-alkanes (C_{17}, C_{19}, and C_{21}), contrary to C_{29} for the majority of the Yedoma samples. The pc1 explains 39 % and pc2 explains 29 % (total 68 %) of the data set variance.

4.5 Discussion

The Buor Khaya Peninsula is a typical Yedoma hill - thermokarst basin Yedoma region landscape (Strauss et al., 2013). The Yedoma deposits cover ~15 % of the peninsula (Günther et al., 2013), which is less than the Yedoma region mean of 30 %, but inside the overall range of Yedoma deposit coverage (Grosse et al., 2013b; Strauss et al., 2013). Thus, the current study of Yedoma and thermokarst deposits is representative for an area covered by similar permafrost deposits of late Pleistocene and Holocene age.

4.5.1 Sediment facies

The grain-size distribution curves (Figure 4-2, Figure appendix IV-1) indicate a constant deposition environment for the Yedoma sequences. According to Strauss et al. (2012), there have been stable deposition conditions during Yedoma accumulation; this hypothesis is supported by the data presented here. The three thermokarst profiles include three different kinds of thermokarst deposits. Buo-05 is dominated by a lake facies containing valves of two freshwater ostracod taxa: *Cytherissa lacustris* and *Cypria* sp. Moreover, shells have been found in Buo-05 (Strauss and Schirrmeister, 2011). An ice wedge is located next to Buo-01, which points to subaerial conditions like a polygon mire. Buo-03 is interpreted as initial thermokarst on top of a Yedoma hill. Thus, the grain-size distributions of Buo-05 and Buo-01 reveal that the thermokarst is granulometrically composed of the same material as Yedoma. The grain size distributions in Buo-03 paint a different picture. This distribution is likely caused by the early state of thermokarst development dominated by peat aggradation. This peat can act like a selective sediment trap influencing the grain-size distributions, e.g. by producing a less distinct coarse silt-fine sand peak.

4.5.2 Organic matter degradation

The organic matter proxies of Yedoma deposits are less variable than those of thermokarst deposits (Buo-01 and 03). Except for the paleocryosols, the cryopedolith parts of the Yedoma and the Buo-05 thermokarst profile reveal a rather homogenous picture (Figure 4-3, Figure 4-4). Constant grain-size distributions, less $TOC_{wt\%}$, and smaller absolute lipid concentration scattering reveal that the OC stored in the Yedoma deposits has likely been kept perennially frozen since incorporation. The organic matter signatures (Figure 4-4, Figure appendix IV-2, Figure appendix IV-3)

as well as the grain-size distributions (Figure 4-2, Figure appendix IV-1) of thermokarst deposits, especially in Buo-01 and Buo-03, show broader variations. This is caused by a more complex degradation and re-deposition history due to reworking. The degradation markers of organic matter found in the paleocryosol parts of all profiles reveal a less-degraded state, indicating that the organic matter in these portions is the best preserved.

The mean $TOC_{wt\%}$ content for Yedoma deposits is comparable to other sites (Figure appendix IV-5) in the Yedoma region (Schirrmeister et al., 2011c; Schirrmeister et al., 2013). Intense accumulation and frozen preservation of plant remains (14 kgC/m³ for Yedoma and 24 kgC/m³ for thermokarst deposits) is caused by syngenetic permafrost formation in polygonal tundra landscapes over long periods in the Quaternary (Schirrmeister et al., 2013). But comparing the studied deposits to the overall Yedoma region mean (19 kgC/m³ for Yedoma deposits and 33 kgC/m³ (disregarding wedge-ice content) for thermokarst deposits, Strauss et al., 2013) on Buor Khaya Peninsula reveals that both deposit types contain less OC. Nevertheless, these numbers show that these deposits comprise a large pool of dormant carbon, which could be reactivated due to permafrost thawing. Moreover, thermokarst deposits seem to be the quantitatively more important OC pool (Yedoma:thermokarst carbon ratio ~2:3). The higher carbon inventory in thermokarst deposits is partially related to a concentration effect for reworked Yedoma OC due to thaw subsidence progression including ground ice loss plus input of Holocene OC. Together with ecosystem recovery, thermokarst basins can act as a local sink for portions of the carbon released from thawing permafrost deposits (van Huissteden and Dolman, 2012). Nevertheless, at the same time thermokarst lakes also promote intense organic matter degradation including methane production in the anaerobic environments of organic-rich lake sediments and unfrozen deposits (Walter et al., 2007b). Strauss et al. (2013) found that thermokarst deposits contain the quantitatively more important carbon pool, but the unsolved question is this: Is the thermokarst organic matter pool as degradable as the frozen Pleistocene Yedoma, or has the most labile carbon already been emitted due to thermokarst degradation processes? To answer this question, we visualized the stratigraphically differentiated main proxies in Figure 4-7.

In our study the C/N does not reveal a clear picture. The average values are relatively close together for all profiles (Figure 4-7b). Nevertheless, the medians and means hint at a lower degradation state/better organic matter quality of thermokarst deposits (especially Buo-05 and Buo-03). Moreover, in both Yedoma and thermokarst deposits the same pattern is visible: A positive linear relationship exists between $TOC_{wt\%}$ and C/N ratios (Figure 4-5b). In soil science literature it is agreed that the elemental

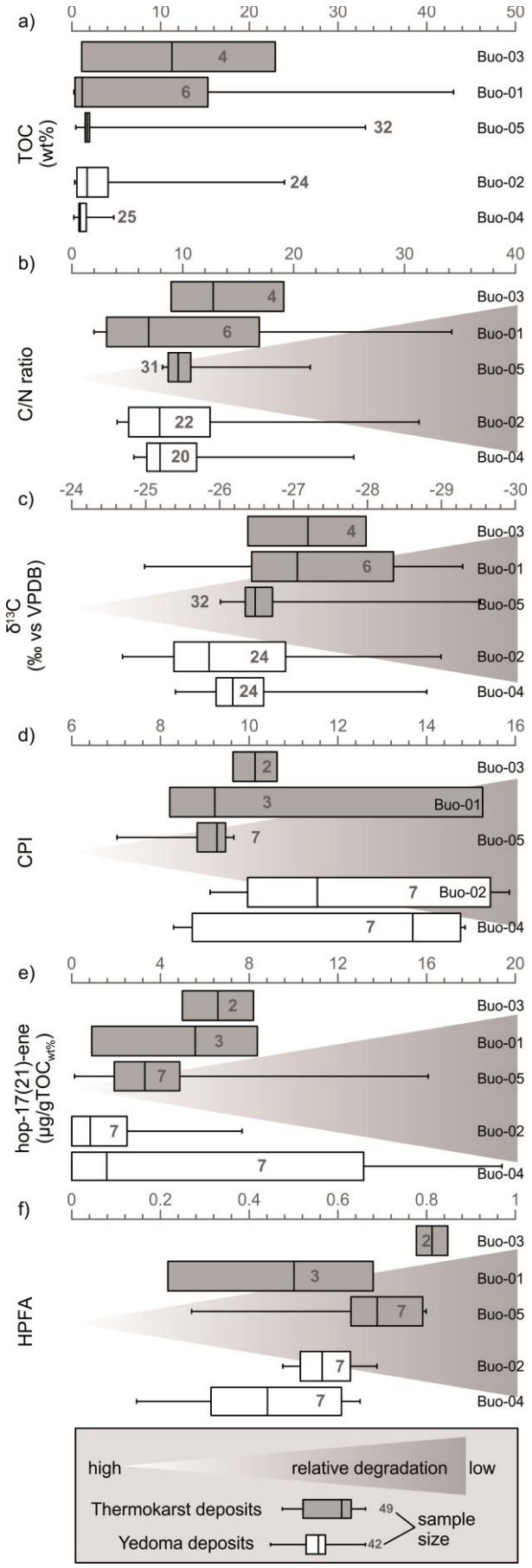

Figure 4-7. Conceptual scheme of the organic matter degradation state, estimated using the different applied proxies with boxplots for each studied profile. The boxplots show the studied profiles separately, with Yedoma deposits (white boxes) shown below the thermokarst deposits (grey boxes). The whiskers illustrate the data range, and the box ends indicate the 25th and the 75th quartile (interquartile range). The vertical lines inside each box show the median (=50th quartile). All diagrams are drawn in such a way as to show more degraded samples on the left and less degraded samples on the right side. Thus, the axis of $\delta^{13}C$ values is descending.

composition of organic matter is affected by the degree of humification and microbial activities that metabolize the organic matter (Kumada, 1987). Ongoing organic matter decomposition will release stored C to the atmosphere and N to the soil (Weintraub and Schimel, 2005), resulting in a lower C/N ratio for more-degraded deposits (Gundelwein et al., 2007). This was found in (sub-) arctic peat deposits and soils, where the C/N ratio decreases with depth (Kuhry and Vitt, 1996; McKane et al., 1997; Ping et al., 1998). Because a high TN content can promote stabilization of organic matter at late stages of decomposition (Berg, 2000), this further supports the interpretation that a low C/N ratio indicates recalcitrant/matured organic matter (Rumpel and Kögel-Knabner, 2011).

Schädel et al. (2014) found, with incubation studies, that the C/N ratio is a good estimator for organic matter decomposability/vulnerability. Although the C/N ratios are lower than in arctic peat deposits (Hugelius et al., 2012; Routh et al., 2014), the ratios are still in the range of or higher than those found in many other deep mineral soils of the temperate zone (Jenkinson et al., 2008; Rumpel and Kögel-Knabner, 2011). Thus, both Yedoma and thermokarst deposits show relatively good organic matter quality. The C/N ratios, especially for the paleocryosols, suggest that good quality organic matter was preserved (by sub- or near 0°C temperatures during thermokarst processes) for future decomposition. This is shown by the $\delta^{13}C$ ratio as well. Neglecting the influence of different sources of organic matter on the $\delta^{13}C$ ratio, which is justified by constant ACL values of >28 (higher land plants, Figure appendix IV-4) for Yedoma and thermokarst deposits, the $\delta^{13}C$ ratio seems to be an appropriate proxy to use to estimate the relative state of degradation. Therefore, the $\delta^{13}C$ would indicate somewhat lower organic matter degradation for the thermokarst samples, implying a better quality than that found in Yedoma samples. The slightly (but still clearly overlapping interquartile range) higher CPI values of the Yedoma deposit organic matter reveal a better quality (Figure 4-7d) than in the thermokarst deposits. We interpret this as a weak signal of the thawing and refreezing history of the old OC incorporated into the frozen thermokarst deposits.

Routh et al. (2014) states that other, more labile compounds like *n*-alcohols and *n*-fatty acids are degraded to *n*-alkanes. Thus, an increase of *n*-alkanes (Figure 4-3and Figure 4-4, absolute lipid concentration column) is an indicator for cumulative decay. We do not see a decreasing trend, which points to a constant low decomposition state. In addition, no increasing *n*-fatty acid CPI with depth (as was shown in an arctic peat by Andersson and Meyers, 2012) was obvious. (Andersson and Meyers, 2012) interpreted this to reflect fatty acid production during humification, but we do not see this humification effect in our data, either in Yedoma, or in the thermokarst

deposits. Moreover, as indicated by the dominance of long-chain *n*-alkane and *n*-fatty-acid compounds vs. compounds of shorter chain length (Höfle et al., 2013), we confirm the interpretation of good organic matter quality in both Yedoma and thermokarst deposits. At first view, the hop-17(21)-ene (Figure 4-7e) concentration does not show a distinct quality difference between both kinds of deposits, because the Buo-04 Yedoma profile contains hopene concentrations in the same range as those found in thermokarst deposits. However, if we focus on the median values, the Yedoma deposits again appear to be slightly more strongly degraded than the thermokarst deposits. With the exception of Buo-01, the HPFA index (Figure 4-7f) also suggests slightly lower degradation and better organic matter quality in the thermokarst deposit profiles (Buo-05 and Buo-03). Our HPFA index, introduced based on Poynter's (1989) HPA index which was tested in the Arctic environment by Routh et al. (2014), is an appropriate indicator of the relative amount of the labile fatty acids that remain in a sample. The uppermost samples just below the surface at Buo-04, Buo-05, and Buo-01 with lower HPFA values are clearly an exception and suggest the entrainment of higher proportions of material influenced by Holocene degradation. This is likely caused by the fairly recent influence of an active layer or transient layer and warmer permafrost temperatures. The Oleanen ratio shows a separation of Yedoma and thermokarst deposits, but this ratio is dominated by numerous 0.0 measurements in the Yedoma deposits. These results might be caused not only by transformation of β-amyrin to Olean-12-ene (by losing the hydroxyl group) or to Olean-13(18)-ene (by losing the double bond), but also by unknown processes in the Yedoma deposits. Thus, because of sparse data, we interpret this proxy as potentially hinting at slightly better Yedoma organic matter quality.

Summing up Figure 4-7, thermokarst organic matter is partly less degraded and of better quality compared to the organic matter sequestered in Yedoma deposits (as revealed by measurements of C/N, $\delta^{13}C$, hop-17(21)-ene, and the HPFA index). The CPI points in the other direction and describes the Yedoma organic matter as better preserved (Figure 4-7). As the interquartile ranges show an overlap for most proxies, we see no significant differences (although better thermokarst organic matter quality is indicated).

The PCA confirms the picture of little difference between the organic matter quality of the Yedoma and the thermokarst samples. Especially Figure 4-6a, supported by Figure 4-2, reveals that Yedoma and thermokarst are composed of similar sediments. The Buo-05 thermokarst profile is very similar to both Yedoma profiles. The PCA of the degradation proxies (Figure 4-6b) also shows no clusters, but exhibits slightly better separation between both kinds of deposits. Figure 4-6b reveals that the C/N

ratio, the $\delta^{13}C$ ratio, and the CPI are correlated. This is also separately illustrated in Figure 4-5a and c. Thus, these proxies seem to confirm each other. The PCA of the *n*-alkane chain length points to a potential dominance of longer chain alkanes in Yedoma and shorter chain alkanes in thermokarst, indicating better quality of Yedoma samples (Höfle et al., 2013). Exceptions are the Buo-05-A-01 and Buo-03-A-03 thermokarst samples which point in the same direction as the n-C_{35} concentration.

The abovementioned overlap of the interquartile range (Figure 4-7) and especially the PCA of the biomarkers (Figure 4-6b and c) show that the organic matter degradation/decomposition vulnerability is heterogeneous and depends (assuming a constant botanical origin) on different decomposition trajectories and differing former decomposition/incorporation histories. This is likely shown in both Yedoma and thermokarst deposits, covering the whole range of degradation proxy values (Figure 4-7b, c, e). To elucidate this was one of the benefits of the applied multiproxy approach. With the addition of biomarker data, it is possible to show that the permafrost organic matter degradation is not a linear function of age or sediment facies, but likely a combination of (interrupted) degradation cycles and a cascade of degradation steps. In particular, the reasonably good organic matter quality of thermokarst deposits reveals that the sediment degradation processes do not necessarily degrade the organic matter. Potentially, the loss of labile OC during thermokarst processes was compensated for by high rates of Holocene OC accumulation in e.g. lake sediments. Nutrient release from thawing permafrost could have stimulated lake productivity, whereas decomposition was slow because of low lake temperatures, resulting in cold anoxic lake environments (Boike et al., 2013; Walter Anthony et al., 2014). When the lake drained, permafrost formation rapidly recovered the sediments (Jones et al., 2011) including any possibly newly-accumulated OC.

4.5.3 Fate of organic matter

The permafrost OC resilience or vulnerability is a topic of recent research (Schuur and Abbott, 2011; Knoblauch et al., 2013; Hodgkins et al., 2014; Li et al., 2014; Mu et al., 2014). Any warming permafrost is potentially vulnerable to thawing. The remaining important question is this: What is the fate of the organic matter exposed to degradation after permafrost has thawed? The occurrence of >1 mg/l acetate, which is an ideal substrate for microorganisms (Smith and Mah, 1980; Kuesel and Drake, 1995; Vieth et al., 2008), indicates that the organic matter in the sediments was, after initial degradation processes, relatively quickly protected against microbial alteration by freezing. This is confirmed by an absent degradation - depth trend which reveals good organic matter quality independent of age. Thus, the very old frozen organic

matter is also vulnerable to degradation after thawing. This interpretation fits results from studies of permafrost-affected Arctic peats (Hugelius et al., 2012; Routh et al., 2014). Walter Anthony et al. (2014) found a net accumulation in thermokarst basins since the last deglaciation, but predict a change to a large carbon source when permafrost thaws and the OC will be available for oxidation. Due to ongoing climate warming in the Arctic, Grosse et al. (2011b) suppose an increasing occurrence and magnitude of disturbance processes, especially fire and thermokarst, which will accelerate permafrost degradation. Because our sedimentological and biomarker proxies show a low degradation state, especially for the paleocryosol sequences, we expect a significant vulnerability to microbial degradation after thawing. As evidence that the OC is vulnerable when thawed, Gaglioti et al. (2014) found that ~10 times more ancient OC found in permafrost was made available for degradation during warm times of the Holocene (Holocene Thermal Maximum (11.7-9.0 ka) and Bølling-Allerød periods) than is available today. By increased disturbances like deep surface subsidence caused by thawing and the draining of excess water from melting ice in a warmer climate, the Yedoma and, to a lesser degree because of lower excess ice content, the thermokarst organic matter could become deeply bioavailable. The wedge-ice volume is estimated at up to ~60 vol% for Yedoma and up to ~10 vol% for thermokarst deposits (Ulrich et al., 2014). When added to segregated ice, ~80 vol% and ~65 vol% mean sedimentary ice volume exists in Yedoma and thermokarst, respectively (Strauss et al., 2013). When it becomes available and is exported as dissolved OC to e.g. river systems, Vonk et al. (2013a) and Mann et al. (2014) found that dissolved OC in ancient Yedoma is exceptionally biolabile. But if it is not dissolved, the eroded ancient organic matter could be protected from extensive degradation by organo-mineral bonds, which stabilize the organic matter (Höfle et al., 2013) and, in an aquatic environment, promote rapid settling because they weigh down the organic matter (Vonk et al., 2010).

From the modeling perspective, global-scale models are limited so far because they implement one-dimensional vertical thaw only (Koven et al., 2011; Schneider von Deimling et al., 2012; Schaphoff et al., 2013). Thus, the potentially labile Yedoma and thermokarst deep OC pool described in this study is not realistically implemented in these models, because the models disregard rapid phenomena like thermokarst processes. Thermokarst processes, despite being local in nature, can be widespread on the regional scale (Grosse et al., 2011a) and may constitute the crucial process making the deep OC studied here microbiologically available.

4.6 Conclusions

As being freeze-locked, the great amount of organic matter in the studied sediments is highly decomposable. Generally, in all applied proxies there is no obviously clear degradation - depth trend, revealing that permafrost acts like a freezer, preserving the organic matter at constant quality. Based on interpreting the mean values of the C/N ratio, isotope ratio ($\delta^{13}C$), hop-17(21)-ene concentration, and the HPFA index, the thermokarst organic matter is less degraded and of better quality compared to the organic matter sequestered in Yedoma deposits. The CPI points in the other direction, describing the Yedoma organic matter as being better preserved. We do not see any conflict between these two determinations, because the interquartile ranges overlap for most proxies. We interpret this to indicate similar quality in both kind of deposits, with perhaps slightly better thermokarst organic matter quality.

Thus, the fate of mobilized Yedoma deposit OC depends largely on the environmental conditions that exist during the thermokarst processes and in the resulting thermokarst basin. When the conditions are good for organic matter preservation, for example cold (slightly above 0°C) or anoxic (lake) conditions, and reworked fossil organic matter can rapidly refreeze to permafrost, good-quality organic matter can be maintained and inputs could compensate for losses due to degradation.

In conclusion, we found that a combination of classical sedimentological proxies and biomarker ratios is useful for getting closer to an understanding of the complex history of organic matter delivery and degradation in permafrost, as well as the future fate of organic matter when it is exposed due to active layer deepening and further thermokarst development.

Acknowledgements

We acknowledge support of this research by the German Ministry of Science and Education (the “System Laptev Sea” and "CarboPerm" projects). We also thank the Russian and German partners who were involved in the "Eastern Laptev Sea - Buor Khaya Peninsula 2010" expedition. J.S. was supported by a grant by the Studienstiftung des deutschen Volkes (German National Academic Foundation).

5 Synthesis

The major aim of this thesis was to significantly improve the understanding concerning the question of the Yedoma region's origin, including its organic carbon (OC) pool size and quality. In recent years, the permafrost and Yedoma region carbon pool was frequently called 'Pandora's freezer' (Brown, 2013), 'sleeping giant' (Mascarelli, 2009), or 'permafrost carbon bomb' (Treat and Frolking, 2013). These characterizations of this region are indeed correct, although the sparse number of studies and hence the sparse data base prevent a full understanding. This thesis assesses the permafrost carbon stock using a multiproxy and interdisciplinary approach (Figure 1-7) and provides substantial progress towards a better understanding of the permafrost carbon pool size and quality. The approach was based on local field observations and studies, combined with laboratory analyses for assessing the carbon quantity and quality (Strauss et al., 2012; 2013; Hugelius et al., 2014; 2014; Schneider von Deimling et al., 2014). To broaden the scale to the Yedoma region and the circum-Arctic, statistical calculations were applied and a new data base was developed (Hugelius et al., 2013a; Hugelius et al., 2014). Using a modeling approach (Schneider von Deimling et al., 2014), the response of the permafrost carbon pool, including its deep carbon, to climate warming was estimated. In the following, the research questions defined in section 0 and Figure 1-6 are answered.

5.1 Yedoma origin: How did Yedoma deposits accumulate?

The overarching similarities of Yedoma deposits in different regions are fine-grained sediments, large syngenetic ice wedges, unique frozen deposit cryostructures, and late Pleistocene mammoth mega-fauna and tundra-steppe flora fossils. To explain these characteristics there are different viewpoints concerning the genesis of the Yedoma deposits in Beringia (the former interconnected and unglaciated landmass stretching from the Taymyr Peninsula to Alaska), as briefly introduced in Table 1-1. There is still no overall accepted concept of Yedoma genesis, but it seems clear that neither glacial-related sedimentation (postulated by Nagaoka et al., 1995 and Grosswald, 1998), nor shallow-marine sedimentation (postulated by Bolshiyanov et al., 2009) were involved. The greatest differences of interpretation exist between researchers working in former western (Siberia) and eastern (Alaska) Beringia (Schirrmeister et al., 2011c). These differences center on the relevance of aeolian processes during Yedoma formation. Researchers working in the Yukon area and Alaska often characterize Yedoma silts as loess (Schirrmeister et al., 2013). In contrast, researchers working in Siberia have proposed several hypotheses about the sedimentation regime of Yedoma (Table 1-1). In general, the aeolian and the polyge-

netic hypothesis are the most popular ones in the recent scientific literature (Schirrmeister et al., 2013).

In this thesis, Yedoma deposits are described as ice-saturated or supersaturated, composed of syngenetic ice wedges representing a mean of 48 vol% (Strauss et al., 2013, range from 31 to 63 vol%, Ulrich et al., 2014) and segregation ice representing ~30 to 40 vol% of the frozen material (total deposit volume including wedge-ice volume (Strauss et al., 2013)). Thus, Yedoma deposits are composed of ~80 vol% ice (Kanevskiy et al., 2011; Strauss et al., 2013), making ice their major component. This point is not in agreement with primary loess characteristics, where coarse silt/fine sand is the dominating component of the deposit. Another point against classifying Yedoma deposits as loess is poorly sorted bi- to multi-modal grain-size distributions (Strauss et al., 2012; Schirrmeister et al., 2013). This indicates for a variety of (re-)transport processes and likely seasonal differentiation. Following the case study on the Duvanny Yar Yedoma stratotype (Chapter 2, Strauss et al., 2012) based on poorly-sorted sediments lacking in carbonates, and the absence of glaciers and ice sheets with their grinding processes (Seppälä, 2004) in northeast Siberian lowlands (Velichko et al., 1997; Hubberten et al., 2004; Svendsen et al., 2004), Yedoma deposits genesis is interpreted to be of polygenetic origin. Water-related (like floodplain overbank deposition or alluvial runoff) and aeolian deposition were the major processes (Figure 5-1).

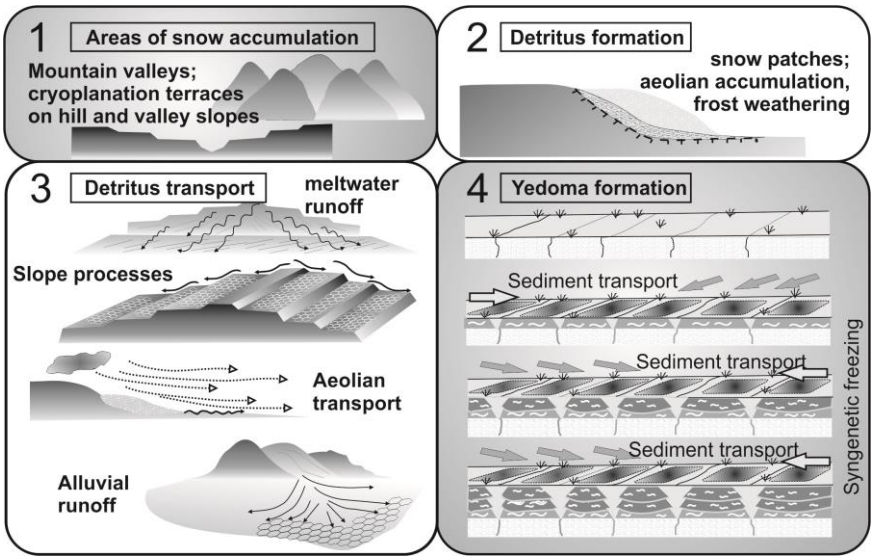

Figure 5-1. Stages (1 to 4) of Yedoma genesis based on a polygenetic concept; modified after Schirrmeister et al. (2011c)

A possible scenario of seasonal deposition is flooding of alluvial areas after snowmelt and during periods of high river discharge. Aeolian deposition likely occurs in dryer seasons. During fall and winter, river discharge volume is extremely reduced. As a consequence, parts of the formerly submerged floodplain areas become susceptible to wind activity (Muhs and Bettis, 2003). The concept of polygenetic Yedoma

genesis proposed here integrates several previous concepts shown in Table 1-1 and combines the two major processes, (1) sedimentation and (2) syngenetic freezing, which were largely controlled by similar landscape (polygonal network surfaces) and relief characteristics (stable and poorly-drained accumulation areas), harsh climate conditions (highly continental, cold-arid), periglacial processes, and the occurrence of nearby sediment sources (Figure 5-1). In eastern Beringia, the aeolian component is more pronounced (Péwé, 1975; Froese et al., 2009), but the variety of included processes are similar (Strauss et al., 2013).

5.2 Storage of organic carbon: How much is stored in the Yedoma and permafrost region?

5.2.1 Yedoma region

Different approaches have been used to calculate the Yedoma region carbon inventory. It was originally estimated to be 450 Gt (Zimov et al., 2006a) based on a mean deposit thickness of 25 m, 1,000,000 km² areal coverage, 2.6 wt% total organic carbon (TOC), a bulk density (BD) of 1.65 10^3 kg/m³, and 50 vol% wedge-ice volume (WIV). Schirrmeister et al. (2011b) postulated a reduction of this pool by 25 to 50 % due to a lower BD (0.89 to 0.96 10^3 kg/m³). This would result in a pool of roughly 225 to 338 Gt. A recent study by Walter Anthony et al. (2014) calculated a total Pleistocene-carbon pool size of 284±40 Gt for the Yedoma region as the sum of Pleistocene carbon in (1) undisturbed Yedoma (129±30 Gt), and (2) thermokarst basins (155 Gt, of which 41 Gt has been reworked in thermokarst deposits, and 114 Gt exists in thawed and in situ refrozen deposits below the thermokarst deposits (taberites)). By adding Holocene carbon (13±1 Gt as peat on top of Yedoma deposits and 159±24 Gt of Holocene carbon stored in thermokarst basins), Walter Anthony et al. (2014) estimated a Yedoma region carbon inventory of 456±45 Gt including non-frozen deposits. Adding the Yedoma-derived taberite deposits (114 Gt OC) and not considering non-parametrical statistical methods (see Table appendix III-1), the Yedoma region estimate of Chapter 3 (Strauss et al., 2013) would yield a Yedoma-region carbon pool of 466 Gt, which is similar to the calculation by Walter Anthony et al. (2014).

To consider the observed skewness of the data distribution as an important attribute of the data, which adds a degree of uncertainty (Figure 3-3 and Figure appendix III-5), in Chapter 3 (Strauss et al., 2013) observation-based bootstrapping mean values rather than simple means were selected as a more appropriate approach for inventory calculation. Using this method, the calculated Yedoma region inventory is 83+61/-57 Gt OC for Yedoma deposits and 128+99/-96 Gt OC for thermokarst deposits, for a total of 211+160/-153 Gt OC for the entire Yedoma region. To reduce

the uncertainty of the calculations shown in Chapter 3 (Strauss et al., 2013), here and in Appendix I (Hugelius et al., 2014) an adjusted bootstrapping algorithm is used. When 10,000 separate bootstrapping runs were conducted and a mean pool size was derived from every bootstrapping run, one mean calculated from 10,000 observation-based bootstrapping means was derived. Thus, the single estimator's uncertainty is remarkably lower compared to Strauss et al. (2013) (Figure 5-2). The new estimates are 83±12 Gt for Yedoma deposit carbon and 130±29 Gt for thermokarst deposits. Based on this calculation 213±41 Gt OC are stored in the Yedoma region. Of this pool, approximately 32 Gt OC are stored in the first ~1 to 3 m of soil (Hugelius et al., 2014).

The question arises: Which uncertainties should be used? The uncertainty used in Strauss et al. (2013) mirrors the complete natural inherent heterogeneity of the dataset. This is regarded as a conservative uncertainty calculation approach. To calculate the estimator's (observation-based mean) uncertainty instead of the data uncertainty, several independent bootstrapping runs with the mean being calculated in each case would be necessary.

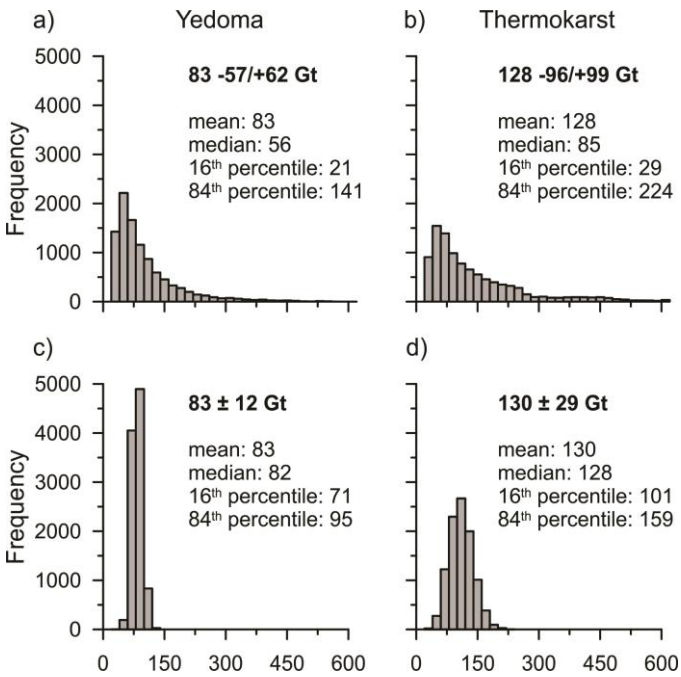

Figure 5-2. Histogram of different bootstrapping approaches for Yedoma (a and c) and thermokarst (b and d) deposits. Histograms a) and b) are based on one single bootstrapping run (10,000 resamples) of the observed values; averages are calculated afterwards. Histograms c) and d) are based on 10,000 separate bootstrapping runs (10,000 resamples each), a data set of 10,000 means is created and the averages and uncertainties are calculated from these data.

Consequently, the above-mentioned question could be answered as follows: If a conservative uncertainty range of OC carbon budget is applied, the single-run observation-based bootstrapping technique should be used. But if producing a single estimator, including its uncertainty, is the goal, for example adding the Yedoma region carbon budget as a part of a bigger pool like in Hugelius et al. (2014), the approach based on the reduced uncertainty range would be a feasible option.

Although a reduction of the estimate of the Yedoma region carbon stock by nearly a factor of two compared to Zimov et al. (2006a), this frozen OC is still significant for inducing a permafrost carbon feedback to climate warming. The frozen deposits of the Yedoma region store as much carbon as the tropical forest vegetation (Dixon et al., 1994; Lai, 2004), and 40 % of the amount of carbon recently incorporated in the global vegetation (Figure 5-3). Although a large amount of carbon is sequestered in frozen Yedoma and thermokarst deposits, the Yedoma region includes even more OC in other inventories. First and foremost, there is carbon stored in the seasonally-thawed active layer. According to data published by Beer et al. (2013), the active-layer depth in the Siberian part of the Yedoma region is estimated to be 0 to ~2 m thick. For the following inventory calculation, a very rough mean active-layer depth of 1 m and a Yedoma and thermokarst deposit coverage of 1,200,000 km² is assumed. Combining this with the 0 to 1 m pool from Hugelius et al. (2014) (472 Gt for the circum-arctic permafrost region (18,700,000 km²) according to Hugelius et al., 2013b), the Yedoma region active layer includes ~30 Gt OC. This calculation estimates only the approximate magnitude of this pool; the confidence in this estimate is because it includes the mean carbon content from outside the Yedoma region and because the active-layer depth is very heterogeneous from year to year (over time) as well as due to relief position and latitude (over space, Figure 1-2).

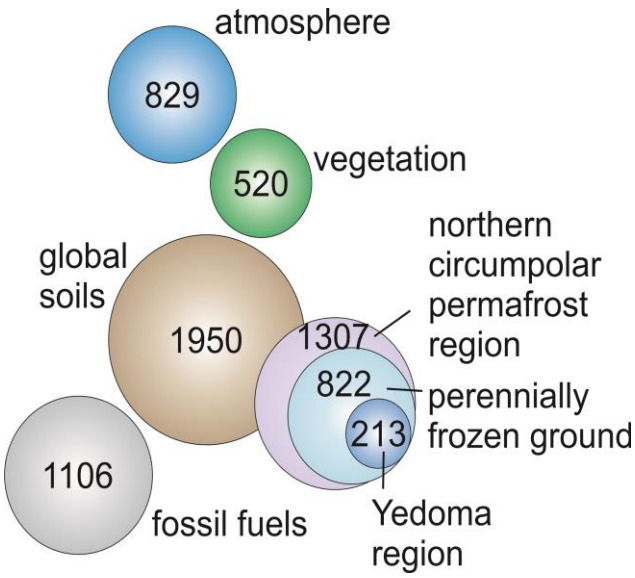

Figure 5-3. Terrestrial carbon stock and atmospheric carbon in relation to the carbon stored in the Yedoma region. The surface area of the circles represents the size of the carbon stock. The stocks are given in Gt. For global soils (1950 Gt), atmosphere (829 Gt), vegetation (520 Gt), and fossil fuels (1106 Gt), means are taken of the minimum - maximum ranges given in Ciais et al. (2013). The 1307 Gt of the northern circumpolar permafrost region are calculated in Hugelius et al. (2014). The Yedoma region carbon (213 Gt) is taken from Chapter 3.

Another additional OC stock introduced by Schirrmeister et al. (2011b) is the abovementioned taberite pool, which is calculated to be 114 Gt by Walter Anthony et al. (2014). Moreover, according to Schirrmeister et al. (2011b), deeper stratigraphic units (Figure 5-4) also contain OC. As shown by Schirrmeister et al. (2011b), the TOC content in the sandy deposits below the Yedoma is relatively low and Eemian thermokarst deposits or late Saalian ice-rich deposits are only found in a small part of the Yedoma

region. Due to diverse geologic patterns and unknown and different spatial extensions of these deposits, it is not possible to calculate these carbon stocks at this point.

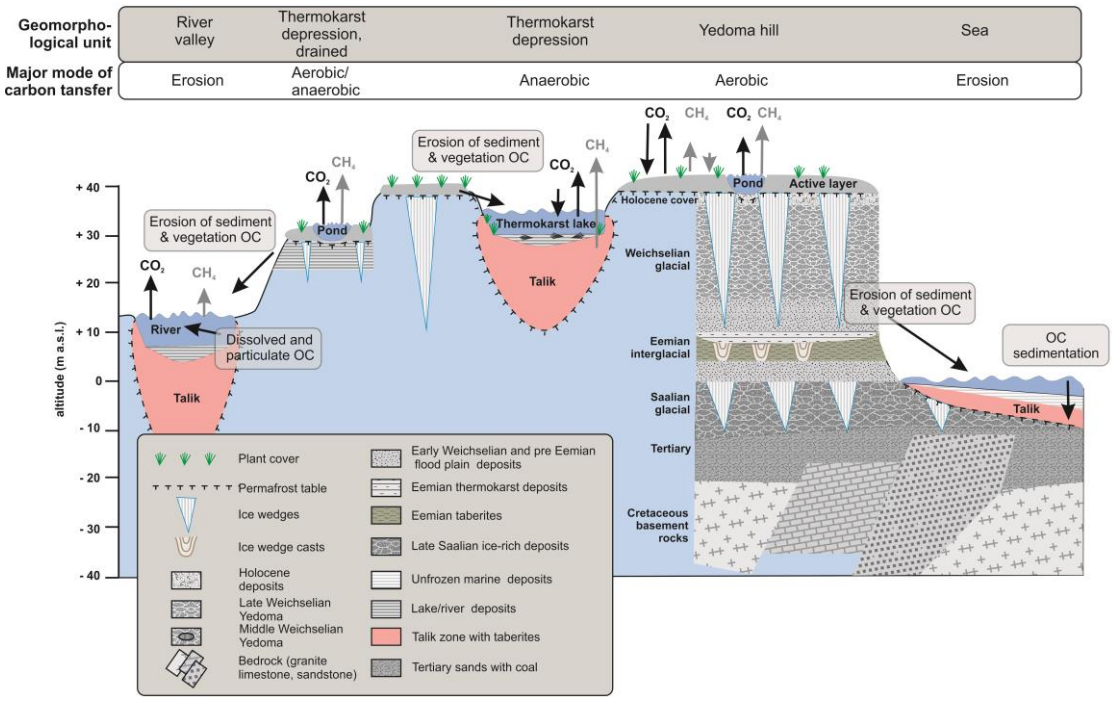

Figure 5-4: Simplified stratigraphical diagram of the Yedoma region (here the Dmitry Laptev Strait is given as an example) and the major modes of sediment carbon transfer for the different geomorphological units. Modified after Schirrmeister et al. (2011b) and van Huissteden and Dolman (2012).

Carbon stored in the ground ice component of the deposits is another neglected OC inventory in quantity calculation. After Fritz et al. (in preparation), segregated ice from Muostakh Island (Siberia) contains 0.35 kg/m³ dissolved organic carbon (DOC). Based on this single dataset and taking the segregated ice volume (~40 vol% of the sediment and excluding ice wedges), Yedoma and thermokarst segregated ice together contain ~1 Gt DOC. Assuming a WIV of 48 vol% for Yedoma and 7 vol% for thermokarst deposits (Strauss et al., 2013), the Yedoma ice wedges contain 0.00053 kg/m³ and thermokarst wedges 0.000051 kg/m³ DOC (Fritz et al., in preparation). Combined with deposit thickness and volumes from Strauss et al. (2013), this corresponds to approximately 0.05 Gt DOC in the Yedoma region (Fritz et al., in preparation). Segregated and wedge ice do not contain much carbon compared to the pools described above, but because of potentially excellent DOC biodegradability (Vonk et al., 2013a; Cory et al., 2014), this pool is relevant as well. The estimation of DOC in ground ice of the Yedoma region is made in order to approximate the magnitude of this pool, but due to very limited data, confidence in these calculations must be low.

To separate the Yedoma region carbon pool into Siberian and Alaskan pools, the Yedoma region coverage was divided as follows: The potential Yedoma deposit area

in Siberia was assumed to be 1,141,000 km² (Romanovskii, 1993) plus ~45,000 km² for regions with smaller known Yedoma deposit occurrences (e.g. Taymyr Peninsula and Chukotka). For Alaska, 181,000 km² (Jorgenson et al., 2008) plus 20,000 km² for smaller known Yedoma deposit occurrences (e.g. Yukon Territory) were used. Assuming that 70 % of the Yedoma region is affected by degradation or erosion, the remaining Yedoma deposits cover 355,800 km² in Siberia and 60,300 km² in Alaska. By subtracting the thermokarst lake area (127,000 km² for Siberia, 22,000 km² for Alaska; after Grosse et al. 2013b) and for Siberia the river delta area (47,000 km²) after Walker (1998), the Siberian Yedoma region includes 656,000 km² thermokarst deposits, the Alaskan 119,000 km². Total WIV was used according to Chapter 3, not apportioned separately for the two regions. Separated TOC, BD, and thickness are given in Table 5-1. A separate bootstrapping results in 74±20 Gt for Siberian Yedoma deposits and 9±3 Gt for Alaskan Yedoma. Siberian thermokarst deposits store 117±45 Gt, Alaskan thermokarst 17±7 Gt (Table 5-1).

Table 5-1. Yedoma and thermokarst deposit parameters and organic carbon inventory separated into Siberian and Alaskan sub-regions. The Siberian and Alaskan carbon pool sample size is related to a 10,000 times re-sampling procedure (bootstrapping) and mean calculation.

	Total organic carbon (wt%)		Bulk density (10^3kg/m³)		Thickness (m)		Carbon pool (Gt)	
				Yedoma				
	Siberia	**Alaska**	**Siberia**	**Alaska**	**Siberia**	**Alaska**	**Siberia**	**Alaska**
Mean	3.2	2.0	0.87	0.95	20	18	74	9
Median	2.0	1.1	0.86	0.94	15	15	73	9
16th percentile	0.9	0.6	0.63	0.67	9	12	62	7
84th percentile	4.7	2.9	1.11	1.26	29	25	86	11
n	585	97	351	77	15	5	10,000	10,000
				Thermokarst				
Mean	6.2	9.0	0.94	0.74	6	3	118	17
Median	2.2	7. 8	1.05	0.70	5	3	115	17
16th percentile	1.5	3.2	0.55	0.61	2	2	89	13
84th percentile	10.0	11.0	1.27	0.76	10	4	143	21
n	199	20	108	9	8	2	10,000	10,000

5.2.2 Northern circumpolar permafrost region

Because the Yedoma region is part of the northern circumpolar permafrost region, this section briefly synthesizes the overall carbon pool calculated in Appendix I (Hugelius et al., 2014). In this section the Yedoma region estimates of section 5.2.1 and Figure 5-2 are included.

The estimate of OC stock size and variability in the northern circumpolar permafrost region is restricted to soils depth from 0 to 3 m, but it also accounts for deeper deposits in arctic deltas and the Yedoma region. The northern circumpolar permafrost region stores 217±12 Gt in the top layer of 0 to 0.3 m depth, 472±27 Gt in the 0 to 1 m layer

and 1034±150 Gt for the complete 0 to 3 m interval. Adding 91±52 Gt in >3 m depth in deltaic alluvium of permafrost river deltas and the >3 m OC stocks of 181±54 Gt in the Yedoma region, the northern circumpolar permafrost region contains ~1300 Gt OC. Of this, ~60 % is perennially frozen and thus decoupled from the short-term carbon cycle. The wide uncertainty ranges reflect difficulties in assessing highly variable carbon pools in this region, which was shown representatively for the Yedoma region in Chapter 3.

To emphasize the relevance of the northern circumpolar OC stock for the global carbon cycle, $^{2}/_{3}$ of the global soil carbon (1950 after Ciais et al., 2013) is stored here (Figure 5-3).

5.3 Quality of organic carbon Quality: What is the susceptibility of the permafrost region's carbon for future decomposition?

5.3.1 Yedoma region's carbon quality

Because there is concern that thawing permafrost will mobilize and release ancient OC to the atmosphere (Kuhry et al., 2013), it is of high interest to assess the quality of the Yedoma region OC. Based on differences in permafrost organic matter origins for

(1) the Pleistocene Yedoma deposit carbon (accumulated under aerobic conditions; froze within decades to centuries after burial; remained frozen for tens of thousands of years) and
(2) the Holocene thermokarst deposit carbon pool (accumulated (1) predominately under lacustrine anaerobic conditions and remained unfrozen for centuries to millennia prior to freezing after lake drainage, and (2) exits as both aerobic and anaerobic (peat) deposits after lake drainage; Figure 5-4),

it was assumed that soil organic matter degradability differs significantly between these two pools (Walter Anthony et al., 2014). This difference between Yedoma and thermokarst deposits was not found in Chapter 4, revealing that the organic matter vulnerability is heterogeneous and depends on different decomposition trajectories and the previous decomposition/incorporation history. Missing depth trends reveal that permafrost acts like a giant freezer, preserving the constant quality of ancient organic matter. Also, long-term laboratory incubation studies (Knoblauch et al., 2013) found similar mineralization rates in Yedoma and thermokarst deposits and confirm the finding of Strauss et al. (2014).

5.3.2 Potential response of the permafrost region's organic carbon to warming

As stated in two reviews (McGuire et al., 2010; van Huissteden and Dolman, 2012), the Arctic is currently estimated to be a CO_2 sink of 0.3 to 0.6 Gt OC/a and a CH_4 source of 0.023 to 0.075 Gt OC/a. Moreover, it is an assumed source of river-transported organic and inorganic carbon of 0.08 Gt OC/a. Coastal and wind erosion contribute an additional 0.008 Gt OC/a to the Arctic Ocean (McGuire et al., 2010). Walter Anthony et al. (2014) found a net carbon accumulation in Yedoma region thermokarst basins since the last deglaciation. By comparing the carbon contents of Yedoma (19+13/-11 kg/m³) and thermokarst deposits (33+25/-19 kg/m³), the data in Chapter 3 confirm this finding. Being in a low degradation state (Chapter 4), a significant vulnerability to microbial degradation after thawing is expected. Due to ongoing climate warming in the Arctic, Grosse et al. (2011b) assume an increase in the occurrence and magnitude of disturbance processes, especially wildfire and thermokarst, that will result in enhanced decomposition of permafrost carbon.

The Yedoma region includes an enormous amount of ground ice, up to ~80 vol% and ~65 vol% in Yedoma and thermokarst deposits, respectively (Strauss et al., 2013; Ulrich et al., 2014); this region is prone to deep disturbance processes (Grosse et al., 2011b) when the ice melts and drains. Because microbial processes govern the carbon decomposition, it is agreed that only a slight increase of ground temperature can lead to a substantial increase of OC decomposition (Wagner et al., 2007). Regarding DOC, Vonk et al. (2013b) found that WI melt water can catalyze DOC degradation. Thus, compared to non-WI- containing permafrost, the vulnerability of WI-containing permafrost upon melting highlights the potential of Yedoma deposits to induce a positive feedback to climate warming.

As a result, when permafrost degrades, the sequestered OC is available for oxidation, and a change of permafrost from carbon sink to source is very likely. As is shown in Figure 5-4, the sedimentary OC could become accessible by (1) active layer thickening (Hinkel and Nelson, 2003; Schuur et al., 2008; Schaefer et al., 2011), (2) surface subsidence due to rapidly thawing (Grosse et al., 2011b; Biskaborn et al., 2013; Morgenstern et al., 2013), and (3) erosion in thaw slumps, active-layer slides, and gullies at lake and river banks and sea coasts (Rachold et al., 2000; Jones et al., 2009; Günther et al., 2013; Kanevskiy et al., in preparation). However, the rates of organic matter degradation, especially in the Yedoma region, are debated in the scientific literature. By comparing thawed samples from thermally-eroded slopes, neglecting the possibility of mixing of thawed material from different stratigraphic units (Figure 5-4), Vonk et al. (2012) estimate ~60 % of the Yedoma deposit OC is released prior to expulsion into water. Direct measurements reveal a potential OC mineraliza-

tion of Yedoma deposits of ~1 to 2 % to CO_2 in an assumed thawing season of 3 to 4 months (Dutta et al., 2006; Knoblauch et al., 2013).

When it enters river and sea waters, Vonk et al. (2013a) and Mann et al. (2014) found that DOC in ancient Yedoma is exceptionally biolabile. But if it is not dissolved, the eroded ancient OC could be protected from extensive degradation by organo-mineral bonds, which stabilize the organic matter (Höfle et al., 2013) and, in an aquatic environment, promote rapid settling because of their weight (Vonk et al., 2010).

Based on incubation studies, Schädel et al. (2014) developed a three-pool (fast, slow, and passive) decomposition model. Fast-cycling carbon (<1 a at 5°C) was found to be less than 5 % of the carbon in permafrost soils. Moreover, Schädel et al. (2014) projected that between 20 and 90 % of the OC could potentially be mineralized to CO_2 within 50 incubation years (at 5°C). Thus, based on 1034 Gt OC in the first 3 m of the northern circumpolar permafrost region (Appendix I), this would mean 207 to 930 Gt OC could be emitted when exposed to 5°C for 50 years. Microbial decomposition has happened in the past as well. During past warming events, like the Middle Weichselian (MIS 3) interstadial and the early Holocene, considerable amounts of CH_4 emissions were shown by Bischoff et al. (2013). Moreover Bischoff et al. (2013) predict an analogue shift of microbial communities and an associated increase in CH_4 emission in future warming environments.

Besides a positive carbon feedback, a negative feedback mechanism could also be initiated in a warming Arctic. It has been suggested that warmer conditions lead to more uptake of carbon due to lengthening the period of plant photosynthesis (van Huissteden and Dolman, 2012; Schaphoff et al., 2013), but Parmentier et al. (2011) show that the overall variability in net carbon uptake is low, and no relationship with growing season length was found. Thus, they suggest that site-specific differences, such as climate and soil types, are important, and that changes in the carbon cycle with longer growing seasons will not be uniform around the Arctic; in consequence the direction of this feedback is uncertain.

Global-scale models are limited so far because they implement one-dimensional vertical thaw only (Koven et al., 2011; Schneider von Deimling et al., 2012; Schaphoff et al., 2013). Thus, the potentially labile Yedoma and thermokarst deep OC pools described in Chapter 4 are not realistically implemented, because the models disregard abrupt thaw processes like thermokarst or coastal erosion. By first implementing rapid thaw (Appendix II), Schneider von Deimling et al. (2014) run the model under various future warming scenarios, ranging from moderate (Representative Concentration Pathway (RCP) 2.6) to extensive (RCP8.5) conditions. Under the moderate warming of the RCP2.6 scenario, CO_2 fluxes from thawed permafrost car-

bon amount to as much as ~60 Gt carbon by the year 2100 and reach up to ~100 Gt carbon by 2300. Extensive warming (RCP8.5) results in a cumulative CO_2 release of up to ~140 Gt and ~310 Gt by the years 2100 and 2300, respectively. Simulated CH_4 fluxes infer the largest contributions of about 0.05 Gt CH_4 per year around the middle of the 21st century (simulated thermokarst lake extent is at its maximum) under the strong warming scenario (RCP8.5). Moreover, Schneider von Deimling et al. (2014) show that a release from organic matter stored in deep Yedoma region deposits crucially affects the simulated circum-arctic CH_4 fluxes. Converted to temperature analogues, the additional warming due to carbon release from newly-thawed permafrost proved to be only slightly dependent on the pathway of anthropogenic emission and is projected to amount to about 0.03 to 0.14°C by the year 2100. The warming increased further in the 22nd and 23rd century and was most pronounced under the RCP6.0 scenario, which projected an increase of up to 0.4°C in simulated global mean surface air temperatures.

5.4 Outlook: opportunities for future research

The subject of permafrost carbon characteristics and quantity discussed in this thesis is an important topic of recent climate change research (Knoblauch et al., 2013; Hodgkins et al., 2014; Li et al., 2014; Mu et al., 2014; Walter Anthony et al., 2014). However, the magnitude and timing of carbon fluxes as a consequence of permafrost degradation are highly uncertain. For reducing these knowledge gaps the following opportunities for future research would help to elucidate the (1) characteristics, (2) quantity, and (3) quality of OC in ice-rich permafrost.

(1) Studies on heavy mineral composition would improve the identification of Yedoma deposit source areas. For reconstructing the transport pathways (aeolian vs. others) scanning electron microscopy of the quartz grains from Yedoma deposits could be useful.

(2) For refining the quantity of OC in ice-rich permafrost, prioritized areas of future sampling could be inland areas, i.e. upstream of the Lena, Yana, and Kolyma rivers in Siberia, and the Colville and Yukon rivers in Alaska. If drilling campaigns are planned, choosing sites in interior areas of the Yana-Indigirka and Kolyma lowlands will fill current knowledge gaps. Further studies on coverage and volumes of OC-bearing sediments below the Yedoma and surface level would be useful. Moreover, future studies should include an adequate statistical model, like bootstrapping or Monte Carlo simulations. To reduce the inventory uncertainties, adding data on Yedoma deposit thickness is required. An approach to estimate this could be to measure the subsidence depth of thermokarst depres-

sions using remote-sensing methods. According to Ulrich et al. (2014), more data on WIVs are needed to reduce the OC quantity uncertainties.

(3) For refining the uncertainties of OC quality, future studies could divide the OC into different fractions based on e.g. density or chemical properties. These OC fractions should be characterized concerning their vulnerability to degradation (e.g. by biomarker analyses or in situ or laboratory incubations) to distinguish between labile and passive OC components. Since an important part of degradation takes place during transport, studies on a degradation transect along the pathway from mobilization to deposition will improve the understanding of the Arctic response to climate forcing. Especially in the context of multi-proxy studies of methods from microbiology and organic geochemistry, this thesis revealed that biomarker-based approaches and proxies are valuable to assess OC vulnerability and resilience. Therefore, such studies could be essential to elucidating the importance of the Arctic region for the global carbon cycle. Moreover, an OC quality/lability analogue to the OC quantity map presented in Appendix I (Figure appendix I-3) is needed.

References

This list of references includes the references of the chapters 1 to 5, as well as the references of the appendix chapters.

Abnizova, A., Siemens, J., Langer, M., and Boike, J.: Small ponds with major impact: The relevance of ponds and lakes in permafrost landscapes to carbon dioxide emissions, Global Biogeochemical Cycles, 26, GB2041, doi:10.1029/2011gb004237, 2012.

Ahlenius, H.: Permafrost extent in the Northern Hemisphere, in: Global outlook for ice and snow - Chapter 7, edited by: Romanovsky, V. E., Gruber, S., Instanes, A., Jin, H., Marchenko, S. S., Smith, S. L., Trombotto, D., and Walter, K. M., United Nations Environment Programme, 183, 2007.

Allen, M. R., Frame, D. J., Huntingford, C., Jones, C. D., Lowe, J. A., Meinshausen, M., and Meinshausen, N.: Warming caused by cumulative carbon emissions towards the trillionth tonne, Nature, 458, 1163-1166, doi:10.1038/nature08019, 2009.

AMAP: Snow, water, ice and permafrost in the Arctic (SWIPA): Climate change and the cryosphere, Arctic Monitoring and Assessment Programme (AMAP), Oslo, Norway, 2011.

Andersson, R. A., Kuhry, P., Meyers, P., Zebühr, Y., Crill, P., and Mörth, M.: Impacts of paleohydrological changes on n-alkane biomarker compositions of a Holocene peat sequence in the eastern European Russian Arctic, Organic Geochemistry, 42, 1065-1075, doi:10.1016/j.orggeochem.2011.06.020, 2011.

Andersson, R. A., and Meyers, P. A.: Effect of climate change on delivery and degradation of lipid biomarkers in a Holocene peat sequence in the Eastern European Russian Arctic, Organic Geochemistry, 53, 63-72, doi:10.1016/j.orggeochem.2012.05.002, 2012.

Anisimov, O., and Reneva, S.: Permafrost and changing climate: The Russian perspective, AMBIO: A Journal of the Human Environment, 35, 169-175, doi:10.1579/0044-7447(2006)35[169:PACCTR]2.0.CO;2, 2006.

Arcos, D. R.: Classification of periglacial landforms based on high resolution multispectral remote sensing data. A contribution to the landscape description of the north Siberian Buor Khaya Pensinsula, diploma thesis, Institute of Earth and Environmental Science, Potsdam University, Potsdam, 71 pp., 2012.

Arkhangelov, A. A., Popov, V. V., and L'yanos-Mas, A. V.: About permfrost-facial structure of the Yedoma horizon of Dyvanny Yar, Kolyma Lowland, in: Problems of cryolithology, Moscow University Press, 145-156, 1979.

Arp, C. D., Jones, B. M., Lu, Z., and Whitman, M. S.: Shifting balance of thermokarst lake ice regimes across the Arctic Coastal Plain of northern Alaska, Geophysical Research Letters, 39, L16503, doi:10.1029/2012gl052518, 2012.

Ashley, G. M.: Interpretation of polymodal sediments, The Journal of Geology, 86, 411-421, 1978.

Avis, C. A., Weaver, A. J., and Meissner, K. J.: Reduction in areal extent of high-latitude wetlands in response to permafrost thaw, Nature Geoscieince, 4, 444-448, doi:10.1038/ngeo1160, 2011.

Aylsworth, J., Burgess, M., Desrochers, D., Duk-Rodkin, A., Robertson, T., and Traynor, J.: Surficial geology, subsurface materials, and thaw sensitivity of sediments, in: The physical environment of the Mackenzie Valley, Northwest Territories: A base line for the assessment of environmental change, edited by: Dyke, L. D., and Brooks, G. R., Geological Survey of Canada Bulletin 547, Ottawa, 31-39, 2000.

Barandova, Y. P.: Essay on the geomorphology of the eastern Kolyma Lowland, in: Materials for geology and resources of Northeast USSR, Magadan Publishing House, 208-222, 1957.

Batjes, N. H.: Total carbon and nitrogen in the soils of the world, European Journal of Soil Science, 47, 151-164, 1996.

Battle, M., Bender, M. L., Tans, P. P., White, J. W. C., Ellis, J. T., Conway, T., and Francey, R. J.: Global carbon sinks and their variability inferred from atmospheric O_2 and $\delta^{13}C$, Science, 287, 2467-2470, doi:10.1126/science.287.5462.2467, 2000.

Beer, C., Fedorov, A. N., and Torgovkin, Y.: Permafrost temperature and active-layer thickness of Yakutia with 0.5-degree spatial resolution for model evaluation, Earth System Science Data, 5, 305-310, doi:10.5194/essd-5-305-2013, 2013.

Berg, B.: Litter decomposition and organic matter turnover in northern forest soils, Forest Ecology and Management, 133, 13-22, doi:10.1016/S0378-1127(99)00294-7, 2000.

Bischoff, J., Mangelsdorf, K., Gattinger, A., Schloter, M., Kurchatova, A. N., Herzschuh, U., and Wagner, D.: Response of methanogenic archaea to Late Pleistocene and Holocene climate changes in the Siberian Arctic, Global Biogeochemical Cycles, 27, 305-317, doi:10.1029/2011gb004238, 2013.

Biskaborn, B. K., Herzschuh, U., Bolshiyanov, D. Y., Schwamborn, G., and Diekmann, B.: Thermokarst processes and depositional events in a tundra lake, northeastern Siberia, Permafrost and Periglacial Processes, 24, 160-174, doi:10.1002/ppp.1769, 2013.

Biske, S. F.: Quaternary deposits of the Kolyma Lowlands, in: Materials for geology and resources of Northeast USSR, Magadan Publishing House, 1957.

Blott, S. J., and Pye, K.: GRADISTAT: A grain size distribution and statistics package for the analysis of unconsolidated sediments, Earth Surface Processes and Landforms, 26, 1237-1248, doi:10.1002/esp.261, 2001.

Boereboom, T., Samyn, D., Meyer, H., and Tison, J. L.: Stable isotope and gas properties of two climatically contrasting (Pleistocene and Holocene) ice wedges from Cape Mamontov Klyk, Laptev Sea, northern Siberia, The Cryosphere, 7, 31-46, doi:10.5194/tc-7-31-2013, 2013.

Boike, J., Bolshiyanov, D. Y., Schirrmeister, L., and Wetterich, S.: Russian-German Cooperation SYSTEM LAPTEV SEA: The Expedition Lena - New Siberian Islands 2007 during the International Polar Year 2007/2008, Reports on polar and marine research, Alfred Wegener Institute for Polar and Marine Research, Bremerhaven, 265 pp., 2008.

Boike, J., Langer, M., Lantuit, H., Muster, S., Roth, K., Sachs, T., Overduin, P., Westermann, S., and McGuire, A. D.: Permafrost–physical aspects, carbon cycling, databases and uncertainties, in: Recarbonization of the biosphere, edited by: Lal, R., Lorenz, K., Hüttl, R. F., Schneider, B. U., and von Braun, J., Springer, Amsterdam, 159-185, 2012.

Boike, J., Kattenstroth, B., Abramova, K., Bornemann, N., Chetverova, A., Fedorova, I., Fröb, K., Grigoriev, M., Grüber, M., Kutzbach, L., Langer, M., Minke, M., Muster, S., Piel, K., Pfeiffer, E. M., Stoof, G., Westermann, S., Wischnewski, K., Wille, C., and Hubberten, H. W.: Baseline characteristics of climate, permafrost and land cover from a new permafrost observatory in the Lena River Delta, Siberia (1998-2011), Biogeosciences, 10, 2105-2128, doi:10.5194/bg-10-2105-2013, 2013.

Bolshiyanov, D. Y., Grigoriev, M. N., Schneider, W., Makarov, A. S., and Gusev, E. A.: Sea-level fluctuations, and Ice Complex formation on the Laptev Sea coast during the Late Pleistocene, in: System of the Laptev Sea and the adjacent Arctic seas, edited by: Kassens, H., Lisitzin, A. P., Thiede, J., Pelyakova, Y. I., Timokhov, L. A., and Frolov, I. E., Moscow University Press, Moscow, 349-356, 2009.

Bray, E. E., and Evans, E. D.: Distribution of n-paraffins as a clue to recognition of source beds, Geochimica et Cosmochimica Acta, 22, 2-15, doi:10.1016/0016-7037(61)90069-2, 1961.

Brosius, L. S., Walter Anthony, K. M., Grosse, G., Chanton, J. P., Farquharson, L. M., Overduin, P. P., and Meyer, H.: Using the deuterium isotope composition of permafrost meltwater to constrain thermokarst lake contributions to atmospheric CH_4 during the last deglaciation, Journal of Geophysical Research: Biogeosciences, 117, G01022, doi:10.1029/2011jg001810, 2012.

Brown, A.: Permafrost carbon storage: Pandora's freezer?, Nature Climate Change, 3, 442, doi:10.1038/nclimate1896, 2013.

Brown, J., Ferrians, O. J., Heginbottom, J. A., and Melnikov, E. S.: Circum-Arctic map of permafrost and and ground-ice conditions, US Geological Survey in cooperation with the Circum-Pacific Council for Energy and Mineral Resources, Washington, DC, 1997.

Brown, J., Ferrians, O. J., Heginbottom, J. A., and Melnikov, E. S.: Circum-Arctic map of permafrost and and ground-ice conditions, version 2, National Snow and Ice Data Center, Boulder, 2002.

Burke, E. J., Hartley, I. P., and Jones, C. D.: Uncertainties in the global temperature change caused by carbon release from permafrost thawing, The Cryosphere, 6, 1063-1076, doi:10.5194/tc-6-1063-2012, 2012a.

Burke, E. J., Jones, C. D., and Koven, C. D.: Estimating the permafrost-carbon climate response in the CMIP5 climate models using a simplified approach, Journal of Climate, 26, 4897-4909, doi:10.1175/jcli-d-12-00550.1, 2012b.

Burn, C. R.: Tundra lakes and permafrost, Richards Island, western Arctic coast, Canada, Canadian Journal of Earth Sciences, 39, 1281-1298, doi:10.1139/e02-035, 2002.

Ciais, P., Tagliabue, A., Cuntz, M., Bopp, L., Scholze, M., Hoffmann, G., Lourantou, A., Harrison, S. P., Prentice, I. C., Kelley, D. I., Koven, C., and Piao, S. L.: Large inert carbon pool in the terrestrial biosphere during the Last Glacial Maximum, Nature Geoscience, 5, 74-79, doi:10.1038/ngeo1324, 2012.

Ciais, P., Sabine, C., Bala, G., Bopp, L., Brovkin, V., Canadell, J., Chhabra, A., DeFries, R., Galloway, J., Heimann, M., Jones, C., Le Quéré, C., Myneni, R. B., Piao, S., and Thornton, P.: Carbon and other biogeochemical cycles, in: Climate change 2013: The physical science basis. Contribution of working group 1 to the fifth assessment report of the Intergovernmental Panel on Climate Change, edited by: Stocker, T. F., Qin, D., Plattner, G.-K., Tignor, M., Allen, S. K., Boschung, J., Nauels, A., Xia, Y., Bex, V., and Midgley, P. M., Cambridge University Press, Cambridge, and New York, 2013.

Conrad, R., Klose, M., and Claus, P.: Pathway of CH_4 formation in anoxic rice field soil and rice roots determined by 13C-stable isotope fractionation, Chemosphere, 47, 797-806, doi:10.1016/S0045-6535(02)00120-0, 2002.

Cory, R. M., Crump, B. C., Dobkowski, J. A., and Kling, G. W.: Surface exposure to sunlight stimulates CO_2 release from permafrost soil carbon in the Arctic, Proceedings of the National Academy of Sciences, 110, 3429–3434, doi:10.1073/pnas.1214104110, 2013.

Cory, R. M., Ward, C. P., Crump, B. C., and Kling, G. W.: Sunlight controls water column processing of carbon in Arctic fresh waters, Science, 345, 925-928, doi:10.1126/science.1253119, 2014.

Dankers, R., Burke, E. J., and Price, J.: Simulation of permafrost and seasonal thaw depth in the JULES land surface scheme, The Cryosphere, 5, 773-790, doi:10.5194/tc-5-773-2011, 2011.

Davidson, E. A., and Janssens, I. A.: Temperature sensitivity of soil carbon decomposition and feedbacks to climate change, Nature, 440, 165-173, 2006.

DeConto, R. M., Galeotti, S., Pagani, M., Tracy, D., Schaefer, K., Zhang, T., Pollard, D., and Beerling, D. J.: Past extreme warming events linked to massive carbon release from thawing permafrost, Nature, 484, 87-91, doi:10.1038/nature10929, 2012.

Dietze, E., Hartmann, K., Diekmann, B., Ijmker, J., Lehmkuhl, F., Opitz, S., Stauch, G., Wünnemann, B., and Borchers, A.: An end-member algorithm for deciphering modern detrital processes from lake sediments of Lake Donggi Cona, NE Tibetan Plateau, China, Sedimentary Geology, 243–244, 169-180, doi:10.1016/j.sedgeo.2011.09.014, 2012.

Dixon, R. K., Solomon, A. M., Brown, S., Houghton, R. A., Trexier, M. C., and Wisniewski, J.: Carbon pools and flux of gobal forest ecosystems, Science, 263, 185-190, doi:10.1126/science.263.5144.185, 1994.

Dlugokencky, E., and Tans, P.: Trends in Atmospheric Carbon Dioxide: http://www.esrl.noaa.gov/gmd/ccgg/trends/global.html, access: 23.03.2014.

Drachev, S. S., Savostin, L. A., Groshev, V. G., and Bruni, I. E.: Structure and geology of the continental shelf of the Laptev Sea, eastern Russian Arctic, Tectonophysics, 298, 357-393, doi:10.1016/S0040-1951(98)00159-0, 1998.

Drozdov, D. S., Rivkin, F. M., Rachold, V., Ananjeva-Malkova, G. V., Ivanova, N. V., Chehina, I. V., Koreisha, M. M., Korostelev, Y. V., and Melnikov, E. S.: Electronic atlas of the Russian Arctic coastal zone, Geo-Marine Letters, 25, 81-88, doi:10.1007/s00367-004-0189-7, 2005.

Dutta, K., Schuur, E. A. G., Neff, J. C., and Zimov, S. A.: Potential carbon release from permafrost soils of Northeastern Siberia, Global Change Biology, 12, 2336-2351, doi:10.1111/j.1365-2486.2006.01259.x, 2006.

Ehlers, J., and Gibbard, P. L.: Extent and chronology of glaciations, Quaternary Science Reviews, 22, 1561-1568, doi:10.1016/S0277-3791(03)00130-6, 2003.

Ekici, A., Beer, C., Hagemann, S., Boike, J., Langer, M., and Hauck, C.: Simulating high-latitude permafrost regions by the JSBACH terrestrial ecosystem model, Geoscientific Model Development, 7, 631-647, doi:10.5194/gmd-7-631-2014, 2014.

Eliseev, A. V., Mokhov, I. I., Arzhanov, M. M., Demchenko, P. F., and Denisov, S. N.: Interaction of the methane cycle and processes in wetland ecosystems in a climate model of intermediate complexity, Izvestiya Atmospheric and Oceanic Physics, 44, 139-152, 2008.

EPA: Methane and nitrous oxide emissions from natural sources, United States Environmental Protection Agency, Washington, 2010.

Euskirchen, E. S., McGuire, A. D., Kicklighter, D. W., Zhuang, Q., Clein, J. S., Dargaville, R. J., Dye, D. G., Kimball, J. S., McDonald, K. C., Melillo, J. M., Romanovsky, V. E., and Smith, N. V.: Importance of recent shifts in soil thermal dynamics on growing season length, productivity, and carbon sequestration in terrestrial high-latitude ecosystems, Global Change Biology, 12, 731-750, doi:10.1111/j.1365-2486.2006.01113.x, 2006.

Euskirchen, E. S., Goodstein, E. S., and Huntington, H. P.: An estimated cost of lost climate regulation services caused by thawing of the Arctic cryosphere, Ecological Applications, 23, 1869-1880, doi:10.1890/11-0858.1, 2013.

Farenhorst, A., and Bryan, R. B.: Particle size distribution of sediment transported by shallow flow, Catena, 25, 47-62, doi:10.1016/0341-8162(94)00041-c, 1995.

Folk, R. L., and Ward, W. C.: Brazos River bar: A study in the significance of grain size parameters, Journal of Sedimentary Petrology, 27, 3-26, 1957.

Frauenfeld, O. W., Zhang, T., Barry, R. G., and Gilichinsky, D.: Interdecadal changes in seasonal freeze and thaw depths in Russia, Journal of Geophysical Research: Atmospheres, 109, D05101, doi:10.1029/2003jd004245, 2004.

French, H. M.: The periglacial environment, Wiley, 458 pp., 2007.

Friedlingstein, P., Cox, P., Betts, R., Bopp, L., von Bloh, W., Brovkin, V., Cadule, P., Doney, S., Eby, M., Fung, I., Bala, G., John, J., Jones, C., Joos, F., Kato, T., Kawamiya, M., Knorr, W., Lindsay, K., Matthews, H. D., Raddatz, T., Rayner, P., Reick, C., Roeckner, E., Schnitzler, K. G., Schnur, R., Strassmann, K., Weaver, A. J., Yoshikawa, C., and Zeng, N.: Climate-carbon cycle feedback analysis: Results from the C4MIP model intercomparison, Journal of Climate, 19, 3337-3353, doi:10.1175/jcli3800.1, 2006.

Fritz, M., Opel, T., Meyer, H., Tanski, G., Eulenburg, A., Herzschuh, U., and Lantuit, H.: Dissolved organic carbon in ground ice, The Cryosphere, in preparation.

Froese, D. G., Zazula, G. D., Westgate, J. A., Preece, S. J., Sanborn, P. T., Reyes, A. V., and Pearce, N. J.: The Klondike goldfields and Pleistocene environments of Beringia, GSA Today, 19, 4-10, doi:10.1130/GSATG54A.1, 2009.

Frolking, S., Talbot, J., Jones, M. C., Treat, C. C., Kauffman, J. B., Tuittila, E.-S., and Roulet, N.: Peatlands in the Earth's 21st century climate system, Environmental Reviews, 19, 371-396, doi:10.1139/a11-014, 2011.

Gaglioti, B. V., Mann, D. H., Jones, B. M., Pohlman, J. W., Kunz, M. L., and Wooller, M. J.: Radiocarbon age-offsets in an arctic lake reveal the long-term response of permafrost carbon to climate change, Journal of Geophysical Research: Biogeosciences, 2014JG002688, doi:10.1002/2014jg002688, 2014.

Galabala, R. O.: Pereletki and the initiation of glaciation in Siberia, Quaternary International, 41–42, 27-32, doi:10.1016/S1040-6182(96)00033-X, 1997.

Gao, X., Schlosser, A. C., Sokolov, A., Walter Anthony, K., Zhuang, Q., and Kicklighter, D.: Permafrost degradation and methane: low risk of biogeochemical climate-warming feedback, Environmental Research Letters, 8, 035014, doi:10.1088/1748-9326/8/3/035014, 2013.

Giterman, R. E., Sher, A. V., and Matthews, J. V.: Comparison of the development of tundra-steppe environments in West and East Beringia: Pollen and macrofossil evidence from key sections, in: Paleoecology of Beringia, edited by: Hopkins, D. M., Matthews, J. V., Schweger, C. E., and Young, S. B., Academic Press, New York, 43-73, 1982.

Glombitza, C., Mangelsdorf, K., and Horsfield, B.: Maturation related changes in the distribution of ester bound fatty acids and alcohols in a coal series from the New Zealand Coal Band covering diagenetic to catagenetic coalification levels, Organic Geochemistry, 40, 1063-1073, doi:10.1016/j.orggeochem.2009.07.008, 2009.

Goidts, E., Van Wesemael, B., and Crucifix, M.: Magnitude and sources of uncertainties in soil organic carbon (SOC) stock assessments at various scales, European Journal of Soil Science, 60, 723-739, doi:10.1111/j.1365-2389.2009.01157.x, 2009.

Goslar, T., Czernik, J., and Goslar, E.: Low-energy ^{14}C AMS in Poznań radiocarbon laboratory, Poland, Nuclear Instruments and Methods in Physics Research Section B: Beam Interactions with Materials and Atoms, 223–224, 5-11, doi:10.1016/j.nimb.2004.04.005, 2004.

Gouttevin, I., Menegoz, M., Dominé, F., Krinner, G., Koven, C., Ciais, P., Tarnocai, C., and Boike, J.: How the insulating properties of snow affect soil carbon distribution in the continental pan-Arctic

area, Journal of Geophysical Research: Biogeosciences, 117, G02020, doi:10.1029/2011jg001916, 2012.

Graversen, R. G., Mauritsen, T., Tjernstrom, M., Kallen, E., and Svensson, G.: Vertical structure of recent Arctic warming, Nature, 451, 53-56, doi:10.1038/nature06502, 2008.

Grigoriev, M. N.: Cryomorphogenesis in the Lena Delta, Permafrost Institute Press, Yakutsk, 1993.

Grigoriev, M. N., Rachold, V., Bolshiyanov, D. Y., Pfeiffer, E.-M., Schirrmeister, L., Wagner, D., and Hubberten, H.-W.: Russian-German Cooperation SYSTEM LAPTEV SEA - The Expedition LENA 2002, Reports on Polar and Marine Research, Alfred Wegener Institute for Polar and Marine Research, Bremerhaven, 341 pp., 2003.

Grosse, G., Schirrmeister, L., Kunitsky, V. V., and Hubberten, H.-W.: The use of CORONA images in remote sensing of periglacial geomorphology: An illustration from the NE Siberian Coast, Permafrost and Periglacial Processes, 16, 163-172, doi:10.1002/ppp.509, 2005.

Grosse, G., Schirrmeister, L., and Malthus, T. J.: Application of Landsat-7 satellite data and a DEM for the quantification of thermokarst-affected terrain types in the periglacial Lena-Anabar coastal lowland, Polar Research, 25, 51-67, doi:10.1111/j.1751-8369.2006.tb00150.x, 2006.

Grosse, G., Schirrmeister, L., Siegert, C., Kunitsky, V. V., Slagoda, E. A., Andreev, A. A., and Dereviagyn, A. Y.: Geological and geomorphological evolution of a sedimentary periglacial landscape in Northeast Siberia during the Late Quaternary, Geomorphology, 86, 25-51, 2007.

Grosse, G., Romanovsky, V. E., Walter, K. M., Morgenstern, A., Lantuit, H., and Zimov, S.: Distribution of thermokarst lakes and ponds at three Yedoma sites in Siberia, Proceedings of the 9th International Conference on Permafrost, 1, 551-556, 2008.

Grosse, G., Harden, J., Turetsky, M. R., McGuire, A. D., Camill, P., Tarnocai, C., Frolking, S., Schuur, E. A. G., Jorgenson, T., Marchenko, S., Romanovsky, V., Wickland, K. P., French, N., Waldrop, M. P., Bourgeau-Chavez, L., and Striegl, R. G.: Vulnerability of high-latitude soil organic carbon in North America to disturbance, Journal of Geophysical Research: Biogeosciences, 116, G00K06, doi:10.1029/2010JG001507, 2011a.

Grosse, G., Romanovsky, V., Jorgenson, T., Anthony, K. W., Brown, J., and Overduin, P. P.: Vulnerability and feedbacks of permafrost to climate change, Eos, Transactions American Geophysical Union, 92, 73-74, doi:10.1029/2011eo090001, 2011b.

Grosse, G., Jones, B., and Arp, C. D.: Thermokarst lakes, drainage, and drained basins, in: Treatise in Geomorphology, edited by: Shroder, J. F., Academic Press, San Diego, 325-353, 2013a.

Grosse, G., Robinson, J. E., Bryant, R., Taylor, M. D., Harper, W., DeMasi, A., Kyker-Snowman, E., Veremeeva, A., Schirrmeister, L., and Harden, J.: Distribution of late Pleistocene ice-rich syngenetic permafrost of the Yedoma Suite in east and central Siberia, Russia, US Geological Survey Open File Report, 1078, 37, 2013b.

Grosse, G.: A synthesis of thermokarst and thermo-erosion rates in northern permafrost regions, in preparation.

Grosswald, M. G.: Late-Weichselian ice sheets in Arctic and Pacific Siberia, Quaternary International, 45, 3-18, 1998.

Gubin, S. V.: Late Pleistocene soil formation on coastal lowlands of northern Yakutia, Eurasian Soil Science, 27, 19-32, 1995.

Gubin, S. V., and Veremeeva, A. A.: Parent materials enriched in organic matter in the northeast of Russia, Eurasian Soil Science, 43, 1238-1243, doi:10.1134/s1064229310110062, 2010.

Gundelwein, A., Muller-Lupp, T., Sommerkorn, M., Haupt, E. T. K., Pfeiffer, E., and Wiechmann, H.: Carbon in tundra soils in the Lake Labaz region of arctic Siberia, European Journal of Soil Science, 58, 1164-1174, doi:10.1111/j.1365-2389.2007.00908.x, 2007.

Günther, F., Overduin, P. P., Sandakov, A., Grosse, G., and Grigoriev, M. N.: Thermo-erosion along the Yedoma Coast of the Buor Khaya Peninsula, Laptev Sea, East Siberia, Proceedings of the 10th International Conference on Permafrost, Volume 1: International Contributions, 137-142, 2012.

Günther, F., Overduin, P. P., Sandakov, A. V., Grosse, G., and Grigoriev, M. N.: Short- and long-term thermo-erosion of ice-rich permafrost coasts in the Laptev Sea region, Biogeosciences, 10, 4297-4318, doi:10.5194/bg-10-4297-2013, 2013.

Hammer, Ø., Harper, D. A. T., and Ryan, P. D.: PAST: Paleontological statistics software package for education and data analysis, Palaeontolia Electronica, 4, 1-10, 2012.

Harden, J. W., Trumbore, S. E., Stocks, B. J., Hirsch, A., Gower, S. T., O'Neill, K. P., and Kasischke, E. S.: The role of fire in the boreal carbon budget, Global Change Biology, 6, 174-184, doi:10.1046/j.1365-2486.2000.06019.x, 2000.

Harden, J. W., Meier, R., Silapaswan, C., Swanson, D. K., and McGuire, A. D.: Soil drainage and its potential for influencing wildfires in Alaska, US Geological Survey Professional Paper 1678, 139-144, 2001.

Harden, J. W., Manies, K. L., Turetsky, M. R., and Neff, J. C.: Effects of wildfire and permafrost on soil organic matter and soil climate in interior Alaska, Global Change Biology, 12, 2391-2403, doi:10.1111/j.1365-2486.2006.01255.x, 2006.

Harden, J. W., Koven, C. D., Ping, C. L., Hugelius, G., McGuire, A. D., Camill, P., Jorgenson, T., Kuhry, P., Michaelson, G. J., O'Donnell, J. A., Schuur, E. A. G., Tarnocai, C., Johnson, K., and Grosse, G.: Field information links permafrost carbon to physical vulnerabilities of thawing, Geophysical Research Letters, 39, L15704, doi:10.1029/2012gl051958, 2012.

Hayes, D. J., McGuire, A. D., Kicklighter, D. W., Gurney, K. R., Burnside, T. J., and Melillo, J. M.: Is the northern high-latitude land-based CO_2 sink weakening?, Global Biogeochemical Cycles, 25, GB3018, doi:10.1029/2010gb003813, 2011.

Hayes, D. J., Kicklighter, D. W., McGuire, A. D., Chen, M., Zhuang, Q., Yuan, F., Melillo, J. M., and Wullschleger, S. D.: The impacts of recent permafrost thaw on land–atmosphere greenhouse gas exchange, Environmental Research Letters, 9, 045005, doi:10.1088/1748-9326/9/4/045005, 2014.

Heginbottom, J. A., Brown, J., Ferrians, O. J., and Melnikov, E. S.: Circum-arctic map of permafrost and ground ice conditions, 6th International Conference on Permafrost, Beijing, 1132-1136, 1993.

Heginbottom, J. A.: Permafrost distribution and ground ice in surficial materials, in: The physical environment of the Mackenzie Valley, Northwest Territories: A base line for the assessment of environmental change, edited by: Dyke, L. D., and Brooks, G. R., Geological Survey of Canada Bulletin 547, Ottawa, 31-39, 2000.

Heyer, J., Hübner, H., and Maaβ, I.: Isotopenfraktionierung des Kohlenstoffs bei der mikrobiellen Methanbildung, Isotopes in Environmental and Health Studies, 12, doi:10.1080/10256017608543912, 1976.

Hinkel, K. M., and Nelson, F. E.: Spatial and temporal patterns of active layer thickness at Circumpolar Active Layer Monitoring (CALM) sites in northern Alaska, 1995–2000, Journal of Geophysical Research: Atmospheres, 108, 8168, doi:10.1029/2001jd000927, 2003.

Hjulström, F.: Transportation of detritus by moving water, in: Recent marine sediments, edited by: Trask, P. D., 4, American Association of Petroleum Geologists, 5-31, 1939.

Hodgkins, S. B., Tfaily, M. M., McCalley, C. K., Logan, T. A., Crill, P. M., Saleska, S. R., Rich, V. I., and Chanton, J. P.: Changes in peat chemistry associated with permafrost thaw increase greenhouse gas production, Proceedings of the National Academy of Sciences, 111, 5819-5824, doi:10.1073/pnas.1314641111, 2014.

Hoffmann, K.: Holocene climate variability of the central Lena Delta, Northern Siberia – Implications from ground ice, master thesis, Department of Geography, University of Bonn, Bonn, 148 pp., 2011.

Höfle, S., Rethemeyer, J., Mueller, C. W., and John, S.: Organic matter composition and stabilization in a polygonal tundra soil of the Lena Delta, Biogeosciences, 10, 3145-3158, doi:10.5194/bg-10-3145-2013, 2013.

Hopkins, D. M.: Aspects of the paleogeography of Beringia during the Late Pleistocene, in: Paleoecology of Beringia, edited by: Hopkins, D. M., Matthews, J. V., Schweger, C. E., and Young, S. B., Academic Press, 3-28, 1982.

Horn, R.: Bodenphysik, in: Scheffer/Schachtschabel - Lehrbuch der Bodenkunde, 15 ed., edited by: Blume, H.-P., Brummer, G. W., Schwertmann, U., Horn, R., Kögel-Knabner, I., Stahr, K., Auerswald, K., Beyer, L., Hartmann, A., Litz, N., Scheinost, A., Stanjek, H., Welp, G., and Wilke, B.-M., Spektrum Akademischer Verlag Heidelberg, 155-271, 2002.

Horwath Burnham, J., and Sletten, R. S.: Spatial distribution of soil organic carbon in northwest Greenland and underestimates of high Arctic carbon stores, Global Biogeochemical Cycles, 24, GB3012, doi:10.1029/2009gb003660, 2010.

Houghton, R. A.: Balancing the global carbon budget, Annual Review of Earth and Planetary Sciences, 35, 313-347, doi:10.1146/annurev.earth.35.031306.140057, 2007.

Hubberten, H. W., Andreev, A., Astakhov, V. I., Demidov, I., Dowdeswell, J. A., Henriksen, M., Hjort, C., Houmark-Nielsen, M., Jakobsson, M., Kuzmina, S., Larsen, E., Pekka Lunkka, J., Lysa, A., Mangerud, J., Möller, P., Saarnisto, M., Schirrmeister, L., Sher, A. V., Siegert, C., Siegert, M. J., and Svendsen, J. I.: The periglacial climate and environment in northern Eurasia during the Last Glaciation, Quaternary Science Reviews, 23, 1333-1357, doi:10.1016/j.quascirev.2003.12.012, 2004.

Hugelius, G., and Kuhry, P.: Landscape partitioning and environmental gradient analyses of soil organic carbon in a permafrost environment, Global Biogeochemical Cycles, 23, GB3006, doi:10.1029/2008gb003419, 2009.

Hugelius, G., Virtanen, T., Kaverin, D., Pastukhov, A., Rivkin, F., Marchenko, S., Romanovsky, V., and Kuhry, P.: High-resolution mapping of ecosystem carbon storage and potential effects of permafrost thaw in periglacial terrain, European Russian Arctic, Journal of Geophysical Research: Biogeosciences, 116, G03024, doi:10.1029/2010jg001606, 2011.

Hugelius, G.: Spatial upscaling using thematic maps: An analysis of uncertainties in permafrost soil carbon estimates, Global Biogeochemical Cycles, 26, GB2026, doi:10.1029/2011gb004154, 2012.

Hugelius, G., Routh, J., Kuhry, P., and Crill, P.: Mapping the degree of decomposition and thaw remobilization potential of soil organic matter in discontinuous permafrost terrain, Journal of Geophysical Research: Biogeosciences, 117, G02030, doi:10.1029/2011jg001873, 2012.

Hugelius, G., Bockheim, J. G., Camill, P., Elberling, B., Grosse, G., Harden, J. W., Johnson, K., Jorgenson, T., Koven, C. D., Kuhry, P., Michaelson, G., Mishra, U., Palmtag, J., Ping, C.-L., O'Donnell, J., Schirrmeister, L., Schuur, E. A. G., Sheng, Y., Smith, L. C., Strauss, J., and Yu, Z.: A new data set for estimating organic carbon storage to 3m depth in soils of the northern circumpolar permafrost region, Earth System Science Data, 5, 393-402, doi:10.5194/essd-5-393-2013, 2013a.

Hugelius, G., Tarnocai, C., Broll, G., Canadell, J. G., Kuhry, P., and Swanson, D. K.: The northern circumpolar soil carbon database: Spatially distributed datasets of soil coverage and soil carbon storage in the northern permafrost regions, Earth System Science Data, 5, 3-13, doi:10.5194/essd-5-3-2013, 2013b.

Hugelius, G., Strauss, J., Zubrzycki, S., Harden, J., Schuur, E. A. G., Ping, C.-L., Schirrmeister, L., Grosse, G., Michaelson, G., Koven, C., O'Donnel, J., Elberling, B., Mishra, U., Camill, P., Yu, Z., Palmtag, J., and Kuhry, P.: Estimated stocks of circumpolar permafrost carbon with quantified uncertainty ranges and identified data gaps, Biogeosciences, 11, 6573-6593, doi:10.5194/bg-11-6573-2014, 2014.

Jafarov, E. E., Marchenko, S. S., and Romanovsky, V. E.: Numerical modeling of permafrost dynamics in Alaska using a high spatial resolution dataset, The Cryosphere, 6, 613-624, doi:10.5194/tc-6-613-2012, 2012.

Jenkinson, D. S., Poulton, P. R., and Bryant, C.: The turnover of organic carbon in subsoils. Part 1. Natural and bomb radiocarbon in soil profiles from the Rothamsted long-term field experiments, European Journal of Soil Science, 59, 391-399, doi:10.1111/j.1365-2389.2008.01025.x, 2008.

Johannessen, O. M., Bengtsson, L., Miles, M. W., Kuzmina, S. I., Semenov, V. A., Alekseev, G. V., Nagurnyi, A. P., Zakharov, V. F., Bobylev, L. P., Pettersson, L. H., Hasselmann, K., and Cattle, H. P.: Arctic climate change: Observed and modelled temperature and sea-ice variability, Tellus Series A, 56, 328-341, doi:10.1111/j.1600-0870.2004.00060.x, 2004.

Johnson, K. D., Harden, J., McGuire, A. D., Bliss, N. B., Bockheim, J. G., Clark, M., Nettleton-Hollingsworth, T., Jorgenson, M. T., Kane, E. S., Mack, M., O'Donnell, J., Ping, C.-L., Schuur, E. A. G., Turetsky, M. R., and Valentine, D. W.: Soil carbon distribution in Alaska in relation to soil-forming factors, Geoderma, 167–168, 71-84, doi:10.1016/j.geoderma.2011.10.006, 2011.

Johnston, G. H., and Brown, R. J. E.: Stratigraphy of the Mackenzie River Delta, Northwest Territories, Canada, Geological Society of America Bulletin, 76, 103-112, doi:10.1130/0016-7606(1965)76[103:sotmrd]2.0.co;2, 1965.

Jones, B. M., Arp, C. D., Jorgenson, M. T., Hinkel, K. M., Schmutz, J. A., and Flint, P. L.: Increase in the rate and uniformity of coastline erosion in Arctic Alaska, Geophysical Research Letters, 36, L03503, doi:10.1029/2008gl036205, 2009.

Jones, B. M., Grosse, G., Arp, C. D., Jones, M. C., Walter Anthony, K. M., and Romanovsky, V. E.: Modern thermokarst lake dynamics in the continuous permafrost zone, northern Seward Peninsula, Alaska, Journal of Geophysical Research: Biogeosciences, 116, G00M03, doi:10.1029/2011JG001666, 2011.

Jones, M. C., Grosse, G., Jones, B. M., and Walter Anthony, K. M.: Peat accumulation in drained thermokarst lake basins in continuous, ice-rich permafrost, northern Seward Peninsula, Alaska, Journal of Geophysical Research: Biogeosciences, 117, G00M07, doi:10.1029/2011JG001766, 2012.

Jones, M. C., Booth, R. K., Yu, Z. C., and Ferry, P.: A 2200-year record of permafrost dynamics and carbon cycling in a collapse-scar bog, Interior Alaska, Ecosystems, 16, 1-19, doi:10.1007/s10021-012-9592-5, 2013.

Jorgenson, M. T., Shur, Y. L., and Pullman, E. R.: Abrupt increase in permafrost degradation in Arctic Alaska, Geophysical Research Letters, 33, L02503, doi:10.1029/2005gl024960, 2006.

Jorgenson, M. T., Yoshikawa, K., Kanveskiy, M., Shur, Y., Romanovsky, V., Marchenko, S., Grosse, G., Brown, J., and Jones, B.: Permafrost characteristics of Alaska, Proceedings of the 9th International Conference on Permafrost, 3, 121–122, 2008.

Jorgenson, M. T., Romanovsky, V., Harden, J., Shur, Y., O'Donnell, J., Schuur, E. A. G., Kanevskiy, M., and Marchenko, S.: Resilience and vulnerability of permafrost to climate change, Canadian Journal of Forest Research, 40, 1219-1236, doi:10.1139/x10-060, 2010.

Kaakinen, A., and Lunkka, J. P.: Sedimentation of the Late Miocene Bahe Formation and its implications for stable environments adjacent to Qinling mountains in Shaanxi, China, Journal of Asian Earth Sciences, 22, 67-78, doi:10.1016/s1367-9120(03)00044-0, 2003.

Kanevskiy, M., Shur, Y., Fortier, D., Jorgenson, M. T., and Stephani, E.: Cryostratigraphy of late Pleistocene syngenetic permafrost (yedoma) in northern Alaska, Itkillik River exposure, Quaternary Research, 75, 584-596, doi:10.1016/j.yqres.2010.12.003, 2011.

Kanevskiy, M., Shur, Y., Connor, B., Dillon, M., Stephani, E., and O'Donnell, J.: Study of the ice-rich syngenetic permafrost for road design (Interior Alaska), Proceedings of the 10th International Conference on Permafrost, 1, 191-196, 2012.

Kanevskiy, M., Shur, Y., Jorgenson, M. T., Ping, C. L., Michaelson, G. J., Fortier, D., Stephani, E., Dillon, M., and Tumskoy, V.: Ground ice in the upper permafrost of the Beaufort Sea coast of Alaska, Cold Regions Science and Technology, 85, 56-70, doi:10.1016/j.coldregions.2012.08.002, 2013.

Kanevskiy, M., Shur, Y. L., Fortier, D., French, H., Jorgenson, M. T., Stephani, E., Strauss, J., and Vasiliev, A.: Patterns and rates of riverbank erosion in the area of ice-rich permafrost (Yedoma), Itkillik River, Northern Alaska, Geomorphology, in preparation.

Kaplina, T. N., Giterman, R. E., Lakhtina, O. V., Abrashov, B. A., Kiselyov, S. V., and Sher, A. V.: Duvannyy Yar - a key section of Upper Pleistocene deposits of the Kolyma lowland, Bulletin of Quaternary Research Commission, 48, 49–65, 1978.

Kaplina, T. N., Kostalyndina, N. K., and Leibman, M. O.: Relief analysis of the Kolyma lowlands for cryolithological mapping, in: Formation of frozen ground and prognosis of cryogenic processes, Nauka, Moscow, 51-60, 1986.

Kaufman, D. S., Ager, T. A., Anderson, N. J., Anderson, P. M., Andrews, J. T., Bartlein, P. J., Brubaker, L. B., Coats, L. L., Cwynar, L. C., Duvall, M. L., Dyke, A. S., Edwards, M. E., Eisner, W. R., Gajewski, K., Geirsdóttir, A., Hu, F. S., Jennings, A. E., Kaplan, M. R., Kerwin, M. W., Lozhkin, A. V., MacDonald, G. M., Miller, G. H., Mock, C. J., Oswald, W. W., Otto-Bliesner, B. L., Porinchu, D. F., Rühland, K., Smol, J. P., Steig, E. J., and Wolfe, B. B.: Holocene thermal maximum in the western Arctic (0–180°W), Quaternary Science Reviews, 23, 529-560, doi:10.1016/j.quascirev.2003.09.007, 2004.

Kenkkilä, J.: The laser diffraction grain size analysis of late Miocene flood-plain sediments from Lantian, in Shaanxi province, northern China, Department of Geology, University of Helsinki, 43 pp., 2005.

Kessler, M. A., Plug, L. J., and Walter Anthony, K. M.: Simulating the decadal- to millennial-scale dynamics of morphology and sequestered carbon mobilization of two thermokarst lakes in NW Alaska, Journal of Geophysical Research: Biogeosciences, 117, G00M06, doi:10.1029/2011jg001796, 2012.

Khvorostyanov, D. V., Ciais, P., Krinner, G., and Zimov, S. A.: Vulnerability of east Siberia's frozen carbon stores to future warming, Geophysical Research Letters, 35, L10703, doi:10.1029/2008GL033639, 2008.

Killops, S. D., and Killops, V. J.: Introduction to organic geochemistry, John Wiley & Sons, New York, 393 pp., 2009.

Kleinen, T., Brovkin, V., and Schuldt, R. J.: A dynamic model of wetland extent and peat accumulation: results for the Holocene, Biogeosciences, 9, 235-248, doi:10.5194/bg-9-235-2012, 2012.

Klovan, J., and Imbrie, J.: An algorithm and Fortran-IV program for large-scale Q-mode factor analysis and calculation of factor scores, Mathematical Geology, 3, 61-77, doi:10.1007/bf02047433, 1971.

Knoblauch, C., Beer, C., Sosnin, A., Wagner, D., and Pfeiffer, E.-M.: Predicting long-term carbon mineralization and trace gas production from thawing permafrost of Northeast Siberia, Global Change Biology, 19, 1160–1172, doi:10.1111/gcb.12116, 2013.

Kokelj, S. V., Lacelle, D., Lantz, T. C., Tunnicliffe, J., Malone, L., Clark, I. D., and Chin, K. S.: Thawing of massive ground ice in mega slumps drives increases in stream sediment and solute flux across a range of watershed scales, Journal of Geophysical Research: Earth Surface, 118, 681-692, doi:10.1002/jgrf.20063, 2013.

Konishchev, V. N.: Cryolithological evidences of the heterogeneous structure of "Ice Complex" deposits in the Dyvanny Yar section, in: Problems of cryolithology, Moscow University Press, 56-64, 1983.

Konishchev, V. N.: Origin of loess-like silt in Northern Jakutia, USSR, GeoJournal, 15, 135-139, 1987.

Konishchev, V. N., and Rogov, V. V.: Investigations of cryogenic weathering in Europe and Northern Asia, Permafrost and Periglacial Processes, 4, 49-64, doi:10.1002/ppp.3430040105, 1993.

Koven, C., Friedlingstein, P., Ciais, P., Khvorostyanov, D., Krinner, G., and Tarnocai, C.: On the formation of high-latitude soil carbon stocks: Effects of cryoturbation and insulation by organic matter in a land surface model, Geophysical Research Letters, 36, L21501, doi:10.1029/2009GL040150, 2009.

Koven, C. D., Ringeval, B., Friedlingstein, P., Ciais, P., Cadule, P., Khvorostyanov, D., Krinner, G., and Tarnocai, C.: Permafrost carbon-climate feedbacks accelerate global warming, Proceedings of the National Academy of Sciences, 108, 14769-14774, doi:10.1073/pnas.1103910108, 2011.

Koven, C. D., Riley, W. J., and Stern, A.: Analysis of permafrost thermal dynamics and response to climate change in the CMIP5 earth system models, Journal of Climate, 26, 1877-1900, doi:10.1175/JCLI-D-12-00228.1, 2013a.

Koven, C. D., Riley, W. J., Subin, Z. M., Tang, J. Y., Torn, M. S., Collins, W. D., Bonan, G. B., Lawrence, D. M., and Swenson, S. C.: The effect of vertically resolved soil biogeochemistry and alternate soil C and N models on C dynamics of CLM4, Biogeosciences, 10, 7109-7131, doi:10.5194/bg-10-7109-2013, 2013b.

Krinner, G., and Boike, J.: A study of the large-scale climatic effects of a possible disappearance of high-latitude inland water surfaces during the 21st century, Boreal Environment Research 15, 203-217, 2010.

Kuesel, K., and Drake, H. L.: Effects of environmental parameters on the formation and turnover of acetate by forest soils, Applied and environmental microbiology, 61, 3667-3675, 1995.

Kuhry, P., and Vitt, D. H.: Fossil carbon/nitrogen ratios as a measure of peat decomposition, Ecology, 77, 271-275, doi:10.2307/2265676, 1996.

Kuhry, P., Ping, C.-L., Schuur, E. A. G., Tarnocai, C., and Zimov, S.: Report from the International Permafrost Association: Carbon pools in permafrost regions, Permafrost and Periglacial Processes, 20, 229-234, doi:10.1002/ppp.648, 2009.

Kuhry, P., Dorrepaal, E., Hugelius, G., Schuur, E. A. G., and Tarnocai, C.: Potential remobilization of belowground permafrost carbon under future global warming, Permafrost and Periglacial Processes, 21, 208-214, doi:10.1002/ppp.684, 2010.

Kuhry, P., Grosse, G., Harden, J. W., Hugelius, G., Koven, C. D., Ping, C. L., Schirrmeister, L., and Tarnocai, C.: Characterisation of the Permafrost Carbon Pool, Permafrost and Periglacial Processes, 24, 146-155, doi:10.1002/ppp.1782, 2013.

Kumada, K.: Chemistry of soil organic matter, Developments in Soil Science, Elsevier, Amsterdam, 1987.

Kunitsky, V. V., Schirrmeister, L., Grosse, G., and Kienast, F.: Snow patches in nival landscapes and their role for the Ice Complex formation in the Laptev Sea coastal lowlands, Polarforschung, 70, 53-67, 2002.

Kutzbach, L., Wille, C., and Pfeiffer, E. M.: The exchange of carbon dioxide between wet arctic tundra and the atmosphere at the Lena River Delta, Northern Siberia, Biogeosciences, 4, 869-890, doi:10.5194/bg-4-869-2007, 2007.

Lai, R.: Soil carbon sequestration in natural and managed tropical forest ecosystems, Journal of Sustainable Forestry, 21, 1-30, doi:10.1300/J091v21n01_01, 2004.

Langer, M., Westermann, S., Heikenfeld, M., Dorn, W., and Boike, J.: Satellite-based modeling of permafrost temperatures in a tundra lowland landscape, Remote Sensing of Environment, 135, 12-24, doi:10.1016/j.rse.2013.03.011, 2013.

Lantuit, H., Overduin, P. P., Couture, N., Wetterich, S., Aré, F., Atkinson, D., Brown, J., Cherkashov, G., Drozdov, D. S., Forbes, D. L., Graves-Gaylord, A., Grigoriev, M., Hubberten, H.-W., Jordan, J., Jorgenson, T., Ødegård, R. S., Ogorodov, S., Pollard, W. H., Rachold, V., Sedenko, S., Solomon, S., Steenhuisen, F., Streletskaya, I., and Vasiliev, A. A.: The arctic coastal dynamics database: A new classification scheme and statistics on Arctic permafrost coastlines, Estuaries and Coasts, 35, 383-400, doi:10.1007/s12237-010-9362-6, 2012.

Lantz, T. C., and Kokelj, S. V.: Increasing rates of retrogressive thaw slump activity in the Mackenzie Delta region, N.W.T., Canada, Geophysical Research Letters, 35, L06502, doi:10.1029/2007gl032433, 2008.

Laurion, I., Vincent, W. F., MacIntyre, S., Retamal, L., Dupont, C., Francus, P., and Pienitz, R.: Variability in greenhouse gas emissions from permafrost thaw ponds, Limnology and Oceanography, 55, 115, 2010.

Lawrence, D., and Slater, A.: Incorporating organic soil into a global climate model, Climate Dynamics, 30, 145-160, doi:10.1007/s00382-007-0278-1, 2008.

Lawrence, D. M., Oleson, K. W., Flanner, M. G., Thornton, P. E., Swenson, S. C., Lawrence, P. J., Zeng, X., Yang, Z.-L., Levis, S., Sakaguchi, K., Bonan, G. B., and Slater, A. G.: Parameterization improvements and functional and structural advances in Version 4 of the Community Land Model, Journal of Advances in Modeling Earth Systems, 3, M03001, doi:10.1029/2011ms00045, 2011.

Lee, H., Schuur, E. A. G., Inglett, K. S., Lavoie, M., and Chanton, J. P.: The rate of permafrost carbon release under aerobic and anaerobic conditions and its potential effects on climate, Global Change Biology, 18, 515-527, doi:10.1111/j.1365-2486.2011.02519.x, 2012.

Lee, S. H., Jang, I., Chae, N., Choi, T., and Kang, H.: Organic layer serves as a hotspot of microbial activity and abundance in Arctic tundra soils, Microbial Ecology, 65, 405-414, doi:10.1007/s00248-012-0125-8, 2013.

Lehner, B., and Döll, P.: Development and validation of a global database of lakes, reservoirs and wetlands, Journal of Hydrology, 296, 1-22, doi:10.1016/j.jhydrol.2004.03.028, 2004.

Li, J., Luo, Y., Natali, S., Schuur, E. A. G., Xia, J., Kowalczyk, E., and Wang, Y.: Modeling permafrost thaw and ecosystem carbon cycle under annual and seasonal warming at an Arctic tundra site in Alaska, Journal of Geophysical Research: Biogeosciences, 119, 2013JG002569, doi:10.1002/2013jg002569, 2014.

Lide, D. R., Baysinger, G., Kehiaian, H. V., Berger, L. I., Kuchitsu, K., Goldberg, R. N., Roth, D. L., Haynes, W. M., and Zwillinger, D.: Properties of ice and supercooled water, in: CRC Handbook of Chemistry and Physics, 89th ed., edited by: Lide, D. R., Baysinger, G., Kehiaian, H. V., Berger, L. I., Kuchitsu, K., Goldberg, R. N., Roth, D. L., Haynes, W. M., and Zwillinger, D., CRC Press/Taylor and Francis, Boca Raton, Florida, 1101, 2008.

Ling, F., and Zhang, T.: Numerical simulation of permafrost thermal regime and talik development under shallow thaw lakes on the Alaskan Arctic coastal plain, Journal of Geophysical Research: Atmospheres, 108, 4511, doi:10.1029/2002jd003014, 2003.

Ling, F., Wu, Q., Zhang, T., and Niu, F.: Modelling open-talik formation and permafrost lateral thaw under a thermokarst lake, Beiluhe Basin, Qinghai-Tibet Plateau, Permafrost and Periglacial Processes, 23, 312-321, doi:10.1002/ppp.1754, 2012.

Lopatina, D., and Zanina, O.: Paleobotanical analysis of materials from fossil gopher burrows and upper pleistocene host deposits, the Kolyma River lower reaches, Stratigraphy and Geological Correlation, 14, 549-560, doi:10.1134/s0869593806050078, 2006.

Luo, Q., Yu, S., Liu, Y., Zhang, Y., Han, H., Qi, L., and Zhong, N.: Existence and implications of hop-17(21)-enes in the lower Cretaceous of the Saihantala Sag, Erlian Basin, China, Petroleum Science, 9, 154-160, doi:10.1007/s12182-012-0195-8, 2012.

MacDougall, A. H., Avis, C. A., and Weaver, A. J.: Significant contribution to climate warming from the permafrost carbon feedback, Nature Geoscience, 5, 719-721, doi:10.1038/ngeo1573, 2012.

Mack, M. C., Bret-Harte, M. S., Hollingsworth, T. N., Jandt, R. R., Schuur, E. A. G., Shaver, G. R., and Verbyla, D. L.: Carbon loss from an unprecedented Arctic tundra wildfire, Nature, 475, 489-492, doi:10.1038/nature10283, 2011.

Mackelprang, R., Waldrop, M. P., DeAngelis, K. M., David, M. M., Chavarria, K. L., Blazewicz, S. J., Rubin, E. M., and Jansson, J. K.: Metagenomic analysis of a permafrost microbial community reveals a rapid response to thaw, Nature, 480, 368-371, doi:10.1038/nature10576, 2011.

Magens, D.: Late Quaternary climate and environmental history of the Siberian Arctic - Permafrost records from Cape Mamontovy Klyk, Laptev Sea, master thesis, Department of Geography, Christian-Albrechts-University Kiel, Kiel, 131 pp., 2005.

Mangelsdorf, K., Finsel, E., Liebner, S., and Wagner, D.: Temperature adaptation of microbial communities in different horizons of Siberian permafrost-affected soils from the Lena Delta, Chemie der Erde - Geochemistry, 69, 169-182, doi:10.1016/j.chemer.2009.02.001, 2009.

Mann, P. J., Sobczak, W. V., LaRue, M. M., Bulygina, E., Davydova, A., Vonk, J. E., Schade, J., Davydov, S., Zimov, N., Holmes, R. M., and Spencer, R. G. M.: Evidence for key enzymatic controls on metabolism of Arctic river organic matter, Global Change Biology, 20, 1089-1100, doi:10.1111/gcb.12416, 2014.

Manson, V., and Imbrie, J.: FORTRAN program for factor and vector analysis of geologic data using an IBM 7090 or 7094/1401 computer system, State Geological Survey, University of Kansas, Lawrence, 46 pp., 1964.

Marcott, S. A., Shakun, J. D., Clark, P. U., and Mix, A. C.: A reconstruction of regional and global temperature for the past 11,300 years, Science, 339, 1198-1201, doi:10.1126/science.1228026, 2013.

Marzi, R., Torkelson, B. E., and Olson, R. K.: A revised carbon preference index, Organic Geochemistry, 20, 1303-1306, doi:10.1016/0146-6380(93)90016-5, 1993.

Mascarelli, A.: A sleeping giant?, Nature Reports Climate Change, 3, 46-49, doi:10.1038/climate.2009.24, 2009.

McGuire, A. D., Anderson, L. G., Christensen, T. R., Dallimore, S., Guo, L., Hayes, D. J., Heimann, M., Lorenson, T. D., Macdonald, R. W., and Roulet, N.: Sensitivity of the carbon cycle in the Arctic to climate change, Ecological Monographs, 79, 523-555, doi:10.1890/08-2025.1, 2009.

McGuire, A. D., Macdonald, R. W., Schuur, E. A. G., Harden, J. W., Kuhry, P., Hayes, D. J., Christensen, T. R., and Heimann, M.: The carbon budget of the northern cryosphere region, Current Opinion in Environmental Sustainability, 2, 231-236, doi:10.1016/j.cosust.2010.05.003, 2010.

McKane, R. B., Rastetter, E. B., Shaver, G. R., Nadelhoffer, K. J., Giblin, A. E., Laundre, J. A., and Chapin, F. S.: Climatic effects on tundra carbon storage inferred from experimental data and a model, Ecology, 78, 1170-1187, doi:10.1890/0012-9658(1997)078[1170:ceotcs]2.0.co;2, 1997.

Mergelov, N., and Targulian, V.: Accumulation of organic matter in the mineral layers of permafrost-affected soils of coastal lowlands in East Siberia, Eurasian Soil Science, 44, 249-260, doi:10.1134/s1064229311030069, 2011.

Meyer, H., Dereviagin, A., Siegert, C., and Hubberten, H. W.: Paleoclimate studies on Bykovsky Peninsula, North Siberia - Hydrogen and oxygen isotopes in ground ice, Polarforschung, 70, 37–51, doi:10.1594/PANGAEA.728530, 2002a.

Meyer, H., Dereviagin, A., Siegert, C., Schirrmeister, L., and Hubberten, H.-W.: Palaeoclimate reconstruction on Big Lyakhovsky Island, north Siberia - Hydrogen and oxygen isotopes in ice wedges, Permafrost and Periglacial Processes, 13, 91-105, doi:10.1002/ppp.416, 2002b.

Meyer, H., Yoshikawa, K., Schirrmeister, L., and Andreev, A.: The Vault Creek tunnel (Fairbanks region, Alaska): A Late Quaternary palaeoenvironmental permafrost record, 9th International Conference on Permafrost, Fairbanks, Alaska, 1191-1196, 2009.

Meyers, P. A.: Preservation of elemental and isotopic source identification of sedimentary organic matter, Chemical Geology, 114, 289-302, doi:10.1016/0009-2541(94)90059-0, 1994.

Michaelson, G. J., Ping, C., and Kimble, J.: Carbon storage and distribution in tundra soils of Arctic Alaska, USA, Arctic and Alpine Research, 414-424, doi:10.2307/1551852, 1996.

Miesch, A. T.: Q-mode factor analysis of geochemical and petrologic data matrices with constant row sums, US Geological Survey Professional Paper 574-G, 47, 1976.

Mishra, U., Jastrow, J., Matamala, R., Hugelius, G., Koven, C., Harden, J., Ping, C., Michaelson, G., Fan, Z., and Miller, R.: Empirical estimates to reduce modeling uncertainties of soil organic carbon in permafrost regions: A review of recent progress and remaining challenges, Environmental Research Letters, 8, 035020, doi:10.1088/1748-9326/8/3/035020, 2013.

Morgenstern, A., Grosse, G., and Schirrmeister, L.: Genetic, morphological, and statistical characterization of lakes in the permafrost-dominated Lena Delta, 9th International Conference on Permafrost, Fairbanks, 1239-1244, 2008.

Morgenstern, A., Grosse, G., Günther, F., Fedorova, I., and Schirrmeister, L.: Spatial analyses of thermokarst lakes and basins in Yedoma landscapes of the Lena Delta, The Cryosphere, 5, 849-867, doi:10.5194/tc-5-849-2011, 2011.

Morgenstern, A.: Thermokarst and thermal-erosion: Degradation of Siberian ice-rich permafrost, PhD thesis, Institute of Earth and Environmental Science and Alfred Wegener Institute for Polar and Marine Research, Potsdam University, Potsdam, 116 pp., 2012.

Morgenstern, A., Ulrich, M., Günther, F., Roessler, S., Fedorova, I. V., Rudaya, N. A., Wetterich, S., Boike, J., and Schirrmeister, L.: Evolution of thermokarst in East Siberian ice-rich permafrost: A case study, Geomorphology, 201, 363-379, doi:10.1016/j.geomorph.2013.07.011, 2013.

Mu, C., Zhang, T., Schuster, P. F., Schaefer, K., Wickland, K. P., Repert, D. A., Liu, L., Schaefer, T., and Cheng, G.: Carbon and geochemical properties of cryosols on the North Slope of Alaska, Cold Regions Science and Technology, 100, 59-67, doi:10.1016/j.coldregions.2014.01.001, 2014.

Muhs, D. R., and Bettis, E.: Quaternary loess-paleosol sequences as examples of climate-driven sedimentary extremes, in: Extreme depositional environments: Mega end members in geologic time, edited by: Chan, M. A., and Archer, A. W., Geological Society of America Special Paper 370, Boulder, Colorado, 53-74, 2003.

Myhre, G., Highwood, E. J., Shine, K. P., and Stordal, F.: New estimates of radiative forcing due to well mixed greenhouse gases, Geophysical Research Letters, 25, 2715-2718, doi:10.1029/98GL01908, 1998.

Nagaoka, D.: Properties of Ice Complex deposits in eastern Siberia, 2nd Symposium on the Joint Siberian Permafrost Studies between Japan and Russia, Tsukuba, Japan, 14–18, 1994.

Nagaoka, D., Saijo, K., and Fukuda, M.: Sedimental environment of the Edoma in high Arctic eastern Siberia, Proceedings of the 3rd Symposium on the Joint Siberian Permafrost Studies between Japan and Russia, Tsukuba, Japan, 8-13, 1995.

Natali, S. M., Schuur, E. A. G., Webb, E. E., Pries, C. E. H., and Crummer, K. G.: Permafrost degradation stimulates carbon loss from experimentally warmed tundra, Ecology, 95, 602-608, doi:10.1890/13-0602.1, 2014.

O'Donnell, J. A., Harden, J. W., McGuire, A. D., Kanevskiy, M. Z., Jorgenson, M. T., and Xu, X.: The effect of fire and permafrost interactions on soil carbon accumulation in an upland black spruce ecosystem of interior Alaska: implications for post-thaw carbon loss, Global Change Biology, 17, 1461-1474, doi:10.1111/j.1365-2486.2010.02358.x, 2011.

O'Haver, T.: Interactive Peak Fitter: http://terpconnect.umd.edu/~toh/spectrum/InteractivePeakFitter.htm, access: 2010/10/12,2010.

Oksanen, J.: Multivariate Analysis of Ecological Communities in R: vegan tutorial, University of Oulu, Oulu, 43 pp., 2013.

Olefeldt, D., Turetsky, M. R., Crill, P. M., and McGuire, A. D.: Environmental and physical controls on northern terrestrial methane emissions across permafrost zones, Global Change Biology, 19, 589-603, doi:10.1111/gcb.12071, 2013.

Opel, T., Dereviagin, A. Y., Meyer, H., Schirrmeister, L., and Wetterich, S.: Palaeoclimatic information from stable water isotopes of Holocene ice wedges on the Dmitrii Laptev Strait, northeast Siberia, Russia, Permafrost and Periglacial Processes, 22, 84-100, doi:10.1002/ppp.667, 2011.

Osterkamp, T. E.: Causes of warming and thawing permafrost in Alaska, Eos, Transactions American Geophysical Union, 88, 522-523, doi:10.1029/2007eo480002, 2007.

Parmentier, F. J. W., van der Molen, M. K., van Huissteden, J., Karsanaev, S. A., Kononov, A. V., Suzdalov, D. A., Maximov, T. C., and Dolman, A. J.: Longer growing seasons do not increase net

carbon uptake in the northeastern Siberian tundra, Journal of Geophysical Research: Biogeosciences, 116, G04013, doi:10.1029/2011jg001653, 2011.

Péwé, T. L.: Quaternary geology of Alaska, US Geological Survey Professional Paper 835, 1975.

Péwé, T. L., and Journaux, A.: Origin and character of loesslike silt in unglaciated south-central Yakutia, Siberia, USSR, US Geological Survey Professional Paper 1262, 1983.

Pfeiffer, E.-M., and Janssen, H.: Characterization of organic carbon, using the delta13C-value of a permafrost site in the Kolyma-Indigirka-Lowland, Northeast Siberia, Conference on Classification, Correleation, and Management, and Management of Permafrost-affected Soils, 90–98, 1993.

Ping, C.-L., Michaelson, G. J., Guo, L., Jorgenson, M. T., Kanevskiy, M., Shur, Y., Dou, F., and Liang, J.: Soil carbon and material fluxes across the eroding Alaska Beaufort Sea coastline, Journal of Geophysical Research: Biogeosciences, 116, G02004, doi:10.1029/2010jg001588, 2011.

Ping, C. L., Bockheim, J. G., Kimble, J. M., Michaelson, G. J., and Walker, D. A.: Characteristics of cryogenic soils along a latitudinal transect in arctic Alaska, Journal of Geophysical Research: Atmospheres, 103, 28917-28928, doi:10.1029/98jd02024, 1998.

Ping, C. L., Michaelson, G. J., Jorgenson, M. T., Kimble, J. M., Epstein, H., Romanovsky, V. E., and Walker, D. A.: High stocks of soil organic carbon in the North American Arctic region, Nature Geoscience, 1, 615-619, 2008.

Plug, L. J., and West, J. J.: Thaw lake expansion in a two-dimensional coupled model of heat transfer, thaw subsidence, and mass movement, Journal of Geophysical Research: Earth Surface, 114, F01002, doi:10.1029/2006jf000740, 2009.

Poynter, J., and Eglinton, G.: 14. Molecular composition of three sediments from hole 717C: The Bengal Fan, Proceedings of the Ocean Drilling Program: Scientific results, 116, 155-161, 1990.

Poynter, J. G.: Molecular stratigraphy: The recognition of palaeoclimatic signals in organic geochemical data, PhD thesis, School of Chemistry, University of Bristol, Bristol, 324 pp., 1989.

Prins, M. A., and Weltje, G. J.: End-member modeling of siliciclastic grain-size distributions: The late Quaternary record of eolian and fluvial sediment supply to the Arabian Sea and its paleoclimatic significance., in: Numerical Experiments in Stratigraphy: Recent Advances in Stratigraphic and Sedimentologic Computer Simulations, SEPM, edited by: Harbaugh, J., Watney, L., Rankey, G., Slingerland, R., Goldstein, R., and Franseen, E., Society for Sedimentary Geology, pp. 91-111, 1999.

Pye, K.: Aeolian dust and dust deposits, Academic Press London, 334 pp., 1987.

Pye, K.: The nature, origin and accumulation of loess, Quaternary Science Reviews, 14, 653-667, 1995.

Rachold, V., Grigoriev, M. N., Are, F. E., Solomon, S., Reimnitz, E., Kassens, H., and Antonow, M.: Coastal erosion vs riverine sediment discharge in the Arctic Shelf seas, International Journal of Earth Sciences, 89, 450-460, doi:10.1007/s005310000113, 2000.

Radke, M., Willsch, H., and Welte, D. H.: Preparative hydrocarbon group type determination by automated medium pressure liquid chromatography, Analytical Chemistry, 52, 406-411, doi:10.1021/ac50053a009, 1980.

Raynolds, M. K., Walker, D. A., Ambrosius, K. J., Brown, J., Everett, K. R., Kanevskiy, M., Kofinas, G. P., Romanovsky, V. E., Shur, Y., and Webber, P. J.: Cumulative geoecological effects of 62 years of infrastructure and climate change in ice-rich permafrost landscapes, Prudhoe Bay Oilfield, Alaska, Global Change Biology, 20, 1211-1224, doi:10.1111/gcb.12500, 2014.

Reineck, H. E., and Singh, I. B.: Depositional Sedimentary Environments, 2nd ed., Springer, Berlin, Heidelberg, New York, 549 pp., 1980.

Rigor, I. G., Colony, R. L., and Martin, S.: Variations in surface air temperature observations in the Arctic, 1979-97, Journal of Climate, 13, 896-914, 2000.

Roddick, J. C.: Generalized numerical error analysis with applications to geochronology and thermodynamics, Geochimica et Cosmochimica Acta, 51, 2129-2135, doi:10.1016/0016-7037(87)90261-4, 1987.

Romanovskii, N. N.: Fundamentals of Cryogenesis of Lithosphere, Moscow University Press, Moscow, 336 pp., 1993.

Romanovskii, N. N., Hubberten, H. W., Gavrilov, A. V., Tumskoy, V. E., Tipenko, G. S., Grigoriev, M. N., and Siegert, C.: Thermokarst and land–ocean interactions, Laptev sea region, Russia, Permafrost

and Periglacial Processes, 11, 137-152, doi:10.1002/1099-1530(200004/06)11:2<137::aid-ppp345>3.0.co;2-l, 2000.

Romanovskii, N. N., Hubberten, H. W., Gavrilov, A. V., Tumskoy, V. E., and Kholodov, A. L.: Permafrost of the east Siberian Arctic shelf and coastal lowlands, Quaternary Science Reviews, 23, 1359-1369, doi:10.1016/j.quascirev.2003.12.014, 2004.

Romanovsky, V. E., Gruber, S., Instanes, A., Jin, H., Marchenko, S. S., Smith, S. L., Trombotto, D., and Walter, K. M.: Frozen ground (Chapter 7), in: Global outlook for ice and snow, UNEP, 183–200, 2007.

Romanovsky, V. E., Drozdov, D. S., Oberman, N. G., Malkova, G. V., Kholodov, A. L., Marchenko, S. S., Moskalenko, N. G., Sergeev, D. O., Ukraintseva, N. G., Abramov, A. A., Gilichinsky, D. A., and Vasiliev, A. A.: Thermal state of permafrost in Russia, Permafrost and Periglacial Processes, 21, 136-155, doi:10.1002/ppp.683, 2010a.

Romanovsky, V. E., Smith, S. L., and Christiansen, H. H.: Permafrost thermal state in the polar Northern Hemisphere during the international polar year 2007–2009: A synthesis, Permafrost and Periglacial Processes, 21, 106-116, doi:10.1002/ppp.689, 2010b.

Routh, J., Hugelius, G., Kuhry, P., Filley, T., Tillman, P. K., Becher, M., and Crill, P.: Multi-proxy study of soil organic matter dynamics in permafrost peat deposits reveal vulnerability to climate change in the European Russian Arctic, Chemical Geology, 368, 104-117, doi:10.1016/j.chemgeo.2013.12.022, 2014.

Rowland, J. C., Jones, C. E., Altmann, G., Bryan, R., Crosby, B. T., Hinzman, L. D., Kane, D. L., Lawrence, D. M., Mancino, A., Marsh, P., McNamara, J. P., Romanvosky, V. E., Toniolo, H., Travis, B. J., Trochim, E., Wilson, C. J., and Geernaert, G. L.: Arctic landscapes in transition: Responses to thawing permafrost, Eos, Transactions American Geophysical Union, 91, 229-230, doi:10.1029/2010eo260001, 2010.

Rumpel, C., and Kögel-Knabner, I.: Deep soil organic matter - A key, but poorly understood, component of terrestrial C cycle, Plant and Soil, 338, 143-158, doi:10.1007/s11104-010-0391-5, 2011.

Sannel, A. B. K., and Kuhry, P.: Warming-induced destabilization of peat plateau/thermokarst lake complexes, Journal of Geophysical Research: Biogeosciences, 116, G03035, doi:10.1029/2010jg001635, 2011.

Scanlon, D., and Moore, T.: Carbon dioxide production from peatland soil profiles: the influence of temperature, oxic/anoxic conditions and substrate, Soil Science, 165, 153-160, 2000.

Schädel, C., Schuur, E. A. G., Bracho, R., Elberling, B., Knoblauch, C., Lee, H., Luo, Y. Q., Shaver, G. R., and Turetsky, M. R.: Circumpolar assessment of permafrost C quality and its vulnerability over time using long-term incubation data, Global Change Biology, 20, 641-652, doi:10.1111/gcb.12417, 2014.

Schaefer, K., Zhang, T., Bruhwiler, L., and Barrett, A. P.: Amount and timing of permafrost carbon release in response to climate warming, Tellus Series B, 63, 165-180, doi:10.1111/j.1600-0889.2011.00527.x, 2011.

Schaefer, K., Lantuit, H., Romanovsky, V. E., Schuur, E. A., and Witt, R.: The impact of the permafrost carbon feedback on global climate, Environmental Research Letters, 9, 085003, doi:10.1088/1748-9326/9/8/085003, 2014.

Schaphoff, S., Heyder, U., Ostberg, S., Gerten, D., Heinke, J., and Lucht, W.: Contribution of permafrost soils to the global carbon budget, Environmental Research Letters, 8, 014026, doi:10.1088/1748-9326/8/1/014026, 2013.

Schirrmeister, L., Siegert, C., Kuznetsova, T., Kuzmina, S., Andreev, A., Kienast, F., Meyer, H., and Bobrov, A.: Paleoenvironmental and paleoclimatic records from permafrost deposits in the Arctic region of Northern Siberia, Quaternary International, 89, 97-118, doi:10.1016/S1040-6182(01)00083-0, 2002.

Schirrmeister, L., Grosse, G., Kunitsky, V., Magens, D., Meyer, H., Dereviagin, A., Kuznetsova, T., Andreev, A., Babiy, O., Kienast, F., Grigoriev, M., Overduin, P. P., and Preusser, F.: Periglacial landscape evolution and environmental changes of Arctic lowland areas for the last 60 000 years (western Laptev Sea coast, Cape Mamontov Klyk), Polar Research, 27, 249-272, doi:10.1111/j.1751-8369.2008.00067.x, 2008a.

Schirrmeister, L., Kunitsky, V. V., Grosse, G., Kuznetsova, T. V., Derevyagin, A. Y., Wetterich, S., and Siegert, C.: The Yedoma suite of the Northeastern Siberian shelf region: Characteristics and concept of formation, Proceedings of the 9th International Conference on Permafrost, 2, 1595-1601, 2008b.

Schirrmeister, L., Grosse, G., Schnelle, M., Fuchs, M., Krbetschek, M., Ulrich, M., Kunitsky, V., Grigoriev, M., Andreev, A., Kienast, F., Meyer, H., Babiy, O., Klimova, I., Bobrov, A., Wetterich, S., and Schwamborn, G.: Late Quaternary paleoenvironmental records from the western Lena Delta, Arctic Siberia, Palaeogeography, Palaeoclimatology, Palaeoecology, 299, 175-196, doi:10.1016/j.palaeo.2010.10.045, 2011a.

Schirrmeister, L., Grosse, G., Wetterich, S., Overduin, P. P., Strauss, J., Schuur, E. A. G., and Hubberten, H.-W.: Fossil organic matter characteristics in permafrost deposits of the northeast Siberian Arctic, Journal of Geophysical Research: Biogeosciences, 116, G00M02, doi:10.1029/2011jg001647, 2011b.

Schirrmeister, L., Kunitsky, V., Grosse, G., Wetterich, S., Meyer, H., Schwamborn, G., Babiy, O., Derevyagin, A., and Siegert, C.: Sedimentary characteristics and origin of the Late Pleistocene Ice Complex on north-east Siberian Arctic coastal lowlands and islands - A review, Quaternary International, 241, 3-25, doi:10.1016/j.quaint.2010.04.004, 2011c.

Schirrmeister, L., Froese, D. G., Tumskoy, V., Grosse, G., and Wetterich, S.: Yedoma: Late Pleistocene ice-rich syngenetic permafrost of Beringia, in: Encyclopedia of Quaternary Sciences, 2 ed., edited by: Elias, S. A., Elsevier, Amsterdam, 542-552, 2013.

Schmidt, M. W. I., Torn, M. S., Abiven, S., Dittmar, T., Guggenberger, G., Janssens, I. A., Kleber, M., Kogel-Knabner, I., Lehmann, J., Manning, D. A. C., Nannipieri, P., Rasse, D. P., Weiner, S., and Trumbore, S. E.: Persistence of soil organic matter as an ecosystem property, Nature, 478, 49-56, 2011.

Schneider von Deimling, T., Meinshausen, M., Levermann, A., Huber, V., Frieler, K., Lawrence, D. M., and Brovkin, V.: Estimating the near-surface permafrost-carbon feedback on global warming, Biogeosciences, 9, 649-665, doi:10.5194/bg-9-649-2012, 2012.

Schneider von Deimling, T., Grosse, G., Strauss, J., Schirrmeister, L., Morgenstern, A., Schaphoff, S., Meinshausen, M., and Boike, J.: Observation-based modeling of permafrost carbon fluxes with accounting for deep carbon deposits and thermokarst activity, Biogeosciences Discuss., 11, 16599-16643, doi:10.5194/bgd-11-16599-2014, 2014.

Schulte, S., Mangelsdorf, K., and Rullkötter, J.: Organic matter preservation on the Pakistan continental margin as revealed by biomarker geochemistry, Organic Geochemistry, 31, 1005-1022, doi:10.1016/S0146-6380(00)00108-X, 2000.

Schuur, E. A. G., Bockheim, J., Canadell, J. G., Euskirchen, E., Field, C. B., Goryachkin, S. V., Hagemann, S., Kuhry, P., Lafleur, P. M., and Lee, H.: Vulnerability of permafrost carbon to climate change: Implications for the global carbon cycle, BioScience, 58, 701-714, doi:10.1641/B580807, 2008.

Schuur, E. A. G., Vogel, J. G., Crummer, K. G., Lee, H., Sickman, J. O., and Osterkamp, T. E.: The effect of permafrost thaw on old carbon release and net carbon exchange from tundra, Nature, 459, 556-559, doi:10.1038/nature08031, 2009.

Schuur, E. A. G., and Abbott, B.: High risk of permafrost thaw, Nature, 480, 32-33, doi:10.1038/480032a, 2011.

Schuur, E. A. G., Abbott, B. W., Bowden, W. B., Brovkin, V., Camill, P., Canadell, J. G., Chanton, J. P., Chapin, F. S., III, Christensen, T. R., Ciais, P., Crosby, B. T., Czimczik, C. I., Grosse, G., Harden, J., Hayes, D. J., Hugelius, G., Jastrow, J. D., Jones, J. B., Kleinen, T., Koven, C. D., Krinner, G., Kuhry, P., Lawrence, D. M., McGuire, A. D., Natali, S. M., O'Donnell, J. A., Ping, C. L., Riley, W. J., Rinke, A., Romanovsky, V. E., Sannel, A. B. K., Schädel, C., Schaefer, K., Sky, J., Subin, Z. M., Tarnocai, C., Turetsky, M. R., Waldrop, M. P., Walter Anthony, K. M., Wickland, K. P., Wilson, C. J., and Zimov, S. A.: Expert assessment of vulnerability of permafrost carbon to climate change, Climatic Change, 119, 359-374, doi:10.1007/s10584-013-0730-7, 2013.

Schwamborn, G., Rachold, V., Schneider, W., Grigoriev, M., and Nixdorf, U.: Ground penetrating radar and shallow seismic-stratigraphic and permafrost investigations of Lake Nikolay, Lena Delta, Arctic Siberia, 8th International Conference on Ground Penetrating Radar, Brisbane, 783-789, 2000.

Schwamborn, G., Andreev, A., Rachold, V., Hubberten, H.-W., Grigoriev, M. N., Tumskoy, V. E., Pavlova, E. Y., and Dorozhkina, M. V.: Evolution of Lake Nikolay, Arga Island, Western Lena River Delta, during Late Pleistocene and Holocene time, Polarforschung, 70, 69-82, 2002a.

Schwamborn, G., Rachold, V., and Grigoriev, M. N.: Late Quaternary sedimentation history of the Lena Delta, Quaternary International, 89, 119-134, doi:10.1016/S1040-6182(01)00084-2, 2002b.

Schwamborn, G., Förster, A., Diekmann, B., Schirrmeister, L., and Fedorov, G.: Mid- to Late-Quaternary cryogenic weathering conditions at Elgygytgyn Crater, Northeastern Russia: Inference from mineralogical and microtextural properties of the sediment record, 9th International Conference on Permafrost, University of Alaska Fairbanks, 1601-1606, 2008.

Segers, R.: Methane production and methane consumption: a review of processes underlying wetland methane fluxes, Biogeochemistry, 41, 23-51, doi:10.1023/a:1005929032764, 1998.

Seppälä, M.: Wind as a geomorphic agent in cold climates, Cambridge Univiversity Press, 358 pp., 2004.

Serreze, M. C., and Barry, R. G.: Processes and impacts of Arctic amplification: A research synthesis, Global and Planetary Change, 77, 85-96, doi:10.1016/j.gloplacha.2011.03.004, 2011.

Shakhova, N., Semiletov, I., Salyuk, A., Yusupov, V., Kosmach, D., and Gustafsson, Ö.: Extensive methane venting to the atmosphere from sediments of the East Siberian Arctic Shelf, Science, 327, 1246-1250, doi:10.1126/science.1182221, 2010.

Sheng, Y., Smith, L. C., MacDonald, G. M., Kremenetski, K. V., Frey, K. E., Velichko, A. A., Lee, M., Beilman, D. W., and Dubinin, P.: A high-resolution GIS-based inventory of the west Siberian peat carbon pool, Global Biogeochemical Cycles, 18, GB3004, doi:10.1029/2003gb002190, 2004.

Sher, A. V.: Mammals and stratigraphy of the Pleistocene of the extreme northeast of the USSR and North America, Nauka, 1971.

Sher, A. V., Kaplina, T. N., Giterman, R. E., Lozhkin, A. V., Arkhangelov, A. A., Kiselyov, S. V., Kouznetsov, Y. V., Virina, E. I., and Zazhigin, V. S.: Late Cenozoic of the Kolyma Lowland, 14th Pacific Science Congress, Khabarovsk, 1979.

Sher, A. V., Kaplina, T. N., and Ovander, M. G.: Unified regional stratigraphic chart for the Quaternary deposits in the Yana-Kolyma lowland and its mountainous surroundings - Explanatory note, Interdepartmental Stratigraphic Conference on the Quaternary of the East USSR, Magadan, USSR, 1987.

Sher, A. V.: Is there any real evidence for a huge shelf ice sheet in East Siberia?, Quaternary International, 28, 39-40, 1995.

Sher, A. V., Kuzmina, S. A., Kuznetsova, T. V., and Sulerzhitsky, L. D.: New insights into the Weichselian environment and climate of the East Siberian Arctic, derived from fossil insects, plants, and mammals, Quaternary Science Reviews, 24, 533-569, doi:10.1016/j.quascirev.2004.09.007, 2005.

Shindell, D. T., Faluvegi, G., Koch, D. M., Schmidt, G. A., Unger, N., and Bauer, S. E.: Improved attribution of climate forcing to emissions, Science, 326, 716-718, doi:10.1126/science.1174760, 2009.

Shur, Y. L., and Jorgenson, M. T.: Patterns of permafrost formation and degradation in relation to climate and ecosystems, Permafrost and Periglacial Processes, 18, 7-19, doi:10.1002/ppp.582, 2007.

Siegert, C., Schirrmeister, L., Kunitsky, V., Meyer, H., Kuznetsova, T. P., Derevyagin, S., Kuzmina, S., Tumskoy, V. E., and Sher, A. V.: Paleoclimate signals of ice-rich permafrost, Reports on Polar and Marine Research, Alfred Wegener Institut for Polar and Marine Research, Bremerhaven, 145-259 pp., 1999.

Sitch, S., Smith, B., Prentice, I. C., Arneth, A., Bondeau, A., Cramer, W., Kaplan, J. O., Levis, S., Lucht, W., Sykes, M. T., Thonicke, K., and Venevsky, S.: Evaluation of ecosystem dynamics, plant geography and terrestrial carbon cycling in the LPJ dynamic global vegetation model, Global Change Biology, 9, 161-185, doi:10.1046/j.1365-2486.2003.00569.x, 2003.

Slagoda, E. A.: Genesis and microstructure of cryolithogenic deposits at the Bykovsky Peninsula and the Muostakh Island, Permafrost Institute, Russian Academy of Sciences, Yakutsk, Russia, 218 pp., 1993.

Slater, A. G., and Lawrence, D. M.: Diagnosing present and future permafrost from climate models, Journal of Climate, 26, 5608-5623, doi:10.1175/jcli-d-12-00341.1, 2013.

Smalley, I. J., and Smalley, V.: Loess material and loess deposits: Formation, distribution and consequences, in: Developments in sedimentology 38 - Eolian sediments and processes, edited by: Brookfield, M. E., and Ahlbrandt, T. S., Elsevier, 51-68, 1983.

Smith, I. R.: The seismic shothole drillers' log database and GIS for Northwest Territories and northern Yukon: An archive of near-surface lithostratigraphic surficial and bedrock geology data, Geological Survey of Canada, Open File Report 6833, doi:10.4095/288754, 2011.

Smith, L. C., Sheng, Y., MacDonald, G. M., and Hinzman, L. D.: Disappearing Arctic lakes, Science, 308, 1429, doi:10.1126/science.1108142, 2005a.

Smith, M. R., and Mah, R. A.: Acetate as sole carbon and energy source for growth of Methanosarcina strain 227, Applied and Environmental Microbiology, 39, 993-999, 1980.

Smith, S. L., Burgess, M. M., Chartrand, J., and Lawrence, D. E.: Digital borehole geotechnical database for the Mackenzie Valley/Delta region, Geological Survey of Canada, Open File Report 4924, 30, 2005b.

Soil Survey Staff: Soil taxonomy: A basic system of soil classification for making and interpreting soil surveys, 2 ed., United States Department of Agriculture, Washington, 869 pp., 1999.

Sollins, P., Spycher, G., and Glassman, C. A.: Net nitrogen mineralization from light- and heavy-fraction forest soil organic matter, Soil Biology and Biochemistry, 16, 31-37, doi:10.1016/0038-0717(84)90122-6, 1984.

Stevens, C. W., Moorman, B. J., Solomon, S. M., and Hugenholtz, C. H.: Mapping subsurface conditions within the near-shore zone of an Arctic delta using ground penetrating radar, Cold Regions Science and Technology, 56, 30-38, doi:10.1016/j.coldregions.2008.09.005, 2009.

Stevenson, F. J.: Humus chemistry: Genesis, composition, reactions, John Wiley & Sons, New York, 1994.

Stieglitz, M., Déry, S. J., Romanovsky, V. E., and Osterkamp, T. E.: The role of snow cover in the warming of arctic permafrost, Geophysical Research Letters, 30, 1721, doi:10.1029/2003gl017337, 2003.

Strauss, J., and Schirrmeister, L.: Permafrost Sequences of Buor Khaya Peninsula, in: Russian-German Cooperation SYSTEM LAPTEV SEA: The expedition Eastern Laptev Sea-Buor Khaya Peninsula 2010, edited by: Wetterich, S., Overduin, P. P., and Grigoriev, M., Reports on polar and marine research, Alfred Wegener Institute for Polar and Marine Research, Bremerhaven, 35-50, 2011.

Strauss, J., Schirrmeister, L., Wetterich, S., Borchers, A., and Davydov, S. P.: Grain-size properties and organic-carbon stock of Yedoma Ice Complex permafrost from the Kolyma lowland, northeastern Siberia, Global Biogeochemical Cycles, 26, GB3003, doi:10.1029/2011GB004104, 2012.

Strauss, J., Schirrmeister, L., Grosse, G., Wetterich, S., Ulrich, M., Herzschuh, U., and Hubberten, H.-W.: The Deep Permafrost Carbon Pool of the Yedoma Region in Siberia and Alaska, Geophysical Research Letters, 2013GL058088, doi:10.1002/2013GL058088, 2013.

Strauss, J., Schirrmeister, L., Mangelsdorf, K., Eichhorn, L., Wetterich, S., and Herzschuh, U.: Organic matter quality of deep permafrost carbon - a study from Arctic Siberia, Biogeosciences Discussions, 11, 15945–15989, doi:10.5194/bgd-11-15945-2014, 2014

Stuiver, M., Reimer, P., and Reimer, R.: CALIB 6.0, ^{14}C CHRONO Centre, Queens University Belfast, Belfast, 2010.

Sun, D., Bloemendal, J., Rea, D. K., Vandenberghe, J., Jiang, F., An, Z., and Su, R.: Grain-size distribution function of polymodal sediments in hydraulic and aeolian environments, and numerical partitioning of the sedimentary components, Sedimentary Geology, 152, 263-277, doi:10.1016/s0037-0738(02)00082-9, 2002.

Svendsen, J. I., Alexanderson, H., Astakhov, V. I., Demidov, I., Dowdeswell, J. A., Funder, S., Gataullin, V., Henriksen, M., Hjort, C., Houmark-Nielsen, M., Hubberten, H. W., Ingólfsson, Ó., Jakobsson, M., Kjær, K. H., Larsen, E., Lokrantz, H., Lunkka, J. P., Lyså, A., Mangerud, J., Matiouchkov, A., Murray, A., Möller, P., Niessen, F., Nikolskaya, O., Polyak, L., Saarnisto, M., Siegert, C., Siegert, M. J., Spielhagen, R. F., and Stein, R.: Late Quaternary ice sheet history of northern Eurasia, Quaternary Science Reviews, 23, 1229-1271, doi:10.1016/j.quascirev.2003.12.008, 2004.

Tarnocai, C., Kimble, J., and Broll, G.: Determining carbon stocks in cryosols using the Northern and Mid Latitudes soil database, in: Permafrost, edited by: Philips, M., Springman, S. M., and Arenson, L. U., Swets and Zeitlinger, Lisse, Netherlands, 1129-1134, 2003.

Tarnocai, C., Kettles, I. M., and Lacelle, B.: Peatlands of Canada database, Agriculture and Agri-Food Canada, Ottawa, 2005.

Tarnocai, C., and Stolbovoy, V.: Northern peatlands: Their characteristics, development and sensitivity to climate change, in: Peatlands: Evolution and records of environmental and climate changes edited by: Martini, I. P., Martınez Cortizas, A., and Chesworth, W., Elsevier, Amsterdam, 17-51, 2006.

Tarnocai, C., Canadell, J. G., Schuur, E. A. G., Kuhry, P., Mazhitova, G., and Zimov, S.: Soil organic carbon pools in the northern circumpolar permafrost region, Global Biogeochemical Cycles, 23, GB2023, doi:10.1029/2008GB003327, 2009.

Taylor, A. E., Dallimore, S. R., and Judge, A. S.: Late Quaternary history of the Mackenzie–Beaufort region, Arctic Canada, from modelling of permafrost temperatures. 2. The Mackenzie Delta–Tuktoyaktuk Coastlands, Canadian Journal of Earth Sciences, 33, 62-71, doi:10.1139/e96-007, 1996.

Taylor, K. E., Stouffer, R. J., and Meehl, G. A.: An overview of CMIP-5 and the experiment design, Bulletin of the American Meteorological Society, 93, 485-498, doi:10.1175/bams-d-11-00094.1, 2011.

Thompson, S. K.: Sampling, John Wiley and Sons, New York, 343 pp., 1992.

Tieszen, L.: Photosynthesis and respiration in arctic tundra grasses: Field light intensity and temperature responses, Arctic and Alpine Research, 239-251, 1973.

Tomirdiaro, S. V.: Evolution of lowland landscapes in northeastern Asia during Late Quaternary time, in: Paleoecology of Beringia, edited by: Hopkins, D. M., Matthews, J. V., Schweger, C. E., and Young, S. B., Academic Press, New York, 29-37, 1982.

Tomirdiaro, S. V., Arslanov, K. A., Chernen'kiy, B. I., Tertychnaya, T. V., and Prokhorova, T. N.: New data on the formation of loess-ice sequences in northern Yakutia and ecological conditions of the mammoth fauna in the Arctic during the late Pleistocene, Doklady Akademiy Nauk, 6, 1446-1449 1984.

Treat, C. C., and Frolking, S.: Carbon Storage: A permafrost carbon bomb?, Nature Climate Change, 3, 865-867, doi:10.1038/nclimate2010, 2013.

Turetsky, M. R., Kane, E. S., Harden, J. W., Ottmar, R. D., Manies, K. L., Hoy, E., and Kasischke, E. S.: Recent acceleration of biomass burning and carbon losses in Alaskan forests and peatlands, Nature Geoscience, 4, 27-31, doi:10.1038/ngeo1027, 2011.

Ulrich, M., Hauber, E., Herzschuh, U., Härtel, S., and Schirrmeister, L.: Polygon pattern geomorphometry on Svalbard (Norway) and western Utopia Planitia (Mars) using high-resolution stereo remote-sensing data, Geomorphology, 134, 197-216, doi:10.1016/j.geomorph.2011.07.002, 2011.

Ulrich, M., Grosse, G., Strauss, J., and Schirrmeister, L.: Quantifying wedge-ice volumes in Yedoma and thermokarst basin deposits, Permafrost and Periglacial Processes, doi:10.1002/ppp.1810, 2014.

UNEP: Policy implications of warming permafrost, edited by: Schaefer, K., Lanuit, H., Romanovsky, V. E., Schuur, E. A. G., and Gaertner-Roer, I., United Nations Environment Programme, Nairobi, Kenya, 29 pp., 2012.

van der Molen, M. K., van Huissteden, J., Parmentier, F. J. W., Petrescu, A. M. R., Dolman, A. J., Maximov, T. C., Kononov, A. V., Karsanaev, S. V., and Suzdalov, D. A.: The growing season greenhouse gas balance of a continental tundra site in the Indigirka lowlands, NE Siberia, Biogeosciences, 4, 985-1003, doi:10.5194/bg-4-985-2007, 2007.

van Everdingen, R. O.: Multi-language glossary of permafrost and related ground-ice terms, National Snow and Ice Data Center, Boulder, USA, 2005.

van Huissteden, J., Berrittella, C., Parmentier, F. J. W., Mi, Y., Maximov, T. C., and Dolman, A. J.: Methane emissions from permafrost thaw lakes limited by lake drainage, Nature Climate Change, 1, 119-123, doi:10.1038/nclimate1101, 2011.

van Huissteden, J., and Dolman, A. J.: Soil carbon in the Arctic and the permafrost carbon feedback, Current Opinion in Environmental Sustainability, 4, 545-551, doi:10.1016/j.cosust.2012.09.008, 2012.

Vasil'chuk, Y. K., Vasil'chuk, A. C., Rank, D., Kutschera, W., and Kim, J. C.: Radiocarbon dating of delta O-18-delta D plots in Late Pleistocene ice-wedges of the Duvanny Yar (Lower Kolyma River, Northern Yakutia), Radiocarbon, 43, 541-553, 2001.

Vasil'chuk, Y. K., Vaikmae, R. A., Punning, J.-M. K., and M.O. Leibman: Oxygen-isotope distribution, palynology and hydrochemistry wedge ice in organic-mineral complex of Duvanny Yar type section, Transactions (Doklady) of the USSR Academy of Sciences, Earth Science Section 292, 69-72, 1988.

Vasil'chuk, Y. K.: Oxygen isotope composition of ground ice: Application to paleogeocryological reconstructions, Geological Faculty of Moscow State University, Russian Academy of Sciences, Moscow, 1992.

Velichko, A. A., Kononov, Y. M., and Faustova, M. A.: The last glaciation of earth: Size and volume of ice-sheets, Quaternary International, 41-42, 43-51, doi:10.1016/S1040-6182(96)00035-3, 1997.

Velichko, A. A., Catto, N., Drenova, A. N., Klimanov, V. A., Kremenetski, K. V., and Nechaev, V. P.: Climate changes in East Europe and Siberia at the Late Glacial-Holocene transition, Quaternary International, 91, 75-99, doi:10.1016/S1040-6182(01)00104-5, 2002.

Veremeeva, A., and Gubin, S. V.: Modern tundra landscapes of the Kolyma Lowland and their evolution in the Holocene, Permafrost and Periglacial Processes, 20, 399-406, doi:10.1002/ppp.674, 2009.

Vieth, A., Mangelsdorf, K., Sykes, R., and Horsfield, B.: Water extraction of coals – potential for estimating low molecular weight organic acids as carbon feedstock for the deep terrestrial biosphere, Organic Geochemistry, 39, 985-991, doi:10.1016/j.orggeochem.2008.02.012, 2008.

Vonk, J. E., Sánchez-García, L., Semiletov, I., Dudarev, O., Eglinton, T., Andersson, A., and Gustafsson, Ö.: Molecular and radiocarbon constraints on sources and degradation of terrestrial organic carbon along the Kolyma paleoriver transect, East Siberian Sea, Biogeosciences, 7, 3153-3166, doi:10.5194/bg-7-3153-2010, 2010.

Vonk, J. E., Sanchez-Garcia, L., van Dongen, B. E., Alling, V., Kosmach, D., Charkin, A., Semiletov, I. P., Dudarev, O. V., Shakhova, N., Roos, P., Eglinton, T. I., Andersson, A., and Gustafsson, O.: Activation of old carbon by erosion of coastal and subsea permafrost in Arctic Siberia, Nature, 489, 137-140, doi:10.1038/nature11392, 2012.

Vonk, J. E., Mann, P. J., Davydov, S., Davydova, A., Spencer, R. G. M., Schade, J., Sobczak, W. V., Zimov, N., Zimov, S., Bulygina, E., Eglinton, T. I., and Holmes, R. M.: High biolability of ancient permafrost carbon upon thaw, Geophysical Research Letters, 40, 2689-2693, doi:10.1002/grl.50348, 2013a.

Vonk, J. E., Mann, P. J., Dowdy, K. L., Davydova, A., Davydov, S. P., Zimov, N., Spencer, R. G. M., Bulygina, E. B., Eglinton, T. I., and Holmes, R. M.: Dissolved organic carbon loss from Yedoma permafrost amplified by ice wedge thaw, Environmental Research Letters, 8, 035023, doi:10.1088/1748-9326/8/3/035023, 2013b.

Vtyurin, B. I., Grigoriev, N. F., Katasanov, E. M., Kuznetsova, T. P., Shvetsov, P. F., and Shumsky, P. A.: Local stratigraphic scheme of Quaternary deposits at the coast of the Laptev Sea, Proceedings of the interdepartmental council for the edition of an unified stratigraphical scheme of Siberia, 564-572, 1957.

Wagner, D., Gattinger, A., Embacher, Pfeiffer, E. M., Schloter, M., and Lipinski, A.: Methanogenic activity and biomass in Holocene permafrost deposits of the Lena Delta, Siberian Arctic and its implication for the global methane budget, Global Change Biology, 13, 1089-1099, doi:10.1111/j.1365-2486.2007.01331.x, 2007.

Waldrop, M. P., Wickland, K. P., White III, R., Berhe, A. A., Harden, J. W., and Romanovsky, V. E.: Molecular investigations into a globally important carbon pool: Permafrost-protected carbon in Alaskan soils, Global Change Biology, 16, 2543-2554, doi:10.1111/j.1365-2486.2009.02141.x, 2010.

Walger, E.: Die Korngrößenverteilung von Einzellagen sandiger Sedimente und ihre genetische Bedeutung, Geologische Rundschau, 51, 494-507, doi:10.1007/BF01820015, 1962.

Walker, D. A., Raynolds, M. K., Daniëls, F. J., Einarsson, E., Elvebakk, A., Gould, W. A., Katenin, A. E., Kholod, S. S., Markon, C. J., and Melnikov, E. S.: The circumpolar Arctic vegetation map, Journal of Vegetation Science, 16, 267-282, 2005.

Walker, H. J.: Arctic deltas, Journal of Coastal Research, 14, 718-738, 1998.

Walter Anthony, K. M., Anthony, P., Grosse, G., and Chanton, J.: Geologic methane seeps along boundaries of Arctic permafrost thaw and melting glaciers, Nature Geoscience, 5, 419-426, doi:10.1038/ngeo1480, 2012.

Walter Anthony, K. M., Zimov, S. A., Grosse, G., Jones, M. C., Anthony, P. M., Chapin III, F. S., Finlay, J. C., Mack, M. C., Davydov, S., Frenzel, P., and Frolking, S.: A shift of thermokarst lakes from carbon sources to sinks during the Holocene epoch, Nature, 511, 452–456, doi:10.1038/nature13560, 2014.

Walter, B. P., and Heimann, M.: A process-based, climate-sensitive model to derive methane emissions from natural wetlands: Application to five wetland sites, sensitivity to model parameters, and climate, Global Biogeochemical Cycles, 14, 745-765, 2000.

Walter, K. M., Zimov, S. A., Chanton, J. P., Verbyla, D., and Chapin, F. S.: Methane bubbling from Siberian thaw lakes as a positive feedback to climate warming, Nature, 443, 71-75, doi:10.1038/nature05040, 2006.

Walter, K. M., Edwards, M. E., Grosse, G., Zimov, S. A., and Chapin, F. S.: Thermokarst lakes as a source of atmospheric CH_4 during the last deglaciation, Science, 318, 633-636, 2007a.

Walter, K. M., Smith, L. C., and Chapin, S. F.: Methane bubbling from northern lakes: Present and future contributions to the global methane budget, Philosophical Transactions of the Royal Society A: Mathematical, Physical and Engineering Sciences, 365, 1657-1676, doi:10.1098/rsta.2007.2036, 2007b.

Weintraub, M. N., and Schimel, J. P.: Nitrogen cycling and the spread of shrubs control changes in the carbon balance of Arctic tundra ecosystems, BioScience, 55, 408-415, doi:10.1641/0006-3568(2005)055[0408:ncatso]2.0.co;2, 2005.

Welker, J. M., Wookey, P. A., Parsons, A. N., Press, M. C., Callaghan, T. V., and Lee, J. A.: Leaf carbon isotope discrimination and vegetative responses of Dryas octopetala to temperature and water manipulations in a High Arctic polar semi-desert, Svalbard, Oecologia, 95, 463-469, doi:10.1007/bf00317428, 1993.

Weltje, G. J.: End-member modeling of compositional data: numerical-statistical algorithms for solving the explicit mixing problem, Mathematical Geology, 29, 503-549, 1997.

Weltje, G. J., and Prins, M. A.: Genetically meaningful decomposition of grain-size distributions, Sedimentary Geology, 202, 409-424, doi:10.1016/j.sedgeo.2007.03.007, 2007.

Wetterich, S., Kuzmina, S., Andreev, A. A., Kienast, F., Meyer, H., Schirrmeister, L., Kuznetsova, T., and Sierralta, M.: Palaeoenvironmental dynamics inferred from late Quaternary permafrost deposits on Kurungnakh Island, Lena Delta, Northeast Siberia, Russia, Quaternary Science Reviews, 27, 1523-1540, doi:10.1016/j.quascirev.2008.04.007, 2008.

Wetterich, S., Schirrmeister, L., Andreev, A. A., Pudenz, M., Plessen, B., Meyer, H., and Kunitsky, V. V.: Eemian and Late Glacial/Holocene palaeoenvironmental records from permafrost sequences at the Dmitry Laptev Strait (NE Siberia, Russia), Palaeogeography, Palaeoclimatology, Palaeoecology, doi:10.1016/j.palaeo.2009.05.002, 2009.

Wetterich, S., Schirrmeister, L., and Kholodov, A. L.: The joint Russian-German expedition BERINGIA/KOLYMA 2008 during the International Polar Year (IPY) 2007/2008, Reports on polar and marine research, Alfred Wegener Institute for Polar and Marine Research, Bremerhaven, Germany, 48 pp., 2011.

Wolfe, S. A., Gillis, A., and Robertson, L.: Late Quaternary aeolian deposits of northern North America: Age and extent, Geological Survey of Canada Open File 6006, 2009.

Wright, J., Smith, B., and Whalley, B.: Mechanisms of loess-sized quartz silt production and their relative effectiveness: Laboratory simulations, Geomorphology, 23, 15-34, 1998.

Yi, S., Manies, K., Harden, J., and McGuire, A. D.: Characteristics of organic soil in black spruce forests: Implications for the application of land surface and ecosystem models in cold regions, Geophysical Research Letters, 36, L05501, doi:10.1029/2008gl037014, 2009.

Yi, S., Wischnewski, K., Langer, M., Muster, S., and Boike, J.: Freeze/thaw processes in complex permafrost landscapes of northern Siberia simulated using the TEM ecosystem model: Impact of thermokarst ponds and lakes, Geoscientific Model Development, 7, 1671-1689, doi:10.5194/gmd-7-1671-2014, 2014.

Yoshikawa, K., and Hinzman, L. D.: Shrinking thermokarst ponds and groundwater dynamics in discontinuous permafrost near council, Alaska, Permafrost and Periglacial Processes, 14, 151-160, doi:10.1002/ppp.451, 2003.

Yu, Z. C.: Northern peatland carbon stocks and dynamics: A review, Biogeosciences, 9, 4071-4085, doi:10.5194/bg-9-4071-2012, 2012.

Zanina, O. G., Gubin, S. V., Kuzmina, S. A., Maximovich, S. V., and Lopatina, D. A.: Late-Pleistocene (MIS 3-2) palaeoenvironments as recorded by sediments, palaeosols, and ground-squirrel nests at Duvanny Yar, Kolyma lowland, northeast Siberia, Quaternary Science Reviews, doi:10.1016/j.quascirev.2011.01.021, 2011.

Zech, M., Zech, R., Zech, W., Glaser, B., Brodowski, S., and Amelung, W.: Characterisation and palaeoclimate of a loess-like permafrost palaeosol sequence in NE Siberia, Geoderma, 143, 281-295, doi:10.1016/j.geoderma.2007.11.012, 2008.

Zhang, T., Barry, R. G., Knowles, K., Heginbottom, J. A., and Brown, J.: Statistics and characteristics of permafrost and ground-ice distribution in the Northern Hemisphere, Polar Geography, 1, 47-68, doi:10.1080/10889370802175895, 2008.

Zimov, S. A., Davydov, S. P., Zimova, G. M., Davydova, A. I., Schuur, E. A. G., Dutta, K., and Chapin, F. S.: Permafrost carbon: Stock and decomposability of a globally significant carbon pool, Geophysical Research Letters, 33, L20502, doi:10.1029/2006GL027484, 2006a.

Zimov, S. A., Schuur, E. A. G., and Chapin, F. S.: Permafrost and the global carbon budget, Science, 312, 1612-1613, doi:10.1126/science.1128908, 2006b.

Zubrzycki, S., Kutzbach, L., Grosse, G., Desyatkin, A., and Pfeiffer, E. M.: Organic carbon and total nitrogen stocks in soils of the Lena River Delta, Biogeosciences, 10, 3507-3524, doi:10.5194/bg-10-3507-2013, 2013.

Financial and technical support

My PhD project was funded by a grant of the Studienstiftung des deutschen Volkes (German National Academic Foundation). The host institution was the Alfred Wegener Institute Helmholtz Centre for Polar and Marine Research (AWI) in Potsdam where I was able to use all facilities including the laboratories. For the lab work on biomarkers, I was allowed to use the facilities of the Organic Geochemistry section 4.3 of the Helmholtz Centre Potsdam - German Research Centre for Geosciences (GFZ). My field work in Siberia (Buor Khaya Peninsula) was part of the Russian-German research project "System Laptev Sea", funded by the German Federal Ministry of Education and Research (BMBF). The collaboration with the University of Alaska Fairbanks, including field work in Alaska (Itkillik River), was also funded by the BMBF, grant number 01DM12011.

For traveling to conferences and cooperation partners, I received funding by the Helmholtz Graduate School for Polar and Marine Research (Polmar), the Potsdam Graduate School (PoGS) and the Studienstiftung des deutschen Volkes.

Appendix I Estimated stocks of circumpolar permafrost carbon with quantified uncertainty ranges and identified data gaps

Hugelius, G.[1], Strauss, J.[2], Zubrzycki, S.[3], Harden, J. W.[4], Schuur, E. A. G.[5,6,7], Ping, C.-L.[8], Schirrmeister, L.[2], Grosse, G.[2], Michaelson, G. J.[6], Koven, C. D.[9], O'Donnell, J. A.[10], Elberling, B.[11], Mishra, U.[12], Camill, P.[13], Yu, Z.[14], Palmtag, J.[1], and Kuhry, P.[1]

[1]Department of Physical Geography and Quaternary Geology, Stockholm University, 106 91 Stockholm, Sweden
[2]Alfred Wegener Institute Helmholtz Centre for Polar and Marine Research, Periglacial Research Unit Potsdam, Telegrafenberg A43, 14473 Potsdam, Germany
[3]Institute of Soil Science, Center for Earth System Research and Sustainability (CEN), Universität Hamburg, Allende-Platz 2, 20146 Hamburg, Germany
[4]US Geological Survey, Menlo Park, CA 94025, USA
[5]Department of Biology, University of Florida, Gainesville, FL 32611, USA
[6]Center for Ecosystem Science & Society, Northern Arizona University, Flagstaff, AZ 86001, USA
[7]Biological Sciences, Northern Arizona University, Flagstaff, AZ 86001, USA
[8]Palmer Research Center, University of Alaska Fairbanks, 1509 S. Georgeson Drive, Palmer, AK 99645, USA
[9]Lawrence Berkeley National Lab, Berkeley, CA, USA
[10]Arctic Network, National Park Service, 4175 Geist Rd. Fairbanks, AK 99709, USA
[11]CENPERM (Center for Permafrost), Department of Geosciences and Natural Resource Management, University of Copenhagen, Øster Voldgade 10, 1350 Copenhagen, Denmark
[12]Environmental Science Division, Argonne National Laboratory, 9700 South Cass Av., Argonne, IL 60439, USA
[13]Earth and Oceanographic Science Department and Environmental Studies Program, Bowdoin College, Brunswick, ME 04011, USA
[14]Department of Earth and Environmental Sciences, Lehigh University, 1 West Packer Av., Bethlehem, PA 18015, USA

Submitted to: Biogeosciences, previous version published in Biogeosciences Discussions (doi:10.5194/bgd-11-4771-2014)

Citation: Hugelius, G., Strauss, J., Zubrzycki, S., Harden, J. W., Schuur, E. A. G., Ping, C.-L., Schirrmeister, L., Grosse, G., Michaelson, G. J., Koven, C. D., O'Donnell, J. A., Elberling, B., Mishra, U., Camill, P., Yu, Z., Palmtag, J., and Kuhry, P.: Estimated stocks of circumpolar permafrost carbon with quantified uncertainty ranges and identified data gaps, Biogeosciences, 11, 6573-6593, doi:10.5194/bg-11-6573-2014, 2014

Remark:
In this publications the unit Petagram (Pg) is used. The relation between Pg and the unit used in the thesis (Gigatonne (Gt)) is the following: 1 Pg = 1×10^{15}g = 1×10^{9}t = 1 Gt

I-1 Abstract

Soils and other unconsolidated deposits in the northern circumpolar permafrost region store large amounts of soil organic carbon (SOC). This SOC is potentially vulnerable to remobilization following soil warming and permafrost thaw, but SOC stock estimates were poorly constrained and quantitative error estimates were lacking. This study presents revised estimates of permafrost SOC stocks, including quantitative uncertainty estimates, in the 0 to 3 m depth range in soils as well as for sediments deeper than 3 m in deltaic deposits of major rivers and in the Yedoma region of Siberia and Alaska. Revised estimates are based on significantly larger databases compared to previous studies. Despite this there is evidence of significant remaining regional data gaps. Estimates remain particularly poorly constrained for soils in the High Arctic region and physiographic regions with thin sedimentary overburden (mountains, highlands and plateaus) as well as for deposits below 3 m depth in deltas and the Yedoma region. While some components of the revised SOC stocks are similar in magnitude to those previously reported for this region, there are substantial differences in other components, including the fraction of perennially frozen SOC. Upscaled based on regional soil maps, estimated permafrost region SOC stocks are 217±12 and 472±27 Pg for the 0 to 0.3 m and 0 to 1 m soil depths, respectively (±95 % confidence intervals). Storage of SOC in 0 to 3 m of soils is estimated to 1034±150 Pg. Of this, 34±16 Pg C is stored in poorly developed soils of the High Arctic. Based on generalized calculations, storage of SOC below 3 m of surface soils in deltaic alluvium of major Arctic rivers is estimated to 91±52 Pg. In the Yedoma region, estimated SOC stocks below 3 m depth are 181±54 Pg, of which 74±20 Pg is stored in intact Yedoma (late Pleistocene ice- and organic-rich silty sediments) with the remainder in refrozen thermokarst deposits. Total estimated SOC storage for the permafrost region is ~1300 Pg with an uncertainty range of ~1100 to 1500 Pg. Of this, ~500 Pg is in non-permafrost soils, seasonally thawed in the active layer or in deeper taliks, while ~800 Pg is perennially frozen. This represents a substantial ~300 Pg lowering of the estimated perennially frozen SOC stock compared to previous estimates.

I-2 Introduction

As permafrost warming and thaw occurs, large pools of frozen soil organic carbon (SOC) that were previously protected may become available for mineralization, leading to increased greenhouse gas fluxes to the atmosphere (Schuur et al., 2008). Incorporating permafrost related soil processes into Earth System Models (ESMs) has demonstrated that permafrost C and associated climate feedbacks have been underes-

timated in previous modeling studies and that high-latitude soil processes may further accelerate global warming (Koven et al., 2011; Schaefer et al., 2011; Burke et al., 2012b; Schneider von Deimling et al., 2012).

At high latitudes, low soil temperatures and poor soil drainage have reduced decomposition rates of soil organic matter (SOM) (Davidson and Janssens, 2006). Over millennial timescales, processes such as cryoturbation, accumulation of peat and repeated deposition and stabilization of organic-rich material (alluvium, proluvium, colluvium or wind-blown deposits) have led to accumulation of permafrost SOC in mineral soils, peat deposits (organic soils), silty late-Pleistocene syngenetic organic- and ice-rich deposits (Yedoma), deltaic deposits and other unconsolidated Quaternary deposits (e.g. Ping et al., 1998; Tarnocai and Stolbovoy, 2006; Ping et al., 2011; Schirrmeister et al., 2011b; 2011c; Strauss et al., 2012). Using the Northern Circumpolar Soil Carbon Database (NCSCD), a digital soil map database linked to extensive field-based SOC storage data, Tarnocai et al. (2009) estimated the 0 to 0.3 m and 0 to 1 m SOC stocks in the northern circumpolar permafrost region to be 191 Pg and 496 Pg, respectively. Based on limited field data, but in recognition of the key pedogenic processes that transport C to depth in permafrost soils, Tarnocai et al. (2009) provided a first-order SOC mass estimate for 0 to 3 m soil depth of 1024 Pg. This 0 to 3 m estimate was based on 46 pedons in Canada and was not included into the spatially distributed NCSCD. Hugelius et al. (2013b) recently compiled an updated pedon data set for soils in the northern circumpolar permafrost region extending down to 2 and 3 m depths (n=524 and 356, respectively), which were incorporated into an updated NCSCDv2 and is now available to improve characterization of the 1 to 3 m SOC stocks.

A first-order estimate of SOC stocks in Yedoma terrain of 450 Pg (Zimov et al., 2006a) was calculated from a small-scale map of Yedoma extent (Romanovskii, 1993), using generalized data of Yedoma deposit thickness, massive ice content, organic C% and bulk density. This estimate was recalculated to 407 Pg to avoid double counting of SOC stocks in the top 3 m of deposits when included into a summative circumpolar estimate of Tarnocai et al. (2009). Schirrmeister et al. (2011b) suggested that Yedoma SOC stocks may be 25 % to 50 % lower than previously reported because of overestimated mean bulk density value in Yedoma deposits. Using newly compiled data on deposit thickness, spatial extent of thermokarst, bulk density, segregated ice content and massive wedge-ice content, Strauss et al. (2013) provide an updated estimate of 211 Pg SOC (with an uncertainty range from 58 to 371 Pg) stored in permafrost sediments of the Yedoma region (including intact Yedoma and thermokarst sediment with Holocene cover deposits) of Siberia and Alaska, not in-

cluding active layer, thawed sediments underlying lakes and rivers or areas covered by deltaic or fluvial sediments.

Based on field data from the Mackenzie River Delta, Tarnocai et al. (2009) estimated SOC storage in the deltaic deposits of seven selected Arctic river deltas to be 241 Pg. Since this first-order estimate demonstrated the potential importance of deltaic permafrost deposits, new knowledge has become available regarding deeper SOC stores in Arctic Deltas. Field-studies from the Alaskan Beaufort Sea coast (Ping et al., 2008) and the Siberian Lena River Delta (Schirrmeister et al., 2011c; Zubrzycki et al., 2013) provide new information on SOC stocks in near-surface deltaic deposits. There is also additional information regarding the spatial extent and depth of deltaic deposits (Johnston and Brown, 1965; Taylor et al., 1996; Walker, 1998; Aylsworth et al., 2000; Schwamborn et al., 2002b; Smith et al., 2005b).

Tarnocai et al. (2009) provided a total estimate of circumpolar SOC storage in soils (0 to 3 m depth), Yedoma and deltaic deposits of 1672 Pg, of which 1466 Pg is stored in permafrost terrain. This is about twice as much C as what is currently stored in the atmosphere (Houghton, 2007). While it is recognized that this pool of SOC stored in permafrost regions is large and potentially vulnerable to remobilization following permafrost thaw, estimates are poorly constrained and quantitative error estimates are lacking (Mishra et al., 2013). Tarnocai et al. (2009) assigned qualitative levels of confidence for different components of the permafrost region SOC stock estimate. In recognition of the limited field observations on which estimates are based, estimates for SOC stocks stored in deep soil (1 to 3 m), Yedoma and deltaic deposits were assigned the lowest degree of confidence.

The aim of this paper is to update and synthesize the current state of knowledge on permafrost SOC stocks. We revise estimates of the permafrost SOC stocks for the 0 to 3 m depth range in soils as well as for deeper sediments in deltaic and Yedoma region deposits. Compared to previous studies (Zimov et al., 2006a; Tarnocai et al., 2009), the number of individual field sites or pedons available for calculations has increased by a factor of 11 for 1 to 2 m soils, a factor of 8 for 2 to 3 m soils and deltaic alluvium and a factor of 5 for Yedoma region deposits. The first ever spatially distributed, quantified estimates for the 0 to 3 m depth range in soils are upscaled based on regional soil maps in the NCSCDv2. Estimates of 0 to 3 m SOC stock are calculated by separating physiographic regions of thick and thin sedimentary overburden, corresponding to lowland and highland areas, respectively (Heginbottom et al., 1993; Brown et al., 2002). In recognition of limited soil development in some high latitude regions (Horwath Burnham and Sletten, 2010), SOC stocks in thin soils of the High Arctic bioclimatic zone are upscaled separately. A revised estimate of

SOC stocks in deltaic deposits is based on new field data and updated information to calculate the spatial extent and depth of deltaic alluvium. For the Yedoma region, the estimate of Strauss et al. (2013) is recalculated by implementing an updated methodology for estimating uncertainty ranges and removing spatial overlap with SOC stored in surface soils. The different components of the permafrost region SOC stocks are summarized and presented together with quantitative uncertainty estimates. A primary goal of this study is to quantify uncertainties associated with permafrost SOC stocks estimates, and to improve understanding of the permafrost SOC pool size and distribution for model simulations of the permafrost-carbon feedback on the climate system.

I-3 Methods

Below we present a summary of methods used to obtain our estimates. More detailed descriptions of methods, including the datasets used for different calculations, are available in the supplemental material.

I-3.1 Calculating 0 to 3 m SOC stocks

Calculation of SOC stocks (absolute amount of SOC reported as either kg or Pg SOC) based on thematic soil maps is done in three steps (Hugelius, 2012). First, the SOC storage (SOC amount per area unit, given in kg C m^{-2}) for individual pedons (a pedon is a three-dimensional body of soil as sampled, described and classified in soil studies) is calculated to the selected reference depths. Second, the pedon data are grouped into suitable thematic upscaling classes, and mean SOC storage (with confidence intervals) for each class and reference depth is calculated. Finally, the mean SOC storage of each class is multiplied with estimates of the areal coverage of thematic upscaling classes to calculate total SOC stocks (including uncertainty ranges) for different classes and reference depths.

For this study, SOC stocks were estimated separately for the 0 to 0.3 m, 0 to 1 m, 1 to 2 m and 2 to 3 m depth ranges using the NCSCDv2. The NCSCDv2 is a polygon-based digital database adapted for use in Geographic Information Systems (GIS), which has been compiled from harmonized national or regional soil classification maps. Map data on soil coverage have been linked to pedon data with SOC storage from the northern permafrost regions to estimate geographically upscaled total SOC stocks (Hugelius et al., 2013a).

The SOC stocks estimates for the 0 to 0.3 m and 0 to 1 m depth ranges were calculated separately in each NCSCDv2-region (i.e., Alaska, Canada, Contiguous USA, Europe, Greenland, Iceland, Kazakhstan, Mongolia, Russia and Svalbard) following

the methodology of Tarnocai et al. (2009). Separate SOC stock estimates were calculated for the High Arctic region. Outside the High Arctic, estimates of 1 to 3 m SOC stocks are based on a geographical subdivision following physiography. This spatial subdivision was chosen because it is expected to reflect different important pedogenic processes occurring across the studied region. Pedons and mapped soil areas in the northern circumpolar permafrost region were separated following physiographic regions of thick and thin sedimentary overburden (Figure appendix I-1; see Heginbottom et al., 1993). Areas of thick sedimentary overburden are described as "areas of lowlands, highlands and intra- and inter-montane depressions characterized by thick overburden, wherein ground ice is expected to be generally fairly extensive" (Heginbottom et al., 1993). Areas of thin sedimentary overburden are described as "areas of mountains, highlands, and plateaus characterized by thin overburden and exposed bedrock, where generally lesser amounts of ground ice are expected to occur" (Heginbottom et al., 1993).

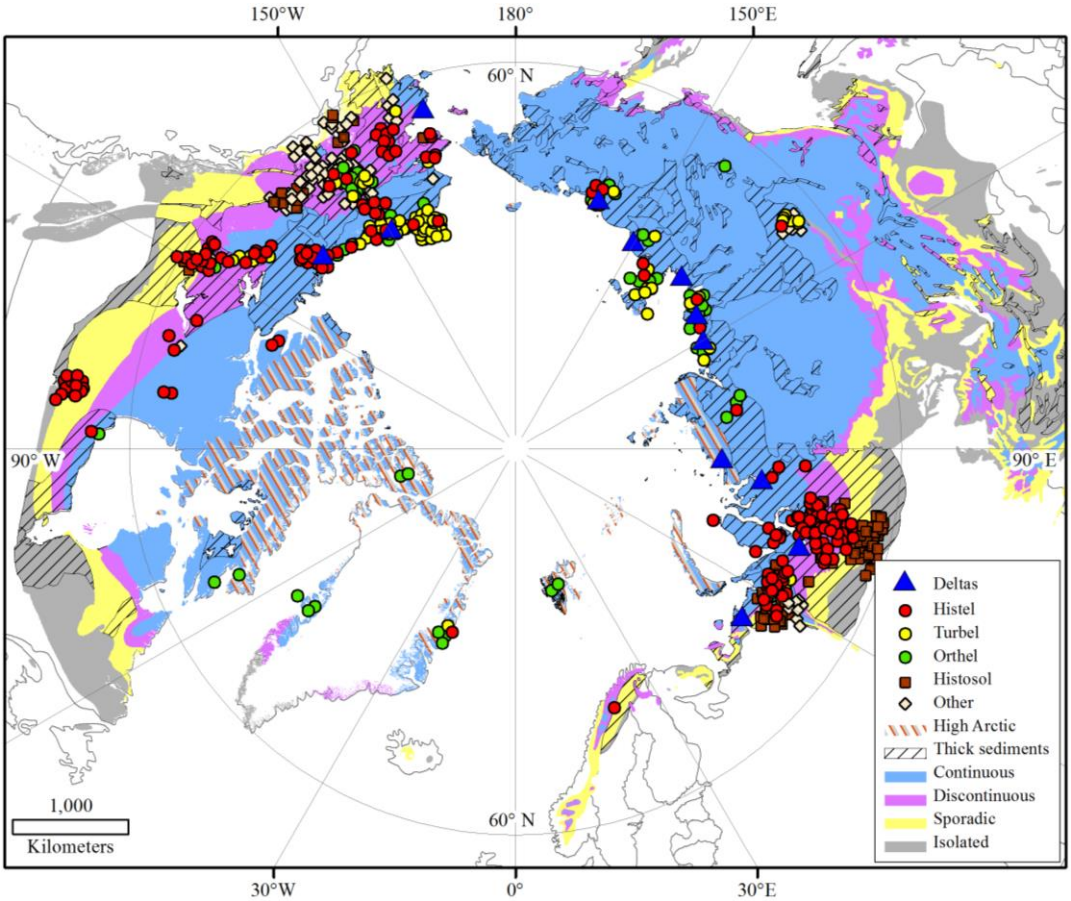

Figure appendix I-1. Geographical distribution of regions with thick sedimentary overburden and permafrost zonation in the northern circumpolar permafrost region (Brown et al., 2002). Map shows locations of the included Arctic river deltas as well as pedons with data in the 0 to 3 m depth range (pedon dataset 2), grouped according to NCSCDv2 upscaling classes. Exact pedon locations have been manipulated for cartographic representation; projection: Azimuthal Equidistant, datum: WGS84. Adapted from Hugelius et al. (2013b).

The upscaled SOC stock estimates for the 0 to 0.3 m and 0 to 1 m depth ranges were calculated separately for each soil order, following USDA Soil Taxonomy (Soil Survey Staff 1999), within the separate NCSCDv2-regions. Permafrost-affected soils (Gelisol soil order) are further differentiated for upscaling into its three suborders: Turbels (cryoturbated permafrost soils), Histels (organic permafrost soils) and Orthels (non-cryoturbated permafrost-affected mineral soils).

For the 1 to 2 m and 2 to 3 m depth ranges, a reduced thematic resolution with aggregated upscaling classes was used. Stocks were calculated separately for the Turbel, Histel and Orthel suborders of the Gelisol soil order and for the Histosol soils order (organic soils without permafrost). All remaining soil orders were grouped as non-permafrost mineral soils.

Table appendix I-1. Summary of number of available pedons (with > 1 m data) in areas with thick and thin sedimentary overburden for soil taxa from different regions (regional subdivision following NCSCD database structure) in the northern circumpolar region. [1]*There are no pedons in the NCSCD regions: Contiguous U.S.A., Mongolia, Iceland or Kazakhstan.* [2]*A total of eight Gelisol pedons from thin sediment regions were used separately to upscale soils of High Arctic tundra soils (five from Greenland and three from Canada).*

	Soil types (n of pedons at 1 to 2 m / 2 to 3 m depths)							
Soil order		*Gelisols*		*Histosols*	*Alfisols*	*Entisols*	*Inceptisols*	*Spodosols*
Soil suborder	*Histels*	*Turbels*	*Orthels*					
			Thick sediment					
NCSCD region[1]								
Alaska	27/27	52/8	27/8	1/1	-	8/1	37/8	2/-
Canada	30/29	4/3	5/3	6/6	2/2	3/1	9/5	-
Greenland	-	-	-	-	-	-	-	-
Scandinavia/Svalbard	1/1	-	2/2	-	-	-	-	-
Russia	89/89	22/14	27/21	60/60	-	1/1	2/-	4/1
Thick sed. sum:	147/146	78/25	61/34	67/67	2/2	12/3	48/13	6/1
			Thin sediment					
NCSCD region[1]								
Alaska	4/4	1/-	2/-	5/5	-	8/-	8/-	6/-
Canada	26/26	3/2	1/-	2/2	3/3	-	1/-	-
Greenland	-	-	3/-	-	-	-	-	-
Scandinavia/Svalbard	-	-	-	-	-	-	-	-
Russia	5/4	2/-	-	1/1	-	1/1	7/7	-
High Arctic[2]	1/1	1/1	6/2					
Thin sed. sum:	36/35	7/3	12/3	8/8	3/3	9/1	16/7	6/-
Total sum:	183/181	85/28	73/37	75/75	5/5	21/4	64/20	12/1

The SOC storage (kg C m^{-2}) values for the 0 to 0.3 m and 0 to 1 m depth ranges were based on 1778 individual pedons from around the northern circumpolar permafrost region (mainly from Gelisol and Histosol orders), which have been complemented with SOC data from Batjes (1996) where data for non-permafrost soil orders was missing (this pedon dataset is hereafter called pedon dataset 1). More detailed information regarding this pedon dataset, including details regarding which soil orders were supplemented with information from Batjes (1996), can be found in Table appendix I-7 to Table appendix I-12 of the supplementary materials. For further details regarding the NCSCD GIS-database and the methods for pedon sampling and calculation of 0 to 0.3 and 0 to 1 m SOC stocks, see Hugelius et al. (2013a). For the deeper soil layers (1 to 2 m and 2 to 3 m depth ranges) a newly compiled pedon database which has been integrated into the NCSCDv2 was used (Figure appendix I-1). From this pedon compilation we included 518 pedons that extend down to 2 m and 351 pedons that extend down to 3 m (this pedon dataset is hereafter called pedon dataset 2). Table appendix I-1 summarizes the number of individual deep pedons available from different geographical regions and areas of thick/thin sedimentary overburden in pedon dataset 2. More detailed information regarding this pedon dataset can be found in Table appendix I-7 to Table appendix I-12 of the supplementary materials.

I-3.2 Calculating deltaic SOC stocks

Deltaic SOC stocks in this study are estimated following the methodology that builds on that of Tarnocai et al. (2009) who used data on the mean depth of alluvium, mean delta lake coverage/depth and mean alluvium SOC density (kg C m^{-3}) from the Mackenzie River Delta (Canada) combined with data on the spatial coverage of seven large Arctic river deltas. Here we combined the data used by Tarnocai et al. (2009) with updated information (from scientific literature and databases) on the areal extent of deltas, mean depth of alluvium, delta lake coverage, permafrost extent and segregated ice content in deltaic deposits. The total volume of alluvium for each delta was calculated from the mapped sub-aerial delta extents and the mean depth of alluvial deposits, subtracting the volume that was estimated to be occupied by massive ice and water bodies. To avoid double counting, the top 0 to 3 m of soil were removed from the calculation. In addition, known Yedoma deposits located in the Lena Delta were removed to avoid spatial overlap with estimates for this region. When the total volume of alluvium was calculated, the total SOC stock of each delta was estimated using field data of mean alluvium SOC density (kg C m^{-3}). In all cases, mean values from other deltas were used when there was no direct data for any specific variable in a delta. Table appendix I-5 summarizes all input data used to es-

timate deltaic alluvium volume and SOC stocks. More detailed descriptions of calculations are available in the supplemental material.

I-3.3 Calculating Yedoma region permafrost SOC stocks

For the purpose of these calculations, the Yedoma region was subdivided into areas of intact Yedoma deposits (late Pleistocene ice- and organic-rich silty sediments) and permafrost deposits formed in thaw-lake basins (generalized as thermokarst deposits which may be either mineral soils, lake sediment or peat deposits). Volumes of unfrozen sediment underlying water bodies and areas covered by deltaic or fluvial sediments were excluded. Twenty-two Yedoma and 10 thermokarst deposit profiles were studied and sampled from river or coastal bluffs exposed by rapid thaw and erosion (Strauss et al., 2013). Total SOC stocks in intact Yedoma and perennially frozen thermokarst deposits below 3 m are calculated based on individual observations of: deposit thickness (n=20 and 8, respectively), organic C content (weight %, n=682 and 219), bulk density (n=428 and 117), and wedge-ice content (volume %, n=10 and 6). The upper 3 m of sediment were excluded to avoid spatial overlap with estimates of storage in 0 to 3 m soils based on the NCSCDv2. For details regarding calculations of the spatial extent of different sediments, data collection and spatial distribution of field observations see Strauss et al. (2013). Because of high inherent (spatial) heterogeneity and non-normal distributed input parameters, the SOC stock calculations are based on bootstrapping techniques using resampled observed values (similar to Strauss et al., 2013). The applied methodology differed from that of Strauss et al. (2013) in several ways. The number of resampling steps for each parameter was connected to the original number of observations of the different parameters deposit thickness, C%, bulk density, and wedge-ice. We did 10,000 separate bootstrapping runs and the total mean SOC stock size estimate was derived afterward for every bootstrapping run. This resulted in an overall mean value calculated from 10,000 observation-based bootstrapping means. Because organic C% and bulk density of individual sediment samples are correlated, paired values were used in the resampling process. Computations were performed using R software (boot package).

I-3.4 Estimating SOC stock uncertainties

Spatial upscaling using mean values of classes from thematic maps, such as soil maps, builds on the premise that an empirical connection between map classes and the investigated variable can be established through point sampling (Hugelius, 2012). Sources of upscaling uncertainty in such thematic mean upscaling can be divided into database uncertainty arising from insufficient field-data representation to describe natural soil variability within an upscaling class and spatial uncertainties

caused by areal misrepresentation of classes in the upscaling map (Hugelius, 2012). Database uncertainty can be estimated based on the standard error (reflects variance and number of independent replicates) and the relative contribution towards the total stock of each upscaling class. This procedure assumes that the available sample is sufficiently replicated to accurately reflect the natural variability within a class. If this is not the case, the uncertainty arising from this so-called representation error can be estimated. Spatial errors in individual upscaling classes can be assessed if dedicated, comprehensive ground truth datasets to assess map accuracy are available, which is not the case in this study. All uncertainty estimates in this study assume that the spatial extent of different soil orders, deltas and the Yedoma region within the northern circumpolar permafrost region are correctly mapped.

Calculations of uncertainty ranges for the different depth ranges and regions of 0 to 3 m soil SOC stocks and deltaic alluvium are based on the methodology described by Hugelius (2012), modified to also include the estimated representation error in those cases where estimates for one region were based on small statistical samples. The uncertainty ranges are 95 % confidence interval (CI) ranges calculated from the standard deviation (StD) and proportional areal/volumetric contribution of each upscaling class. The relative contribution to total uncertainty by individual soil classes is defined as the proportion of combined StD and proportional areal/volumetric contribution of that class.

The uncertainty ranges for Yedoma region deposits are the 5th and 95th percentiles of bootstrapped observations (based on the methodology of Strauss et al., 2013). These ranges are considered equivalent to 95 % CI ranges. The uncertainty ranges of the different SOC stock components are combined using a formula for additive error propagation of covarying variables (Roddick, 1987). More detailed descriptions of all calculations, including formulas and a schematic overview of uncertainty calculations (Figure appendix I-5) are available in the supplemental material.

I-3.5 Statistical tests of significance

Because different pedon datasets were used to calculate 0 to 1 m SOC stocks (pedon dataset 1) and 1 to 3 m SOC stocks (pedon dataset 2), there was a concern that these two dataset may not accurately reflect the same statistical populations (Hugelius, 2012). Therefore, the circumpolar mean 0 to 1 m SOC storage (kg C m^{-2}) between the two databases was compared using Student's t-test with α=0.05 (test from parameters, software PAST v2.17b, Hammer et al., 2012). These tests were performed at the reduced thematic resolution used to calculate deeper SOC stocks. Because the individual pedon observations and coordinates are no longer available for

pedon dataset 1, the tests could not be done separately for the different physiographic regions (mean, standard deviation and n values of pedon dataset 1 for the separate regions are not known).

For each soil upscaling class (at reduced thematic resolution), SOC storage (kg C m^{-2}) in the individual depth ranges (0 to 1 m, 1 to 2 m and 2 to 3 m) were also compared across physiographic regions of thick and thin sedimentary overburden using a two tailed Student's t-test with α=0.05 (software PAST v2.17b).

I-4 Results

I-4.1 Mean 0 to 3 m SOC storage and depth distribution in soil classes across regions

I-4.1.1 Mean pedon SOC storage used for upscaling

Table appendix I-2 summarizes the SOC storage (kg C m^{-2}) and uncertainty ranges (95 % CI) for the different soil classes used in upscaling. More detailed information regarding the databases used to calculate mean SOC storage of different soil upscaling classes in all depth ranges can be found in Table appendix I-7 to Table appendix I-12 of the supplementary materials. In general, the highest mean SOC storages are in the organic soils (Histosols and Histels), followed by Turbels, Orthels and non-permafrost mineral soils. Organic soils and permafrost-affected soils also store more SOC below 1 m depth (except Orthels in regions of thin sediment overburden). Storage of SOC in poorly developed permafrost soils of the High Arctic is considerably lower than other permafrost soils. Estimates for soils of the High Arctic and physiographic regions of thin sedimentary overburden are associated with wide uncertainty ranges.

The mean SOC storage estimates used for upscaling (Table appendix I-2) are based on two different pedon datasets (pedon dataset 1 above 1 m depth and dataset 2 for deeper soils). However, both datasets have data for the top meter of soil. These two pedon datasets represent independent samples for estimating SOC storage (kg C m^{-2}) in the top meter of soils in the northern circumpolar permafrost region. If both datasets are assumed to be unbiased, representative samples of SOC storage, they should provide similar estimates. Therefore, inter-comparisons of these estimates are informative. Comparing the 0 to 1 m SOC storage (kg C m^{-2}) values from the two pedon datasets region revealed that there are no significant differences between the datasets for mean 0 to 1 m SOC storage (based on all circumpolar pedons) in the Orthel and Histel classes (t-test, $p>0.05$). Turbels and non-permafrost mineral soils

have significantly higher SOC in pedon dataset 2 (t-test, $p<0.05$). Histosols have significantly lower SOC in pedon dataset 2 (t-test, $p<0.05$).

Table appendix I-2- Summary of mean SOC storage in different depth ranges of the soil upscaling classes for the upscaling regions applied in this study. Numbers for soils above 1 m depth are based on pedon dataset 1 while numbers for soils from 1 to 3 m depth are based on pedon dataset 2. Note that for soils below 1 m depth all non-permafrost mineral soils (Non-pf. min.) are combined in one upscaling class. Per our definition of High Arctic soils, these soils are not found in physiographic regions with thick sedimentary overburden.

Region:	Circumpolar		Thick sediment		Thin sediment	
Depth range:	0 to 0.3 m	0 to 1 m	1 to 2 m	2 to 3 m	1 to 2 m	2 to 3 m
Soil class:	*SOC storage ± 95 % CI (kg C m^{-2})*					
Alfisols	4.7 ± 0.4	7.9 ± 0.7				
Entisols	1.1 ± 0.8	7.7 ± 1.7				
Inceptisols	4.9 ± 0.2	9.5 ± 0.4				
Spodosols	11.7 ± 2	21.3 ± 5				
Natric soils	2.9 ± 0.6	10.6 ± 2.2				
Aquic soils	9.2 ± 0.4	16.8 ± 0.7				
Vertisols	5.7 ± 2.1	13.5 ± 4.9				
Mollisols	6.4 ± 0.4	12.2 ± 0.7				
Aridisols	1.6 ± 1.8	1.7 ± 5.4				
Andisols	11.4 ± 0.4	25.4 ± 0.2				
Ultisols	5.1 ± 1.2	9.4 ± 3.2				
Non-pf. min.			9.5 ± 3.3	10.3 ± 3.3	9.1 ± 4.6	0.5 ± 0.6
Histosols	22.5 ± 0.5	69.1 ± 0.9	58 ± 9	29.8 ± 9	95.7 ± 43.4	46.1 ± 44.2
Turbels	14.7 ± 1.5	33 ± 3.5	23.2 ± 4.1	20.1 ± 4.1	31.6 ± 33.1	19.5 ± 17.5
Orthels	15.8 ± 2.6	25.3 ± 4.1	27 ± 9.5	21.6 ± 9.5	2.6 ± 2	1.3 ± 16.9
Histels	18.1 ± 3	49.3 ± 8.4	43.6 ± 5.1	24.8 ± 5.1	49 ± 9.2	30.5 ± 8.8
High Arctic	9.8 ± 7.4	17.8 ± 11			6.9 ± 6.7	2.8 ± 5.6

I-4.1.2 Comparison of SOC storage across regions and depth

Pedon dataset 1 has no data below 1 m depth and for consistency in comparisons only pedon dataset 2 is referred to regarding all descriptions or comparisons of SOC storage across regions or depth distribution of SOC within soil classes. The vertical distribution of SOC through the profile varies greatly between soil orders (Figure appendix I-2). In most soil classes the upper 1 m of soil stores more SOC than the deeper depth ranges but for Histosols, the highest estimated SOC storage is in the 1 to 2 m depth range (Figure appendix I-2G and H). In Orthels in regions of thin sediment overburden, non-permafrost mineral soils and soils of the High Arctic a large fraction (30 % to 50 %) of total 0 to 3 m SOC is stored in the top-soil (upper 0.3 m;

Figure appendix I-2E, I, J and K). Outside of the High Arctic, organic soils, Turbels and Orthels in thick sediment regions store ~50 % or more of SOC below 1 m depth.

Statistical comparison of SOC storage between physiographic regions of thick and thin sediment overburden shows significantly higher SOC in thick sediment regions across all depth ranges for Orthels and for non-permafrost mineral soils in 2 to 3 m depth (Figure appendix I-2E, F, I and J; t-test, $p<0.05$). At depths down to 2 m, Histosol SOC storage is significantly higher in thin sediment regions (Figure appendix I-2G and H; t-test, $p<0.05$). Other soil upscaling classes show no significant differences between physiographic regions.

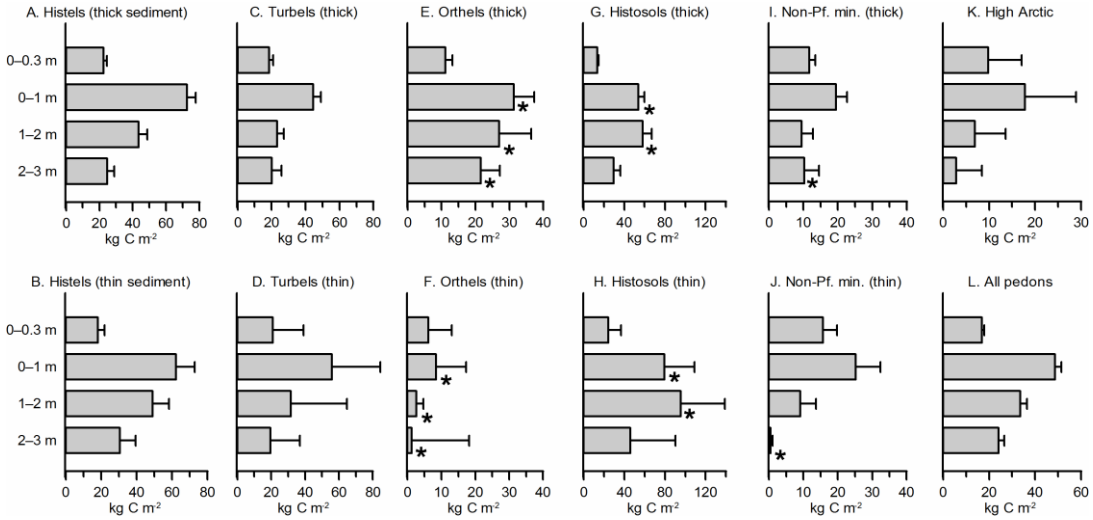

Figure appendix I-2. Mean SOC storage (kg C m^{-2}) with error bars showing 95 % confidence intervals of the mean, for different soil upscaling classes calculated using pedon dataset 2. Different panels A to J show SOC storage estimates for the different depth ranges in areas of thick and thin sedimentary overburden, respectively. Panels K and J show mean SOC storage for the High Arctic region and for all pedons grouped together. Asterisks mark depth intervals in soil upscaling classes where SOC storage is significantly different from the equivalent interval in the other region (t-test, $p<0.05$).

I-4.2 Upscaled soil area and SOC stocks across regions

The estimated soil area of the northern circumpolar permafrost region is 17.8×10^6 km^2 (excluding exposed bedrock, glaciers and ice-sheets and water bodies). This also includes the full areal extent of regions where permafrost coverage is non-continuous so that a significant fraction of the area is not in permafrost terrain. Physiographic regions with thick sedimentary overburden occupy 35 % and regions with thin sedimentary overburden 65 % of the soil area (Table appendix I-3). The North American continent (including Greenland) accounts for 39 % of the soil area and Eurasia for 61 % of the soil area.

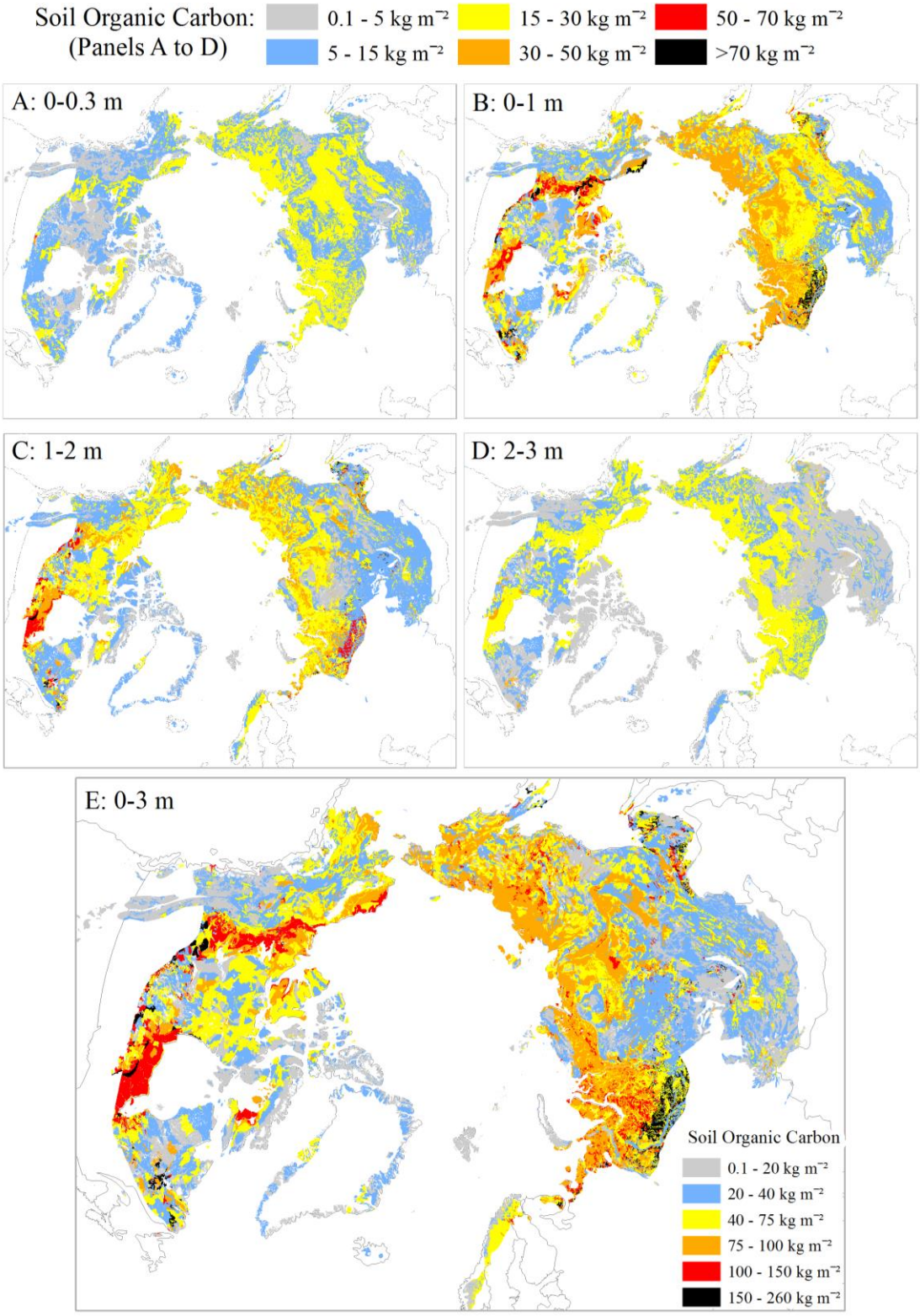

Figure appendix I-3. Map of estimated 0 to 3 m SOC storage (kg C m^{-2}) in the northern circumpolar permafrost region. Shows estimates based on sediment thickness upscaling. Panels show 0 to 1 m SOC calculated subdivided following NCSCD regions while 1 to 2 m and 2 to 3 m SOC is calculated subdivided for Eurasia vs. North America and areas of thick vs. thin sediments, respectively. Projection: Azimuthal Equidistant, datum: WGS84.

Total estimated northern circumpolar permafrost region SOC stocks (±95 % CI) are 217±12 Pg for the 0 to 0.3 m depth and 472±27 Pg for the 0 to 1 m depth (Table appendix I-3). Estimated deeper SOC stocks are 355±81 Pg for the 1 to 2 m depth and 207±42 Pg for the 2 to 3 m depth (Table appendix I-2). The summarized SOC stocks for 0 to 2 m depth are 827±108 Pg and for 0 to 3 m depth are 1034±150 Pg.

Table appendix I-3. Summary of estimated soil area and SOC stocks (with ±95 % CI where available) subdivided into physiographic regions of thick and thin sedimentary overburden (following Brown et al., 2002), the High Arctic region and summarized for the northern circumpolar permafrost.

	Thick sediments	Thin sediments	High Arctic region	Circumpolar
Soil area (km^2):	6.2×10^6 (35 %)	10.6×10^6 (59 %)	1.0×10^6 (6 %)	17.8×10^6
SOC stocks (Pg):				
0 to 0.3 m	90	117	10 ± 3	217 ± 12
0 to 1 m	213	235	24 ± 8	472 ± 27
1 to 2 m	161 ± 14	187 ± 79	7 ± 5	355 ± 81
2 to 3 m	119 ± 16	86 ± 39	3 ± 3	207 ± 42
0 to 2 m	374	422	31 ± 13	827 ± 108
0 to 3 m	493	507	34 ± 16	1034 ± 150

Thick sediment areas have lower total SOC stocks than thin sediment areas in the 0 to 0.3 m, 0 to 1 m and 1 to 2 m depth ranges (corresponding to a significantly smaller areal coverage). However, in the 2 to 3 m depth range the total SOC stocks are higher in areas of thick sediments, reflecting the very low estimated SOC contents below 2 m depth for some soil classes which have significant areal extent in thin sediment regions (i.e. Orthels and non-permafrost mineral soils; Figure appendix I-2 and Table appendix I-7 to Table appendix I-12). There is a clear trend of wider uncertainty ranges in thin sediment regions, caused by variable mean SOC storage (Figure appendix I-2) and a low number of available pedons for this very large region (Table appendix I-1). Maps of estimated SOC content (Figure appendix I-3) show clear differences in estimated SOC stocks, with higher numbers in thick sediment regions than in the thin sediment regions.

The High Arctic region occupies 6 % of the northern circumpolar permafrost region and stores an estimated 34±16 Pg SOC in the 0 to 3 m depth range (3 % of total permafrost region 0 to 3 m SOC stocks). Most of this is in the upper meter of the soil with 10±3 and 24±8 Pg SOC in the 0 to 0.3 m and 0 to 1 m depth ranges, respectively. Estimates of SOC stocks in deeper soil layers in the High Arctic are lower, 7±5 and 3±3 Pg SOC in the 1 to 2 m and 2 to 3 m depth ranges, respectively.

Permafrost-affected soils dominate SOC storage in the permafrost region with 70 % of total stocks (Table appendix I-4). Turbels outside of the High Arctic region, which

account for 31 % of the soil area, store 41 % of total 0 to 3 m SOC stocks (Table appendix I-4), and is the single dominant upscaling class across all depth ranges and regions (Table appendix I-7 to Table appendix I-12). In the 1 to 2 m depth range, the organic soils (Histels and Histosols) contribute more to the total SOC stocks, due to higher mean SOC storage in that depth interval (Figure appendix I-2). Histosols are especially important in regions of thick sedimentary overburden where the mean depth of peat deposits (data not shown) and mean SOC stocks are greater. Outside of continuous permafrost coverage, non-permafrost mineral soils cover 38 % of the northern circumpolar permafrost region, but accounts for only 15 % of the SOC mass.

Table appendix I-4. Summary of areal coverage (% of total permafrost region coverage) and total estimated SOC stocks (with % of total) of soil upscaling classes with reduced thematic resolution. *[1]Applies to Gelisol suborders outside of the High Arctic region. [2]A very small fraction (<1 %) of the High Arctic is mapped as non-Gelisols but these soils are equally subdivided to Gelisol suborders here. [3]Note that this class is not used in upscaling and is included here for summative purposes only.*

Soil classes	Area km²	SOC stocks in 0 to 3 m Pg
Turbels [1]	5.5 (31 %)	454 (44 %)
Orthels [1]	2.3 (13 %)	92 (9 %)
Histels [1]	1.2 (7 %)	147 (14 %)
High Arctic soils[2]	1.1 (6 %)	34 (3 %)
High Arctic Turbels	0.7 (4 %)	22 (2 %)
High Arctic Orthels	0.2 (1 %)	6 (0.6 %)
High Arctic Histels	0.2 (1 %)	6 (0.6 %)
Gelisols sum:[3]	10.1 (57 %)	727 (70 %)
Histosols	0.9 (5 %)	149 Pg (14 %)
Non-Gelisols, mineral	6.8 (38 %)	158 Pg (15 %)
Total	17.8×10^6 km^2	1035

Estimates for permafrost soils are the most uncertain. For the 0 to 1 m SOC stock estimate, Turbels, Orthels and Histels together account for 89 % of the total estimated uncertainty (61 %, 14 % and 15 % respectively). At greater depths, uncertainties increase further. Overall, the Turbels introduces the most uncertainty to the SOC stock estimates across depth ranges, especially at depths below 1 m. Turbels account for 54 % to 89 % and 72 % to 90 % of upscaling uncertainty (1 to 2 m and 2 to 3 m depth ranges, respectively). The particularly large uncertainties of Turbel SOC storage estimates in physiographic regions of thin sedimentary overburden are caused by few available pedons that show large within-class variability. The relative uncertainties of High Arctic soil SOC stocks are large. However, these soils have low SOC stocks (0.2 to 4 % of total permafrost region SOC stocks across upscaling regions

and depth ranges) and contribute little towards the uncertainty of the total estimates. More detailed information regarding the total soil area, SOC stocks and relative contribution towards the estimated uncertainty ranges of different soil upscaling classes in all depth ranges can be found in Table appendix I-7 to Table appendix I-12 of the supplementary materials.

I-4.3 Storage of SOC below 3 m depth in deltaic deposits

Table appendix I-5 summarizes data sources, the different parameters used to estimate the volume and SOC content of deltaic alluvium and calculated results for the individual deltas. The total estimated area of major river deltas in the northern circumpolar permafrost region is 75,800 km^2. This estimate includes twelve deltas ranging in size from 500 to 32,000 km^2. The combined estimated alluvium volume below 3 m depth in these deltas is ca. 3,500 km^3 (stored between 3 and 60 m depth, mean alluvium depth is 54 m). Field-based observations of alluvium depth are very limited and estimates are based on only one observation for the Lena River Delta and five different observations for the Mackenzie River Delta. Estimates for mean alluvium SOC density are available from the literature for five different delta units and range from 8.3 to 56.2 kg C m^{-3}. For deltas where no direct observations are available, alluvium depth and SOC content is estimated from the mean values of those deltas that have data.

Estimated SOC stocks in deltaic alluvium below 3 m depth are 91±52 Pg. Because of high mean alluvium SOC density total stocks in the Mackenzie River Delta (34 Pg) are higher than those of the Lena River Delta (23 Pg), which is considerably larger and accounts for 44 % of the total estimated volume of alluvium. The Yana River Delta stores an estimated 7 Pg and alluvial deposits of the remaining nine deltas store the remaining 27 Pg (≤ 5 Pg each). Between 51 and 92 % (mean 84 %) of deltaic alluvium is stored in permafrost. Estimated SOC stocks in perennially frozen alluvium are 69±38 Pg. For most of the deltas included in this estimate, no field-observations of alluvium depth or SOC content are available. Calculated CI intervals indicate that uncertainties arising from limited observations of alluvium depth (±49 Pg) are greater than uncertainties from poorly estimated alluvium SOC density (±18 Pg).

Table appendix I-5. Summary of input data and estimated total volume of alluvium and SOC stocks in major, permafrost-affected Arctic river deltas. In the cases where a parameter is taken from a map that reports ranges of data, the values used for calculations are given in brackets. For the estimated volume of alluvium, the fraction of alluvium that is perennially frozen is given in brackets. [a]*If nothing else is stated, delta areas are from Walker (1998). Refers to sub-aerial delta area. Note that subsea deltaic deposits or deltaic deposits covered under other deposits are not included in the current estimate;* [b]*Schwamborn et al. (2000), in Schwamborn et al. (2002b);* [c]*Heginbottom (2000);* [d]*Mean calculated between the depth range 10-30 m (Aylsworth et al., 2000), ≥56 m (Smith et al., 2005a), 50 m (Tarnocai et al., 2009), 55 m (Johnston and Brown, 1965) and 58 m (Taylor et al., 1996).;* [e]*Tarnocai et al. (2009);* [f]*Assumed to be 60 m (Schwamborn et al., 2002b) minus a 20 m Ice Complex coverage (Schirrmeister et al., 2011a);* [g]*Calculated based on proportional cover of geomorphic units reported by Zubrzycki et al. (2013) and references therein, assuming uniform water surface area distribution across the delta;* [h]*If nothing else is stated, permafrost extent and ground ice contents are from Brown et al. (2002). Ground ice content refers to segregation ice, injection ice and reticulate ice. Values are assumed to be valid for the upper 15 m of alluvium below which there is assumed to be no massive ice;* [i]*Smith (2011);* [j]*Schirrmeister et al. (2011a) ;* [k]*Zubrzycki et al. (2013);* [l]*Calculated mean from those delta regions where data is available;* [m]*Calculated based on data from Ping et al. (2011);* [n]*The fluvial sands underlying the third terrace Ice Complex deposit is assumed to have similar characteristics to the fluvial deposits in the second terrace (Schirrmeister et al., 2011a);* [o]*Not applicable, surface is covered by Ice Complex and not included in calculations;* [p]*±95 % CI range are the combined uncertainties from estimates of mean alluvium SOC content (±18 Pg) and from estimates of mean alluvium depth (±49 Pg). Both estimates include representation error (see method section for details).*

River name	Delta area[a] (km^2)	Depth of alluvium (m)	Water bodies coverage (%)	Permafrost extent[h] (% value used for calculations)	Ground-ice content (% value used for calculations)	Alluvium SOC density mean± SD, kg C m^{-3} (n, sampling depth range)	Volume of alluvium, km^3 (% in permafrost)	Alluvium SOC stock, Pg (±95 % CI)
Lena	32,000							
Active floodplain	13,203[g]	60	31[k]	Continuous (90)	>20 (25)	11.6±7.6 (n=7, 50–100 cm)[k]	651 (92)	8
First terrace	7,117[g]	60	31[k]	Continuous (90)	>20 (25)	29.9±15.1 (n=22, 50–100 cm)[k]	351 (92)	10
Second terrace	9,120[g]	60[b]	31[k]	Continuous (90)	>20 (25)	8.3±6.9 (n=3, 0–409 cm)[j]	450 (92)	4
Third terrace	2,560[g]	40[f]	NA[o]	Continuous (90)	>20 (25)	8.3±6.9[n]	97 (90)	0.8
Mackenzie	13,000	48[d]	41[i]	35–65 %[c] (50)	5–15 (10)[c]	56.2±8.4[e] (n=5, 2–200 cm)	609 (51)	34
Yana	6,600	54[l]	36[l]	Continuous (90)	>20 (25)	25.8±18.8[l]	285 (91)	7
Indigirka	5,000	54[l]	36[l]	Continuous (90)	>20 (25)	25.8±18.8[l]	216 (91)	5
Yenisey	4,500	54[l]	36[l]	Continuous (90)	10–20 (15)	25.8±18.8[l]	201 (91)	5
Kolyma	3,200	54[l]	36[l]	Continuous (90)	>20 (25)	25.8±18.8[l]	138 (91)	4
Ob	3,200	54[l]	36[l]	Continuous (90)	10–20 (15)	25.8±18.8[l]	143 (91)	4
Pechora	3,200	54[l]	36[l]	Continuous (90)	<10 (5)	25.8±18.8[l]	148 (90)	4
Yukon	3,000	54[l]	36[l]	Continuous (90)	10–20 (15)	25.8±18.8[l]	134 (91)	3
Pyasina	1,000	54[l]	36[l]	Continuous (90)	>20 (25)	25.8±18.8[l]	43 (91)	1
Colville	600	54[l1]	36[l]	Continuous (90)	<10 (5)	21.2±3.8 (n=4, 55–270 cm)[m]	28 (90)	0.6
Olenek	500	54[l]	36[l]	Continuous (90)	>20 (25)	25.8±18.8[l]	22 (91)	0.5
Sum / mean	75,800 km^2	54 m	34 %	83 %	19 %	26.0 kg C m^{-3}	3,514 (84 %)	91 ±52 Pg

I-4.4 Storage of permafrost SOC in the Yedoma region

The combined area of the Yedoma core region in Siberia (Romanovskii, 1993) and Alaska (Jorgenson et al., 2008) is 1,387,000 km^2. Of this 416,000 km^2 (30 %) is considered intact Yedoma and 775,000 km^2 (56 %) is comprised of permafrost deposits that have previously gone through thermokarst cycling (refrozen sediments accumulated in thaw-lake basins, including mineral soil, lake sediment or peat deposits) (Grosse et al., 2013b; Strauss et al., 2013). Within this Yedoma core region, thawed sediments underlying lakes and rivers (150,000 km^2) and areas covered by deltaic or fluvial sediments (47,000 km^2) are excluded from calculations.

The estimated stocks of permafrost SOC below 3 m depth in the Yedoma region is 181 Pg with an uncertainty range of 130 to 239 Pg (hereafter approximated to ±54 Pg). Of this an estimated 74 Pg with an uncertainty range of 55 to 94 Pg (hereafter approximated to ±20 Pg) is stored in intact Yedoma while 107 with an uncertainty range of 60 to 161 Pg (hereafter approximated to ±50 Pg) is stored in perennially frozen thermokarst basin deposits.

The estimated total stocks of permafrost SOC in the Yedoma region is 213 Pg with an uncertainty range of 164 to 267 Pg (hereafter approximated to ±52 Pg). Of this an estimated 83 Pg with an uncertainty range of 64 to 104 Pg (hereafter approximated to ±20 Pg) is stored in intact Yedoma while 130 Pg with an uncertainty range of 85 to 180 Pg (hereafter approximated to ±45 Pg) is stored in perennially frozen thermokarst basin deposits.

I-5 Discussion

This study presents updated estimates of SOC stocks in the northern circumpolar permafrost region based on markedly improved databases. The study includes the first spatially distributed quantification of 1 to 3 m SOC stocks as well as the first quantitative uncertainty ranges for SOC stocks in this region. In recognition of the limited soil development in high latitude areas with thin sediments, the High Arctic region was treated separately in upscaling. Adding up SOC stocks in 0 to 3 m soils, deltaic deposits and Yedoma region permafrost deposits for the northern circumpolar permafrost region results in an estimate of 1307 Pg with an uncertainty range of 1140 to 1476 Pg (roughly ±170 Pg). Of this, 999 Pg of SOC is stored in permafrost terrain (defined as storage in Gelisols/High Arctic soils and in deposits below 3 m depth). The SOC stock in perennially frozen soil and sediment is estimated to be 822 Pg (or 63 %) or less (assuming an active layer depth of 30 cm or more in all Gelisols and High Arctic soils).

I-5.1 Differences to previous estimates

The scope of this estimate is similar to the previous depth-integrated estimate of permafrost region SOC stocks by Tarnocai et al. (2009). Revised databases and methodology lead to substantial reductions of estimated total SOC stocks (Table appendix I-6) especially below 3 m depth. There is a considerable reduction in estimates of SOC stored in permafrost terrain and in permafrost.

Table appendix I-6. Summative comparison of permafrost SOC stocks between the previous estimates in Tarnocai et al. (2009) and this study. [1]*Estimated assuming an active layer depth of 30 cm or more in all Gelisols/High Arctic soils, following the methodology of Kuhry et al. (2013).* [2]*Defined as storage in Gelisols/High Arctic soils and in permafrost in Yedoma or permafrost deltaic deposits below 3 m depth.*

Soil organic carbon stocks	Tarnocai et al. (2009) Pg (% of region total)	This study Pg (% of region total)	Difference Pg
	Soils in the 0 to 3 m depth range		
Turbels	581 (35 %)	476 (36 %)	-105
Orthels	53 (3 %)	98 (7 %)	+45
Histels	184 (11 %)	153 (12 %)	-31
Sub-total Gelisols	818 (49 %)	727 (56 %)	-91
Gelisols in permafrost[1]	692 (41 %)	572 (44 %)	-120
Histosols	94 (6 %)	149 (11 %)	+55
Non-Gelisols, mineral	112 (7 %)	158 (12 %)	+46
Total for 0 to 3 m soils	1024 (61 %)	1035 (79 %)	+11
	Deposits below 3 m depth		
Deltaic alluvium	241 (14 %)	91 (7 %)	-150
Yedoma region	407 (24 %)	181 (14 %)	-226
Combined SOC in soils (0 to 3 m), deltaic alluvium and Yedoma region sediments			
In permafrost terrain[2]	1466 (88 %)	977 (75 %)	-489
In permafrost[1]	1134 (68 %)	822 (63 %)	-312
Total permafrost region	1672	1307	-365

The updated estimates of northern circumpolar permafrost region SOC stocks in 0 to 0.3 m and 0 to 1 m depth are largely based on the same data as the equivalent estimates of Tarnocai et al. (2009). Differences between estimates (+26 Pg and −24 Pg, respectively) are due to gap-filling procedures and updating of the NCSCD spatial framework (Hugelius et al., 2013a; Hugelius et al., 2013b) and to new SOC estimates for the High Arctic region. The updated pedon database used to estimate SOC between 1 and 3 m depth includes spatial representation across the northern circum-

polar permafrost region and about a ten-fold increase in the number of pedons compared to that of Tarnocai et al. (2009). While the relative changes in the total 0 to 3 m SOC stocks are small, there are considerable differences between individual soil orders. The revised estimates are considerably lower for Turbels and Histels but higher for Orthels Histosols and non-permafrost mineral soils (Table appendix I-6). This results in a 120 Pg reduction of SOC stored in permafrost in the 0 to 3 m depth range compared to the previous estimate. Note that the estimates of the fraction of SOC stored in permafrost are highly uncertain as they are based on an assumption that the average active layer depth in all Gelisols is 0.3 m or more (see Kuhry et al., 2013).

Using a subset of pedon dataset 2 and soil (sub)order coverage from the NCSCD, Harden et al. (2012) estimated total northern Gelisol SOC stocks to be 1060 Pg, compared to 727 Pg in this estimate. The major cause for this difference is that Harden et al. (2012) does not subdivide the upscaling following physiographic regions, which leads to higher estimated mean SOC storage in Gelisol soil orders for regions of thin sedimentary overburden.

In recognition of the limited soil development in high latitude areas with thin sediments, the High Arctic region was treated separately in upscaling. A previous study estimated active layer SOC stocks for this region to be 12 Pg (Horwath Burnham and Sletten, 2010), which falls within current SOC estimates of 10±3 Pg and 24±8 Pg in the 0 to 0.3 m and 0 to 1 m depth ranges, respectively.

The previous estimate of deltaic SOC stocks by Tarnocai et al. (2009) was extrapolated based on field data from the Mackenzie River Delta only. The revised, substantially lower, estimate presented here builds on this same basic methodology but with some additional sources of data from the literature. The difference between estimates is mainly caused by lower estimates of mean alluvium SOC density (kg C m^{-3}) when including new available data from the Colville and Lena river deltas (Ping et al., 2011; Schirrmeister et al., 2011c; Zubrzycki et al., 2013). There are smaller differences in the estimated total volume of deltaic alluvium. This is calculated based on areal extent and depth of alluvium, accounting for the volume of water bodies (assuming a mean water depth of 5 m) and volumetric massive ice content. While the areal extent of deltas for the updated estimate is based on an entirely different source (Walker, 1998) and includes a larger subset of individual deltas, the difference in total estimated sub-aerial delta surfaces is relatively small. The estimated depth of alluvium in deltas is also similar to the original estimate. Tarnocai et al. (2009) consider all deltaic alluvium below 3 m to be in permafrost and do not consider any reduced alluvium volume caused by occurrences of massive ice. If no massive ice con-

tent is assumed in this study, the equivalent estimate would increase from 91±52 Pg to 98±54 Pg.

The updated estimate of permafrost SOC storage below 3 m depth in the Yedoma region is based on the same dataset as the estimate for the total permafrost SOC stocks in this region developed by Strauss et al. (2013). Removing depth overlap with the 0 to 3 m soil estimate resulted in a reduction from 213 Pg to 181 Pg. The substantial reduction compared to the previous depth-integrated estimate by Tarnocai et al. (2009) is mainly caused by a twofold reduction of estimated bulk density, a reduction of estimated deposit thickness, and different assumptions regarding the characteristics of intact Yedoma compared to refrozen thermokarst sediments (see Figure 3 in Strauss et al., 2013).

I-5.2 Distribution patterns of SOC stored in 0 to 3 m soil

I-5.2.1 SOC distribution by regions

When compiling pedon dataset 2 for upscaling of SOC stocks in the 1 to 3 m depth range Hugelius et al. (2013b) subdivided pedons and upscaled SOC stocks based on a continental subdivision (North America vs. Eurasia) as opposed to the upscaling based on physiographic regions used in this study. A first version of this study included both continental and physiographic upscaling (Hugelius et al., 2014). This study is based only on physiographic upscaling as we argue that this approach reflects a more accurate assessment of SOC distribution than subdivision by continent. The physiographic regions reflect differences between upland and lowland areas across the northern circumpolar permafrost region (Heginbottom et al., 1993) and are better suited to reflect different soil types and important pedogenic processes. This is also consistent with other studies that have utilized physiography and its influence on soil drainage to upscale soil properties (Harden et al., 2001; Yi et al., 2009). A map of mean SOC storage (Figure appendix I-3) upscaled using physiography shows important patterns that were lacking in continent based upscaling (Hugelius et al., 2014). For example, in the 1 to 2 m depth range, mountainous regions in Siberia emerge as having low SOC stocks below 1 m. This estimate upscaled based on physiographic regions reflects differences between upland and lowland areas across the northern circumpolar permafrost region (Heginbottom et al., 1993). In thin sediment areas ("areas of mountains, highlands, and plateaus characterized by thin overburden and exposed bedrock") we would generally expect conditions to be less favorable for accumulation of large SOC stocks than in areas of thick sediment overburden ("areas of lowlands, highlands and intra- and inter-montane depressions characterized by thick overburden"). The overall upscaled SOC stock estimates follows this pattern of

higher stocks in thick sediment areas, but some individual soils classes do not. Our estimates for thin sediment areas are characterized by large variability, poor pedon representation, and wide uncertainty ranges (see I-5.3.1 below). We emphasize that this dichotomous subdivision into two distinct physiographic landscape types is not realistic at a local scale where transitions are more discrete. For studies at finer scales we would not recommend the use of this relatively coarse subdivision.

I-5.2.2 SOC distribution by soil types

In general, the permafrost soils and organic soils dominate 0 to 3 m SOC storage in the northern circumpolar permafrost region, especially at depths >1 m. This is in accordance with previous results from this region (e.g. Ping et al., 2008; Tarnocai et al., 2009) and reflects current understanding of the processes that lead to accumulation of SOC in permafrost region soils (cryoturbation, accumulation of peat and repeated deposition and stabilization of organic-rich material).

Because of their substantial areal extent and high mean SOC storage (kg C m^{-2}), cryoturbated mineral soils are important SOC reservoirs. Turbels south of the High Arctic region store 41 % of SOC stocks with 31 % areal coverage (Table appendix I-4). There are no significant differences in mean SOC storage between physiographic regions of thick and thin sedimentary overburden regions but there is notable variability in the data at all depths. Especially in areas of thin sediment overburden, low data availability (Table appendix I-1) combined with great natural variability leads to wider relative uncertainty ranges of estimates.

The mean SOC storage (kg C m^{-2}) is highest in organic soils (Histosols and Histels; Table appendix I-2), and these soils also contribute greatly to total SOC stocks (both classes store 14 % each of 0 to 3 m SOC stocks with only 5 % and 7 % areal coverage, respectively). Regions dominated by organic soils, such as the West Siberian Lowlands or the lower Mackenzie River basin, are especially SOC-rich across depths (Figure appendix I-3). There is relatively large variability in SOC storage of organic soils across regions. Unexpectedly, the upper 2 m of Histosols in regions of thin sediment overburden have significantly higher SOC storage than Histosols from thick sediment areas (Figure appendix I-2). Considering the low degree of replication for Histosols in areas of thin sediment overburden (n=8), additional field observations are needed to further evaluate this result. This high estimated mean SOC storage of Histosols in thin sediment regions is heavily influenced by a few very SOC-rich pedons and should be interpreted with caution.

Mineral permafrost soils unaffected by cryoturbation (Orthels) differ greatly across regions. In areas with recurring deposition and stabilization of organic-rich sediment

(alluvium, proluvium, colluvium or wind-blown deposits) very large SOC stocks have accumulated over long timescales (Schirrmeister et al., 2011b). In other cases, shallow, non-cryoturbated permafrost soils in e.g. mountain regions store little SOC (Ping et al., 1998). In this study, Orthels in regions with thin sediments (corresponding to upland or montane areas) store little SOC while Orthels in regions with thick sediment have accumulated significant SOC stocks down to 3 m depth (Figure appendix I-2).

In regions of discontinuous permafrost cover (commonly in areas of boreal forest), a large portion of the landscape is covered by non-permafrost mineral soils which also store significant amounts of SOC. Non-permafrost mineral soils cover 38 % of the total permafrost region area and stores 15 % of total 0 to 3 m SOC stocks. In the upper meter, upscaling is based on the eleven different non-permafrost mineral soil orders mapped in the NCSCDv2. Estimated mean SOC storage in this depth interval shows significant variability in estimates with a range from 1.7 to 25.2 kg C m^{-2} (Table appendix I-2). In the 1 to 2 m depth interval estimated SOC storage is ~10 kg C m^{-2} in both thick and thin sediment regions. This remains unchanged below 2 m in thick sediment regions while there is significantly less SOC in thin sediment regions. A large fraction of SOC in these latter soils is stored in the top-soil within O and A horizons where high SOC storage may indicate accumulation of humified organic matter, charcoal, or char-mediated sorption in fire-prone boreal forests. Beneath O and A soil horizons, important mechanisms for stabilizing SOC in permafrost free mineral soils include deep rooting, sorption of leached dissolved organic C to clay particles or formation of complexes with iron and/or aluminum. Lower SOC storage in deeper horizons reflects that these soils are less affected by C stabilization processes such as cryoturbation or repeated deposition typically found in permafrost or organic soils. The very low storage in non-permafrost mineral soils of regions with thin sediments is due to influence from pedons in alpine terrain with limited soil development where bedrock is typically encountered within the upper 3 m.

I-5.3 Estimate uncertainties and data gaps

This study presents the first quantitative uncertainty ranges for estimates of SOC stocks in northern circumpolar permafrost region. The widest uncertainty ranges are associated with those same components that also Tarnocai et al. (2009) identified as being most uncertain. That study assigned low to very low confidence for estimates of SOC stocks stored in deep soil (1 to 3 m), Yedoma region deposits and deltaic deposits.

For 0 to 3 m soils and deltaic deposits the uncertainty ranges were calculated based on within class variability of pedons (or alluvial deposit thickness) and areal/volumetric coverage of classes. For Yedoma region SOC stocks, the uncertainty ranges correspond to the 5th and 95th percentiles of bootstrapped estimates. The former approach integrates all individual soil-horizons to the pedon level and assumes a (log)normal data distribution while the latter allows non-normality, but also differs in that it does not integrate individual sediment layers or horizons at the site/pedon level. These updated estimates are based on collaborative databases where efforts have been made to collect data from across regions and from different research groups. Despite this, substantial regional data gaps remain such as in the High Arctic, central Siberia and many river deltas.

I-5.3.1 Spatial distribution of pedons

The spatial distribution of pedons used to estimate SOC stocks in the 1 to 3 m depth range is highly clustered (Figure appendix I-1). For example, parts of Alaska and western Russia are well represented, but there are significant data gaps in Central Asia, Scandinavia, Greenland, Svalbard and Eastern Canada. There is a clear possibility that the available pedons are not truly representative for those areas where field data are lacking. This source of uncertainty is not addressed in this study but we acknowledge that adding more field-based data from under-sampled regions could substantially improve estimates. A previous comparisons between estimates of 0 to 1 m SOC stocks based on the NCSCD and local scale studies revealed pronounced differences, especially for Turbels and organic soils (Kuhry et al., 2010). A way to potentially address this source of uncertainty in future studies is to assess the upscaled estimates against independent validation datasets. Such approaches could be applied across scale to address uncertainties from site-scale to regional scales.

I-5.3.2 Regional uncertainties of estimates for 0 to 3 m soils

The estimates of SOC stocks in 1 to 3 m soils are based on a highly generalized upscaling scheme. Pedons are grouped based on soil characteristics (defined by absence/presence of permafrost, thick organic layers and cryoturbation) and mean SOC storage values are then assigned to large geographical regions (physiographic regions of thick/thin sediments, respectively). For the estimate of 0 to 1 m soils, a similar simplified scheme was applied to all NCSCD regions except Alaska and Canada (Tarnocai et al., 2009). In Alaska and Canada, SOC storage values were individually assigned to mapped soil series (Alaska) or soil names (Canada) from national soil inventories. Because of these methodological differences, there are some discrepancies across depths for estimates in Alaska and Canada, where 1 to 2 m or 2 to 3 m

soil layers are sometimes estimated to hold more SOC than the upper meter of soils. This applies to some areas in the western Hudson Bay Lowlands and parts of the Canadian Arctic archipelago outside of the High Arctic zone. Clear trends of decreased SOC storage with depth (Figure appendix I-2) indicate that these vertical patterns in SOC storage are not realistic.

The upscaling approach applied here relies on the assumption that our pedon datasets are accurate and unbiased samples of permafrost region soils (Hugelius, 2012). For some regions, the degree of replication in individual soil classes is very low (Table appendix I-1). To correct for potential errors arising from incomplete sample representation in regions of thin sedimentary overburden and the High Arctic region the representation error was estimated and included in the summative uncertainty ranges. The representation error of any class in an under-sampled region is estimated by extracting the variability from repeated subsampling of larger samples available from other regions. For example, we thus assume that Turbels in thick sediment regions are roughly equally variable as Turbels in thin sediment regions.

In the High Arctic region, there is very limited pedon data available and the current estimate is based on only eight pedons (six Orthels, one Histel and one Turbel), which were grouped together as Gelisols for calculations. Because of low SOC stocks, this region does not contribute much to the overall uncertainty of total estimates. However, due to the very limited field data and the large degree of generalization in some High Arctic soil maps (e.g. Svalbard and Greenland, (Hugelius et al., 2013a)) these estimates must be regarded as preliminary and highly uncertain. Storage of SOC in cryoturbated and organic soils is often highly variable, and sample sizes of at least >30 is recommended (Hugelius, 2012). In the current estimate of SOC below 1 m depth, there is very poor representation of Turbels for thin sediment regions outside of the High Arctic (n=6 and 2 for the 1 to 2 m and 2 to 3 m depths, respectively). Based on currently available data, we cannot provide robust estimates of SOC storage in physiographic regions of thin sedimentary overburden or the High Arctic region. This is also reflected in wide uncertainty ranges for SOC stocks in these regions. Considering their large areal extent it is nevertheless important to provide assessments based on what little data are available. Further field sampling and/or data compilation will hopefully provide opportunities to refine these estimates.

I-5.3.3 Differences between soil pedon databases and sampling biases

For the 0 to 1 m depth interval, two independent sources of pedon data to estimate SOC storage (kg C m^{-2}) are available (pedon dataset 1 used to calculate 0 to 1 m

SOC stocks and pedon dataset 2 used to calculate 1 to 3 m SOC stocks). While pedon dataset 2 was not actually used in the quantification of 0 to 1 m SOC stocks, estimates are available for that depth range. If we assume that the two independent datasets are accurate samples of 0 to 1 m SOC stocks, there should be no significant differences between the datasets. We therefore infer that the significant differences in 0 to 1 m SOC storage between pedon datasets 1 and 2 could be an indication of sampling biases. Near surface pedon SOC storage is correlated to SOC storage below 1 m depth (Hugelius et al., 2014) and any biases in 0 to 1 m SOC could therefore also affect our estimates for stocks below 1 m depth. Summarized for the whole permafrost region, there are no significant differences between the datasets for the Orthel and Histel classes, while Turbels and non-permafrost mineral soils may be biased high and Histosols biased low in pedon dataset 2. Because data for pedon dataset 1 is only available aggregated to the whole permafrost region, no statistical comparisons can be made at regional levels. Detailed comparisons reveal that in North America, pedon dataset 2 is consistently estimating higher values than pedon dataset 1 (data not shown). In other regions, there are no clear patterns and results differ across soil classes.

There is an indicated bias towards high SOC in Turbels of pedon dataset 2. Closer examination of regional patterns reveals that this is largely due to very high SOC storage for Turbels in North America (at all depths). For Eurasian Turbels the pattern is opposite with higher estimates in pedon dataset 1. When subdivided following physiographic regions differences between the two datasets are small. The bulk of available North American Turbels are from the North Slope of Alaska (Figure appendix I-1), where previous studies have also shown high mean SOC storage in cryoturbated soils (Michaelson et al., 1996; Ping et al., 1998; Johnson et al., 2011). In general, the available data in pedon dataset 2 is geographically clustered (Figure appendix I-1; Hugelius et al. (2013b)) and more dispersed samples of pedons from across regions could reduce any biases introduced by clustered sampling.

Hugelius et al. (2013a) discuss a potential large bias for organic soils where targeted sampling campaigns may cause sites with thick peat deposits to be overrepresented in datasets. To avoid such a bias, pedon dataset 2 includes all sites with organic soils, even if data from the mineral subsoil was missing (data from mineral C-horizons below organic deposits were extrapolated to full depth or default values were applied). A closer examination of the available data on peat deposit thickness reveals that the peat depths in those sites, where no extrapolation was needed (i.e. where coring was pursued to great depths in the field), are not representative of the true depth distribution of peat deposits based on all available observations from organic

soils. If only pedons without extrapolation are used, mean peat depths are overestimated by a factor 2 (Figure appendix I-4). If only sites without extrapolation were used to calculate SOC stocks, the total SOC stock estimates for organic soils (Histosols and Histels) would increase from the current 302 Pg to 338 Pg. The estimated error introduced by applying default values is on the order of only ±2 Pg (calculated from the standard error of means of the applied default values and mean extrapolation depth of pedons). The use of sites where data on mineral sub-soils was extrapolated may be one factor contributing to the indicated low-bias of Histosols in pedon dataset 2 when compared to pedon dataset 1.

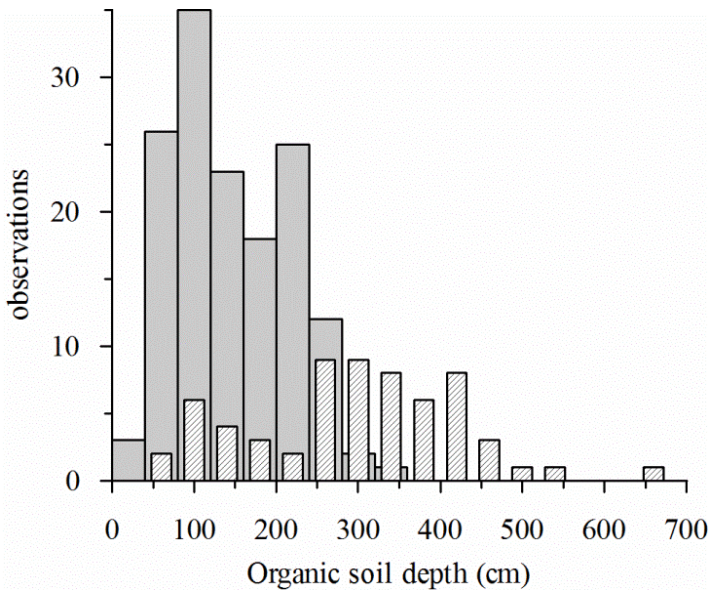

Figure appendix I-4. Histograms illustrating the depth-distribution of peat deposits (organic soil material) in Histosols and Histels of pedon dataset 2 (bins= 40 cm depth). The graph shows separate histograms for pedons that were gap-filled and/or extrapolated (wide gray bars) and pedons where no gap-filling and/or extrapolation were needed (narrow striped bars).

It is difficult to assess the potential bias between pedon datasets 1 and 2 for non-permafrost mineral soils. There is a much larger replication for these soils in pedon dataset 1. However, estimated SOC storage for many pedons in dataset 1 are from the global scale ISRIC database (Batjes, 1996) including all Eurasian permafrost-free soils and North American Aridisols, Andisols and Ultisols. Because of this, the data used for much of the non-permafrost mineral soils in dataset 1 are likely not truly representative of soils in the permafrost region.

I-5.3.4 Data availability and uncertainties of estimates for deltaic deposits

The updated estimate of deltaic SOC storage confirms that a substantial stock of permafrost SOC is stored in these deposits, but it is also clear that more field observations are needed to produce robust estimates. The calculated CI ranges indicate that uncertainties are larger concerning alluvium depth than mean SOC storage value, but the observational base for both estimates are very small and from most major deltas no field observations are available (Table appendix I-5). The estimated uncertainty ranges include an approximation of representation errors caused by the limited

sample sizes. However, these estimates cannot fully account for the fact that most deltas lack field data altogether. Because of these very limited databases these estimates must be considered as preliminary for those deltas where no data is available. Further, the estimates rely on the assumption that alluvial SOC contents measured in the near surface can be extrapolated to full depth and the reported uncertainty ranges assume a correct spatial extent of deltas and correct volumetric extent of water bodies and massive ice.

I-5.3.5 Uncertainties of estimates for Yedoma region deposits

SOC stocks in intact Yedoma and perennially frozen thermokarst deposits are calculated based on bootstrapped analyses of data on deposit thickness, organic C %, bulk density (including segregated ice %), and wedge-ice volume gathered from a total of twenty-two study areas sampled/described in the field. This approach reflects the variability of individual observations (i.e. analyses of discrete sediment samples or individual depth measurements), which is an effective way of estimating stocks with large inherent (spatial) variability. By estimating 1 mean based on 10,000 single observation-based bootstrapping means, our single estimator's uncertainty is remarkably lower compared to Strauss et al. (2013). To further improve SOC stock calculation, sensitivity analysis revealed that enhanced data on ice wedge volume (Ulrich et al., 2014) and Yedoma deposit thickness will reduce uncertainties significantly.

Another potential source of uncertainty is the geographical extent of the Yedoma region, which is challenging to define discretely. As described in Strauss et al. (2013), the definition of the Yedoma region used here is based on estimates from Romanovskii (1993)for Siberia and Jorgenson et al. (2008) for Alaska. Moreover, we added ~65,000 km² for regions with smaller known Yedoma occurrences (e.g. south of Taymyr Peninsula and Chukotka in Russia and the Yukon Territory in Canada). To describe the spatial fragmentation of Yedoma deposit remnants, we used a fragmented Yedoma coverage in the region of 30 %, whereas thermokarst basins with refrozen sediments cover 56 %. Existing thermokarst lakes and rivers were excluded, covering 14 % of the region. To improve this simplified approach, an uncertainty reduction could be reached by implementing spatially explicit data of intact Yedoma distribution based on geological maps for Siberia (Grosse et al., 2013b). Nevertheless, data for thermokarst deposit coverage and intact Yedoma coverage in the Taymyr lowlands, Chukotka, parts of Alaska and north-western Canada are currently not available.

I-5.3.6 Potential error sources not included in uncertainty estimates

The uncertainty ranges calculated for this study are based on the assumption that the various areal extents of soil (sub)orders, deltas, intact Yedoma and thermokarst are correctly mapped. In all cases we thus assume that the maps are right and that spatial errors do not contribute to estimated uncertainties. A regional study of the Northern Usa River Basin (Russian Arctic) showed that uncertainties from map errors were similar in magnitude as uncertainties from insufficient pedon representation or natural variability (95 % CI ranges both estimated at ±8 % for 0 to 1 m SOC stocks (Hugelius, 2012)). Because no dedicated ground-truthing dataset is available to assess the NCSCD soil maps that form the spatial base of upscaling SOC in 0 to 3 m soils, we cannot directly quantify this error. Small scale maps (covering large geographic regions) do not necessarily have lower mapping accuracy than large scale maps (covering small geographic regions), but because of the necessary generalization inherent in map-making, large scale maps from local studies (such as the land cover maps used by Hugelius, 2012) are expected to have higher mapping precision. We would thus expect that uncertainty from spatial errors in the maps used in this study to be equal to or greater than those found for the Northern Usa River Basin (i.e. a 95 % CI of ±8 % or more). If we assume an uncertainty of ±10 % from spatial error component in all estimates, the propagated uncertainty range of the combined estimate of 1307 Pg SOC would increase by ~±30 Pg to ~±200 Pg. However, to properly assess the spatial errors in permafrost region SOC stock estimates, comprehensive ground-truthing datasets for circumpolar soil classification maps, deltaic extent and Yedoma region extent are needed.

Imprecision in field or laboratory measurements (e.g., sample volume, bulk density or C content) are not accounted for in this study. The relative importance of such errors is expected to differ between different studies, scales and landscape types. Goidts et al. (2009) provide a comprehensive analysis and discussion of different sources of uncertainty in SOC stock estimates and their propagation in upscaling. They conclude that following upscaling to landscape scale, imprecision in laboratory measurements of rock mass fragments (>2 mm), SOC concentration (%) and bulk density may propagate and cause substantial uncertainty in estimates. However, as this circumpolar estimate study combines field and laboratory data collected from a multitude of different sources over several decades, quantifying this uncertainty is currently not possible.

I-5.4 Deposits with significant SOC stocks below 3 m depth

This estimate of SOC stocks in the northern circumpolar permafrost region includes 0 to 3 m soils as well as deeper deltaic deposits and permafrost deposits in the Yedoma region. Other deposits with significant SOC stocks below 3 m depth have not been included. In many organic soils of the permafrost region, peat deposits extend below 3 m depth (e.g. Sheng et al., 2004; Tarnocai et al., 2005; Hugelius and Kuhry, 2009; Yu, 2012). Of the organic soils included in pedon dataset 2 in this study, 17 % sites have peat deposits extending below 3 m depth (Figure appendix I-4) and these peat deposits are expected to store substantial SOC stocks in addition to what is included here.

The current estimate for deltaic deposits includes the twelve major deltas in the permafrost region (selection based on Walker, 1998), but all intermediate or small deltas are excluded. Presently, there is no dataset summarizing the aerial extent of deltaic deposits in the northern circumpolar permafrost region, but a geospatial characterization of Arctic permafrost coastlines (Lantuit et al., 2012) shows significant occurrences of deltas along the Arctic coastline besides those included here. New data also reveals that, besides deltas and the Yedoma region, there are significant SOC stocks in other unconsolidated deeper Quaternary deposits of the permafrost region (e.g. Hugelius et al., 2011; Ping et al., 2011; Schirrmeister et al., 2011b). Following the physiographic subdivision, 6.2×10^6 km^2 of the permafrost region is characterized by thick sedimentary overburden (sediments deeper than 5 to 10 m Brown et al., 2002). Deltaic deposits and the Yedoma region included in this study together cover ca. 1.5×10^6 km^2. Any SOC stored in deposits below 3 m depth in the remaining ca. 5×10^6 km^2 of thick sedimentary overburden remains unaccounted for.

I-5.5 Potential vulnerability and remobilization of permafrost region SOC stocks

The substantial SOC stocks of the northern permafrost region are vulnerable to thaw remobilization following permafrost degradation (Schuur et al., 2008; 2013). Key processes of permafrost degradation include active layer deepening, talik or thermokarst formation and thermal erosion (Schuur et al., 2008; Grosse et al., 2011a). While active layer deepening mainly affects near surface soils (Harden et al., 2012), taliks, thermokarst and thermal erosion can cause remobilization and potential mineralization of SOC stored at greater depths. Local scale studies indicate that both active layer deepening and thermokarst (or thermoerosion) can affect substantial fractions of permafrost landscapes over decadal timescales (Hugelius et al., 2011; Jones et al., 2011; Sannel and Kuhry, 2011; Hugelius et al., 2012; Jones et al., 2013).

Both active layer SOC and permafrost is highly susceptible to impacts from wildfire (Harden et al., 2000), which has increased in severity and areal extent with recent warming (Turetsky et al., 2011). SOC stocks in the permafrost region may be reduced directly via combustion, or indirectly due to post-fire increases in soil temperature and decomposition (Harden et al., 2006; Mack et al., 2011). Fire-driven reductions in organic-horizon thickness also decreases sub-soil insulation and cause active layer deepening, which can increase the amount of SOM susceptibly to decomposition in the unfrozen phase (O'Donnell et al., 2011).

Global scale projections of greenhouse-gas emissions from permafrost deposits using Earth System Models (ESMs) demonstrate that inclusion of permafrost soil C stocks lead to the potential for a large positive climate feedback from the permafrost region (Koven et al., 2011; Schaefer et al., 2011; Burke et al., 2012a; MacDougall et al., 2012; Schneider von Deimling et al., 2012). These models are still simplified representations of permafrost carbon cycling and do not resolve high landscape spatial heterogeneity or account for many observed processes, such as thermokarst or post-fire dynamics. The complexity of ESMs also makes it difficult to assign mechanistic sources of model errors. In order to increase confidence in ESMs, it is necessary to better understand the controls on soil C by process, location, and depth so that observations can be used as a benchmark for these models. Extant ESM-based quantifications of the permafrost-climate feedback have not included SOC stocks of deltaic alluvium or Yedoma and the reduced estimates for these stocks would not affect published projected feedback magnitudes. Using a simplified modeling framework, Burke et al. (2012a) demonstrated that uncertainties in quantification of permafrost SOC stocks accounted for ca. half of the variability in ESM projections of increased global mean temperature associated with permafrost carbon thaw (excluding variability caused by different representative concentration pathway scenarios). Using similar approaches together with the quantified uncertainty ranges provided in this study could reveal the relative impact of large SOC estimate uncertainties on ESMs projections of the permafrost-climate feedback.

I-6 Conclusions

This study summarizes present knowledge regarding estimated size and variability of SOC stocks in 0 to 3 m soils, deltas and the Yedoma region across the northern circumpolar permafrost region. The updated estimates of permafrost region SOC stocks are 217 ± 12 Pg for 0 to 0.3 m depth and 472 ± 27 Pg for 0 to 1 m depth (±95 % CI). Estimated SOC storage between 0 and 3 m depth is 1034 ± 150 Pg, with SOC stocks roughly equally divided between physiographic regions of thick and thin sedimen-

tary overburden. Of this, non-permafrost mineral soils store 158 Pg while poorly developed soils in the High Arctic store 34 ± 16 Pg. Estimated SOC storage below 3 m depth in deltaic alluvium of major Arctic rivers is 91 ± 52 Pg. In permafrost sediments of the Yedoma region, estimated SOC stocks below 3 m depth are 181 ± 54 Pg. Combined estimated SOC stocks in 0 to 3 m soils, deltaic deposits and Yedoma region permafrost deposits for the entire northern circumpolar permafrost region are 1307 Pg with an uncertainty range of 1140 to 1476 Pg. An estimated 999 Pg of SOC is stored in permafrost terrain of which 822 Pg is perennially frozen.

There are substantial regional gaps in pedon data to assess SOC storage below 1 m depth. Especially cryoturbated and organic (peatland) soils are highly variable and difficult to assess. The High Arctic bioclimatic zone and physiographic regions characterized by thin sedimentary overburden (areas of mountains, highlands, and plateaus) are poorly represented in the current pedon databases. Future field sampling to reduce these limitations should focus on the following observing strategies: (1) sampling soils in the full 0 to 3 m depth interval throughout the permafrost region, (2) sampling soils in regions of thin sedimentary overburden and the High Arctic, and (3) sampling soils away from current data clusters, particularly in Eurasia. The estimates of SOC stocks in deltaic alluvium and Yedoma region deposits are also based on very limited observational evidence. Improved estimates of deposit thicknesses, mean SOC content and massive ice content could greatly reduce uncertainties in these estimates.

It is important to note that the presented uncertainty ranges do not account for errors in upscaling maps or analytical uncertainties in laboratory measurements. To quantify uncertainties arising from errors in upscaling maps, ground-truthing datasets for soil classification maps, deltaic alluvium extent and Yedoma region extent are needed. We also stress that substantial pools of SOC not included in this present study are stored below 3 m depth in soils and in unconsolidated sediments outside of the Yedoma region and deltaic deposits. The size and potential thaw-vulnerability of these additional SOC pools remains to be determined.

We conclude that soils and sediments of the northern circumpolar permafrost region store large amounts of SOC (~1300 Pg) but that this revised estimates shows that the fraction of SOC that is perennially frozen (~800 Pg) is substantially smaller than previously estimated.

Acknowledgements

We are grateful to C. Tarnocai for providing pedon data as well as insightful comments and suggestions. We are grateful to two anonymous reviewers for providing detailed and insightful comments, especially regarding calculations of estimate uncertainties. This work was supported by grants from the International Permafrost Association, the EU 7th framework PAGE21 project, the Nordic Centres of Excellence DEFROST project, a grant of the Swedish Research Council as a part of the International Program CryoCARB and the Bert Bolin Centre for Climate Research at Stockholm University. This effort is also a contribution to the Global Carbon Project of the Earth System Science Partnership, the Carbon Stocks in Permafrost regions Project of the International Permafrost Association and the Vulnerability of Permafrost Carbon Research Coordination Network under sponsorship of the National Science Foundation. The contributions of J. Strauss were funded by the Federal Ministry of Education and Research (01DM12011) and the German National Academic Foundation. The contributions of S. Zubrzycki were partly supported through the BMBF project “CarboPerm” (03G0836A), and partly supported through the Cluster of Excellence 'CliSAP' (EXC177), Universität Hamburg, funded through the German Research Foundation (DFG). The contributions of G. Grosse were supported by a European Research Council Starting Grant (#338335). The contributions of B. Elberling were supported by the Center for Permafrost, funded by the Danish National Research Foundation (CENPERM DNRF100). The contributions of G.J. Michaelson and C.L. Ping were supported by the USDA-Hatch project. The contributions of Z.C. Yu were supported by the US NSF (ARC-1107981).

I-7 Supplemental material

I-7.1 Supplemental methods

Below is a more exhaustive and detailed description of methods. There is some overlap with the text of the main paper. The description included here is meant to be understandable on its own, without the need to refer to the main text. Stocks of SOC are reported as petagrams (Pg), which is equivalent to 1×10^{12} kg and 1 gigatonne (Gt, also a unit used for C stock quantification). The SOC storage is given as kg C m^{-2} reported to variable reference depths. For a conversion to SOC density (kg C m^{-3}) the depth interval must be recalculated to 1 m (e.g. for the depth interval 0 to 3 m, reported SOC storage divided by 3 is equal to kg C m^{-3}).

I-7.1.1 Calculating 0 to 3 m SOC stocks

Calculation of SOC stocks based on thematic soil maps is done in three steps (Hugelius, 2012). First, the SOC storage (area-normalized SOC given in kg C m^{-2}) for individual pedons (a pedon is a described/classified and sampled three-dimensional body of soil) is calculated to the selected reference depths. Second, the pedon data is grouped into suitable thematic upscaling classes and mean SOC storage (kg C m^{-2}) for each class and reference depth is calculated. Finally, the mean SOC storage (kg C m^{-2}) of each class is multiplied with estimates of the areal coverage of thematic upscaling classes to calculate absolute SOC stocks (kg C) for different classes and reference depths.

For this study, SOC stocks were estimated separately for the 0 to 0.3 m, 0 to 1 m, 1 to 2 m and 2 to 3 m depth ranges (measured from the top of the genetic O-soil horizon, excluding litter, the living capitula of mosses, lichen and other aboveground vegetation) using the NCSCDv2. The NCSCDv2 is a polygon-based digital database adapted for use in Geographic Information Systems (GIS) which has been compiled from harmonized regional soil classification maps. Map data on soil coverage has been linked to pedon data with SOC storage (kg C m^{-2}) from the northern permafrost regions to estimate geographically upscaled total SOC stocks (Hugelius et al., 2013a).

I-7.1.1.1 Regional geographic subdivisions in upscaling

The SOC stocks estimates for the 0 to 0.3 m and 0 to 1 m depth ranges were calculated separately in each NCSCDv2-region (Alaska, Canada, Contiguous USA, Europe, Greenland, Iceland, Kazakhstan, Mongolia, Russia and Svalbard) following the methodology of Tarnocai et al. (2009).

In recognition of the limited soil development at high latitudes, thin soils in the High Arctic bioclimatic region were upscaled separately. The High Arctic region was defined as areas where subzones A, B and C in the Circumpolar Arctic vegetation map (Walker et al., 2005) overlap with regions of thin sedimentary overburden (Brown et al., 1997, 2002). Soil polygons in the NCSCDv2 that had their centroid within this bioclimatic region and had thin sedimentary overburden were selected (final manual editing was performed to include soil polygons in the NCSCDv2 that were clearly within the High Arctic zone but that fell outside the extent of the Circumpolar Arctic vegetation map). SOC stocks in these High Arctic soil polygons were upscaled separately across the 0 to 0.3 m, 0 to 1 m, 1 to 2 m and 2 to 3 m depth ranges.

For the estimates of 1 to 3 m SOC stocks outside the High Arctic, pedons and mapped soil areas in the northern circumpolar permafrost region were separated into areas of thick and thin sedimentary overburden (Figure appendix I-1). The spatial extent of the northern circumpolar permafrost region is defined following the "Circum-Arctic map of permafrost and ground-ice conditions" (Brown et al., 1997, 2002). The spatial base and first order classification criterion used to create this map were regional physiographic or landscape maps (Heginbottom et al., 1993). Based on these regional maps, numerous published data sources and input from regional experts, these authors subdivided the northern circumpolar permafrost region into two broad classes (Heginbottom et al., 1993): (1) "areas of lowlands, highlands and intra- and inter-montane depressions characterized by thick overburden, wherein ground ice is expected to be generally fairly extensive" and (2) "areas of mountains, highlands, and plateaus characterized by thin overburden and exposed bedrock, where generally lesser amounts of ground ice are expected to occur" (thick overburden is defined as >5 to 10 m).

I-7.1.1.2 Thematic subdivisions of soil classes in upscaling

The upscaled SOC stock estimates for the 0 to 0.3 m and 0 to 1 m depth ranges were calculated separately for each soil order (following USDA Soil Taxonomy (Soil Survey Staff 1999)) within the separate NCSCDv2-regions. Permafrost affected soils (Gelisol soil order) are further differentiated for upscaling into its three sub-orders: Turbels (cryoturbated permafrost soils), Histels (organic permafrost soils) and Orthels (non-cryoturbated permafrost-affected mineral soils).

For the 1 to 2 m and 2 to 3 m depth ranges, a reduced thematic resolution was used. Stocks were calculated separately for the Turbel, Histel and Orthel suborders of the Gelisol soil order and for the Histosol soils order (organic soils without permafrost). All remaining soil orders were grouped as non-permafrost mineral soils.

In the High Arctic region, low data availability led us to reduce the thematic resolution so that the three Gelisol suborders were combined into one class. For parts of the northern circumpolar permafrost region located outside of North America, the 0 to 0.3 m and 0 to 1 m depth SOC stocks in the NCSCDv2 are calculated from SOC data generalized over large regions (Hugelius et al., 2013a). The same mean SOC storage (kg C m^{-2}) values were used within soil classes across the full latitudinal ranges in Europe, Greenland, Iceland, Russia, Mongolia, Kazakhstan and Svalbard (Tarnocai et al., 2009). Because of this, new values to estimate 0 to 0.3 m and 0 to 1 m depth SOC storage (kg C m^{-2}) in the High Arctic parts of these regions were derived from pedon data presented by Hugelius et al. (2013b).

I-7.1.1.3 Pedon databases and calculation of SOC content

The mean SOC storage (kg C m^{-2}) used in this study to estimate total SOC stocks for near surface soils (0 to 0.3 m and 0 to 1 m depth ranges) are derived from the same pedon database that was used by Tarnocai et al. (2009), but the GIS-database has been gap-filled for missing data (both missing soil map polygons and missing calculated SOC stock data in some polygons) and updated calculations of soil area have been done following gap-filling. These SOC storage (kg C m^{-2}) values are based on 1778 individual pedons from around the northern circumpolar permafrost region (mainly Gelisol and Histosol pedons), that have been complemented with SOC storage (kg C m^{-2}) data from Batjes (1996) where data for non-permafrost soil orders was missing (this pedon dataset is hereafter called pedon dataset 1). More detailed information regarding this pedon dataset, including details regarding which soil orders were supplemented from Batjes (1996), can be found in Table appendix I-7 to Table appendix I-12 of the supplementary materials. For further details regarding the NCSCD GIS-database and the methods for pedon sampling and calculation of 0 to 0.3 and 0 to 1 m SOC stocks we refer to Hugelius et al. (2013a).

For the deeper soil layers (1 to 2 m and 2 to 3 m depth ranges) a newly compiled pedon database which has been integrated into the NCSCDv2 was used (Figure appendix I-1, Table appendix I-1), from this pedon compilation we included 518 pedons that extend down to 2 m and 351 pedons that extend down to 3 m (this pedon dataset is hereafter called pedon dataset 2). Table appendix I-1 summarizes the number of individual pedons available from different geographical regions and areas of thick/thin sedimentary overburden. More detailed information regarding this pedon dataset can be found in Table appendix I-7 to Table appendix I-12 of the supplementary materials. Pedon dataset 2 includes a large number of pedons that were gap-filled using extrapolated and/or estimated values of bulk density and/or percentage

organic carbon content (OC%) (Hugelius et al., 2013b). This applies particularly to organic soils (Histels and Histosols) where the database also includes all available pedons with O-horizons ≥40 cm, but that lacked full deep characterization. In these cases, to estimate SOC storage in the underlying mineral subsoil, data from mineral soil genetic C-horizons (i.e. bulk density and OC%) were extrapolated to the full 3 m baseline depth (or default values from other similar sites were used). These extensive extrapolations are used to avoid a sampling bias towards deep peat deposits in the database, which would lead to significant overestimation of deep (>1 m) SOC stocks in organic soils. For full data-access and further details regarding the compilation, gap-filling procedures etc. for pedon dataset 2 we refer to Hugelius et al. (2013b).

I-7.1.2 Statistical tests of significance

Because different pedon datasets were used to calculate 0 to1 m SOC stocks (pedon dataset 1) and 1 to 3 m SOC stocks (pedon dataset 2), there was a concern that these two dataset may not accurately reflect the same statistical populations (Hugelius, 2012). Therefore, the circumpolar mean 0 to 1 m SOC storage (kg C m^{-2}) between the two databases was compared using Student's t-test with α=0.05 (test from parameters, software PAST v2.17b (Hammer et al., 2012)). These tests were performed at the reduced thematic resolution used to calculate deeper SOC stocks. Because the individual pedon observations and coordinates are no longer available for pedon dataset 1, the tests could not be done separately for the different physiographic regions (mean, standard deviation and n values of pedon dataset 1 for the separate regions are not known). For each soil upscaling class (at reduced thematic resolution), SOC storage (kg C m^{-2}) in the individual depth ranges (0 to 1 m, 1 to 2 m and 2 to 3 m) were also compared across physiographic regions of thick and thin sedimentary overburden using a two tailed Student's t-test with α=0.05 (software PAST v2.17b).

I-7.1.3 Calculating deltaic SOC stocks

The approach used to estimate deltaic SOC stocks in this study builds on that of Tarnocai et al. (2009) who used data on the mean depth of alluvium, mean delta lake coverage/depth and mean alluvium SOC storage (kg C m^{-3}) from the Mackenzie River Delta (Canada) combined with data on the spatial coverage of seven large arctic deltas. For the calculation presented here we combine the data used by Tarnocai et al. (2009) with updated information (from scientific literature and databases) on the areal extent of deltas, mean depth of alluvium, delta lake coverage, permafrost extent and segregated ice content in deltaic deposits. The total volume of alluvium for each delta is calculated from the mapped sub-aerial deltas extent and the mean depth of alluvial deposits, subtracting the volume that is estimated to be occupied by massive

ice and water bodies. To avoid double counting, the top 3 m of soil as well as known Yedoma deposits located in the Lena Delta are removed from the calculation. When the total volume of alluvium is calculated, the total SOC pool of each delta is estimated using field data of mean alluvium SOC storage (kg C m^{-3}). In all cases, mean values from other deltas were used when there was no direct data for any specific variable in a delta.

Walker (1998) provides a baseline estimate of the sub-aerial spatial extent of major Arctic river deltas. We selected this reference for our estimate of delta spatial extent, and included those deltas that are located within the northern circumpolar permafrost region. Because of the distinct geological histories and general characteristics of the main terraces of the Lena River Delta (Russia) we divided this delta into three terraces and the recent floodplain based on previous research (Grigoriev, 1993; Schwamborn et al., 2002b; Zubrzycki et al., 2013). Estimates of the fraction of delta surfaces covered by water bodies were available for the Mackenzie River Delta (Smith, 2011) and the Lena River Delta (Morgenstern et al., 2008; Morgenstern et al., 2011).

Estimated permafrost extent and massive ice-content in deltaic deposits were extracted from the Circum-Arctic map of permafrost and ground-ice conditions (Brown et al., 2002). Because this product maps massive ice occurrence in the upper 10 to 20 m of sediment, the mapped massive ice is assumed to extend through the upper 15 m of alluvium (we assume zero massive ice-content below this depth). Schwamborn et al. (2002a) show that a talik ca. 95 m deep is developed underneath Lake Nikolay on Arga Island (Lena River Delta). Also, Burn (2002) found that most lakes in the Mackenzie River Delta that exceed critical areal-thresholds (18 % to 27 % of all delta lakes) have taliks that extend through the permafrost while littoral margins under shallow water generally have permafrost in the upper few meters. Because of this evidence of taliks below deltaic water-bodies, unfrozen alluvium is assumed to occur primarily under water bodies for the purposes of our calculations.

Tarnocai et al. (2009) used a 5 m mean depth of delta water-bodies to calculate the volume of water. Boike et al. (2013) report that depths of polygonal ponds on Samoylov Island (Lena Delta, Russia) range from a few cm up to 1.3 m while inventoried thermokarst lakes are up to 6.1 m deep. In the 2nd terrace of the Lena River Delta, lakes reach depths of up to 10 to 30 m, but large lake expanses are typically <2 m deep (Schwamborn et al., 2002a). Field measurements based on ground penetrating radar in the Middle Channel of the Mackenzie River Delta show a maximum depth of ca. 5 m at one location (Stevens et al., 2009). Burn (2002) reports maximum depths from twelve inventoried lakes on Richards Island (Mackenzie River Delta)

ranging from 2.1–13.1 m. Water depths in delta water bodies are highly variable and expected to range outside of the values reported above. Because no comprehensive summative data regarding the mean depth of water bodies on delta surfaces is available we also use a mean depth of 5 m for this study.

Field data on mean alluvial SOC content (kg C m^{-3}) were available from the Mackenzie River Delta (Tarnocai et al., 2009), the Lena River Delta (Schirrmeister et al., 2011b; Zubrzycki et al., 2013) and the Colville River Delta in Alaska (Ping et al., 2011). When calculating mean alluvium SOC storage (kg C m^{-3}), near surface soil horizons showing organic C enrichment from ongoing/recent soil formation were excluded from calculations. Buried organically enriched soil horizons were included in calculations. Much of the available data for calculating alluvium SOC storage is from near surface deposits but we extrapolate this data to the full depth of alluvium, based on an assumption that these alluvium deposits are relatively homogenous across depths.

I-7.1.4 Calculating Yedoma region permafrost SOC stocks

For the purpose of these calculations, the Yedoma region is subdivided into areas of intact Yedoma deposits (late Pleistocene ice- and organic-rich silty sediments) and permafrost deposits formed in thaw-lake basins (generalized as thermokarst deposits) which may be either mineral soils, lake sediments or peat deposits. Areas of unfrozen sediment underlying water bodies and areas covered by deltaic or fluvial sediments were excluded. Twenty-two Yedoma and 10 thermokarst deposit profiles were studied and sampled from river or coastal bluffs exposed by rapid thaw and erosion (Strauss et al., 2013). Total SOC stocks in intact Yedoma and perennially frozen thermokarst deposits for depths > 3 m are calculated based on individual observations of: deposit thickness (n=20 and 8, respectively), organic C (weight %, n=682 and 219), bulk density (n=428 and 117), and wedge-ice volume (volume %, n=10 and 6). For details regarding calculations of the spatial extent of different sediments, data collection and spatial distribution of field observations we refer to Strauss et al. (2013). Because of high inherent (spatial) heterogeneity and non-normal distributed input parameters, the SOC stock calculations are based on bootstrapping techniques using resampled observed values (following methodology of Strauss et al., 2013). Different to Strauss et al. (2013), the number of resampling steps for each parameter was connected to the original number of observations of the different parameters deposit thickness, C%, bulk density, and wedge-ice. Additional to Strauss et al. (2013), we did 10,000 separate bootstrapping runs. The total mean pool size estimate was derived afterward for every bootstrapping run, resulting in one mean value cal-

culated from 10,000 observation-based bootstrapping means. Because organic C% and bulk density of individual sediment samples are correlated, paired values were used in the resampling process. Computations were performed using R software (boot package).

I-7.1.5 Estimating SOC stock uncertainties

Spatial upscaling using mean values of classes from thematic maps, such as soil maps, builds on the premise that an empirical connection between map classes and the investigated variable can be established through point sampling (Hugelius, 2012). Sources of upscaling-uncertainty in such thematic mean upscaling can be divided into data-base uncertainty arising from insufficient field-data representation to describe natural soil variability within an upscaling class and spatial uncertainties caused by areal misrepresentation of classes in the upscaling map (Hugelius, 2012). Data-base uncertainty can be estimated based on the standard error (reflects variance and number of independent replicates) and the relative contribution towards the total stock of each upscaling class. This procedure assumes that the available sample is sufficiently replicated to accurately reflect the natural variability within a class. If this is not the case, the uncertainty arising from this so called representation error can be estimated. Spatial errors in upscaling can be assessed if dedicated, comprehensive ground truth datasets to assess map accuracy are available, which is not the case in this study. All uncertainty-estimates in this present study assume that the spatial extent of different soil orders, deltas and the Yedoma region within the northern circumpolar permafrost region are correctly mapped.

I-7.1.5.1 Uncertainties of SOC estimates in 0 to 3 m soils and deltaic deposits

Figure appendix I-5 provides a schematic overview of how uncertainties of SOC stock estimates in 0 to 3 m soils and deltaic deposits were calculated. We assessed uncertainties in the estimated quantities of SOC stocks for the different soil depth ranges and the deltaic deposits by calculating 95 % confidence interval (CI) ranges. These CI ranges for the total landscape SOC pool (${}_{landscape}CI$) is calculated by summing up the variance and proportional areal/volumetric contribution of each upscaling class (i to j), using the formula (Thompson, 1992):

$${}_{landscape}CI = t \times \sqrt{\left(\sum_{ij}\left(\left(a_{ij}^2 \times StD_{ij}^2\right)/n_{ij}\right)\right)} \qquad \text{eq. appendix I-1}$$

where: t is the upper α/2 of a normal distribution (t≈1.96 for a 95 % CI and t≈2.58 for a 99 % CI), a_{ij} = percentage of the total area/volume for classes i to j, StD_{ij}= standard deviation of SOC stocks of the classes i to j, n_{ij} = number of replicates in classes i to j. For the estimates of near surface soils (0 to 0.3 m and 0 to 1 m), the calculation was done for the whole northern circumpolar permafrost region, using

mean SOC stocks calculated from the NCSCDv2 and values of StD (translated to the NCSCDv2 means by using the coefficient of variation) and n from Tarnocai et al. (2009) and Batjes (1996). All data used to calculate the different CI ranges are summarized in Table appendix I-7 to Table appendix I-12 of the supplementary materials.

For each separate delta, calculations of upscaling uncertainties from variability in estimated alluvium SOC storage (kg C m^{-3}) as well as variability in estimated depth of alluvium were done. When estimating variance of alluvium depth data for individual deltas, the coefficient of variation was assumed to be equal to that of the Mackenzie Delta. Multiple depth observations are only available for the Mackenzie Delta and it is assumed that estimates for other deltas would be equally variable.

Estimates of SOC stocks in the soils of the High Arctic region and physiographic regions with this sedimentary overburden as well as for deltaic alluvium are based on small samples that may not be truly representative. For these estimates the uncertainty arising from the representation error was estimated by a 95 % CI ($_{rep_err}$CI). We estimate the $_{rep_err}$CI for those upscaling classes that are represented by small samples in one region by comparing them to larger samples from another region. For example, if an upscaling class X is represented by a large sample (X_n=100) in thick sediment areas but a small sample in thin sediment areas (X_r=10) we estimated the representation error in thin sediment regions by repeatedly extracting r=10 random replicates from the larger sample n=100. This process was repeated iteratively (n=499) and the estimated mean SOC storage was recorded for each random iteration. The standard deviation from this population of 499 estimated means ($_{rep_err}$StD; scaled using the coefficient of variation) is used to calculate the $_{rep_err}$CI. The $_{rep_err}$CI is calculated with the same formula as the $_{landscape}$CI (eq. appendix I-1), but with the term StD_{ij} exchanged for the $_{rep_err}StD_{ij}$. For all soil upscaling classes the $_{rep_err}$CI of small samples (X_r) in the High Arctic region and physiographic regions with this sedimentary overburden where assessed by iterations from the larger sample (X_n) was taken from the database for physiographic regions with deep sedimentary overburden. For deltaic alluvium the $_{rep_err}$CI for data of mean alluvium SOC concentrations in poorly sampled deltas (X_r) were assessed against the combined database available for the entire Lena Delta (X_n; n=32). The Lena Delta database for SOC concentrations is considered sufficiently replicated with a reasonable geographical spread of sampling locations and has not been assigned any $_{rep_err}$CI. For the $_{rep_err}$CI for estimates of mean alluvium depth in different deltas no single delta was considered well enough replicated to act as the X_n and the X_r of the different deltas was evaluated against a pooled sample of all available observations of alluvium depth (n=7). For deltas

where no field data was available and where SOC and/or depth was estimated based on data from other deltas it is problematic to assess the representation error. In these cases the rep_errCI was calculated with a $_{rep_err}$StD equaling a coefficient of variation of 100 %. For both of the evaluated parameters (SOC concentration and alluvium depth) the observed ranges where ~ ±100 % of the means of all deltas with field data. Therefore, we considered a coefficient of variation of 100 % to be relatively realistic.

I-7.1.5.2 Uncertainties of SOC estimates in Yedoma region deposits

The observation-based bootstrapping method used to estimate SOC stocks in the Yedoma region is inherently different from the approach used to calculate uncertainty in the other SOC stock estimates. The overall mean estimated value is the mean of 10,000 individual bootstrapped observations. The uncertainty ranges are the 5th and 95th percentiles of means from 10,000 bootstrapped observations. These ranges thus reflect the estimator's (observation-based mean) uncertainty and they are considered equivalent to 95 % CI ranges. Computations were performed using the open source software R (boot package).

I-7.1.8.3 Combining confidence intervals/uncertainty estimates

Combined propagated uncertainty ranges when summing up the different depth ranges ($CI_{0-1\ m}$+$CI_{1-2\ m}$ etc.) or different components ($CI_{0-3\ m}$ + CI_{delta} etc.) of the total northern circumpolar permafrost region SOC stocks were calculated using a formula for additive error propagation of covarying variables (Roddick, 1987):

$$_{cov}CI=\sqrt{(CI_x^2+CI_y^2+2\rho_{xy}CI_xCI_y)} \qquad \text{eq. appendix I-2}$$

Where ρ_{xy} is the correlation coefficient of variables x and y. Stocks of SOC between depth ranges in the 0 to 3 m soils were assumed to be fully auto-correlated (ρ_{xy}=1). Stocks of SOC in the 0 to 3 m soils of different regions were assumed to be uncorrelated (ρ_{xy}=0). Stocks of SOC in the 0 to 3 m depth range, the Yedoma region and deltaic alluvium were assumed to be uncorrelated (ρ_{xy}=0).

I-7.2 Supplemental figures and tables

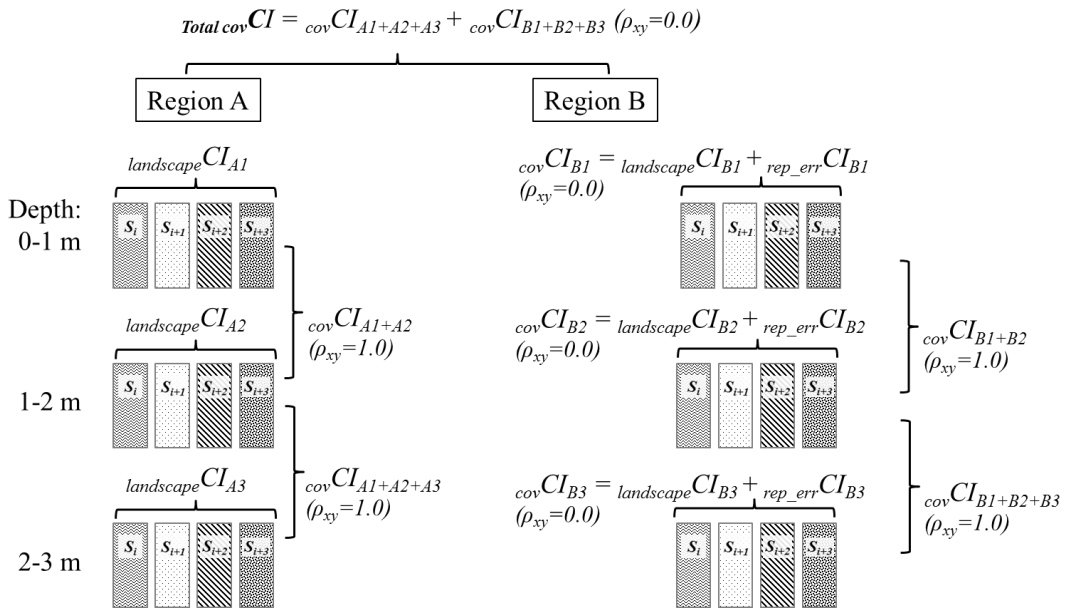

Figure appendix I-5. Schematic diagram illustrating how the different CI ranges were calculated and combined. The formulas for calculating $_{cov}$CI, $_{landscape}$CI and $_{rep_err}$CI are found in the text. The diagram illustrates two separate regions (A and B) with the occurrence of four soil classes (Si+x) over three depth ranges (0 to 1 m, 1 to 2 m and 2 to 3 m). Italic text represents the different applications of formulas and applied correlation coefficients are given in brackets. The complete formulas are provided in the box to the upper right. In this example, region B is represented by very small sample sizes. Therefore, for region B the $_{cov}$CI for each depth range includes both the $_{landscape}$CI and the $_{rep_err}$CI (see text for further explanation).

Table appendix I-7. Detailed information regarding the databases used to calculate mean SOC storage of the Northern Circumpolar Permafrost Region for the 0 to 30 cm depth range. [0]Because of the various gap filling that has been done with the NCSCDv2, the mean SOCC for the 0 to 30 and 0 to 100 cm depth ranges deviate from those reported in Tarnocai et al. (2009). Therefore all StD for the 0 to 30 and 0 to 100 cm depth ranges were based on the coefficient of variation (StD relative to the mean) from the original cited sources. *The n used for calculations of CI should not be summative when mean values from three different classes are combined. Because Tarnocai et al. (2009) reports summative n for all the classes used from Batjes et al. (1996), n was adjusted to include only the mean n of the different classes. [1]Tarnocai et al. (2009). [2]Mean circumpolar SOCC calculated from the NCSCDv2.

Depth range	Upscaling class	n:	Soil area		SOC storage[0]		Representation error		95 % CI	Upscaled SOC stocks		% of contribution to upscaled uncertainty	Source of data for n	Source of data for StD	Source of data for SOCC
Geographic region			km² / %		Mean / StD (kg C m⁻²)		rep_errStD / covStD			Pg C / %		weighted for area, SOC stocks and StD			
0-30 cm	Alfisols	339	629230	4 %	4.7	3.6			0.4	3	1 %	0 %	Batjes, 1996 and [1]*	[1]	[2] *and* Eastern hemisphere Alfisol SOCC are based on a mean value of Luvisols and Podzoluvisols from Batjes (1996)
Permafrost Region	Entisols	198	765829	4 %	1.1	6.1			0.8	1	0 %	0 %	[1]	[1]	[2] *and* Eastern hemisphere Entisol SOCC are based on a mean value of Fluvisols and Regosols from Batjes (1996)
	Inceptisols	871	2797127	16 %	4.9	3.1			0.2	14	6 %	0 %	[1]	[1]	[2] *and* Eastern hemisphere Inceptisol SOCC are based on Cambisols from Batjes (1996)
	Spodosols	88	1528291	9 %	11.7	9.7			2.0	18	8 %	6 %	Batjes, 1996 and [1]*	[1]	[2] *and* Eastern hemisphere Spodosol SOCC are based on Podsols from Batjes (1996)
	Natric soils	67	54368	0 %	2.9	2.4			0.6	0.2	0 %	0 %	[1]	[1]	[2] *and* Eastern hemisphere Natric soil SOCC are based on Solonetz from Batjes (1996)
	Aquic soils	531	255544	1 %	9.2	4.9			0.4	2	1 %	0 %	[1]	[1]	[2] *and* Eastern hemisphere Aquic soil SOCC are based on Gleysols from Batjes (1996)
	Vertisols	11	0.1	0 %	5.7	3.1			2.1	0.0	0 %	0 %	[1]	[1]	[2]
	Mollisols	320	611235	3 %	6.4	3.5			0.4	4	2 %	0 %	Batjes, 1996 and [1]*	[1]	[2] *and* Eastern hemisphere Mollisol SOCC are based on a mean value of Chernozems, Phaeozems and Kastanozems from Batjes (1996)
	Histosols	417	848390	5 %	22.5	18.4			1.8	19	9 %	1 %	[1]	[1]	[2] *and* Eastern hemisphere Histosol SOCC are based on Histosols from Batjes (1996)
	Aridisols	79	51874	0 %	1.6	1.6			0.4	0.1	0 %	0 %	Batjes, 1996	Batjes, 1996	All Aridisol SOCC are based on a mean value of Xerosols and Yermosols from Batjes (1996)
	Andisols	160	33535	0 %	11.4	7.9			1.2	0.4	0 %	0 %	Batjes, 1996	Batjes, 1996	All Andisol SOCC are based on a mean value of Andosols from Batjes (1996)
	Ultisols	309	0.2	0 %	5.1	4.2			0.5	0.0	0 %	0 %	Batjes, 1996	Batjes, 1996	All Ultisol SOCC are based on a mean value of Acrisols from Batjes (1996)
	Turbels	256	6210667	35 %	14.7	12.5			1.5	92	42 %	57 %	[1]	[1]	[2]
	Orthels	131	2500423	14 %	15.8	14.9			2.6	39	18 %	26 %	[1]	[1]	[2]
	Histels	87	1202416	7 %	18.1	14.2			3.0	22	10 %	8 %	[1]	[1]	[2]
Sectors Russia, Svalbard and Greenland	High Arctic Gelisols	8	284430	2 %	9.8	8.5	2.2	8.8	7.4	3	1 %	2 %	Hugelius et al. 2013a	Hugelius et al. 2013a	Mean of Gelisol pedons in within the High Arctic region from Hugelius et al 2013a (pedon dataset 2)

Table appendix I-8. Detailed information regarding the databases used to calculate mean SOC storage of the Northern Circumpolar Permafrost Region for the 0 to 100 cm depth range.

Depth range	Upscaling class	n:	Soil area		SOC storage°		Representation error		95 % CI	Upscaled SOC stocks		% of contribution to upscaled uncertainty	Source of data for n	Source of data for StD	Source of data for SOCC
Geographic region			**km² / %**		**Mean / StD (kg C m⁻²)**		**rep_errStD / covStD**			**Pg C / %**		**weighted for area, SOC stocks and StD**			
0-100 cm	Alfisols	339	626225	4 %	7.9	6.1			0.7	5	1 %	0 %	Batjes, 1996 and [1]*	[1]	[2] *and* Eastern hemisphere Alfisol SOCC are based on a mean value of Luvisols and Podzoluvisols from Batjes (1996)
Northern Circumpolar Permafrost Region	Entisols	198	760348	4 %	7.7	12.3			1.7	2	0 %	0 %	[1]	[1]	[2] *and* Eastern hemisphere Entisol SOCC are based on a mean value of Fluvisols and Regosols from Batjes (1996)
	Inceptisols	871	2780008	16 %	9.5	5.8			0.4	25	5 %	0 %	[1]	[1]	[2] *and* Eastern hemisphere Inceptisol SOCC are based on Cambisols from Batjes (1996)
	Spodosols	49	1520461	9 %	21.3	17.4			5.0	33	7 %	7 %	Batjes, 1996 and [1]*	[1]	[2] *and* Eastern hemisphere Spodosol SOCC are based on Podsols from Batjes (1996)
	Natric soils	67	54199	0 %	10.6	8.9			2.2	0	0 %	0 %	[1]	[1]	[2] *and* Eastern hemisphere Natric soil SOCC are based on Solonetz from Batjes (1996)
	Aquic soils	531	254267	1 %	16.8	8.1			0.7	4	1 %	0 %	[1]	[1]	[2] *and* Eastern hemisphere Aquic soil SOCC are based on Gleysols from Batjes (1996)
	Vertisols	11	0	0 %	13.5	7.3			4.9	0	0 %	0 %	[1]	[1]	[2]
	Mollisols	290	609248	3 %	12.2	6.4			0.7	7	2 %	0 %	Batjes, 1996 and [1]*	[1]	[2] *and* Eastern hemisphere Mollisol SOCC are based on a mean value of Chernozems, Phaeozems and Kastanozems from Batjes (1996)
	Histosols	417	844171	5 %	69.1	56.5			5.4	60	13 %	3 %	[1]	[1]	[2] *and* Eastern hemisphere Histosol SOCC are based on Histosols from Batjes (1996)
	Aridisols	49	51645	0 %	1.7	0.8			0.2	0	0 %	0 %	Batjes, 1996	Batjes, 1996	All Aridisol SOCC are based on a mean value of Xerosols and Yermosols from Batjes (1996)
	Andisols	120	33349	0 %	25.4	17.5			3.2	1	0 %	0 %	Batjes, 1996	Batjes, 1996	All Andisol SOCC are based on a mean value of Andosols from Batjes (1996)
	Ultisols	269	0	0 %	9.4	7.7			0.9	0	0 %	0 %	Batjes, 1996	Batjes, 1996	All Ultisol SOCC are based on a mean value of Acrisols from Batjes (1996)
	Turbels	256	6361383	35 %	33	28.1			3.5	204	43 %	61 %	[1]	[1]	[2]
	Orthels	131	2540231	14 %	25.3	23.9			4.1	63	13 %	14 %	[1]	[1]	[2]
	Histels	87	1200224	7 %	49.3	39.4			8.4	62	13 %	15 %	[1]	[1]	[2]
Sectors Russia, Svalbard and Greenland	High Arctic Gelisols	8	284430	2 %	17.8	12.7	3.8	13.2	11.0	5	1 %	1 %	Hugelius et al. 2013a	Hugelius et al. 2013a	Mean of Gelisol pedons in within the High Arctic region from Hugelius et al 2013a (pedon dataset 2)

Table appendix I-9. Detailed information regarding the databases used to calculate mean SOC storage of thick sediments for the 100 to 200 cm depth range.

Depth range	Upscaling class	n:	Soil area		SOC storage°		Representation error	95 % CI	Upscaled SOC stocks		% of contribution to upscaled uncertainty	Source of data for n	Source of data for StD	Source of data for SOCC
Geographic region			km^2 / %		Mean / StD (kg C m^{-2})		rep_errStD / covStD		Pg C / %		weighted for area, SOC stocks and StD			
100-200 cm	Histosols	67	582515	9 %	58.0	36.7		9.0	34	21 %	13 %	All data from Hugelius et al 2013a	All data from Hugelius et al 2013a	All data from Hugelius et al 2013a
Thick sediments	NPMS	68	1631975	26 %	9.5	13.5		3.3	15	10 %	14 %	All data from Hugelius et al 2013a	All data from Hugelius et al 2013a	All data from Hugelius et al 2013a
	Turbels	78	2624186	42 %	23.2	18.0		4.1	61	38 %	54 %	All data from Hugelius et al 2013a	All data from Hugelius et al 2013a	All data from Hugelius et al 2013a
	Orthels	61	485651	8 %	27.0	37.0		9.5	13	8 %	10 %	All data from Hugelius et al 2013a	All data from Hugelius et al 2013a	All data from Hugelius et al 2013a
	Histels	147	865672	14 %	43.6	31.6		5.1	38	23 %	10 %	All data from Hugelius et al 2013a	All data from Hugelius et al 2013a	All data from Hugelius et al 2013a

Table appendix I-10. Detailed information regarding the databases used to calculate mean SOC storage of thin sediments for the 100 to 200 cm depth range.

Depth range	Upscaling class	n:	Soil area		SOC storage°		Representation error		95 % CI	Upscaled SOC stocks		% of contribution to upscaled uncertainty	Source of data for n	Source of data for StD	Source of data for SOCC
Geographic region			km^2 / %		Mean / StD (kg C m^{-2})		rep_errStD / covStD			Pg C / %		weighted for area, SOC stocks and StD			
100-200 cm	Histosols	8	265471	2 %	95.7	47.2	21.5	51.9	43.4	25	13 %	4 %	All data from Hugelius et al 2013a	All data from Hugelius et al 2013a	All data from Hugelius et al 2013a
Thin sediments	NPMS	34	5079799	44 %	9.1	12.9	2.3	13.2	4.6	46	24 %	5 %	All data from Hugelius et al 2013a	All data from Hugelius et al 2013a	All data from Hugelius et al 2013a
	Turbels	6	2987656	26 %	31.6	30.1	9.4	31.5	33.1	94	49 %	90 %	All data from Hugelius et al 2013a	All data from Hugelius et al 2013a	All data from Hugelius et al 2013a
	Orthels	8	1910528	16 %	2.6	2.1	1.2	2.4	2.0	5	3 %	0 %	All data from Hugelius et al 2013a	All data from Hugelius et al 2013a	All data from Hugelius et al 2013a
	Histels	35	325717	3 %	49.0	26.3	5.6	26.9	9.2	16	8 %	0 %	All data from Hugelius et al 2013a	All data from Hugelius et al 2013a	All data from Hugelius et al 2013a
	High Arctic soils	8	1009905	9 %	6.9	7.7	2.2	8.0	6.7	7	4 %	1 %	All data from Hugelius et al 2013a	All data from Hugelius et al 2013a	All data from Hugelius et al 2013a
													All data from Hugelius et al 2013a	All data from Hugelius et al 2013a	All data from Hugelius et al 2013a

Table appendix I-11. Detailed information regarding the databases used to calculate mean SOC storage of thick sediments for the 200 to 300 cm depth range.

Depth range	Upscaling class	n:	Soil area		SOC storage°		Representation error	95 % CI	Upscaled SOC stocks		% of contribution to upscaled uncertainty	Source of data for n	Source of data for StD	Source of data for SOCC
Geographic region			km^2 / %		Mean / StD (kg C m^{-2})		rep_errStD / covStD		Pg C / %		weighted for area, SOC stocks and StD			
200-300 cm	Histosols	67	582515	9 %	29.8	26.3		9.0	17	15 %	5 %	All data from Hugelius et al 2013a	All data from Hugelius et al 2013a	All data from Hugelius et al 2013a
Thick sediments	NPMS	19	1631975	26 %	10.3	8.9		3.3	17	14 %	16 %	All data from Hugelius et al 2013a	All data from Hugelius et al 2013a	All data from Hugelius et al 2013a
	Turbels	25	2624186	42 %	20.1	13.6		4.1	53	44 %	72 %	All data from Hugelius et al 2013a	All data from Hugelius et al 2013a	All data from Hugelius et al 2013a
	Orthels	34	485651	8 %	21.6	16.1		9.5	11	9 %	3 %	All data from Hugelius et al 2013a	All data from Hugelius et al 2013a	All data from Hugelius et al 2013a
	Histels	146	865672	14 %	24.8	25.5		5.1	21	18 %	5 %	All data from Hugelius et al 2013a	All data from Hugelius et al 2013a	All data from Hugelius et al 2013a

Table appendix I-12. Detailed information regarding the databases used to calculate mean SOC storage of thin sediments for the 200 to 300 cm depth range.

Depth range	Upscaling class	n:	Soil area		SOC storage°		Representation error		95 % CI	Upscaled SOC stocks		% of contribution to upscaled uncertainty	Source of data for n	Source of data for StD	Source of data for SOCC
Geographic region			km^2 / %		Mean / StD (kg C m^{-2})		rep_errStD / covStD			Pg C / %		weighted for area, SOC stocks and StD			
200-300 cm	Histosols	8	265471	2 %	46.1	50.5	15.8	52.9	44.2	12	14 %	7 %	All data from Hugelius et al 2013a	All data from Hugelius et al 2013a	All data from Hugelius et al 2013a
Thin sediments	NPMS	11	5079799	44 %	0.5	0.9	0.1	0.9	0.6	3	3 %	1 %	"	"	All data from Hugelius et al 2013a
	Turbels	5	2987656	26 %	19.5	13.0	5.6	14.1	17.5	58	66 %	90 %	"	"	All data from Hugelius et al 2013a
	Orthels	2	1910528	16 %	1.3	1.8	0.6	1.9	16.9	2	3 %	2 %	"	"	All data from Hugelius et al 2013a
	Histels	35	325717	3 %	30.5	25.1	5.2	25.7	8.8	10	11 %	1 %	"	"	All data from Hugelius et al 2013a
	High Arctic soils	4	1009905	9 %	2.8	3.3	1.3	3.5	5.6	3	3 %	1 %	"	"	All data from Hugelius et al 2013a

Appendix II Observation-based modeling of permafrost carbon fluxes with accounting for deep carbon deposits and thermokarst activity

Schneider von Deimling, T.[1,2], Grosse, G.[2], Strauss, J.[2], Schirrmeister, L.[2], Morgenstern, A.[2], Schaphoff, S.[1], Meinshausen, M.[3], and Boike, J.[2]

[1]Potsdam Institute for Climate Impact Research, Telegrafenberg A43, 14473 Potsdam, Germany

[2]Alfred Wegener Institute Helmholtz Centre for Polar and Marine Research, Periglacial Research Unit Potsdam, Telegrafenberg A43, 14473 Potsdam, Germany

[3]School of Earth Sciences, The University of Melbourne, Victoria 3010, Australia

Submitted to: Biogeosciences

Citation: Schneider von Deimling, T., Grosse, G., Strauss, J., Schirrmeister, L., Morgenstern, A., Schaphoff, S., Meinshausen, M., and Boike, J., Observation-based modeling of permafrost carbon fluxes with accounting for deep carbon deposits and thermokarst activity, Biogeosciences Discussions, 11, 16599-16643, doi:10.5194/bgd-11-16599-2014, 2014.

II-1 Abstract

High-latitude soils store vast amounts of perennially frozen and therefore inert organic matter. With rising global temperatures and consequent permafrost degradation, a part of this carbon store will become available for microbial decay and eventual release to the atmosphere. We have developed a simplified, two-dimensional multi-pool model to estimate the strength and timing of future carbon dioxide (CO_2) and methane (CH_4) fluxes from newly thawed permafrost carbon (i.e. carbon thawed when temperatures rise above pre-industrial levels). We have especially simulated carbon release from deep deposits in Yedoma regions by describing abrupt thaw under thermokarst lakes. The computational efficiency of our model allowed us to run large, multi-centennial ensembles under various scenarios of future warming to express uncertainty inherent to simulations of the permafrost-carbon feedback.

Under moderate warming of the representative concentration pathway (RCP) 2.6 scenario, cumulated CO_2 fluxes from newly thawed permafrost carbon amount to 20 to 58 gigatonnes of carbon (Gt-C) (68 % range) by the year 2100 and reach 40 to 98 Gt-C in 2300. The much larger permafrost degradation under strong warming (RCP8.5) results in cumulated CO_2 release of 42-141Gt-C and 157-313 Gt-C (68 % ranges) in the years 2100 and 2300, respectively. Our simulated methane fluxes contribute a few percent to total permafrost carbon release yet they can cause up to 40 % of total permafrost-affected radiative forcing in the 21st century (upper 68 % range). We infer largest methane emission rates of about 50 Mt-CH_4 per year around the mid of the 21st century when simulated thermokarst lake extent is at its maximum and

when abrupt thaw under thermokarst lakes is accounted for. CH_4 release from newly thawed carbon in wetland-affected deposits is only discernible in the 22nd and 23rd century because of the absence of abrupt thaw processes. We further show that release from organic matter stored in deep deposits of Yedoma regions does crucially affect our simulated circumpolar methane fluxes. The additional warming through the release from newly thawed permafrost carbon proved only slightly dependent on the pathway of anthropogenic emission and amounts about 0.03-0.14°C (68 % ranges) by end of the century. The warming increased further in the 22nd and 23rd century and was most pronounced under the RCP6.0 scenario with adding 0.16-0.39°C (68 % range) to simulated global mean surface air temperatures in the year 2300.

II-2 Introduction

Soils in high northern latitudes represent one of the largest reservoirs of organic carbon in the terrestrial biosphere, holding an estimated 900-1700 gigatonnes (Gt) of organic carbon (Hugelius et al., 2014). While portions of this carbon pool are already affected by seasonal thaw in the active layer, substantial amounts are locked in perennially frozen deposits at depths currently exceeding the seasonal thaw depth. (Zimov et al., 2006a) have estimated that an amount of 450 Gt-C is stored in deep Siberian organic-rich frozen loess and have speculated that this carbon store could significantly contribute to global carbon fluxes when thawed. A more recent study based on updated observations estimates a total of 211 (58-371) Gt-C being stored in ice- and carbon-rich deep deposits in Siberia and Alaska (Strauss et al., 2013). As long as frozen in the ground, permafrost organic matter is not part of the active carbon cycle and can be considered mainly inert. With sustained warming and subsequent degradation of deeper permafrost deposits, a part of this carbon pool will become seasonally thawed. Consequently, it will become prone to microbial decomposition and mineralization. By ultimately increasing the atmospheric concentration of the greenhouse gases CO_2 and CH_4, the carbon release from thawing permafrost regions is considered a potentially large positive feedback in the climate-carbon system (Schaefer et al., 2014). Given the long millennial timescale processes leading to the build-up of old carbon in permafrost soils, future rapid releases from these deposits are irreversible on a human timescale.

However, the magnitude and timing of carbon fluxes as a consequence of permafrost degradation are highly uncertain. This is mainly due to incomplete observational knowledge of the amount of organic matter stored in permafrost deposits, of its quality and decomposability, as well as due to the challenge of modeling the full chain of processes from permafrost thaw to carbon release. Furthermore, conceptual and nu-

merical permafrost landscape models also require suitable upscaling methods ranging from local to global scales, based on field-based knowledge of the surface characteristics, key processes and data collection of key parameters (Boike et al., 2012). The vulnerability of permafrost carbon and its fate when thawed will be strongly determined by various environmental controls (Grosse et al., 2011a) such as soil type and soil moisture, which both affect soil thermal conductivity and therefore determine the timescale of heat penetration into the ground. Additionally, surface conditions such as organic-rich soil surface layers, vegetation cover and snow exert strong controls on subsurface temperatures by insulating the ground from surface air temperatures (Koven et al., 2013a). Mineral permafrost soils are typically more vulnerable to degradation than carbon-rich organic soils: the often higher ice-content of the latter requires a larger energy input for phase transition and the usually anaerobic environments in organic soils slow down carbon mineralization. Therefore, for capturing site-specific pathways of carbon release from permafrost degradation, it is important to consider the differing soil environments under which the organic matter will be thawed. Of key importance is the impact of hydrological conditions which determine whether mineralized carbon will be emitted as CO_2 or CH_4 (Olefeldt et al., 2013). Future changes in hydrological conditions in permafrost regions will therefore crucially affect the high latitude carbon balance. Especially regions of ice-rich late Pleistocene deposits (Yedoma) are considered to become potential hot spots for intensive thermokarst lake formation with consequent increases in the fraction of permafrost-affected sediments under anaerobic environments (Walter et al., 2007a). Apart from affecting hydrological conditions, thermokarst lakes also exert a strong warming of sub-lake sediments and thus enhance abrupt permafrost degradation. If thermokarst lake depths exceed the maximum thickness of winter lake ice, these lakes retain liquid water year-round and provide a strong warming and thawing of the underlying sediments (Arp et al., 2012). As a consequence, mean annual temperatures of thermokarst lake bottom sediments can be up to 10 °C warmer than mean annual air temperatures (Jorgenson et al., 2010).

So far, permafrost carbon dynamics are not included standard climate model projections, possibly due to only recent recognition of the large vulnerable permafrost carbon pool and given the complexity of processes involved. The complexity arises not only from the need to simulate physical changes in soil thermal conditions and phase transitions of water as a consequence of various environmental controls (e.g. interactions among topography, water, soil, vegetation and snow (Jorgenson et al., 2010)). It also arises from the challenge of describing the full chain of bio-geochemical processes for eventual carbon decomposition in the soils and release to the atmosphere.

Therefore, various aspects of permafrost physics and biogeochemistry are only being implemented into current global climate models (formulated e.g. in (formulated e.g. in Lawrence and Slater, 2008; Koven et al., 2009; Dankers et al., 2011; Lawrence et al., 2011; Koven et al., 2013b; Schaphoff et al., 2013; Ekici et al., 2014). First modeling results suggest a very large range in predicted soil carbon losses from thawing permafrost under scenarios of unmitigated climate change (about 20 to 500 Gt-C by 2100, see Schaefer et al. (2014) for an overview). This large range demonstrates the current uncertainty inherent to predictions of the timing and strength of the permafrost carbon feedback.

Yet, these studies are based on models which still miss important mechanisms to capture the full complexity of the permafrost carbon feedback. Grosse et al. (2011b) and van Huissteden and Dolman (2012) underline that none of the current permafrost models consider the spatially inhomogeneous and potentially much more rapid degradation of ice-rich permafrost and lake formation. This omission of abrupt thaw processes may result in underestimating an important part of anaerobic soil carbon decomposition. Studies have also underlined the importance of considering small scales: not only large Arctic lakes, but also the smaller Arctic thaw ponds, are biological hotspots for the emission of CO_2 and CH_4 (Laurion et al., 2010; Abnizova et al., 2012). A recent expert assessment has emphasized the importance of abrupt thaw processes and so far unaccounted carbon stored in deep deposits below three meters (Schuur et al., 2013). Evidence for rapid and abrupt thaw on decadal scale, is already widespread (Jorgenson et al., 2006; Sannel and Kuhry, 2011; Kokelj et al., 2013; Raynolds et al., 2014), is likely to increase with future warming, and thus needs to be considered in order to make realistic projections of carbon dynamics in permafrost regions.

Our study aims to estimate the range of potential carbon fluxes from thawing permafrost by accounting for abrupt thaw processes which can accelerate the degradation of frozen ground beyond what is inferred by standard modeling approaches that consider gradual thaw. By explicitly modeling carbon releases from deep carbon stores below three meters, we contribute to a more complete quantification of the permafrost-carbon feedback. By allocating permafrost organic matter into pools of differing environmental controls, we describe different pathways of carbon release and we especially account for carbon released as methane which is mostly neglected in current modeling approaches. Similarly, permafrost carbon release from deep deposits is mostly not accounted for, although first modeling studies have considered the contribution of permafrost carbon in Yedoma regions (Koven et al., 2011; Schaphoff et al., 2013). Yet in these studies the deep deposits have not contributed significantly to

simulated carbon release because the models did not describe abrupt thaw processes. Khvorostyanov et al. (2008) have inferred a large contribution from Yedoma carbon deposits after the year 2300 when assuming that microbial heat strongly speeds-up permafrost degradation. To the best of our knowledge, our modeling approach is the first to globally quantify the permafrost-carbon feedback for the coming centuries under considering carbon release from deep deposits and accounting for abrupt thaw processes.

II-3 Multi-pool permafrost model

Building on previous work (Schneider von Deimling et al., 2012), we have developed a simplified large-scale two-dimensional model with parameters tuned to match observed permafrost carbon characteristics. The model calculates permafrost degradation and eventual CO_2 and CH_4 release under differing environmental conditions. The newly developed model is shortly described in the following sections while more details are given in the supplementary material.

The model accounts for several processes which are key to the permafrost carbon feedback:

1. Depending on soil-physical factors, hydrologic conditions, and organic matter quality, permafrost carbon inventories were sub-divided into a total of 24 pools.
2. Permafrost thaw was calculated for various scenarios of global warming to determine the amount of carbon vulnerable to eventual release. Anaerobic soil fractions were calculated to determine the amount of organic matter stored in wetland- and thermokarst-affected sediments.
3. Permafrost carbon release as either CO_2 or CH_4 was calculated based on typical rates for aerobic and anaerobic carbon release.
4. By using a simplified climate-carbon model, we have determined the additional increase in global mean temperature through the permafrost carbon feedback.

The computational efficiency of our model allows us to explore the range of simulated permafrost carbon feedbacks by running large ensembles. Our proceeding expresses the uncertainty inherent to current knowledge of permafrost carbon release. Our framework allows identifying key model parameters and processes and thus enables us to assess the importance of these factors for shaping the strength and timing of the permafrost carbon feedback.

II-3.1 Model structure

The magnitude and timing of carbon release from thawing permafrost soils will be strongly determined by soil-physical factors such as soil composition and organic matter decomposability, hydrologic state, and surface conditions. To account for these factors, we have developed a simplified but observationally constrained and computationally efficient two-dimensional model which allocates permafrost soil organic matter into various carbon pools. These pools describe carbon amount and quality, soil environments, and hydrological conditions (Figure appendix II-1).

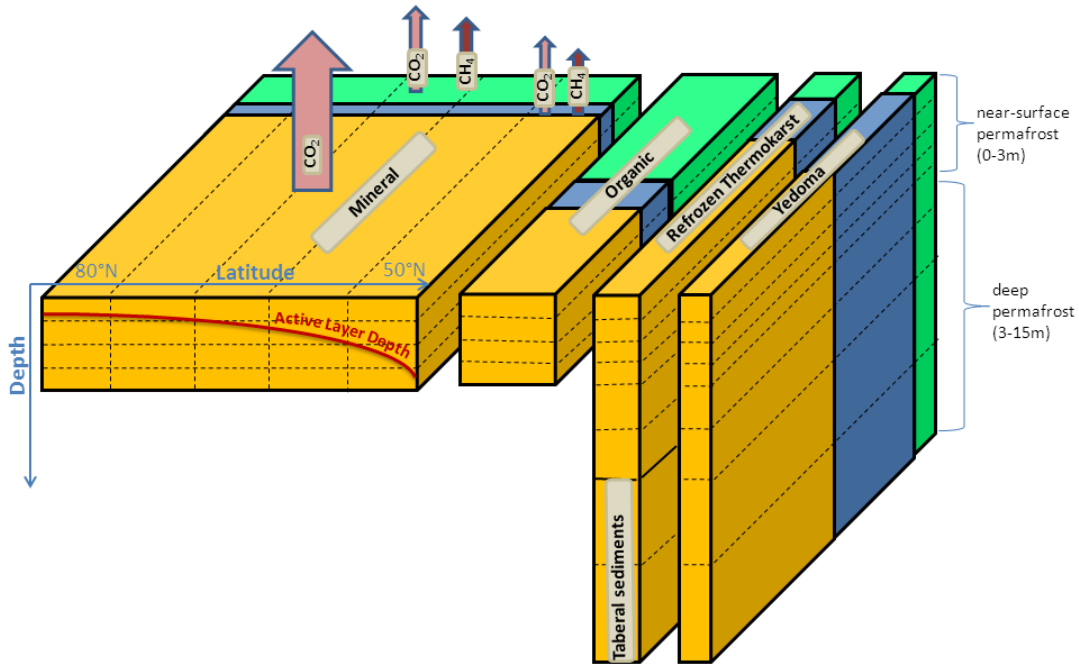

Figure appendix II-1. Schematic subdivision of permafrost soil carbon stocks into the four main pools (mineral soils, organic soils, refrozen thermokarst deposits (including taberal), and Yedoma deposits) and into aerobic (dark yellow) and anaerobic (blue: thermokarst lake, green: wetland) fractions. Individual boxes indicate the vertical extent and overall soil carbon quantity, as well as the aerobic and anaerobic fractions (not fully to scale). The dashed lines illustrate the model resolution into latitudinal bands (only shown for the mineral soil carbon pool) and vertical layers. Exemplarily, for the mineral soil carbon pool the North-South gradient of active layer depth (red line) and soil carbon release as CO_2 and CH_4 are also shown (broad arrows). Not shown is the additional differentiation into a fast and slow pool component.

To account for deposit-specific permafrost carbon vulnerability, we divide our carbon inventory into two near-surface pools (*mineral* and *organic,* 0 to 3 m) and into two deep-ranging pools (*Yedoma* and *refrozen thermokarst* (including taberal sediments), 0 to 15 m, see next section and Table appendix II-1). By taberal deposits we understand Early Quaternary permafrost sediments that underwent thawing in a talik (a layer of year-round unfrozen ground in permafrost areas) and subsequent refreezing, with incorporating often depleted organic carbon into the soils (Grosse et al., 2007).

We describe differing hydrological controls by further subdividing each carbon pool into one aerobic fraction and two anaerobic fractions. Hereby we account for anaerobic conditions provided in wetland soils and by water-saturated sediments under thermokarst lakes. In the following we define wetland soils from a purely hydrological viewpoint, i.e. by assuming that these soils are water-saturated and not affected by thermokarst. We further assume that anaerobic soil fractions are not stationary but will increase or decrease with climate change. Therefore, we re-calculate the wetland and thermokarst fraction for each time step (see supplementary material for model details). We assume a linear increase in wetland extent with global warming with mean maximum increases up to 30 % above pre-industrial wetland extent (see Table appendix II-1). To capture changes in future thermokarst lake coverage, we have developed a conceptual model by making the simplifying assumption that future increases in high latitude surface air temperatures are the main driver for thermokarst formation. We hereby assume that future warming results in a gradual increase of thermokarst lake areas (Smith et al., 2005a; Walter et al., 2007b; Plug and West, 2009) until a maximum extent is reached (see Table appendix II-1). With further warming our model describes a decrease in thermokarst lake extent as we assume that lake drainage is becoming a key factor which strongly limits thermokarst lake area ((Smith et al., 2005b; Jones et al., 2011; Morgenstern et al., 2011; van Huissteden et al., 2011); see also Figure appendix II-6).

As the quality of organic matter is a further key determinant for the timescale of carbon release (Strauss et al., 2014) we subdivide the carbon of each individual pool into a fast and a slowly decomposing fraction, with annual or respectively decadal timescales (Table appendix II-1). We do not describe permafrost organic matter of low quality (passive pool) which decays on a multi-centennial to millennial timescale. The partitioning of permafrost organic matter results in a total of 24 separate carbon pools which all contribute individually to simulated carbon fluxes (Figure appendix II-1).

All pools and processes are stratified along latitudinal bands that provide a simplified gradient of climate and permafrost types. To describe the climate control exerted by surface-air and ground temperatures in each latitude band, we assume that large-scale climate effects can be described by a general north-south temperature gradient. We acknowledge that longitudinal patterns can also be pronounced, but with a focus on large-scale regional rather than local changes we expect that the dominant climate control can be described by a profile of coldest permafrost temperatures at the northern limit and warmest temperatures at the southern limit (Romanovsky et al., 2010b; Beer et al., 2013).

Table appendix II-1. Permafrost model parameters and uncertainties. Some parameters are soil pool specific (MS: mineral soils, ORG: organic soils, Y: Yedoma, RTK: refrozen thermokarst deposits (separated into surface and taberal sediments), some parameters depend on hydrologic conditions (AER:aerobic, WET: wetland anaerobic, TKL: thermokarst lake anaerobic), and some parameters depend on organic matter quality (FAST and SLOW).

Parameter	Unit	Default setting		Uncer-tainty	References
Carbon inventory					
Mineral soils (MS) 0-3 m (orthels & turbels)	Gt-C		540	±40 %	Hugelius et. al. (2014)
Organic soils (ORG), 0-3 m (histels)	Gt-C		120	±40 %	Hugelius et. al. (2014)
Yedoma (Y) 0-15 m	Gt-C		83	±75 %	Strauss et al. (2013)
Refrozen thermokarst deposits $RTK_{Surface}$ (0-5 m) $RTK_{Taberal}$ (5-15 m)	Gt-C		128 114	±75 % ±75 %	Strauss et al. (2013) Walter-Anthony et al. (2014)
Fraction Fast Pool [(a)]	%		2.5	1-4	Dutta et al. (2006), Burke et al. (2012a), Schädel et al. (2014)
Fraction Slow Pool	%		45	30-60	Sitch et al. (2003), Koven et al. (2011), Burke et al. (2012a)
Carbon release					
Turnover time of aerobic slow pool at 5°C [(b)]	yrs		25	10-40	Sitch et al. (2003), Dutta et al. (2006), Burke et al. (2012a)
Ratio of production CH_4:$CO_2^{aerobic}$			1:50	±50 %	Segers (1998), Schuur et al. (2008), Lee et al. (2012)
Ratio of production CH_4:$CO_2^{anaerobic}$ [(c)]		FAST SLOW	1:1 1:7	±20 % ±50 %	Walter-Anthony et al. (2014) Lee et al. (2012)
Q^{10} sensitivity aerobic			2.5	(1.5-3.5)	Schädel et al. (2014) and references therein
Q^{10} sensitivity anaerobic			3.0	(2-6)	Walter and Heimann (2000)
CH_4 oxidation rate	%	TKL WET	15 40	10-20 20-60	See Burke et al. (2012a) and references therein
Permafrost thaw					
Thaw rate (MS, AER) for warm and cold permafrost [(d)]	cm/yr/K		1.0 0.1	±50 % ±50 %	Frauenfeld et al. (2004) Hayes et al. (2014)
Scale factor thermal diffusivity WET:AER [(e)]			1/3	±30 %	see [(e)]
Scale factor thermal diffusivity TKL:AER [(e)]			9.3	±30 %	Kessler et al. (2012)
Wetland description					
Wetland extent [(f)] (pre-industrial)	%	MS ORG Y, RTK	2 60 40	±50 % ±10 % ±10 %	GLWD, Lehner and Döll (2004) Burke et al. (2012a)
maximum increase in wetland extent [(g)] (above pre-industrial)	%	MS ORG,Y,RTK	30 10	±50 % ±50 %	Gao et al. (2013)
Thermokarst description					
Newly formed thermokarst lake fraction F^{TKLmax}	% (coverage per latitude)	MS ORG Y RTK	8 16 40 25	±25 % ±25 % ±25 % ±25 %	see supplementary material
High latitude temperature anomaly dT'^{TKLmax} at F^{TKLmax} [(h)]	°C	5		4-6	see supplementary material

[(a)] *For Yedoma deposits, we assume a doubled labile fraction (5±3 %) as sedimentation of organic material was rather fast and had favored the burial of fresh organic carbon with little decomposition*

in the past (Strauss et al., 2013). In contrast, we assume a reduced labile fraction in taberal sediments of 1 % as these deposits had been thawed over long timescales in the past and are therefore depleted in high quality organic matter (Walter et al., 2007b; Kessler et al., 2012). [(b)] We assume the turnover time of the fast pool to be one year. [(c)] We discard very small ratios of CH_4:$CO_2^{anaerobic}$ inferred from incubation experiments as it is likely that these ratios are strongly affected by a large CO_2 pulse during the initial phase of the incubation. [(d)] Indicated thaw rates are exemplary for warm and cold permafrost (corresponding to a MAGT of just below 0°C and -10°C). They were calculated based on equation (1) by assuming that above-zero temperatures prevail during four months per year and that thaw is driven by a surface temperature warming anomaly of 1°C. [(e)] We prescribe aggregated thermal diffusivities for soils under aerobic conditions and use scale factors to determine modified thermal diffusivities under anaerobic conditions. For the wetland pools, we assume reduced thaw rates as water-saturated soils require an increased latent heat input for thaw of ice-filled pore volumes. For the thermokarst soil carbon pools, we tuned scaling factors to reproduce long-term behavior of talik propagation as simulated by Kessler et al. (2012). [(f)] Based on the GLWD database, Burke et al. (2012a) estimate an area coverage of 9 % for wetlands and 3 % for lakes for all permafrost regions. Based on calculated permafrost deposit extents (Hugelius et al., 2014), we estimate an area weighting of 80 %:15 %:2.5 %:2.5 % for the permafrost extents of our four soil pools (MS:ORG:Y:RTK).This results in a total weighted initial wetland extent of about 13 %. [(g)] The potential for increases in wetland extent in mineral soils is considered larger than for the other soil pools because the initial assumed wetland fraction in mineral soils is rather small. [(h)] Early Holocene warming by a few degrees Celsius in northern hemisphere land areas (Velichko et al., 2002; Kaufman et al., 2004; Marcott et al., 2013) resulted in rapid and intensive thermokarst activity (Walter et al., 2007a; Brosius et al., 2012).

Our model also resolves vertical information to account for varying carbon density with depth and to track active layer changes. We chose a model resolution of 20 latitudinal bands (corresponding to a gridding of 2°) and of 27 vertical soil layers (corresponding to layer thicknesses of 25 cm for the upper four meters, and of 1 m for the depth range 4 to 15 m).

II-3.2 Model initialization

The flexibility of our model allows us to tune model parameters to observed data, e.g. to permafrost carbon inventories, carbon qualities, or active layer depths. This approach assures that our simulations do not suffer from an initial bias in the amount of modeled permafrost carbon. This is contrary to model studies, which fully simulate soil thermal conditions with potentially large biases in initial permafrost extent (Slater and Lawrence, 2013). Such biases result in a large spread in simulated initial permafrost carbon stores (Gouttevin et al., 2012; Mishra et al., 2013). Based on updated Arctic soil carbon data (Hugelius et al., 2013a; Strauss et al., 2013; Hugelius et al., 2014; Walter Anthony et al., 2014) we allocate permafrost carbon pools in different regions: two deep-ranging pools (0 to 15 m) in regions with Yedoma (80 Gt-C) and refrozen thermokarst deposits (240 Gt-C), and two near-surface pools (0 to 3 m) in remaining regions with mineral soils (540 Gt-C) and organic soils (120 Gt-C), see the supplementary material and Table appendix II-1. We then initialize each latitude band with a mean annual ground temperature between -0.5°C and -10°C based on summer air temperature climatology data from the *Berkeley Earth dataset* (http://berkeleyearth.org/data; see supplementary material). By assuming that the

equilibrium active layer depth is determined by mean annual ground temperature and by the seasonal cycle of soil temperatures (Koven et al., 2013a), we calculate typical minimum seasonal thaw depths of about 0.3 m (northernmost permafrost regions) and maximum seasonal thaw of about 2.5 to 3 m (southernmost regions) for present-day climate conditions (see supplementary material). Although topography, soil type, as well as organic layer, vegetation cover, and snow cover variability can lead to spatially very heterogeneous patterns of active layer thicknesses, our scheme describes a latitudinal tendency of a strong north-south gradient of both subsoil temperature and active-layer thickness that generally matches observations (Beer et al., 2013).

By calculating the active layer depth for each carbon pool and in each latitudinal band, we can determine the fraction of permafrost carbon below the active layer and therefore the amount of organic matter perennially frozen under our baseline climate conditions (i.e. pre-industrial climate). Large amounts of organic matter in permafrost soils reside in the active layer and were affected by past decomposition and release over millennia. It is unclear to what extent the quality of this seasonally-thawed organic material will allow extensive microbial decay in the future. Therefore we follow a strategy similar to Burke et al. (2012a) and Harden et al. (2012) of considering only the part of permafrost carbon which was locked in perennially frozen grounds since pre-industrial times[1] and thus was not part of the active carbon cycle for millennia. When accounting for uncertainty in model parameters, we infer a range of about 400 to 1100 Gt of carbon perennially frozen under pre-industrial climate. Further, we account for the fact that a large part of the permafrost carbon inventory (i.e. the passive pool) will likely be recalcitrant to decay on a multi-centennial timescale (Schmidt et al., 2011). Assuming a passive pool fraction of about 40 to 70 %, only about 120 to 660 Gt of permafrost carbon can become vulnerable for eventual carbon release in our simulation setting.

To capture uncertainty in modeled carbon fluxes from thawing permafrost deposits, we have sampled a set of 18 key model parameters who are subject to either observational or to model description uncertainty. For each warming scenario, we have performed 500 ensemble runs by applying a statistical Monte-Carlo sampling and by assuming uniformly and independently distributed parameters and initial values.

[1]We assume that our considered carbon inventory describes organic matter in continuous and discontinuous permafrost. This carbon is likely to represent organic matter perennially frozen since pre-industrial climate conditions. We do not consider soil carbon stored in younger permafrost deposits (sporadic and isolated patches) which likely had been thawed for the majority of the Holocene and therefore is likely depleted in labile organic matter.

II-3.3 Permafrost thaw and carbon release

With increasing high latitude warming the active layer will deepen. We model this process by assuming that climate-driven long-term thaw rates can be described depending on four key factors: physical ground properties, mean annual ground temperatures, depth of the thawed sediment layer, and magnitude of the warming anomaly which drives permafrost degradation (see supplementary material). Hereby we capture factors which strongly affect pool-specific thaw dynamics, e.g. talik formation under thermokarst lakes, dampening of the thaw signal with depth, variable soil-ice contents. We therefore can determine the amount of newly thawed organic matter under various anthropogenic emission scenarios as a consequence of warming above pre-industrial temperatures. We hereby assume carbon emissions proportional to the amount of newly thawed carbon in each pool. Eventual carbon emission as CO_2 or CH_4 is determined through calculated aerobic and anaerobic emission rates (see supplementary material).

Finally, the permafrost model was coupled to a simple multi-pool climate-carbon cycle model to close the feedback loop: while the permafrost model simulates permafrost degradation and subsequent carbon release (as CO_2 and CH_4), the climate carbon-cycle model calculates atmospheric changes in CO_2 and CH_4 concentrations and subsequent increases in global mean surface air temperatures. Based on state-of-the-art climate models (CMIP-5 (Taylor et al., 2011)), we infer polar amplification factors to describe surface air warming in each latitudinal band which then drives permafrost degradation in the next time step.

II-3.4 Model limitations

Our approach of modeling permafrost thaw relies on the simplifying assumption that the main driver of permafrost degradation is the rise of Arctic air temperatures. Yet soil thermal conditions can be influenced by factors other than temperature (e.g. vegetation cover, snow thickness, topography (Jorgenson et al., 2010; Jafarov et al., 2012). We motivate our modeling approach by focusing on the large-scale and long-term deepening of active layer thickness under various warming scenarios. Although snow cover is considered a key factor for simulating present day permafrost extent consistent with observations (Stieglitz et al., 2003; Osterkamp, 2007; Koven et al., 2013a; Langer et al., 2013), it is unclear how strongly future changes in high-latitude snow cover will affect permafrost degradation. Given that no high-quality data products are available for a circumarctic mapping of snow cover, snow depth, and snow density – and given that climate models simulate strongly divergent pathways of future snowfall – we here make the simplifying assumption that the long term evolu-

tion of permafrost is largely driven by changes in surface air temperatures. Similarly, our simplified approach of describing thermokarst dynamics is based on the assumption that future thermokarst formation is largely affected by increasing surface air temperature. Temperature-unrelated, local factors (such as topography, precipitation changes or wildfire) can also be key determinants for thermokarst dynamics. We understand our approach mainly as quantifying carbon fluxes under different hypotheses of future thermokarst development rather than providing deterministic and explicit predictions of individual thermokarst terrains. An alternative scenario of a reduction in high-latitude inland water surface area under future warming was e.g. investigated by (Krinner and Boike, 2010).

Nutrient limitation in the soils and abrupt carbon release after wildfires are considered two further, potentially important mechanisms for the carbon balance of thawed permafrost deposits which we do not consider in our model design (Mack et al., 2011; Turetsky et al., 2011). Probably the largest effect of unaccounted processes on our simulated carbon fluxes comes from the omission of high latitude vegetation dynamics. Increased carbon uptake in a warmer climate through more productive vegetation can strongly affect the Arctic carbon balance (Schaphoff et al., 2013). The capturing of this feedback component requires the implementation of a dynamic vegetation model which is beyond the scope of this study. Also of importance in this respect is the potential restoration of carbon sinks after lake drainage which could, on the long-term, partially compensate for high CH_4 emission (Jones et al., 2012; Kessler et al., 2012; van Huissteden and Dolman, 2012; Walter Anthony et al., 2012).

Our simulated wetland CH_4 fluxes describe methane produced from newly thawed permafrost carbon. Yet the full carbon balance of wetlands is rather complex and possibly more affected by future changes in soil moisture, soil temperature, and vegetation composition than by the delivery of newly thawed organic matter through permafrost degradation (Olefeldt et al., 2013). The accounting of these additional factors requires the implementation of comprehensive wetland models (such as suggested by Eliseev et al., 2008; Frolking et al., 2011; Kleinen et al., 2012).

II-4 Model results

II-4.1 Permafrost degradation

We have run our model under various scenarios of future warming, ranging from moderate (RCP2.6) to extensive (RCP8.5). Under RCP2.6, global greenhouse gas emissions peak by 2020 and decline strongly afterwards. We simulate subsequent increases in global mean surface-air temperatures which are constrained to below two degrees above pre-industrial levels. In case of unmitigated climate change

(RCP8.5), global mean surface air temperatures continuously increase and reach 10°C by the end of the 23rd century at the upper range of our simulations. This pronounced difference in simulated surface air temperatures results in strongly differing pathways of long-term permafrost degradation (Figure appendix II-2).

Depending on initial mean annual ground temperatures ($MAGT_{t0}$), we exemplarily infer for cold ($MAGT_{t0}$=-10°C), medium ($MAGT_{t0}$=-5°C), and warm ($MAGT_{t0}$=-0.5°C) permafrost mean active layer depths of 20 cm, 70 cm, and 250 cm, respectively. As projections of surface air temperatures only start to diverge strongly after mid of the 21st century, continuous but slow deepening of the active layer is similar under RCP2.6 and RCP8.5 until 2050 (Figure appendix II-2).

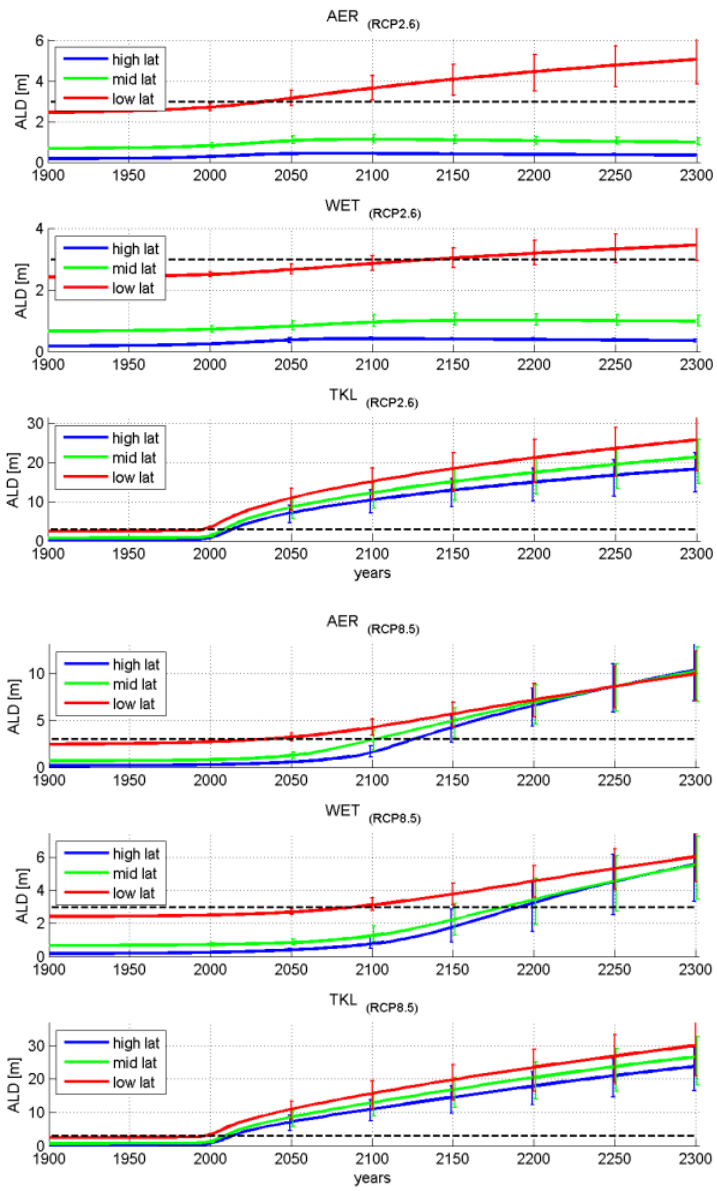

Figure appendix II-2. Simulated changes in active layer depths ALD for mineral soils under moderate (RCP2.6) and extensive (RCP8.5) warming (top and bottom panels). Shown is the deepening of the active layer from the year 1900 until 2300 for a north-south gradient of different initial permafrost temperatures (blue: $MAGT_{t0}$=-10°C, green: $MAGT_{t0}$=-5°C, red: $MAGT_{t0}$=-0.5°C) and for different hydrologic conditions (AER: aerobic, WET: wetland, TKL: thermokarst lake). Vertical bars illustrate the model spread inferred from an ensemble of 500 runs (68 % range). The horizontal dashed lines denote the near-surface permafrost boundary (3 m). Note the different y-axes scales.

We first focus on active layer deepening of the largest pool of permafrost carbon, i.e. organic matter in mineral soils under aerobic conditions (Figure appendix II-2, upper panels). Under moderate warming (RCP2.6), active layer depths stabilize after 2100 for cold and medium permafrost temperatures (blue and green curves). Yet permafrost in southerly warm regions will degrade in our simulations with disappearance of near-surface permafrost before 2100 (red curve). Under strong warming (RCP8.5), a sharp increase in thawing rates in the second half of the 21st century can be seen and the majority of model runs suggest a degradation of near-surface permafrost towards the end of the century. In northern and cold permafrost regions, a complete disappearance of near-surface permafrost is only realized after 2150 (blue curve, upper right panel). The sustained long-term warming leads to a continuous deepening of the permafrost table which can reach about 10 m (~7 to 13 m, 68 % range) by the year 2300 in our simulations.

Under wetland conditions (i.e. water/ice-saturated sediments), the active layer shows a similar but slower deepening in response to rising surface air temperatures (Figure appendix II-2, mid panels). In contrast, when considering thermokarst lake formation, thaw rates increase sharply (Figure appendix II-2, lower panels). In the first years after intense thermokarst formation, sub-lake talik progression is very pronounced and annual thaw rates amount many decimeters (see supplementary material) – in line with observational and modeling studies (Kessler et al., 2012; Ling et al., 2012; Grosse, in preparation). The abrupt thaw dynamics results in disappearance of near-surface permafrost well before 2050 (Figure appendix II-2, lower panels). By the year 2100, typical talik depths amount to 10 to 15 meters. The evolution of active layer depths in thermokarst-affected deposits does not strongly differ between moderate and extensive warming (Figure appendix II-2, lower panels). This is because the degradation in thermokarst-affected sediments is driven by lake bottom temperatures. Averaged over a full year, lake bottom temperatures do not strongly differ between moderate and strong surface-air warming (see supplementary material).

In our model setting, we explicitly account for permafrost carbon in deep inventories (Yedoma and refrozen thermokarst deposits). By the end of the 23rd century, typical depths of the permafrost table in these carbon- and ice-rich sediments reach about 5 to 9 meters under the RCP8.5 scenario if no abrupt thaw is considered (not shown). Thus even under strong surface air warming, our simulations suggest a large part of the deep carbon deposits will remain perennially frozen over the coming centuries if only gradual thaw is considered. In contrast, in most latitudes of ice-rich Yedoma regions which are affected by new thermokarst formation, thaw reaches the maximum model depth of 15 m before 2300.

II-4.2 Permafrost carbon release

We define permafrost carbon fluxes similar to Burke et al. (2012a) and Harden et al. (2012) as the release from newly thawed permafrost carbon, i.e. the contribution of perennially frozen soil organic matter which becomes part of the active carbon cycle if warmed above pre-industrial temperatures. We stress that these fluxes do not describe the full carbon balance of permafrost regions which is also affected by changes in vegetation uptake, new carbon inputs into deeper soil layers, and carbon release from soil surface layers which were already seasonally thawed under pre-industrial climate (see discussion in section 'model tuning').

Depending on the degree of ground warming and thus on the extent of active layer deepening, differing amounts of newly thawed carbon will be made available for microbial decomposition and eventual release to the atmosphere. Figure appendix II-3 illustrates permafrost carbon thaw and emissions under a scenario of moderate warming (RCP2.6, upper panels) and extensive warming (RCP8.5, lower panels). Under RCP2.6, largest increases in newly thawed permafrost carbon (Figure appendix II-3, first column) are realized until mid of the 21st century with a total of 167 Gt-C (113 to 239 Gt-C, 68 % range) of which 40 to 70 % is assumed part of the passive carbon pool and thus recalcitrant on the timescale considered here. In contrast, the pronounced and continuous warming under RCP8.5 results in much larger amounts of newly thawed permafrost carbon. By the year 2100, 367 Gt-C are thawed (233 to 497 Gt-C, 68 % range), and through further permafrost degradation in the 22nd and 23rd century, a total of 564 Gt-C (392 to 734 Gt-C, 68 % range) of organic matter is newly thawed by the year 2300. Focusing on the top three soil meters and considering a larger uncertainty spread in the permafrost carbon inventory, two recent studies estimated a min-max range of 75 to 870 Gt (Burke et al., 2012a) and of 105 to 851 Gt (Harden et al., 2012) of newly thawed permafrost carbon under RCP8.5 until the year 2100.

The intensity of carbon release after permafrost thaw differs strongly among the scenarios in our simulations (Figure appendix II-3). While under RCP2.6, maximum annual CO_2 emission rates are constrained to about 0.4 Gt-C (0.2 to 0.6, 68 % range), peak emission rates under RCP8.5 amount to 1.7 Gt-C/yr (median) and can reach 2.6 Gt-C/yr (upper 68 % range). The decline in emission rates in the 22nd and 23rd century describes the depletion of thawed permafrost carbon through release to the atmosphere. Under all RCPs, peak CO_2 emission rates occur around the end of the 21st century.

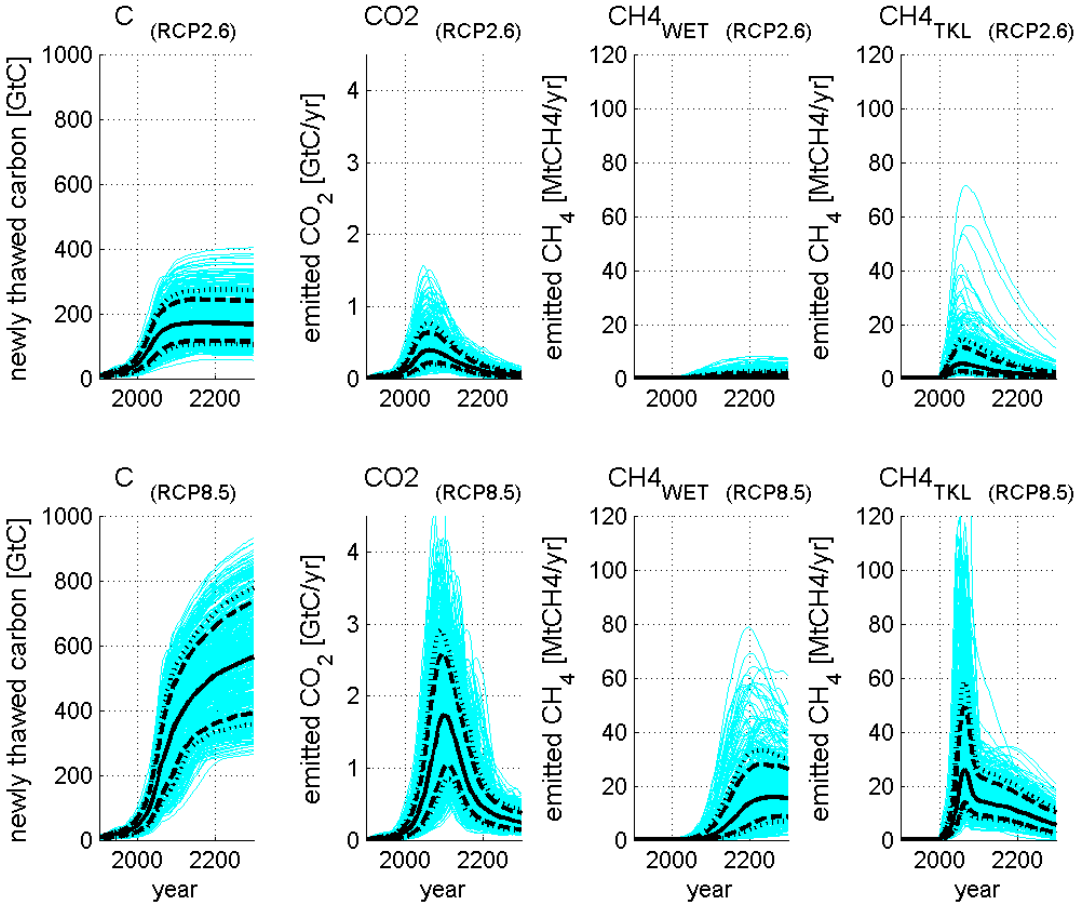

Figure appendix II-3. Simulated increase in newly thawed permafrost carbon C and resulting rates of annual CO_2 and CH_4 release under moderate (upper panels) and extensive (lower panels) global warming for the years 1900 to 2300. CH_4 release is shown separately for fluxes from wetland (WET) and thermokarst lake (TKL) pools. Blue lines show ensemble simulation results based on 500 model runs which account for parameter uncertainty. Black lines show statistical quantiles (solid line: median, dashed lines: 68 % range, dotted lines: 80 % range). Shown are contributions aggregated over all individual pools, summed over all latitudes and depths layers.

Due to much lower anaerobic CH_4 as compared to aerobic CO_2 production rates (Table appendix II-1), and due to the majority of soil carbon being thawed under aerobic conditions, methane emission from thawing permafrost soils amounts only a few percent of total permafrost carbon release. Given the slow progression of permafrost thaw in wetland-affected sediments, CH_4 release from newly thawed permafrost carbon is only discernible after end of this century (Figure appendix II-3). Our simulations suggest maximum annual CH_4 emission rates of a few Mt-CH_4 for moderate warming, about 16 Mt-CH_4 (8 to 28, 68 % range) for strong warming. To the contrary, abrupt thaw under thermokarst lakes results in peak methane emission after mid of this century. Under RCP2.6, maximum annual CH_4 emissions are constrained to about 5.5 Mt-CH_4 (up to 11.5 for the upper 68 % range), while under RCP8.5 peak CH_4 emission reach about 26 Mt-CH_4 (14 to 49, 68 % range). The strong decline in emission rates towards the end of the century is an expression of the sharp decrease

in thermokarst lake extents through increasing drainage under sustained warming (see Figure appendix II-6). A pronounced spike in methane emissions as a consequence of rapidly expanding and subsequently shrinking thermokarst lake areas is in line with hypotheses of past rapid thermokarst lake formation and expansion. Walter et al. (2007a) suggest an annual CH_4 release of 30 to 40 Mt-CH_4 from thermokarst lakes to partially explain CH_4 excursions of early Holocene atmospheric methane levels. Brosius et al. (2012) discuss a yearly contribution from thermokarst lakes of 15±4 Mt-CH_4 during the Younger Dryas and 25±5 Mt-CH_4 during the Preboreal period.

Our modeled total CH_4 fluxes under strong warming are comparable in magnitude to an estimated current release of 24.2±10.5 Mt-CH_4 per year from northern lakes (Walter et al., 2007b). The majority of our results suggest that methane fluxes from newly thawed permafrost carbon are an order of magnitude smaller than the contribution from all current natural (about 200 Mt-CH_4 per year) and anthropogenic (about 350 Mt-CH_4 per year) sources (EPA, 2010). Focusing on thermokarst lakes in ice-rich sediments (i.e. on our Yedoma and refrozen thermokarst deposits), we infer 21st century averaged median emission rates of 6.3 Mt-CH_4/yr which are about double compared to recent model estimates of thermokarst lake CH_4 release (van Huissteden et al., 2011; Gao et al., 2013). Based on a carbon mass balance calculation of methane release from Siberian thermokarst lakes, (Walter et al., 2007b) suggest a contribution of about 50.000 Mt-CH_4 (or 50-100 Mt-CH_4/yr over centuries) in case of a complete thaw of the Yedoma ice-complex. Considering contributions from permafrost wetlands and lakes, Burke et al. (2012a) infer 21st century methane emission rates below 53 Mt-CH_4 per year for the majority of their model runs. Although our CH_4 release estimates, which are inferred by an independent modeling approach, are comparable in magnitude with recent work, a direct comparison with studies extrapolating observed CH_4 fluxes should be considered with care. Observed methane fluxes describe the full carbon balance, including contributions from soil surface layers and vegetation cover, which we do not consider in our model setting.

Under strong warming, our modeled methane emissions accumulate to 836 to 2614 Mt-CH_4 (68 % range) until the year 2100. Maximum contributions until the year 2300 can reach 10.000 Mt-CH_4 (upper 68 % range, see Table appendix II-2).

We have additionally analyzed the impact of uncertainty in initial MAGT distribution on the calculated carbon fluxes. Soil temperatures affect the magnitude of carbon release in two ways. First, MAGTs determine the initial active layer profile and thus the amount of carbon perennially frozen under per-industrial climate. Second, soil temperatures determine the vulnerability of permafrost carbon to future degrada-

tion. Based on a model ensemble with sampling solely uncertainty in MAGT, we inferred a spread in the year 2100 of 32.5±23 % Gt-C and 81.5±8 % Gt-C for the scenarios RCP2.6 and RCP8.5 respectively, which further increase to 60±33 % Gt-C and 235±6 % Gt-C in the year 2300.The factor 3-5 larger fractional uncertainty for the climate mitigation scenario (RCP2.6) illustrates the enhanced sensitivity to initial permafrost temperatures of modeled carbon fluxes under moderate warming.

Table appendix II-2. Cumulated carbon fluxes and increase in global average surface temperature through newly thawed permafrost in the years 2050, 2100, 2200 and 2300. Median and 68 % ranges (in brackets) were calculated from an ensemble of 500 model runs which account for parameter uncertainty.

	Unit	2050	2100	2200	2300
RCP2.6					
cumulated CO_2	[Gt-C]	17 (8 to 29)	36 (20 to 58)	56 (35 to 89)	64 (40 to 98)
cumulated CH_4	[Mt-CH_4]	173 (85 to 354)	446 (218 to 921)	818 (410 to 1753)	1035 (539 to 2236)
dT (PF)	[°C]	0.03 (0.01 to 0.05)	0.06 (0.03 to 0.10)	0.10 (0.06 to 0.15)	0.11 (0.06 to 0.18)
RCP4.5					
cumulated CO_2	[Gt-C]	18 (9 to 32)	54 (28 to 92)	118 (75 to 180)	155 (104 to 216)
cumulated CH_4	[Mt-CH_4]	227 (109 to 466)	1126 (538 to 2356)	3117 (1657 to 5969)	4705 (2592 to 8449)
dT (PF)	[°C]	0.03 (0.01 to 0.05)	0.08 (0.05 to 0.14)	0.16 (0.10 to 0.25)	0.19 (0.13 to 0.29)
RCP6.0					
cumulated CO_2	[Gt-C]	18 (8 to 30)	60 (29 to 101)	156 (103 to 224)	193 (134 270)
cumulated CH_4	[Mt-CH_4]	201 (97 to 407)	1270 (663 to 2440)	3104 (1818 to 5372)	4615 (2664 to 7778)
dT (PF)	[°C]	0.03 (0.01 to 0.05)	0.08 (0.04 to 0.13)	0.18 (0.11 to 0.29)	0.24 (0.16 to 0.39)
RCP8.5					
cumulated CO_2	[Gt-C]	20 (9 to 36)	87 (42 to 141)	194 (136 to 270)	228 (157 to 313)
cumulated CH_4	[Mt-CH_4]	333 (154 to 665)	1474 (836 to 2614)	3592 (2141 to 6093)	5877 (3644 to 9989)
dT (PF)	[°C]	0.03 (0.02 to 0.05)	0.09 (0.05 to 0.14)	0.14 (0.10 to 0.21)	0.16 (0.11 to 0.23)

II-4.3 Contribution of deep deposits

We account for a total of 230 Gt of organic matter buried below 3 meters in Yedoma and refrozen thermokarst deposits (including taberal sediments). Under aerobic or wetland conditions, our simulations suggest only small contributions of these deep deposits to the total release of newly thawed permafrost carbon even under scenarios of strong warming (Figure appendix II-4). Discernible contributions are only inferred towards the end of our simulations (23rd century), with fluxes from deep deposits contributing a maximum of about 10 % to accumulated CO_2 release or about 5 % to total wetland CH_4 release (upper 68 % ranges). The lagged response of deep carbon release is an expression of the slow penetration of heat into the ground. In most latitude bands under the RCP2.6 scenario, no frozen carbon from deep deposits is thawed as the moderate warming does not result in active layer depths exceeding three meters.

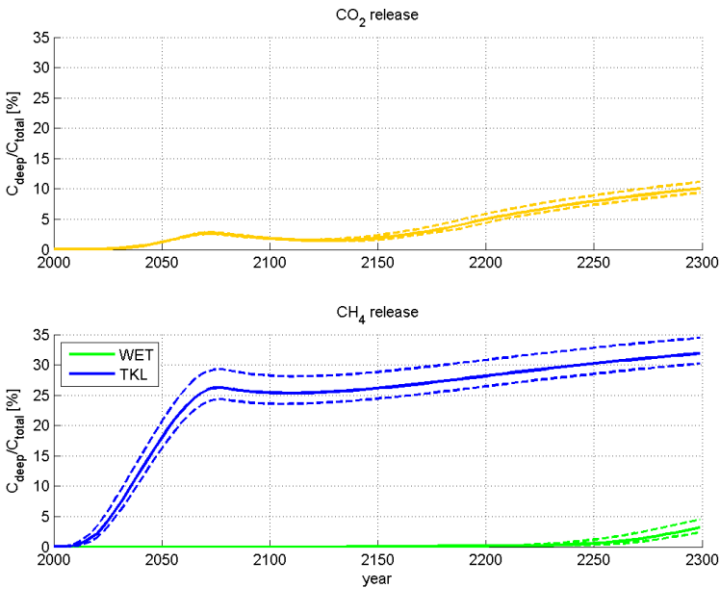

Figure appendix II-4. Contribution of deep permafrost carbon deposits to total carbon fluxes under aerobic (upper panel) and anaerobic (lower panel) conditions. Shown is the contribution of cumulated CO_2 and CH_4 fluxes from deep deposits (3-15 m) to total circumarctic carbon release (0-15 m) under strong warming (RCP8.5). Solid lines represent median values, dashed lines 68 % ranges. CH_4 release is shown separately for wetland-affected sediments (green) and for thermokarst-affected sediments (blue).

Yet if abrupt thaw under thermokarst lakes is accounted for, the fast propagation of sub-lake taliks can unlock large amounts of perennially frozen deep organic matter even within this century. Our simulations suggest that until 2100 about 25 to 30 % of emitted methane from thermokarst lakes stems from contributions of deep permafrost carbon (Figure appendix II-4, lower panel). Maximum contributions until 2300 can amount to 35 % (upper 68 % range).

II-4.4 Permafrost-affected warming

To disentangle the warming caused by anthropogenic greenhouse gas emission from warming caused by permafrost-carbon release, we have performed paired-simulations under identical parameter settings – once with the permafrost module activated and once deactivated. The difference in global mean surface-air temperatures between each pair of ensemble simulations is what we define as the additional global warming caused by newly thawed permafrost carbon (i.e. permafrost-affected warming).

Although permafrost carbon release increases strongly with rising global temperatures (Figure appendix II-3), our results suggest a permafrost-affected global warming of about 0.05°C to 0.15°C (68 % range) until 2100 which is only slightly dependent on the anthropogenic emission pathway. The quasi path-independency of the permafrost temperature feedback is an expression of the decreasing radiative efficiency under high atmospheric greenhouse gas levels. Long-term warming from the release of newly thawed permafrost carbon can add an additional 0.4°C (upper 68 % range) to global temperatures until the year 2300 (Figure appendix II-5). Despite of methane release contributing only a few percent to total permafrost carbon release,

our analyses suggest that it can cause up to about 40 % (upper 68 % range) of permafrost-affected warming. In the 22nd and 23rd century the radiative balance is largely affected by aerobic permafrost carbon release as emitted CO_2 accumulates over centuries in the atmosphere – in contrast to the fast decline in methane anomalies with a typical CH_4 life-time of about a decade.

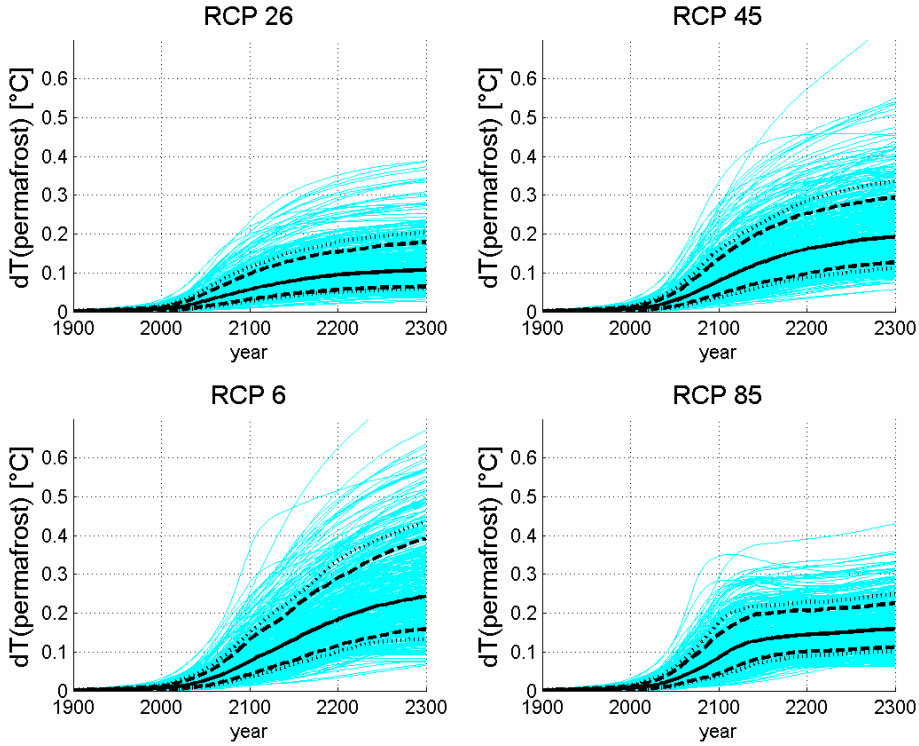

Figure appendix II-5. Increase in global average surface air temperature through newly thawed permafrost carbon under various anthropogenic warming scenarios (RCP2.6 to RCP8.5). Blue lines show ensemble simulation results based on 500 model runs which account for parameter uncertainty. Black lines show statistical quantiles (solid line: median, dashed lines: 68 % range, dotted lines: 80 % range). Shown is the temperature feedback as a consequence of CO_2 and CH_4 release from all individual pools.

II-5 Discussion and conclusions

This paper presents a new observation-based model for assessing long-term climatic consequences of permafrost degradation. Our simulation strategy consisted in partitioning carbon inventories into different pools of varying soil and surface conditions to model site-specific carbon release. Rather than trying to capture permafrost-carbon dynamics in detail, we instead have aimed at describing in a simplified manner a multitude of processes which are key to permafrost carbon release – such as abrupt thaw in thermokarst-affected sediments. We have especially aimed at accounting for the contribution of carbon release from known deep deposits in the 1.3 million km^2 large Yedoma region of Siberia and Alaska (Strauss et al., 2013; Walter Anthony et al., 2014), which had been neglected in most previous modeling studies.

Our computationally efficient model has enabled us to scan the large uncertainty inherent to observing and modeling the permafrost carbon feedback. In our study we had focused on the contribution of newly thawed permafrost carbon which becomes vulnerable through soil warming above pre-industrial temperatures. However, we stress that the full permafrost carbon feedback is also affected by contributions from soil surface layers and changes in high-latitude vegetation which are not considered in this study.

The large spread in future carbon release from permafrost degradation inferred from modeling studies (see Schaefer et al. (2014) for an overview) is caused by various factors. One key issue are pronounced differences in the strength of simulated permafrost degradation. In a recent observationally-constrained model study, Hayes et al. (2014) suggest a mean deepening of the active layer of 6.8 cm over the period 1970 to 2006. We simulate a deepening of 5.9 to 15.5 cm (68 % range) over the same period when focusing on our mineral soil pool under aerobic conditions. By the year 2100, our simulations suggest an active layer deepening of this pool of 40 to 76 cm under RCP2.6, and of 105 to 316 cm under RCP8.5. The latter range covers a large part of previous estimates, although some studies suggest lower values (Schaefer et al., 2014). Yet a comparison of aggregated simulated active layer depths should be considered with care as differences in definitions (e.g. of the considered permafrost domain and its vertical extent) or different assumptions of future warming can lead to estimating systematically lower or higher active layer depths.

Our simulations suggest that permafrost emissions will be strongly constrained when limiting global warming: under a climate mitigation pathway (RCP2.6), the increase in high latitude temperatures results in a moderate deepening of the active layer which stabilizes in most latitudes after the year 2100 (in line with diagnostics based on complex models (Slater and Lawrence, 2013). Until end of the century about 36 Gt (20 to 58 Gt, 68 % range) of carbon can be released as CO_2. Under strong warming (RCP8.5), permafrost degradation proves substantial and cumulated CO_2 emissions can reach 87 Gt-C (42 to 141 Gt-C, 68 % range) by the year 2100. A release of 87 Gt-C corresponds to a mean loss of about 12 % of our initial inventory of 750 Gt of carbon perennially frozen under pre-industrial climate. Modeling studies estimated a loss of 6-33 % of initial permafrost carbon stocks, while the majority of models suggest a loss of 10-20 % (Schaefer et al., 2014). The sustained long-term warming under RCP8.5 results in an almost complete degradation of near-surface permafrost in the 22nd century and illustrates the long-term consequences of permafrost carbon release: our simulations suggest that until the year 2300, a total of about 157 to 313 Gt-C can be released to the atmosphere. Peak emissions occur at the end of the 21st

century and reach 2.5 Gt-C per year under strong warming (RCP8.5, upper 68 % range). In the 22nd and 23rd century depletion of permafrost carbon gets increasingly noticeable and total emissions from newly thawed carbon decline. Our analyses have shown a large potential of reducing uncertainty in simulated carbon fluxes especially for climate mitigation pathways when more and spatially higher resolved data of present day permafrost temperatures will be available.

Based on our conceptual model of thermokarst lake formation and drainage, our results suggest that abrupt thaw can unlock large amounts of frozen carbon within this century. We infer a deepening of the permafrost table by several meters in 100 years after thermokarst initiation, with additional talik propagation large enough to fully thaw sediments to our lower pool boundary (15 m) in the second half of the 22nd century. Subsequent CH_4 release from newly thawed permafrost under RCP8.5 results in peak emissions up to about 50 Mt-CH_4 per year (upper 68 % range) in the 21st century. Our modeled methane releases are of a magnitude comparable to paleo-based estimates from past thermokarst dynamics (Walter et al., 2007a; Brosius et al., 2012) and suggest slightly larger fluxes compared to two recent modeling studies (van Huissteden et al., 2011; Gao et al., 2013). In contrast to abrupt thaw and fast release under thermokarst lakes, methane release from newly thawed carbon in wetland-affected soils is slow with discernible contributions only in the 22nd and 23rd century. Although contributing only a few percent to total permafrost carbon release, our simulated methane fluxes from newly thawed permafrost carbon can cause up to 40 % of permafrost-affected warming in the 21st century. Given the short lifetime of methane, the radiative forcing from permafrost carbon in the 22nd and 23rd century is largely dominated by aerobic CO_2 release.

Under strong warming, our modeled methane emissions from newly thawed permafrost accumulate to some thousand mega tonnes until the year 2100, with maximum contributions of 10.000 Mt-CH_4 (upper 68 % range) until the year 2300 (see Table appendix II-1). Yet the release of this amount of CH_4 would only slightly affect future atmospheric methane levels under projected RCP CH_4 emissions as the anthropogenic contribution will dominate atmospheric CH_4 concentrations. In case of a complete thaw of the Yedoma ice-complex, Walter et al. (2007b) have discussed a contribution of 50.000 Mt of methane being released into the atmosphere.

To put into relation the contribution of carbon fluxes from deep deposits to the total, circumpolar release from newly thawed permafrost, we have analyzed the contribution of individual pools. Our simulations suggest that the omission of deep carbon stores is unlikely to strongly affect CO_2 release from permafrost degradation in the coming centuries. In contrast, CH_4 fluxes from newly thawed permafrost are strongly

influenced by carbon release from organic matter stored in deep deposits. Although our considered deep pools cover only about 12 % of the total area of northern hemisphere gelisols, and despite of the organic matter in these pools being buried deep in the ground, these pools contribute significantly to the total CH_4 balance because abrupt thaw under thermokarst lakes can unlock a large portion of previously inert organic matter. About a quarter of 21st century CH_4 release stems from newly thawed organic matter stored in deep deposits (i.e. from soil layers deeper than 3 m). Further, our analyses revealed that the release from mineralization of labile organic matter contributes disproportionately high to these fluxes. Despite of assuming a fast (labile) pool fraction of only a few percent, our simulated CH_4 fluxes from newly thawed labile organic matter account for up to half of the total thermokarst-affected deep CH_4 release in the 21st century. Therefore, improved observational estimates of the share of labile organic matter would help to reduce uncertainty in simulated methane release from deep carbon deposits (Strauss et al., 2014). The analysis of individual deep pools revealed a methane release about a factor of two larger from refrozen thermokarst compared to unaltered Yedoma.

Our results suggest a mean increase in global average surface temperature of about 0.1°C by the year 2100 (0.03 to 0.14°C, 68 % ranges) caused by carbon release from newly thawed permafrost soils. Long-term warming through the permafrost carbon feedback (year 2300) can add an additional 0.4°C (upper 68 % range) to projected global mean surface air temperatures. Our analyses suggest a permafrost-affected warming which is similar under differing scenarios of anthropogenic emissions – despite of largest carbon release from permafrost degradation under strong warming. The weak path dependency is a consequence of the decreasing radiative efficiency of emitted permafrost carbon under increasing greenhouse gas levels. MacDougall et al. (2012) also modeled a permafrost-carbon feedback largely independent of the emission pathway but inferred larger upper estimates of permafrost-affected warming due to considering a much larger pool available for carbon release triggered by permafrost degradation. An increase in the permafrost temperature feedback with global warming was inferred by Burke et al. (2012a) who considered a much larger spread in the near-surface permafrost carbon inventory (~300 to 1800 Gt-C) and who estimated the permafrost temperature feedback by the year 2100 as 0.02 to 0.11°C and 0.08 to 0.36°C (90 % ranges) under RCP2.6 and RCP8.5 respectively.

II-6 Outlook

We consider our estimates conservative because carbon release from further, in this study unaccounted sources, are likely to increase the strength of the full permafrost-carbon feedback.

First, we do not account for the contribution of newly thawed organic matter of low quality, which we assume recalcitrant on the timescale considered here (i.e. 40 to 70 % of thawed organic matter is not available for release). More data and longer time series of incubation experiments, in combination with modeling work of soil-carbon dynamics, are needed to better constrain timescale assumptions for soil organic matter decomposition. Also of importance are improved data-based estimates of CH_4:$CO_2^{anaerobic}$ production ratios, which determine the share of carbon emitted as CH_4. Second, we do not account for the presence, and potential thaw and mobilization, of deep frozen carbon outside the Yedoma and RTK region. Currently no coherent data is available on the distribution and organic carbon characteristics of soils and sediments below 3 meter depth for large regions in Siberia, Alaska, and Canada. Our model results suggest that these depths will be affected by thaw over the coming centuries and available thawed organic matter would contribute to the permafrost carbon feedback. Third, we do not consider carbon release from degrading submarine permafrost which might result in an underestimation of circumpolar permafrost-affected methane fluxes in our study (Shakhova et al., 2010). Fourth, extensive permafrost degradation can support a large and abrupt release of fossil CH_4 from below the permafrost cap based on presence of regional hydrocarbon reservoirs and geologic pathways for gas migration (Walter Anthony et al., 2012). We do not consider this pathway of abrupt methane release which could lead to a non-gradual increase in the permafrost-carbon feedback if sub-cap CH_4 increases non-linearly with warming. Likely, the most important omission in our study stems from changes in the high-latitude carbon balance caused by altered vegetation dynamics. Here, an increased carbon uptake through more productive high-latitude vegetation and the renewal of carbon sinks in drained thermokarst basins can considerably decrease the net carbon loss on centennial time-scales (van Huissteden et al., 2011; Schaphoff et al., 2013). Yet this loss can be partially compensated through enhanced respiration of soil-surface organic matter which is stored in large amounts in permafrost regions (but which was not incorporated into permafrost in the past and thus is not considered in this study here). On the other hand, a transition from a tundra- towards a taiga-dominated landscape as a consequence of high-latitude warming can strongly decrease surface albedo and therefore additionally warm permafrost regions. We consider the implementation of high-latitude vegetation dynamics into permafrost mod-

els a key step towards an improved capturing of the timing and strength of the full permafrost-carbon feedback.

Acknowledgements

Special thanks to S. Mathesius for the analysis of CMIP-5 data, G. Hugelius for providing soil carbon data for near-surface permafrost inventories, M. Allen for having provided an earlier version of the now extended climate carbon cycle model, H. Lantuit for discussing aspects of permafrost degradation through coastal erosion, C. Schädel for discussing incubation results of soil carbon lability, and Katey Walter Anthony and Hanna Lee for discussing ratios of methane versus carbon dioxide production rates. Portions of this study were supported by UBA project "Permafrost thaw processes under future warming and resulting feedbacks on the climate system" (Project No. 3712 41 106), ERC Starting Grant #338335, and Research Grant 01DM12011. J. Strauss thanks a grant by the Studienstiftung des deutschen Volkes (German National Academic Foundation) and the German Federal Ministry of Education and Research (grant 01DM12011).

II-7 Supplementary material

II-7.1 Model initialization

II-7.1.1 Permafrost carbon inventory

Based on updated soil carbon data (Hugelius et al., 2013b) we describe the amount of organic matter in near-surface permafrost which we allocate into a mineral soil pool (SOCC<20 % per weight, 540 Gt-C) and into an organic soil pool (SOCC>20 %, 120 Gt-C), separately for the depth levels 0 to 1 m, 1 to 2 m, and 2 to 3 m. We hereby focus on carbon in permafrost-affected soils, i.e. orthels and turbels for the mineral pools, and histels for the organic pools (see Figure appendix II-1). Furthermore, we consider two additional pools to describe carbon stored in ice-rich deep deposits ranging from the surface to a depth of 15 meters. Following the inventory classification by Strauss et al. (2013), we consider a Yedoma pool (~80 Gt-C, 0 to 15 m) and a refrozen thermokarst pool (~130 Gt-C, 0 to 5 m). To avoid double-accounting of near-surface inventory estimates, we subtract the amount of permafrost carbon in the top three meters of the Yedoma and refrozen thermokarst pools (Strauss et al., 2013) from the near-surface mineral soil pool (Hugelius et al., 2013b). While the Yedoma pool classifies carbon deposits unaffected by past thermokarst activity, the refrozen thermokarst pool describes organic material buried in sediments which had been subject to abrupt permafrost thaw in the past. In addition to the estimate of Yedoma and thermokarst carbon deposits by Strauss et al. (2013), we also consider permafrost carbon stored in deep taberal sediments (~110 Gt-C (Walter Anthony et al., 2014)) in the depth range 5 to 15 m (Figure appendix II-1). We do not separately consider an estimated 70 Gt-C stored perennially frozen in deep deltaic alluvium (Hugelius et al., 2014). The potential for intensive future thermokarst formation (and thus for deep thaw) in typical deltaic landscapes is rather small, thus we assume that a large portion of this deep carbon store will remain frozen over the next centuries. As we start our simulations from pre-industrial climate, we enlarge our data-based near-surface carbon pools by 10 %. This increase accounts for historical permafrost carbon release and matches the amount of simulated permafrost carbon at the year 2000 with the inventory estimates by Hugelius et al. (2014).

II-7.1.2 Permafrost temperatures and active layer profile

To fully initialize our model, we had to determine permafrost ground temperatures of our carbon inventory. Actual observations, however, are limited and we therefore make the simplifying assumption that ground temperatures are to first order determined by surface air temperatures. We used climatology data from the Berkeley

Earth dataset (http://berkeley earth.org/data) to partition our permafrost grid cells (which range from 47°N to 84°N) into bins of varying surface air temperatures[2]. Based on typical north-south gradients of mean annual ground temperatures (MAGTs) (Romanovsky et al., 2010b; Beer et al., 2013), we assume that the bin with the warmest air temperatures corresponds to southern and warm permafrost with an initial MAGT of –0.5°C ($MAGT_{Max}$), and that the bin with coldest air temperatures corresponds to northern permafrost with an initial MAGT of –10°C ($MAGT_{Min}$). For our default parameter setting, we linearly scale the remainder of temperature bins between $MAGT_{Max}$ and $MAGT_{Min}$. To account for uncertainty, we use a non-linear scaling to allow for clustering towards warmer or colder initial MAGTs (with keeping the total range of –10°C to –0.5°C fixed).

After initialization, MAGT is re-calculated at each time-step for each depth level between the soil surface and the active layer depth by assuming a time-lagged response of soil temperatures to changing surface air temperatures. Hereby we assume an increasing lag with depth, i.e. a maximum lag at the active layer level which decreases towards zero at the soil surface.

We determine the latitudinal profile of the active layer based on our prescribed north-south gradient of initial MAGTs. We assume the seasonal ground temperature cycle to exponentially decay with depth and we choose a typical scale depth to infer temperature profiles consistent with observed, "trumpet-shaped" soil temperature profiles (Romanovsky et al., 2010b; Boike et al., 2013).We then define the equilibrium active layer level for each soil pool and for each latitude as the depth at which maximum soil summer temperatures equal zero degrees. Warmer locations or stronger seasonal cycles result in deeper active layers than colder regions or locations of reduced annual temperature ranges (Koven et al., 2011).

II-7.2 Thaw rate parameterization

We model the process of long-term active layer deepening by assuming that thaw rates can be parameterized depending on four key factors: thermal ground properties, mean annual ground temperatures, active layer depth, and magnitude of the regional warming anomaly which drives permafrost degradation. For each latitude band *lat*, soil type *S*, and aerobic/anaerobic regime *A*, we separately calculate the time evolution of active layer depths by describing individual thaw rates *TR(t)*:

[2] We use summer air temperatures because they are likely to result in a better representation of the soil thermal state compared to annual mean air temperatures. Cold winter air temperatures do not fully penetrate into the ground because snow cover is an effective thermal insulator.

$$TR(t)_{S,A,lat} = \bar{\alpha}_{S,A} * S(t)_{lat} * \frac{dT^*(t)_{A,lat}}{z_{ALD}(t)_{S,A,lat}} \qquad \text{eq. appendix II-1}$$

with $\bar{\alpha}$ describing aggregated soil-specific thermal diffusivities, *S(t)* a soil temperature dependent scaling, dT^* the thaw driving surface warming anomaly, and z_{ALD} the active layer depth. The choice for these four factors is motivated in the following:

$\bar{\alpha}_{S,A}$ is a soil-specific parameter (*aggregated thermal diffusivity*) which determines how effectively heat can penetrate into the ground. Hereby we assume that heat diffusion into the frozen ground is to first order determined by the ice content of the sediments. We first prescribe $\bar{\alpha}_S$ for mineral soils under aerobic conditions and then use scaling factors to infer thermal diffusivities for the remaining carbon pools. As the high latent heat content of ice-rich deposits impedes the rate of downward thawing (Jorgenson et al., 2010), we scale $\bar{\alpha}_S$ according to assumed ice-contents (typical mineral soils: 25 vol%, Yedoma: 70 vol%, refrozen thermokarst: 45 vol% (Schirrmeister et al., 2011b; Strauss et al., 2013). For organic soils we assume a reduced thermal diffusivity compared to mineral soils (factor 0.5) given higher ice-contents and the low thermal conductivity of organic matter. When lakes grow deep enough to prevent winter re-freeze, permafrost degradation increases substantially due to year-round thawing (Arp et al., 2012). To capture the increase in thaw rates after thermokarst formation, we tune $\bar{\alpha}_{S,A}$ to match simulated talik propagation of Kessler et al. (2012). If soils are subject to wetland conditions (i.e. they are moisture-saturated but are not covered by lakes), we assume a reduced thermal diffusivity given the higher ice contents in these soils (see Table appendix II-1).

When permafrost is close to zero degrees, almost all heat is used for the phase transition from ice to water, while for colder conditions the majority of the warming anomaly is used to increase permafrost temperatures with little downward propagation of the thaw front. To capture the difference between much lower thaw rates in cold as compared to warm permafrost, we describe a latitude-dependent scaling factor $S(t)_{lat}$ which non-linearly scales thaw rates by mean annual ground temperatures (MAGTs). Hereby, we describe a quartic dependency of $S(t)_{lat}$ on MAGT to capture the sharp increase in thaw rates when permafrost temperatures approach zero degrees. The scaling factor profile is parameterized to yield a ratio of 1:10 for thaw rates at coldest (MAGT= –10°C) to warmest (MAGT=0°C) permafrost.

We capture the strong dampening of heat propagation with depth by assuming that the thaw rate is inversely proportional to depth (Kessler et al., 2012). This allows us

to reproduce the general tendency of high talik development rates in the first years after thermokarst initiation and gradual decrease with time (Ling and Zhang, 2003).

The magnitude of the regional surface warming anomaly is a further key driver of subsurface permafrost degradation. We assume thaw rates in non-thermokarst affected sediments being proportional to the magnitude of the surface air temperature anomaly, i.e. the warming above pre-industrial temperatures. We calculate the warming anomaly in each latitude band by accounting for the length of the thaw season (i.e. by the yearly fraction of days with non-freezing surface air temperatures). To account for key differences in thaw rates between non-thermokarst and thermokarst-affected sediments, we assume that degradation of the latter is driven over a full year by lake bottom temperatures (and thus not by seasonal surface air temperatures). We calculate lake bottom temperatures based on the annual cycle of surface air temperatures while assuming that the annual summer amplitude is damped by 50 % (Boike et al., 2013) and that winter lake bottom temperatures cannot fall below a minimum of two degrees Celsius.

To ensure that our scheme for describing permafrost thaw dynamics yields robust results, we perform at each time step a consistency check: we calculate the equilibrium active layer depth which would establish under the given climatic boundary conditions (determined by mean annual air temperature and the amplitude of the seasonal cycle). We use this depth as a constraint for maximum thaw rates and thus assure that the parameterization of thaw rates yields physically plausible results.

II-7.3 Anaerobic soil fractions

II-7.3.1 Thermokarst lake pool

To capture future thermokarst dynamics, we have developed a conceptual model of thermokarst formation and drainage. Our simulation approach is chosen to test different hypotheses of future thermokarst evolution rather than providing a deterministic model projection based on small-scale thermokarst processes (such as e.g. Kessler et al., 2012; Ling et al., 2012). To keep our model description as simple as possible, we assume that future increases in surface air temperatures are the main driver for thermokarst formation through melting of near-surface ground ice and subsequent ground subsidence. Moreover, we neglect factors other than temperature (e.g. surface disturbance, precipitation or local topography) which also can affect thermokarst formation (van Huissteden et al., 2011).

To describe the evolution of newly formed thermokarst lakes in each latitudinal band, we use an optimum function which non-linearly scales the latitudinal thermo-

karst lake area fraction $F^{TKL}(t)$ by the surface air temperature anomaly $d\bar{T}'(t)$ (see Figure appendix II-2):

$$F^{TKL}_{S,lat}(t)=d_S*exp\,(a_S*d\bar{T}'(t)-b_S*d\bar{T}'(t)^{c_{lat}*d\bar{T}'(t)} \qquad \text{eq. appendix II-2}$$

For each soil pool $F^{TKL}(t)$ describes the area fraction per latitudinal band which is affected by newly formed thermokarst lakes. The high-latitude surface air temperature anomaly $d\bar{T}'(t)$ drives changes in thermokarst lake extent. It is defined as the annual surface air warming above pre-industrial temperatures, averaged over all permafrost regions. We infer $d\bar{T}'(t)$ based on an analysis of polar amplification factors from state-of-the-art climate models (CMIP-5 (Taylor et al., 2011)). With rising $d\bar{T}'(t)$, $F^{TKL}(t)$ increases towards an optimum at which the maximum thermokarst lake fraction F^{TKLmax} is realized at $d\bar{T}'^{TKLmax}$. With further warming above $d\bar{T}'^{TKLmax}$ drainage and additional processes (such as increasing evaporation and terrestrialization are assumed to outweigh lake formation (van Huissteden and Dolman, 2012). By our model design, further warming above $d\bar{T}'^{TKLmax}$ leads to a decrease in the thermokarst lake area which cannot fall below a prescribed minimum area fraction F^{TKLmin}. We prescribe a decline which is most pronounced in southern permafrost regions where we assume a minimum fraction of remaining lakes F^{TKLmin} of 3 % (see Figure appendix II-2).

In the coldest permafrost regions we assume a minimum fraction of 15 %. The latitudinal gradient expresses the potential for more extensive drainage at the southern, discontinuous permafrost boundary where the permafrost body is thin and where internal drainage (i.e. subterraneous outflow (Yoshikawa and Hinzman, 2003)) is an efficient pathway for water removal. In northern, continuous permafrost regions, we only consider lateral erosion through thermo-erosional landforms and expansion of lakes in thermokarst basins an efficient drainage mechanism (Morgenstern et al., 2011). We determine the soil-specific shape parameters a_S, b_S, d_S by prescribing F^{TKLmax} and $d\bar{T}'(t)$ for each carbon pool individually (see Table appendix II-1). In specific regions, about 80 % of the landscape is affected by thermokarst and thermal erosion (Strauss et al., 2013). Yet it is unlikely that future thermokarst coverage will be as extensive because existing degradational landforms and other topographic lows will favor future lake drainage (Morgenstern et al., 2011). We assume the highest potential for new thermokarst lake formation in unaltered ice-rich Yedoma sediments which had not been affected by past thermokarst activity. We further assume a reduced potential for the formation of second-generation lakes in existing basins

(Morgenstern et al., 2011), i.e. in refrozen thermokarst deposits. The lowest potential of new thermokarst lake formation is assumed for less ice-rich organic and mineral soils (see Table appendix II-1).

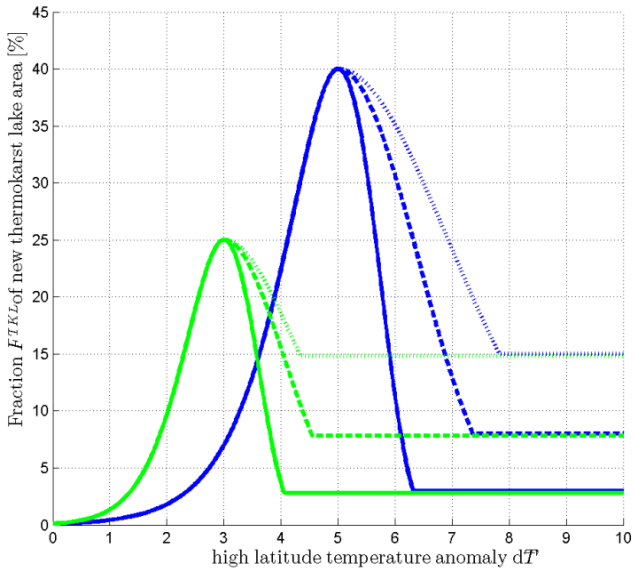

Figure appendix II-6. Temperature dependency of newly formed thermokarst lake area fractions. The figure illustrates the increase and decrease of the new thermokarst lake area fraction F^{TKL} (as percentage of the total permafrost area in each latitude band) with rising high latitude surface air warming $\boldsymbol{d\overline{T}'}$. Curves are shown for two different choices of maximum thermokarst lake extents F^{TKLmax} (green: 25 %, blue: 40 %) and corresponding warming $\boldsymbol{d\overline{T}'^{TKLmax}}$ (green: 3°C, blue: 5°C). The different line styles illustrate the latitudinal dependency of drainage for warming above $\boldsymbol{d\overline{T}'^{TKLmax}}$ (solid: southern permafrost limit, dashed: mid permafrost latitude, dotted: northern permafrost limit).

By newly formed lakes we consider thermokarst lakes which establish under temperatures warmer than pre-industrial. We do not consider existing thermokarst lakes (formed over the last centuries to millennia) as a part of our thermokarst lake pool. These lakes have likely formed deep taliks in the past and are underlain by sediments potentially depleted in labile organic matter. We further only consider lakes being part of our thermokarst pool if they are deep enough to prevent winter refreeze of the lake bottom waters (about 1 to 2 m (Arp et al., 2012; Yi et al., 2014)). As we do not model lake depth expansion we assume that formation of new thermokarst lakes is initiated for any warming above our reference climate (i.e. pre-industrial climate), while we also assume that extensive talik formation under thermokarst lakes is only realized after newly formed lakes have deepened enough to reach the critical depth which prevents winter refreeze (we define this time to be the year 2000). Arctic landscapes are also covered by numerous smaller lakes or ponds which fully refreeze in winter and do not develop deep taliks. Therefore they do not provide conditions for abrupt permafrost degradation and we consider ponds and smaller lakes part of our wetland pool.

We do not account for changes of the CO_2 and CH_4 flux balance through establishment of new vegetation after drainage (Jones et al., 2012; Kessler et al., 2012; van Huissteden and Dolman, 2012; Walter Anthony et al., 2014), see discussion in section model limitations).

II-7.3.2 Wetland pool

In this study we assume that high latitude wetland extent will slightly increase over the near-term with future warming. Such an assumption is supported by projected increases in the hydrologic balance of precipitation minus evaporation. We do not investigate a scenario of potential northern wetland drying (as e.g. investigated by Avis et al., 2011). In our model setting we describe an increase in the wetland area fraction per latitude band by a linear scaling with high latitude warming, i.e. with the high-latitude surface air temperature anomaly $d\bar{T}'(t)$. Each carbon pool is initialized with a minimum wetland extent at pre-industrial temperatures and reaches its maximum extent for a high-latitude warming $d\bar{T}'$ of 10°C (see Table appendix II-1). For further warming the wetland fraction is kept constant at the maximum extent.

Our simulated wetland CH_4 fluxes describe methane produced from newly thawed permafrost carbon. Yet the full carbon balance of wetlands is rather complex and possibly more affected by future changes in soil moisture, soil temperature, and vegetation composition than by the delivery of newly thawed organic matter through permafrost degradation (Olefeldt et al., 2013). The accounting of these additional factors requires the implementation of comprehensive wetland models (such as formulated by Frolking et al., 2011; Kleinen et al., 2012).

II-7.4 Carbon release

Based on our thaw rate parameterization (eq. appendix II-1), we track the active layer depth for each pool at each time step and thus can calculate the amount of carbon which is thawed as a consequence of warming above pre-industrial temperatures. We refer to this newly thawed carbon as vulnerable carbon $VC(t)$ (Burke et al., 2012a). Carbon release $C^{\uparrow}(t)$ for each soil carbon pool S, aerobic/anaerobic environment A, organic matter quality Q, latitude lat, and depth level z is assumed proportional to the pool-specific amount of vulnerable carbon $VC(t)$ and release rate $R(t)$ (see Table appendix II-1):

$$C^{\uparrow}_{S,A,Q,lat,z}(t) = R_{S,A,Q,lat,z}(t) * VC_{S,A,Q,lat,z}(t) \qquad \text{eq. appendix II-3}$$

We do not explicitly account for gaseous transport from subsoil layers to the atmosphere but assume that the timescale involved is small compared to CO_2 and CH_4 production. Therefore, we assume that carbon release rates can be described by CO_2 and CH_4 production rates. Yet we account for pool-specific oxidation during methane release. We hereby assume little oxidation of CH_4 from thermokarst sediments because ebullition is a rather effective pathway with little chance for CH_4 oxidation. To the contrary, CH_4 release from wetlands is likely affected much stronger by oxida-

tion. We therefore assume systematically higher oxidation rates for these soils (see Table appendix II-1).

Under anaerobic degradation of organic matter, methane can be produced via a variety of complex food webs (Segers, 1998). For our fast pool (which describes labile organic matter) we assume that methane production is dominated by fermentation of acetate. Given the stoichiometry of CH_4 production by methanogenesis via this pathway, we assume a 1:1 production ratio of CH_4:$CO_2^{anaerobic}$ (Conrad et al., 2002; Walter Anthony et al., 2014). Incubations studies suggest this ratio can deviate strongly from 1:1 and cover very large ranges with anaerobic CO_2 production one to two orders of magnitude larger than CH_4 production (Segers, 1998; Scanlon and Moore, 2000; Lee et al., 2012). We do not account for very low CH_4:$CO_2^{anaerobic}$ ratios (<0.07) which might be explained by high initial CO_2 production and a strong decline with time after which a stable, much larger CH_4:$CO_2^{anaerobic}$ ratio might establish (Scanlon and Moore, 2000).

Compared to the amount of labile organic matter, the slow carbon pools describe a much larger inventory of organic material of varying compositions and structures. We assume that methane production can also follow alternative pathways under which alternative electron acceptors are likely becoming important which can reduce CH_4:$CO_2^{anaerobic}$ production ratios. Based on incubation results from Lee et al. (2013), we assume an anaerobic production ratio CH_4:$CO_2^{anaerobic}$ of 1:7 (±50 %) for organic matter in the slow pool (Table appendix II-1).

As microbial soil activity rises with increasing soil temperatures, we account for a Q^{10} temperature sensitivity of carbon decomposition: we calculate carbon release rates R(t) for each carbon pool, each latitude, and each vertical layer by scaling CO_2 and CH_4 production rates P by monthly soil temperatures $TS(t)$:

$$R_{S,A,Q,lat,z}(t) = (1-OX_A)*(P_{A,Q}*Q_A^{10^{(TS_{S,A,lat,z}(t)-10)/10}}) \qquad \text{eq. appendix II-4}$$

We calculate monthly soil temperature $TS(t)$ by assuming an exponential decay of the seasonal temperature cycle with depth. We hereby assume a lagged temperature response with time (i.e. zero lag at the soil surface which is assumed to warm at the same rate as surface air and maximum lag at the active layer depth). When soil temperatures drop below zero degrees we assume soil microbial activity to be negligible and decomposition is halted. $(1-OX_A)$ describes the fraction of released carbon which is not oxidized (with $OX=0$ for CO_2, and $OX=OX_{WET}$ or $OX=OX_{TKL}$ for CH_4, see Table appendix II-1).

II-7.5 Carbon-cycle and climate model

To close the feedback loop of warming-induced permafrost degradation, carbon release, and additional warming, we use a simple multi-box carbon-cycle climate model from Allen et al. (2009) which was designed to span the full range of temperature and carbon cycling dynamics consistent with observations.

The model calculates atmospheric CO_2 concentrations by describing a diffusive uptake of emitted CO_2 through vegetation and surface oceans, and by an advective carbon transport into the deep ocean. The uptake of heat by the ocean is modeled by a diffusive process. We have used the model description by Allen et al. (2009) and have extended their model design by describing a declining diffusive CO_2 uptake with rising temperatures. The extended diffusive description allows us to model a decrease in airborne fractions with rising temperatures inferred from complex models (Friedlingstein et al., 2006). We have tuned model parameters such that we could reproduce individual CO_2 concentration pathways from the RCP database (www.iiasa.ac.at/web-apps/tnt/RcpDb) based on CO_2 emission trajectories of all four standard RCPs. To calculate deviations in atmospheric methane concentrations, we assume an exponential decay of CH_4 anomalies with a typical e-folding lifetime of 11 years.

We calculate radiative forcing of CO_2 and of CH_4 by using standard formulae after Myhre et al. (1998). Hereby, we also assume that indirect methane effects lead to a radiative forcing which is about 15 % larger than when only considering the direct radiative effect of changes in atmospheric CH_4 concentrations (Shindell et al., 2009). By describing uncertainty in the diffusive carbon uptake, in climate sensitivity, and in ocean heat uptake, our parameter sampling accounts for a large spread in simulated carbon-cycle climate responses. Based on the pathway of anthropogenic and permafrost-induced emission of CO_2 and CH_4, we thus can calculate the change in global mean surface air temperature (see also supplementary information in Allen et al. (2009)). As permafrost regions warm much stronger than the globe as a whole, it is important to account for the polar amplification of temperature change to simulate the warming of permafrost regions. We do this by applying latitude-dependent amplification factors which we infer from an analysis of state-of-the-art climate models (CMIP-5 (Taylor et al., 2011)). This analysis has resulted in typical amplification factors between 1.6 at the southernmost permafrost limit and about 2.3 at the northernmost permafrost limit. By using these scaling factors, we thus can translate our simulated global temperature anomalies into regional warming of high-latitude permafrost regions. Based on these scaled temperatures anomalies, we calculate permafrost degradation in each latitude band.

Appendix III Supplementary material for Chapter 3: The deep permafrost carbon pool of the Yedoma region in Siberia and Alaska

Published in: Geophysical Research Letters, 2013, doi:10.1002/2013GL058088

III-1 Terminology and methods

III-1.1 Terminology and abbreviations

III-1.1.1 Terminology

Segregated ice: Ice in discrete layers (bands) or ice lenses (not in wedge ice), formed by freezing of water within the sediments (e.g. Figure 3-2d (according to van Everdingen, 2005)).

Thaw-lake basin (drained): = thermokarst depression (Figure 3-2b). Drained thaw-lake basins are the result of degradation of Yedoma deposits by lake formation. The Russian literature also describes a drained thaw-lake basin as an *"alas"*, defined as a large depression of the ground surface produced when a large area of thick and exceedingly ice-rich permafrost thaws (according to van Everdingen, 2005).

Thermokarst (process): A process by which characteristic landforms, like basins caused by surface subsidence, result from the thawing of ice-rich permafrost (according to van Everdingen, 2005).

Thermokarst deposits: Used in this study to describe the frozen deposits accumulated in drained thaw-lake basins and thermo-erosional valleys.

Wedge ice: A massive, generally wedge-shaped ice body, composed of foliated or vertically banded ice (Figure 3-2a (according to van Everdingen, 2005)).

Yedoma: A suite of late Pleistocene ice- and organic-rich silty sediments that accumulated in Beringia (unglaciated Siberia and Alaska) (Schirrmeister et al., 2013).

Yedoma deposits: Used in this study to emphasize that the deposit itself (not the geomorphic or the stratigraphic position (Schirrmeister et al., 2013) is meant. The studied recent Yedoma deposits are undisturbed and unaltered by thermokarst processes (Figure 3-2a,b).

Yedoma region: We used this term to outline the potential area for Yedoma deposit distribution, not to indicate the area where Yedoma deposits indeed occur (Figure 3-1). The Yedoma region also includes thermokarst areas.

III-1.1.2 Important abbreviations

BD: Bulk density in 10^3 kg/m³ = g/cm³

CH_4: Methane

CO_2: Carbon dioxide

Gt: gigatonne; 1 Gt = 10^9 tonnes = 10^{12}kg = 10^{15}g (= petagram; Pg)

OC: organic carbon

RCP: Representative Concentration Pathways

SEI: Segregated ice

SEIV: Segregated-ice volume

TOC: Total organic carbon

WI: Wedge ice

WIV: Wedge-ice volume

III-1.2 Total organic carbon (TOC) measurement

Before measurement of TOC, the samples were dried, homogenized, and milled using a ball mill (Fritsch pulverisette 5). Carbonate was removed by adding hydrochloric acid (4 %). The sediment samples were measured twice with a carbon-nitrogen-sulphur analyzer (Elementar Vario EL III) or a TOC analyzer (Elementar Vario Max C; a device with integrated inorganic carbon removal). In each series of measurements, a blank capsule was used for background and several capsules of standards (Sulphanilamid, EDTA 10:40, IVA 2150, PACS 1, L-Glutamine, L-Cysteine) were determined with a device-specific accuracy of 0.1 wt%.

III-1.3 Calculation of the bulk density, segregated ice, and organic carbon density

For BD and SEI calculation samples were weighed in wet and oven-dry state during field expeditions. If no data for the density of the solid fraction (sediment density, ρ_s, 10^3 kg/m³) was available, we assumed that ρ_s for BD calculation is equal to the density of its dominant component, quartz (2.65 10^3 kg/m³). Instead of using quartz density, the sediment density of a subset of samples (202) was determined using a helium gas displacement pycnometer (AccuPyc-1330, Micromeritics) for validation. To determine BD (10^3 kg/m³), the volume of the solids (V_s, 10^{-6} m³) was derived first. The mass of solid particles (m_s) and the solid fraction density (ρ_s) are used in eq. appendix III-1:

$$V_s = \frac{m_s}{\rho_s} \qquad \text{eq. appendix III-1}$$

After that, the porosity (n) was calculated (eq. appendix III-2) using pore volume (V_p, 10^{-6} m³):

$$n = \frac{V_p}{V_p + V_s} \qquad \text{eq. appendix III-2}$$

It is appropriate to assume that pores in frozen deposits are ice-saturated if the SEI is >20 wt% (Strauss et al., 2012). With this assumption, the SEI gives an estimation of the pore volume. For determining ice volume an ice density of 0.91 10^3 kg/m³ was assumed. BD was then calculated using its inverse relationship with porosity (eq. 3-1).

For error estimation, we compared measured and calculated BD for a subgroup of the samples (Figure appendix III-2). To assess a mean, the difference between measured and calculated samples is 12 % for both Yedoma (n=90) and thermokarst (n=36) deposits.

To calculate the OC density, the BD calculations and measurements were combined with TOC values and WIV. The volumetric OC calculation (OC density, kg/m³) was performed according to:

$$\text{OC density}\left(\frac{kg}{m^3}\right) = BD\left(\frac{10^3 kg}{m^3}\right) \times \frac{100\text{-}WIV}{100} \times \frac{TOC}{100} \times 1000 \qquad \text{eq. appendix III-3}$$

III-1.4 Calculation of the wedge-ice volume (WIV)

III-1.4.1 Assumptions and calculation

WIV estimation is based on the simplification that polygons are squares. This approach does not account for active-layer thickness, and WIV calculations are only done for layers containing WI. In Figure appendix III-1 the variables are sketched and defined.

For epigenetic ice wedges it is assumed that a frontal cut of an ice wedge has a shape of an isosceles triangle (Figure appendix III-1, right side). The variables used to calculate epigenetic WIV are defined as: VoP: volume of the polygonal block (cuboid with a squared top), with VoP= $A^2 \times H$; A: polygon size, and H: polygon height; VoS: volume of sediment block (truncated pyramid), with VoS = $\frac{1}{3} \times H \times (A^2+AB+B^2)$ and A: polygon size (=base side length), B: surface polygon length (top side length): B = A-C; C: maximum epigenetic ice-wedge width. This approach enables us to calculate the epigenetic WIV using the volume of a truncated pyramid to

represent the sediment block framed by ice wedges (Kanevskiy et al., 2013). The WIV is calculated according to eq. appendix III-4:

$$WIV_{epigenetic}=\frac{VoP-VoS}{VoP}=\frac{H\times(A^2+AB+B^2)}{H\times 3A^2}=1-\frac{A^2+A\times(A-C)+(A-C)^2}{3A^2} \quad \text{eq. appendix III-4}$$

This approach after *Kanevskiy et al.* (2013) is only feasible for epigenetic wedges, which occur mostly in the studied thaw lake basin thermokarst deposits. For syngenetic Yedoma deposit ice wedges, we deduced eq. appendix III-5, assuming that a frontal cut of this ice wedge type is rectangular in shape (Figure appendix III-1, left side). Yedoma deposit VoS is assumed to be VoS = H × (A-D)². Hence, we used a different eq. appendix III-5 for syngenetic WIV calculation:

$$WIV_{syngenetic}=\frac{VoP-VoS}{VoP}=\frac{H\times(A-D)^2}{H\times A^2}=1-\frac{A}{A^2}-\frac{2AD-D^2}{A^2}=\frac{2AD-D^2}{A^2} \quad \text{eq. appendix III-5}$$

D: mean (with depth) width of a syngenetic ice wedge. All other variables are similar to those used in the calculation of $WIV_{epigenetic}$.

III-1.4.2 Measuring required parameters for wedge-ice volume calculation

Wedge-ice width

WI width is based on field measurements extracted from the literature (Meyer et al., 2002a; Meyer et al., 2002b; Grigoriev et al., 2003; Magens, 2005; Boike et al., 2008; Wetterich et al., 2008; Hoffmann, 2011; Kanevskiy et al., 2011; Opel et al., 2011; Kanevskiy et al., 2012; Boereboom et al., 2013; Kanevskiy et al., 2013). Forty-four measured Yedoma ice wedges at 14 sites were identified. The sites were merged to 10 regions/sites (Cape Mamontov Klyk, Lena Delta, Bykovsky Peninsula, Muostakh Island, New Siberian Islands, Dmitry-Laptev Strait, Duvanny Yar, Alaskan North Slope, Beaufort Sea coast, and interior Alaska) and each region was assigned a mean WI width. To determine thermokarst deposit WI width, 40 measured ice wedges were used from 16 sites, grouped into 6 regions/sites (Cape Mamontov Klyk, Lena Delta, Bykovsky Peninsula, Tiksi area, New Siberian Islands, and Dmitry-Laptev Strait) with a mean value shown in Table appendix III-4.

Polygon size

The mean Yedoma and thermokarst deposit polygon sizes were determined by mapping very-high-resolution satellite imagery for four study sites: Cape Mamontov Klyk (1; numbers according to Figure 3-1), Bykovsky Peninsula (5), Buor Khaya Peninsula (7), and Bol'shoy Lyakhovsky Island (13). For thermokarst deposits, the

polygon mapping and size calculation were done according to Ulrich et al. (2011). Polygons were digitized manually within ArcGIS™ using very-high-resolution GeoEye and Kompsat-2 satellite data (Figure appendix III-3). Only if polygons were completely enclosed by rims or troughs, and the individual polygon form could be identified precisely, were they considered in the datasets. Clearly-recognizable fissures and troughs were mapped along their centerlines. The size was calculated as equivalent to the diameter of the polygon area (Ulrich et al., 2011).

Since Yedoma deposits are often covered with thin Holocene deposits, their polygonal pattern is usually obscured. However, along thermokarst or thermo-erosion features, Yedoma polygonal patterns are exposed in the form of thermokarst mounds that represent erosional remnants of the former polygon centers. Yedoma deposit polygon sizes were therefore determined by measuring the distance between adjacent thermokarst-mound centers using a line feature class in ArcGIS™ (Figure appendix III-3, right side) or with measuring tape in the field (Figure appendix III-4c). Only the distances from one individual mound center to each neighboring and clearly identifiable mound center were measured. Field measurements were done in 2002 on the Bykovsky Peninsula (5; according to Figure 3-1), Bel'kovsky Island (9), Kotel'ny Island (10), and Maly Lyakhovsky Island (12) study sites (Figure appendix III-4c).

III-1.5 Calculation of Yedoma region coverage

We based our calculations on the extent of the Yedoma region as delineated in general maps of the potential Yedoma deposit area in Siberia (Romanovskii, 1993) and in maps showing ice-rich silt deposits we identified as the potential Yedoma deposit area in Alaska (Jorgenson et al., 2008), resulting in a total coverage of 1,387,000 km². In detail we assume the Yedoma area as 1,141,000 km² for Siberia, 181,000 km² for Alaska and ~65,000 km² for regions with smaller known Yedoma deposit occurrences (e.g. south of Taymyr Peninsula, Chukotka, and Yukon Territory).

Based on literature data (Grosse et al., 2005; Grosse et al., 2006; Veremeeva and Gubin, 2009; Morgenstern et al., 2011; Arcos, 2012; Jones et al., 2012; Morgenstern, 2012; Grosse et al., 2013a) (Table appendix III-7) the average of Yedoma deposit areas versus areas affected by degradation in several North Siberian sites was estimated, suggesting that 70 % of the Yedoma region is affected by degradation or erosion. This results in an updated coverage for remaining Yedoma deposits of 416,000 km², in addition to about 971,000 km² covered by non-Yedoma deposits. To estimate the coverage of frozen thermokarst deposits in this non-Yedoma deposit

fraction, we subtracted the thermokarst lake area (considered to represent unfrozen deposits; 150,000 km², extracted for the Yedoma region from *Grosse et al.* (2013b) (lakes >0.1 km²) corrected with additional "missing" lake area (up to 80 %) (Grosse et al., 2008) and other literature data (Grosse et al., 2005; Grosse et al., 2006; Veremeeva and Gubin, 2009; Morgenstern et al., 2011; Arcos, 2012; Jones et al., 2012; Morgenstern, 2012; Grosse et al., 2013a) (Table appendix III-7) and the area of river deltas (Olenyok, Lena, Yana, Indigirka, Kolyma) of 47,000 km² in the Yedoma region (Walker, 1998). The rivers, including fluvial and alluvial unfrozen sediments, are also excluded from consideration. The Alaskan deltas (Yukon and Colville) were already excluded in the map that we used (Jorgenson et al., 2008). Hence, we inferred that frozen thermokarst deposits cover approximately 775,000 km².

III-1.6 Calculation of the Yedoma region atmospheric CO_2 contribution

For a rough calculation of the potentially outgassing Yedoma region CO_2, we used the eq. appendix III-6. According to Battle et al. (2000), the release of one Gt of carbon to the atmosphere increases the amount of CO_2 by 0.471 ppm. The amount of CO_2, if 20 % of the Yedoma region OC pool (20 % of 211+160/-153 Gt; min: 11.6 Gt, mean: 42.2 Gt, max: 74.2 Gt) is emitted to the atmosphere, is calculated with eq. appendix III-6:

$$CO_2(\text{ppm}) = \frac{C \times 0.471}{2} \qquad \text{eq. appendix III-6}$$

The factor of ½ is the airborne effect, assuming that half of the CO_2 rise will be incorporated into the ocean and plant biomass.

III-1.7 Mean-bootstrapping technique to calculate organic carbon budgets

This bootstrapping technique is used because of a non-normal distribution of the parameters (Figure 3-3 and Figure appendix III-5) and for the calculation of non-parametric uncertainty estimates. Besides the observation-based bootstrapping, we additionally performed the calculation (5.000 repetitions) based on means for each variable with observations available (TOC, BD, WIV, thickness). We used sampling with replacement, which means that after we randomly draw an observation from the original sample we put it back before drawing the next observation. We calculated the Yedoma deposit frozen OC pool as 14±2 kg/m³ and thermokarst deposits as 55±13 kg/m³. WIV is included in this calculation. Separate from wedge ice, the Yedoma deposit frozen OC pool contain 26±4 kg/m³ and thermokarst deposits 60±14 kg/m³. Adding the total stored Yedoma deposit OC, 111±17 Gt**,** and the frozen thermokarst deposit OC, 237±57 Gt, the total frozen Yedoma region contains

348±73 Gt. The median of the obtained distributions for Yedoma deposit and thermokarst deposit OC budgets, 110 and 232 Gt respectively. However, inferred 16th and 84th percentiles (Yedoma: 95 Gt, 128 Gt; thermokarst: 181 Gt, 232 Gt) are markedly smaller compared to the observation-based bootstrapping because using single value estimates such as mean reduces the variability of the obtained distribution. Sensitivity analyses were conducted by running the OC budget calculation repeatedly; each calculation utilized the uncertainty of a single variable, i.e. by using the mean of all values in the calculation rather than a randomly sampled mean (Table appendix III-9).

III-1.8 Inventory calculation based on simple-mean values

To estimate an OC inventory based on our parameter dataset that is comparable to previous studies (e.g. Zimov et al., 2006a) using the arithmetic mean and assuming normal-distribution, our Yedoma region OC estimate results in 112 Gt for Yedoma deposits and 240 Gt for thermokarst deposits. The total Yedoma region pool using mean values is 352 Gt. Hence, the Yedoma deposit frozen OC pool contains 14 kg/m³ and thermokarst deposits as 56 kg/m³. WIV is included in this calculation. Separate from wedge ice the Yedoma deposit frozen OC pool contain 27 kg/m³ and thermokarst deposits 60 kg/m³ if WIV is not included. Details with error estimates are shown in Table appendix III-1. Nonetheless because of data heterogeneity and non-normal distributions (Figure 3-3, Figure appendix III-5), we assume that applied bootstrapping statistics for OC budget calculation yields more realistic values.

III-2 Supplementary figures

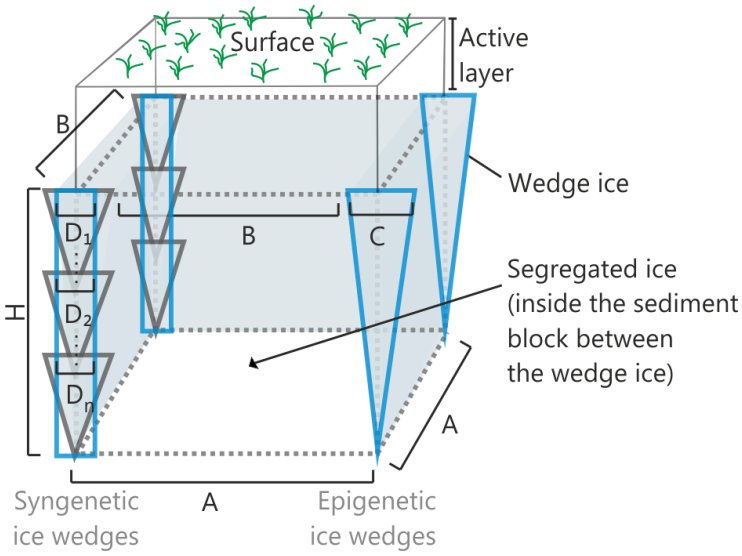

Figure appendix III-1. Idealized polygon scheme demonstrating variables used for wedge-ice volume (WIV) calculation. A: polygon size; B: surface polygon length; C: maximum width of epigenetic ice wedge; D: mean width of syngenetic ice wedge; H: polygon height. The relevant equations for WIV calculation are eq. appendix III-4 and eq. appendix III-5.

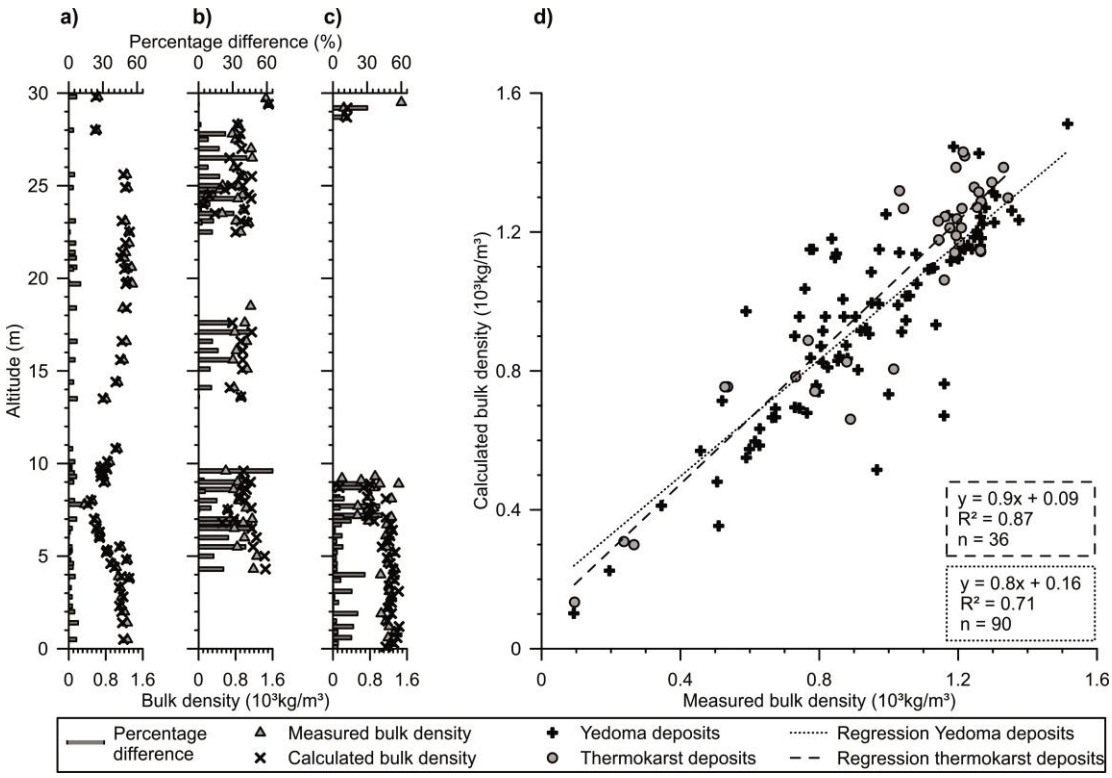

Figure appendix III-2. Measured and modeled bulk density (BD) data and error estimates. (a) Yedoma deposit exposure at Itkillik River, Alaska; (b) Yedoma deposit exposure at Buor Khaya, Laptev Sea, Siberia; (c) thermokarst deposits from Buor Khaya, Laptev Sea, Siberia; (d) relationship between measured and calculated BD of Yedoma and thermokarst deposits.

Figure appendix III-2 shows the error estimates for our BD calculation in comparison with measured data. For this figure we only used samples for which both measurement and calculation were performed. The samples shown in Figure appendix III-2a were measured during a winter expedition to the Itkillik River exposure (Figure 3-1). The temperature in the field laboratory was below 0°C; therefore, it was possible to keep the sample frozen, ideal conditions for pumping a vacuum and measuring the displacement. The samples shown in Figure appendix III-2b and c were collected and measured during the summer on the Buor Khaya Peninsula (Figure 3-1), and it was not possible to generate a perfect vacuum without drawing in thawed material. As a result, the BD differences for these two sites (Figure appendix III-2b, c) are higher than for the first site (Figure appendix III-2a). Figure appendix III-2d plots both measured and calculated BD for all sites and deposit types and indicates a good agreement between measured and calculated BD, with $R^2 = 0.71$ for Yedoma and $R^2 = 0.87$ for thermokarst deposits.

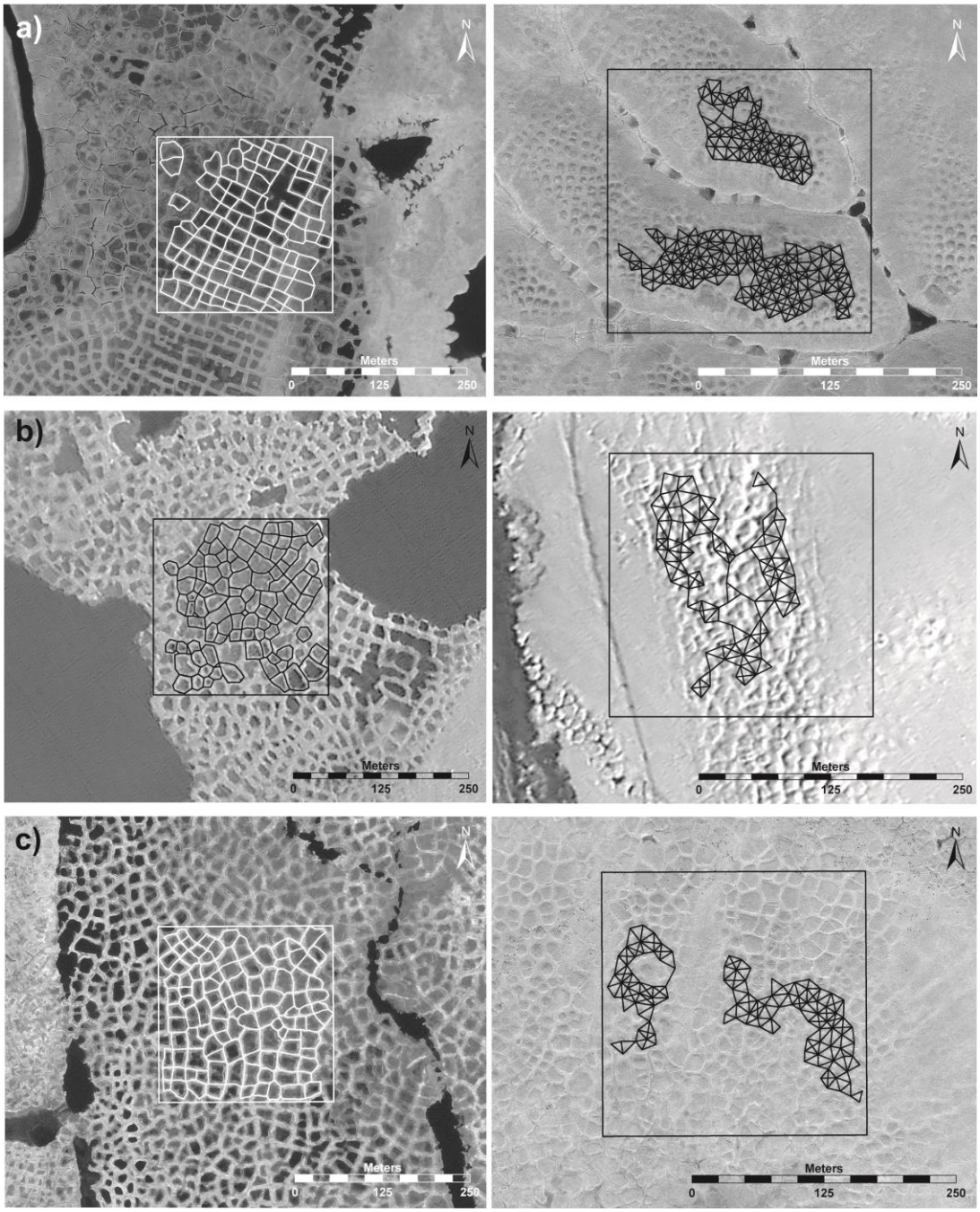

Figure appendix III-3. Methods used to measure polygon size. The satellite-image subsets illustrate polygon mapping for thermokarst deposits (left side) and distance measurements of thermokarst mounds for Yedoma deposits (right side) within a predefined area (box size) of 250 m × 250 m. (a) Cape Mamontov Klyk, site 1 in Figure 3-1 (Geoeye, Band 4, 01.08.2010); (b) Bykovsky Peninsula, site 5 in Figure 3-1 (Kompsat 2; Band 4, 26.08.2010); and (c) Buor Khaya Peninsula, site 7 in Figure 3-1 (Geoeye, Band 4, 13.07.2009).

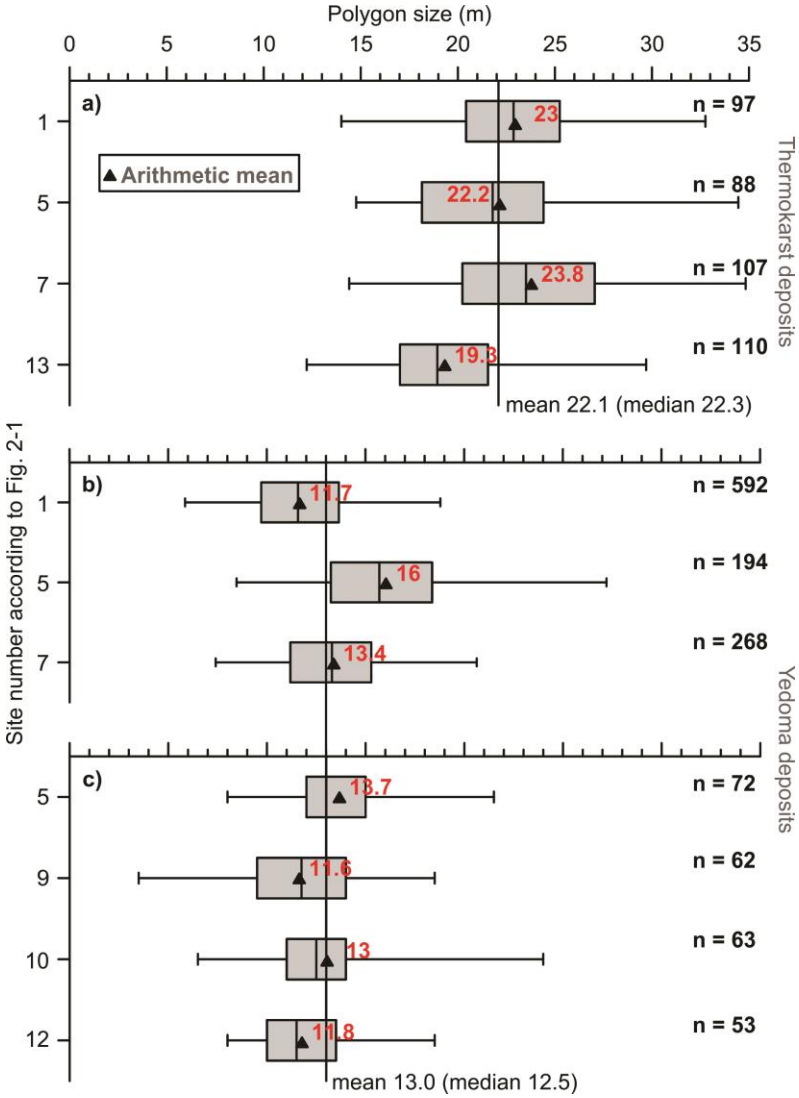

Figure appendix III-4. Boxplots of thermokarst (a) and Yedoma (b, c) deposit polygon sizes, including remote-sensing (a and b) and field data (c). The boxplots are numbered according to Figure 3-1 (1: Cape Mamontov Klyk; 5: Bykovsky Peninsula; 7: Buor Khaya Peninsula; 9: Bel'kovsky Island; 10: Kotel'ny Island; 12: Maly Lyakhovsky Island; 13: Bol'shoy Lyakhovsky Island). For thermokarst deposits (a), intact surface polygons were mapped (Figure appendix III-3, left side); for Yedoma deposits (b and c), distances between thermokarst mound centers were measured (Figure appendix III-3, right side). Yedoma and thermokarst deposit averages are given by the vertical black line.

Further corroborative evidence for the Yedoma deposit polygon sizes illustrated in Figure appendix III-4 are published by Tomirdiaro (1982) and Giterman et al. (1982) for the Siberian lowlands (10-12 m and 9-10 m, respectively) and central Yakutia (11 m) (Tomirdiaro, 1982). Tomirdiaro (1982) describes an average thermokarst deposit polygon size of 20 m (lowlands of northern Yakutia).

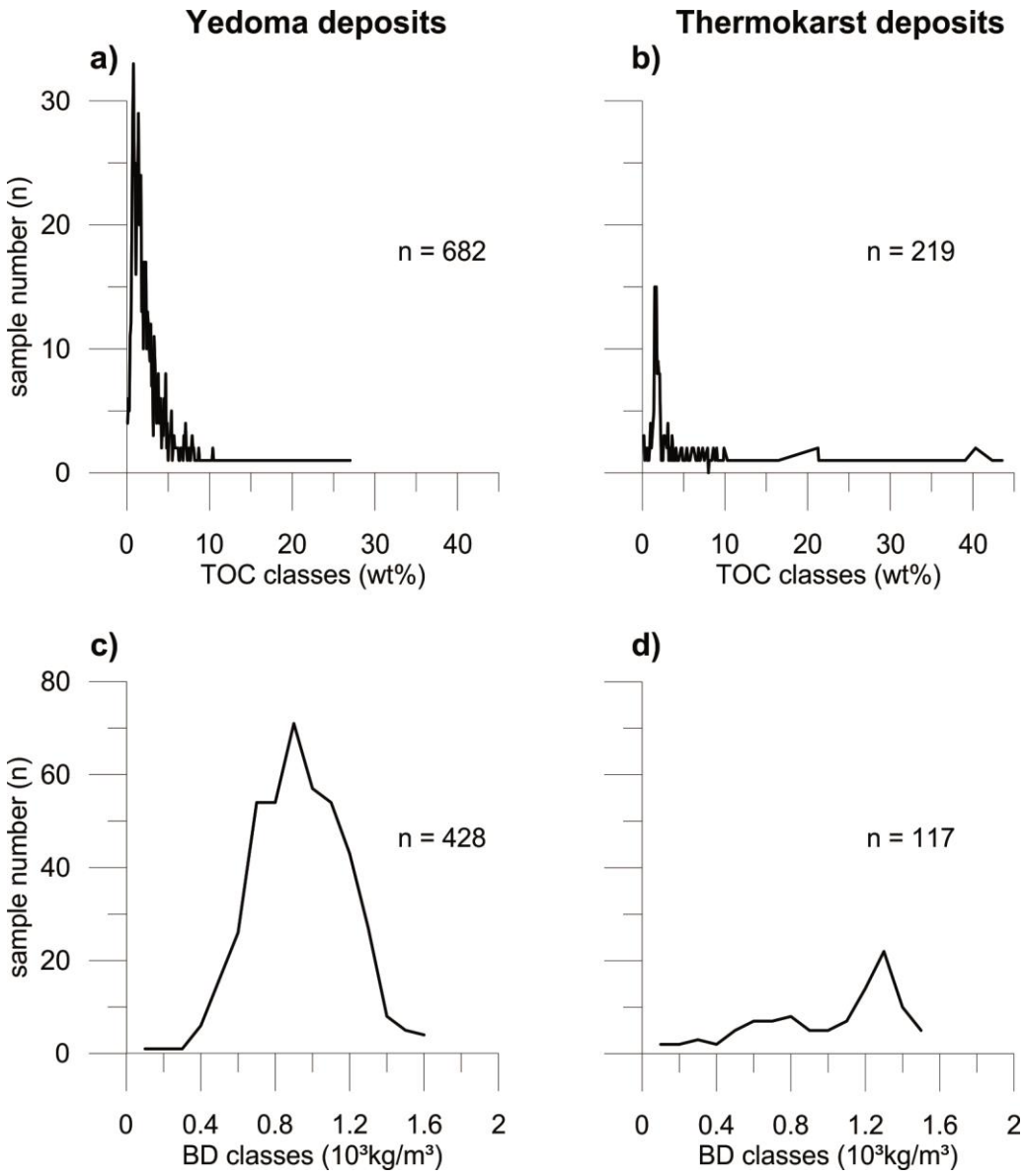

Figure appendix III-5. Distribution curves for total organic carbon (TOC, a and b) and bulk density (BD, c and d) to illustrate the non-normal distribution.

III-3 Supplementary tables

Table appendix III-1. Alternative organic carbon (OC) pool calculations based on simple mean/median. For comparison with previous studies and to illustrate the potential overestimation of the Yedoma region OC pool calculation, the column *"this study (simple mean)"* shows calculations using the arithmetic mean. The column "*this study (simple-median)"* shows an inventory calculation based on median values. [a]Data from *Romanovskii* (1993) and *Jorgenson et al.* (2008), [b]data from *Schirrmeister et al.* (2011b), and [c]data from *Kanevskiy et al.* (2011; 2012; 2013) (sites 20, 21 and 23 in Figure 3-1) are included. We merged the table cells if just one value is available such as for *Zimov et al.* (2006a); [#] not directly described in the publication, but cited in *Walter et al.* (2007b); *In *Zimov et al.* (2006a) the OC density is given as a mean value of ~25.6 kg OC/T, but it is unclear if the WIV is included.

	Zimov et al. (2006a)	this study (simple mean)	this study (simple-median)
Yedoma deposits: coverage (km²)	0.50 million	0.41 million[a]	
Thermokarst deposits: coverage (km²)	0.50 million	0.78 million[a]	
Yedoma deposits: thickness (m)	25.0	19.4	15.1
Thermokarst deposits: thickness (m)	½ × Yedoma deposit thickness	5.5	4.6
Yedoma deposits: area affected by degradation (%)	50	70	70
Yedoma deposits: sample number	71	699	
Thermokarst deposits: sample number		224	
Yedoma deposits: BD (10³kg/m³)	1.65	0.88	0.87
Thermokarst deposits: BD (10³kg/m³)		0.93	0.98
Yedoma deposits: TOC (wt%)	2.56	3.02[b]	1.89[b]
Thermokarst deposits: TOC (wt%)	70 % of Yedoma deposit TOC	6.48[b]	2.59[b]
Yedoma deposits: WIV (vol%)	50	48[c]	52[c]
Thermokarst deposits: WIV (vol%)	n.a.	7	7
Yedoma deposits: SEI (wt%)	n.a.	40.2[b]	39.8[b]
Thermokarst deposits: SEI (wt%)	n.a.	40.7[b]	37.5[b]
Yedoma deposits: OC density (kg/m³) WIV included / WIV not considered	25.6*	14 / 27	8 / 16
Thermokarst deposits OC density (kg/m³) WIV included / WIV not considered		56 / 60	24 / 25
Yedoma deposits: OC inventory (Gt)	n.a., 264[#] (~60 %)	112 (32 %)	50 (37 %)
Thermokarst deposits: OC inventory (Gt)	n.a.	240 (68 %)	84 (63 %)
Total inventory Yedoma region (Gt)	450	352	134

Table appendix III-2. Summary of the key parameters for Yedoma deposit organic carbon (OC) budget calculation. #Data from *Kanevskiy et al.* (2011; 2012; 2013) (sites 20, 21 and 23 in Figure 3-1) are included.

	TOC (wt%)	BD (10^3kg/m^3)	WIV# (vol%)	Thickness (m)
Mean	3.02	0.88	47.9	19.4
Median	1.89	0.87	51.9	15.1
16th percentile	0.8	0.63	36.0	9
84th percentile	4.6	1.14	58.4	30
Min	0.1	0.09	34.7	5
Max	27.0	1.52	59.0	46
n	682	428	10	20

Table appendix III-3. Summary of the key parameters for thermokarst deposit organic carbon (OC) budget calculation.

	TOC (wt%)	BD (10^3kg/m^3)	WIV (vol%)	Thickness (m)
Mean	6.48	0.93	7.0	5.5
Median	2.59	0.98	6.9	4.6
16th percentile	1.5	0.55	2.6	2
84th percentile	10.4	1.26	12.3	9
Min	0.2	0.09	0.8	1
Max	43.5	1.48	12.8	13
n	219	117	6	10

Table appendix III-4. Yedoma deposit parameters separated in a Siberian and an Alaskan subregion.

	TOC (wt%)		BD (10^3kg/m^3)		Thickness (m)	
	Siberia	Alaska	Siberia	Alaska	Siberia	Alaska
Mean	3.20	1.95	0.87	0.95	19.8	18.1
Median	2.03	1.11	0.86	0.94	15.2	15.0
16th percentile	0.9	0.6	0.63	0.67	9	12
84th percentile	4.7	2.9	1.11	1.26	29	25
Min	0.1	0.3	0.09	0.35	5	8
Max	27.0	17.6	1.52	1.40	46	33
n	585	97	351	77	15	5

Table appendix III-5. The thermokarst deposit parameters separated in a Siberian and an Alaskan subregion.

	TOC (wt%)		BD (10^3kg/m^3)		Thickness (m)	
	Siberia	Alaska	Siberia	Alaska	Siberia	Alaska
Mean	6.22	9.03	0.94	0.74	6.1	3.1
Median	2.22	7.78	1.05	0.70	4.6	3.1
16th percentile	1.5	3.2	0.55	0.61	2	2
84th percentile	10.0	11.0	1.27	0.76	10	4
Min	0.2	0.5	0.09	0.41	2	1
Max	43.5	42.3	1.48	1.47	13	5
n	199	20	108	9	8	2

Table appendix III-6. Polygon size and ice-wedge width used for Yedoma and thermokarst deposit WIV calculation. *Data for wedge-ice width from literature (Giterman et al., 1982; Meyer et al., 2002a; 2002b; Grigoriev et al., 2003; Magens, 2005; Boike et al., 2008; Wetterich et al., 2008; Hoffmann, 2011; Kanevskiy et al., 2011; Opel et al., 2011; Kanevskiy et al., 2012; Boereboom et al., 2013; Kanevskiy et al., 2013) and field measurements.

	Yedoma deposit ice-wedge width (m)*	Yedoma deposit polygon size (m)	Thermokarst deposit ice-wedge width (m)*	Thermokarst deposit polygon size (m)
mean	4.0	13.0	1.7	22.1
median	4.2	12.5	1.6	22.3
16th percentile	2.6	11.6	0.6	20.3
84th percentile	4.5	13.4	2.9	23.2
min	2.4	3.5	0.2	12.2
max	6.0	27.2	3.0	34.8
number of sites	10	7	6	4
n total	44	1,304	40	402

Table appendix III-7. Existing data on thermokarst affected areas and lakes in the Yedoma region. *excluding slope areas; **only thaw lake basins without slopes or thermoerosional forms; ***area covered by 11 digitized maps, including areas outside the Yedoma region.

Reference	Region	Study area (km²)	Thermokarst-affected area (km²)	Thermokarst affected area (%)	Yedoma deposit area (km²)	Yedoma deposit area (%)	Lake area (%)
Grosse et al. (2005)*	Bykovsky Peninsula, Siberia	175	93	53	n.a.	n.a.	14.4
Grosse et al. (2006)	Cape Mamontov Klyk, Siberia	2,317	1,807	78	515	22	8.9
Veremeeva and Gubin (2009)	Kolyma Lowland, Siberia	6,528	4,231	65	1,730	27	18
Morgenstern et al. (2011)**	Lena Delta, Siberia	1,689	338	20	n.a.	n.a.	7.0
Morgenstern et al. (2011)	Kurungnakh Island, Siberia	259	172	66	87.4	34	
Arcos (2012)	Buor Khaya Peninsu-la, Siberia	2,000	1,800	90	200	10	8.8
Jones et al. (2012)	northern Seward Peninsula, Alaska	515	391	76	n.a.	n.a.	7
Grosse et al. (2013b)***	northern Siberia	1,716,946	n.a.	n.a.	290,101	17	n.a.

Table appendix III-8. Sensitivity analyses for "mean-based" bootstrapping methods for the four variables for which multiple observations were available. Results were obtained when the uncertainty around a single variable was set to zero (fixed); they were presented as the % of the range obtained from the original run. For comparison, the results of mean, range from the mean to the 16th, and 84th percentiles and 84th-16th absolute percentile range are indicated.

	mean (Gt)	range to 16th per-centile (Gt)	range to 84th per-centile (Gt)	per-centile range (Gt)	TOC fixed (%)	BD fixed (%)	WIV fixed (%)	thickness fixed (%)
Yedoma	111	95	128	33	96	98	93	50
Thermokarst	237	181	294	113	93	100	100	35

Table appendix III-9. Yedoma region organic carbon pool calculated with arithmetic means and standard deviation (StD) estimates

	Yedoma			Thermokarst		
	mean	StD	Std error	mean	StD	Std error
TOC (wt%)	3.0	3.6	0.14	6.5	8.9	0.60
BD (10^3kg/m^3)	0.9	0.2	0.01	0.9	0.4	0.03
(100-WIV)/100	0.5	0.07	0.02	0.9	0.05	0.02
Thickness (m)	19.4	11.5	2.63	5.5	4.0	1.25
OC budget (Gt)	112			240		
± Propagation error	17			60		

Appendix IV Supplementary material for Chapter 4: Organic matter quality of deep permafrost carbon - a study from Arctic Siberia

Submitted to: Biogeosciences Discussions, 11, 15945–15989, doi:10.5194/bgd-11-15945-2014, 2014

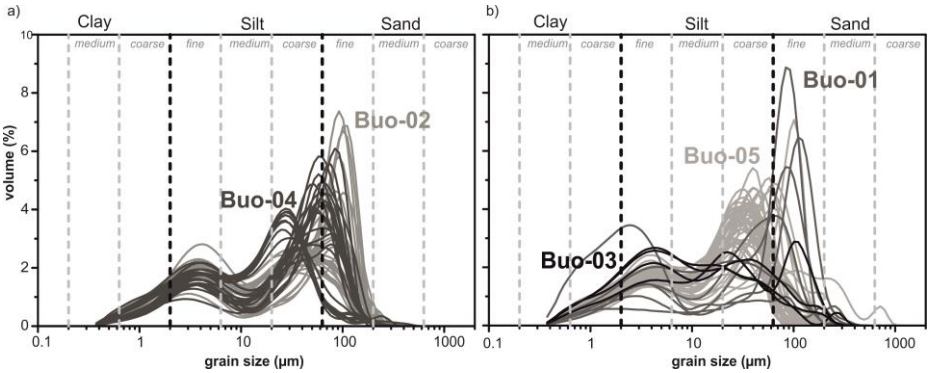

Figure appendix IV-1. Grain-size distribution of a) Yedoma and b) thermokarst profiles. The different profiles are visualized in different shades of grey.

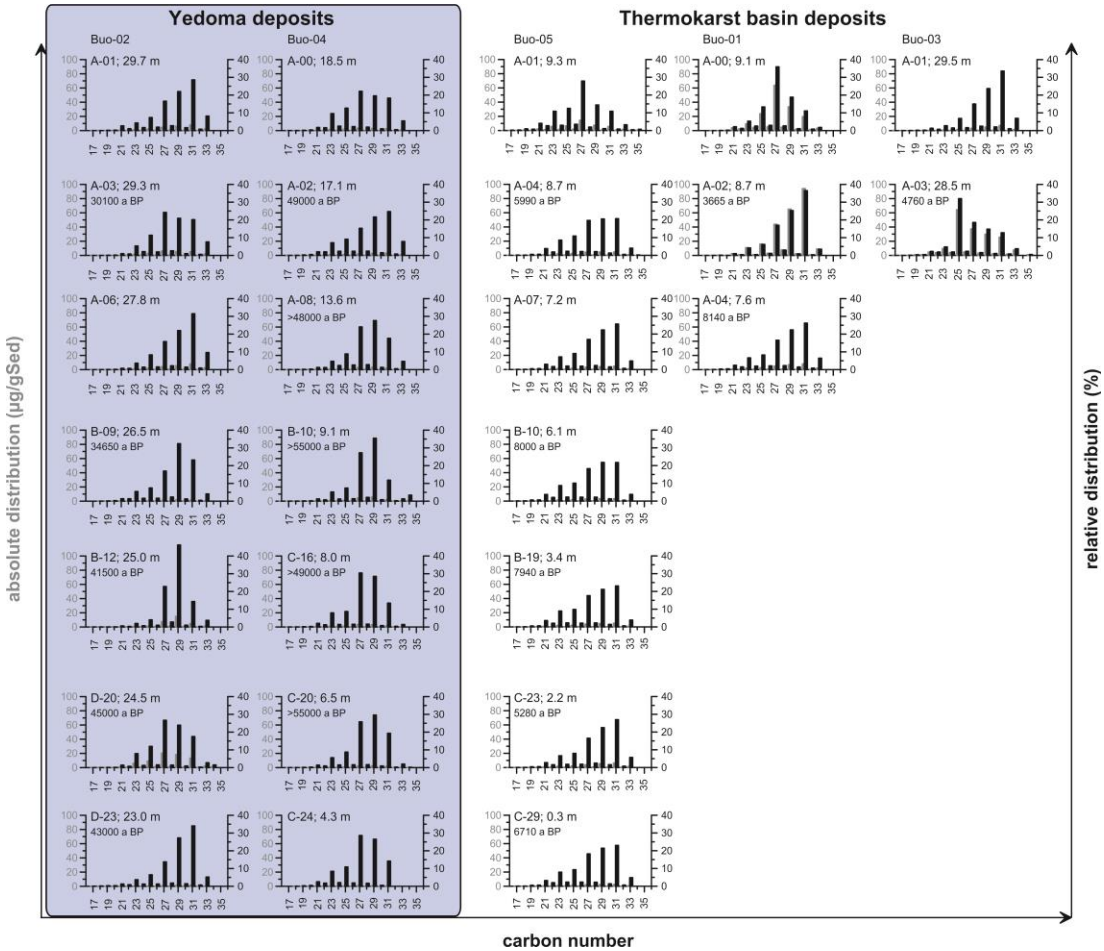

Figure appendix IV-2. Histogram of the *n*-alkanes. The histograms are sorted stratigraphically from left (old) to right (young). The histograms of the Yedoma deposits are visualized with a blue background.

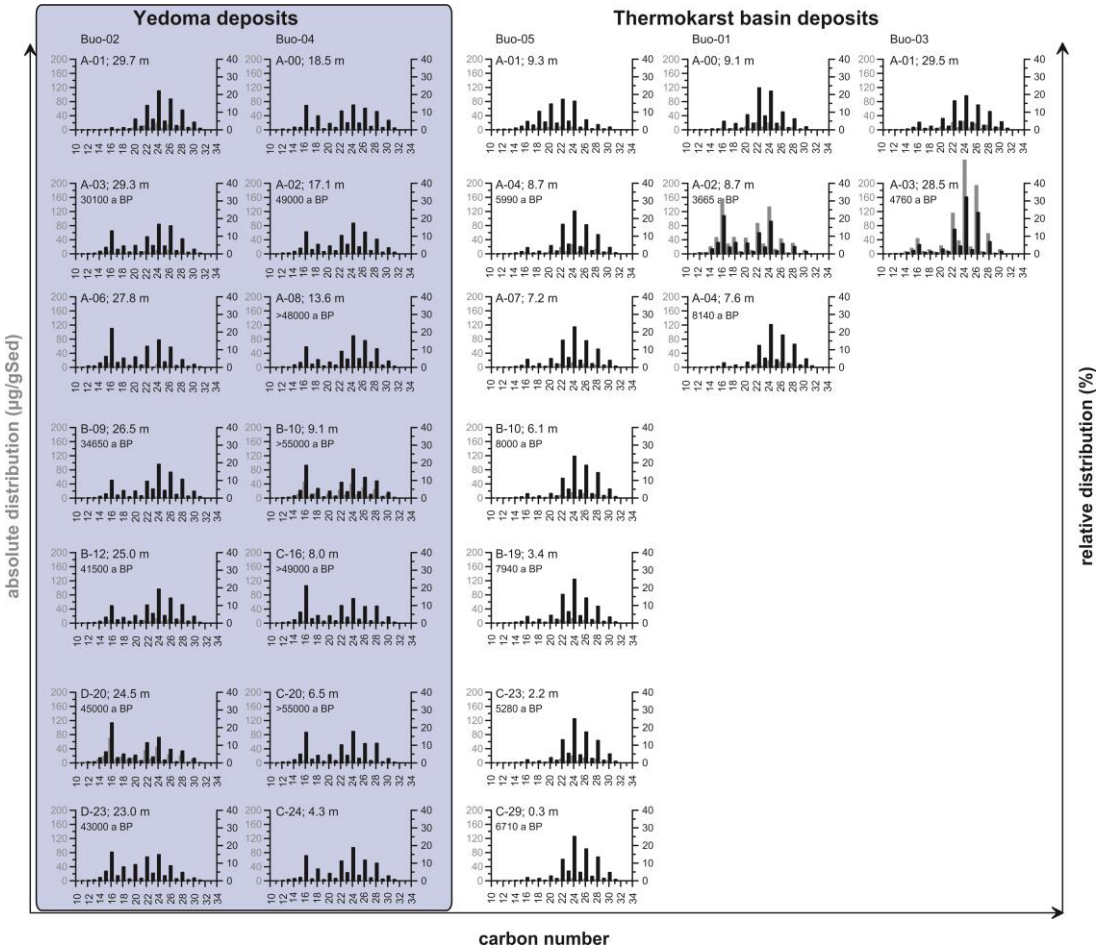

Figure appendix IV-3. Histogram of the *n*-fatty acids. The histograms are sorted stratigraphically from left (old) to right (young). The histograms of the Yedoma deposits are visualized with a blue background.

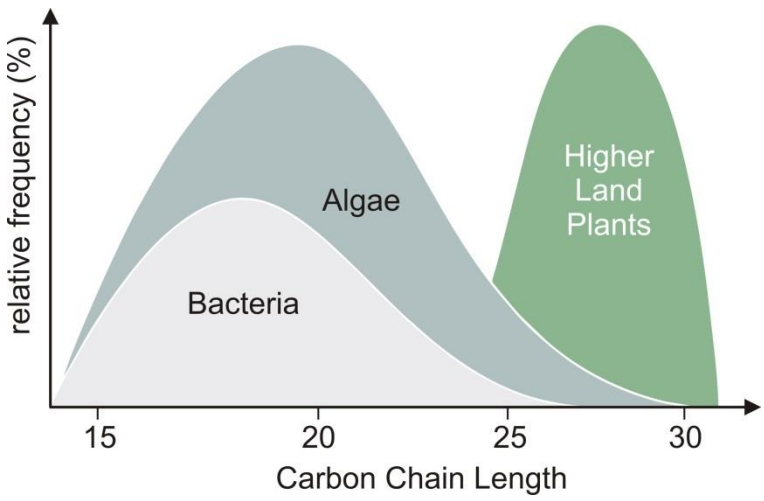

Figure appendix IV-4. Rough schematic of *n*-alkane chain length in different organisms, modified after Killops and Killops (2009).

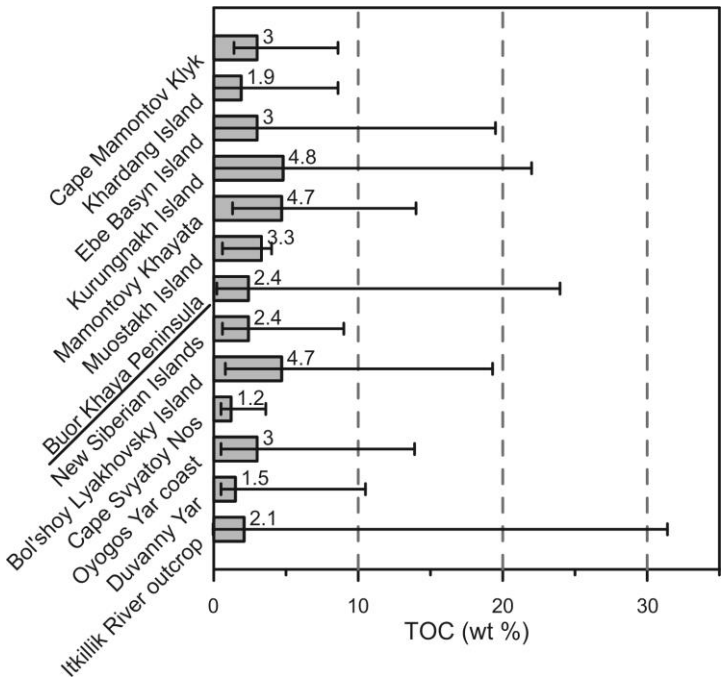

Figure appendix IV-5. TOC variations from different Yedoma studies sorted from easternmost (Itkillik River, Alaskan North Slope) to westernmost (Mamontov Klyk, western Laptev Sea) studies (Schirrmeister et al., 2008a; Schirrmeister et al., 2008b; Schirrmeister et al., 2011b; Strauss et al., 2013), including the present study from Buor Khaya Peninsula. The means are illustrated by the values; the range is shown by the bars.

Acknowledgements - Danksagung

This work would not have been possible without the help and support of many people. First of all, I would like to thank the members of my PhD committee.

My special thanks goes to Dr. Lutz Schirrmeister for being a world-class supervisor, providing excellent guidance, motivating enthusiasm and endless support throughout my work at the Alfred Wegener Institute in Potsdam (AWI) and beyond. Since my early days at the institute as master student, he supported me through (1) great ideas, (2) fatherly advice, (3) help with data interpretation, (4) help with fieldwork campaigns, (5) assistance in writing papers and proposals, (6) straight forward problem-solving, (7) professional guidance to make a smooth transition from student to scientist, (∞)...

Also I would like to thank **Prof. Hans-Wolfgang Hubberten** for providing me with the great opportunity to work at the AWI, his supervision and willingness to review this thesis. He ensured financial support for conference travels and expeditions to Siberia and Alaska. During field expeditions I not only collected samples and data for my thesis, but also got the golden opportunity to experience the fascination of the Arctic. Moreover, thanks for facilitating the exciting and stimulating working atmosphere with in the "AWI-family"!

Additionally, I am indebted to **Dr. Sebastian Wetterich** (AWI) for his invaluable advice during fieldwork but also in scientific writing. Especially, I am thankful for fruitful discussions during coffee breaks and genius drawings of figures on table napkins that greatly improved my papers. I am also thankful for helping me to structure this thesis.

A great thanks also goes to **Dr. Kai Mangelsdorf** (German Research Centre for Geoscience, GFZ) for introducing me to the world of organic geochemistry and for the possibility to carry out my lab work in Potsdam. Thanks also for fruitful discussions and ideas for interpreting biomarker data.

I would like to thank the Studienstiftung des deutschen Volkes (German National Academic Foundation) for supporting me with a doctoral scholarship. Especially, I would like to thank personal support from **Prof. Dr. Peter Saalfrank** (my personal tutor at the University of Potsdam), **Dr. Imke Thamm**, **Dr. Matthias Meyer** and **Dr. Laura Dittmar**. Given the multidisciplinary approach of the thesis, my research greatly benefited from the expertise of several colleagues. **Dr. Mathias Ulrich** (now at University of Leipzig) and **Dr. Guido Grosse** (AWI) gave my project a broader context by providing remote sensing. Statistical analyses greatly benefited from the expertise of **Prof. Dr. Ulrike Herzschuh** (AWI) and insights into biomarker research were provided **by Prof Dr. Gesine Mollenhauer** (AWI) and **Dr. Kai Mangelsdorf** (GFZ).

Any of my Arctic expeditions was based on trusty international teamwork of Russian-US-American-Canadian-German expedition members. A special thanks to "**Team Buor Khaya 2010**" including **Dr. Lutz Schirrmeister**, **Dr. Sebastian Wetterich**, **Dr. Frank Günther**, **Dr. Paul Overduin** (all AWI), **Irina Yakshina** (Lena Delta Reserve), **Dr. Aleksandr Makarov** (AARI), **Aleksandr Sandakov**, and **Dr. Mikhail N. Grigoriev** (Permafrost Institute Yakutsk) and "**Team Itkillik 2012**" including **Prof. Dr. Mikhail Kanevskiy**, **Prof. Dr. Yuri Shur**, **Dr. Amy Breen** (all University of Alaska Fairbanks, UAF), **Prof. Dr. Daniel Fortier** (Université de Montréal), **Dr. Cody Johnson** (CH2Hill Polar Service) and **Kevin Bjella** (Cold Regions Research and Engineering Laboratory). Great thanks also to the AWI

Logistics Department, especially **Waldemar Schneider**, and the German Federal Ministry of Education and Research (BMBF) for financial support of the Russian-German cooperation project "System Laptev Sea" (grant no. 01DM12011), which made these expeditions possible.

I am also grateful to the Graduate School for Polar and Marine Research (**Dr. Claudia Hanfland** and **Dr. Claudia Sprengel**) and Potsdam Graduate School for providing possibilities for my career development including advanced research training and financial support for my travels to conferences and meetings with project collaborators. As a PhD student with children I am also very grateful to the Faculty of Mathematics and Natural Sciences of the University of Potsdam for providing financial support for a student assistant, who assisted me in my research. It helped me a lot to combine work and family life!

My publications benefited from English language correction and valuable comments from **Dr. Candace O'Connor** (UAF) and my brother **Dr. Jan Strauss** (University of East Anglia). Furthermore, **Dr. Lutz Schirrmeister**, **Dr. Sebastian Wetterich**, **Dr. Thomas Opel**, **Dr. Guido Grosse** (all AWI) and **Dr. Kai Mangelsdorf** are acknowledged for their rapid proof-reading of the final version of the thesis. Analytical work would not be possible without the invaluable support of people in the labs. I would like to thank **Ute Kuschel**, **Antje Eulenburg**, **Christin Sawallisch**, **Daniel Gorzawski**, **Dyke Scheidemann**, **Tyne Brückner** (all AWI) as well as **Anke Kaminsky**, **Cornelia Karger** and **Kristin Günther** (all GFZ) who helped me learning sedimentological, geochemical and biomarker methods. **Luise Eichhorn** and **George Tanski** are acknowledged for their collaboration during their master projects.

Ich bedanke mich herzlich bei **Günther "Molo" Stoof** für die Beherbergung in seinem/r "Büro/Werkstatt"; und natürlich für die stetige Versorgung mit leckerem Filterkaffe!

Thanks also to all my PhD colleagues and friends, who supported me along the way. Thanks to my former office mates **Dr. Stephan Opitz**, **Dr. Boris Biskaborn**, **Dr. Andreas Borchers** and **Arne Ramisch** for a great start into my PhD time. Thanks also to **Dr. Mathias Ulrich**, **Dr. Anne Morgenstern**, **Dr. Frank Günther**, **Dr. Michael Fritz**, **Dr. Lars Ganzert**, **Dr. Juliane Bischoff**, **Prof. Dr. Hugues Lantuit**, **Josefine Len**z and **Liv Heinecke** for fruitful scientific discussions and great times at conferences, BBQs, and countless coffee breaks. Thanks also to the "new" PhD generation for the great time during even more coffee breaks and lunches. Especially, I would like to thank **George Tanski**, **Juliane Wolter**, **Stefanie Weege**, **Boris Radosavljevic**, **Romy Zibulski**, **Stefan Schimpf** and **Samuel Stettner** for their warm welcome after two parental leaves and for being patient with a sometimes exhausted young father. Over the last years many people from both work and personal life helped me to finalize this dissertation. To all of you who are not being mentioned by name my warmest thanks!

Mein ganz besonderer und größter Dank geht an meine Frau **Judith**, meine Töchter **Ida** und **Emma**, meinen Bruder **Jan** und meine Eltern **Regina** und **Martin**! Danke für die unglaubliche Unterstützung, welche nicht in Worte zu fassen ist und die Erinnerung daran, was wirklich wichtig ist.

Eidesstattliche Erklärung

Hiermit versichere ich, dass ich die vorliegende Arbeit selbstständig verfasst und keine anderen als die angegebenen Quellen und Hilfsmittel verwendet habe.

Ich habe diese kumulative Dissertation am Alfred-Wegener-Institut Helmholtz Zentrum für Polar und Meeresforschung in Potsdam erarbeitet und in englischer Sprache angefertigt. Diese Dissertation wird erstmalig und ausschließlich an der Universität Potsdam eingereicht.

Die dem Promotionsverfahren zugrundeliegende Promotionsordnung vom 18.09.2013 ist mir bekannt.

Potsdam, den 30.09.2014 Jens Strauß